UNIVERSITÉ DE GENÈVE
Département de physique nucléaire et corpusculaire

FACULTÉ DES SCIENCES
Professeur Allan G. Clark

Search for the Decays $B_d^0 \to \mu^+\mu^-$, $B_s^0 \to \mu^+\mu^-$ and $B_s^0 \to \mu^+\mu^-\phi$ in $p\bar{p}$ Collisions at $\sqrt{s} = 1.8$ TeV

THÈSE

présentée à la Faculté des sciences
de l'Université de Genève
pour l'obtention du grade de Docteur ès sciences,
mention physique

par

Thomas SPEER
d'Autriche

Thèse No 3193

GENÈVE
Atelier de reproduction de la Section de Physique
2000

La Faculté des sciences, sur le préavis de Messieurs A. CLARK, professeur ordinaire et directeur de thèse (Département de physique nucléaire et corpusculaire), A. BLONDEL, professeur ordinaire (Département de physique nucléaire et corpusculaire), P. SPHICAS, professeur (CERN, Division EP et Physics Department, Massachussets Institute of Technology, Cambridge - U.S.A.) et Xin WU, docteur (Département de physique nucléaire et corpusculaire), autorise l'impression de la présente thèse, sans exprimer d'opinion sur les propositions qui y sont énoncées.

Genève, le 12 septembre 2000

Thèse - 3193 -

Le Doyen, Jacques WEBER

La présente thèse a donné lieu à la publication suivante:
F. Abe *et al.*, *Search for the Decays* $B_d^0 \to \mu^+\mu^-$ *and* $B_s^0 \to \mu^+\mu^-$ *in* $p\bar{p}$ *Collisions at* $\sqrt{s} =$ 1.8 TeV, *Phys. Rev.* D **57**, R3811 (1998).

Contents

Chapter 1

Résumé

Cette thèse décrit la recherche des désintégrations à courants neutres $B_d^0 \to \mu^+\mu^-$, $B_s^0 \to \mu^+\mu^-$ et $B_s^0 \to \mu^+\mu^-\phi$, effectuée dans des collisions proton–anti-proton à une énergie de centre de masse de $\sqrt{s} = 1.8$ TeV observées par l'expérience CDF (*Collider Detector at Fermilab*). N'observant aucune indication de la présence de ces désintégrations, des limites supérieures des rapports de branchement sont mesurées.

1.1. Introduction théorique

Le Modèle Standard électro-faible est le modèle théorique décrivant le mieux les interactions électro-faibles. Il prédit avec succès l'existence des courants neutres, découverts au CERN en 1974, et des bosons intermédiaires W et Z^0, découverts également au CERN en 1983. Il fut développé dans les années soixantes par S.L. Glashow, S. Weinberg et A. Salam. Le Modèle Standard est une théorie de jauge non-abélienne spontanément brisée avec une symétrie de jauge locale $SU(2)_L \times U(1)_Y$.

Dans ce modèle, les courants neutres avec changement de saveur sont interdits au premier ordre et ne peuvent avoir lieu qu'au travers de diagrammes d'ordre plus élevés, de type 'pingouins' ou 'boîte'. Les rapports de branchement de processus de ce type, tel que les désintégrations $B_d^0 \to \mu^+\mu^-$, $B_s^0 \to \mu^+\mu^-$ ou $B_s^0 \to \mu^+\mu^-\phi$, sont alors très faibles.

Dans le cadre du Modèle Standard, ces désintégrations permettent d'accéder aux valeurs des éléments de la matrice de mélange des quarks, la matrice de Cabibbo-Kobayashi-Maskawa, et aux masses des quarks. Ces désintégrations permettent aussi de tester la validité du Modèle Standard à de basses énergies. Plusieurs extensions du Modèle Standard permettent à ces désintégrations de procéder via des processus différents. La mesure d'une valeur du rapport de branchement différente de la valeur prédite par le Modèle Standard serait ainsi une indication de l'inadéquation du Modèle Standard.

Les bas rapports de branchement des désintégrations à courants neutres avec changement de saveur n'ont pour l'instant permis, dans le système du B, l'observation expérimentale que d'une seule catégorie de désintégrations, de type $b \to s\gamma$. Les rapports de branchement ainsi mesurés sont en accord avec les prédictions du Modèle Standard, et ont permis de contraindre certaines extensions du Modèle Standard.

1.2. Le collisionneur Tevatron et l'expérience CDF

Le Tevatron, situé au 'Fermi National Accelerator Laboratory' (Fermilab) à Batavia, aux Etats-Unis, est un collisionneur proton–anti-proton d'énergie de centre de masse de $\sqrt{s} = 1.8$ TeV. Jusqu'à la mise en service du LHC (*Large Hadron Collider*) au CERN prévue en 2005, le Tevatron est le collisionneur atteignant la plus haute énergie de centre de masse.

Les données étudiées dans cette analyse ont été récoltées pendant deux périodes de mesures. La première période (Run 1A) s'est déroulée entre 1992 et 1993. Durant celle-ci, un échantillon de données correspondant à une luminosité intégrée de $\int \mathcal{L}dt = (19.5 \pm 1.0)$ pb^{-1} a été récolté. Pendant la seconde période (Run 1B) située entre 1994 et 1995, l'équivalent de $\int \mathcal{L}dt = (89 \pm 7)$ pb^{-1} de données ont été récoltées.

L'expérience CDF est la première des deux expériences construites pour étudier la physique des collisions proton–anti-proton à haute impulsion transverse. C'est un détecteur plurifonctionnel avec des symétries cylindrique et avant-arrière dont le centre coïncide avec le point d'interaction. Une description complète du détecteur et des systèmes de détection le composant peut être trouvée dans la référence [117]. Les systèmes utilisés dans cette analyse sont ceux de trajectographie et de détection de muons.

Les systèmes de trajectographie se trouvent à l'intérieur d'un aimant supraconducteur de 4.8 mètres de long générant un champ magnétique solénoïdale de 1.4 T. Situé immédiatement à l'extérieur du tube à vide du faisceau, le premier de ces systèmes est un détecteur de vertex au silicium(*Silicon Vertex Detector - SVX*) qui mesure la position des traces dans le plan $r-\phi$[1]. Le SVX est composé de deux modules cylindriques indépendants d'une longueur de 25.5 cm chacun, situés de part et d'autre du point central. Chaque module est composé de quatre couches cylindriques concentriques, situées entre des rayons de 3.0 cm et 7.9 cm. La largeur des pistes est de 60 μm sur les trois premières couches et de 55 μm sur la dernière. Avec une résolution de l'ordre de 13 μm pour chaque mesure, la résolution du paramètre d'impact est de $(16 + 40/p_T)$ μm lorsque l'impulsion transverse de la trace p_T est mesurée en GeV/c.

Entourant le SVX, un système de chambres à projection temporelle (*time projection chambers - VTX*) mesure les coordonnées des traces selon l'axe z et reconstruit la coordonnée z du vertex primaire, c'est-à-dire du point d'interaction.

Après le VTX se trouve la chambre de trajectographie centrale (*Central Tracking Chamber - CTC*), une chambre à dérive cylindrique de 3.2 m de long, avec un rayon intérieur de 0.28 m et un rayon extérieur de 1.38 m. La CTC est composée de 84 couches de fils de mesure, groupées en neuf super-couches. Cinq de ces super-couches mesurent les coordonnées des traces dans le plan $r-\phi$ et les quatre autres permettent de reconstruire les coordonnées z de la trace. En combinant les mesures du SVX et de la CTC, les traces peuvent être reconstruites dans la région $|\eta| < 1$.

[1]Dans le système de coordonnées employé à CDF, l'axe z est donné par la direction du faisceau de proton. Le système de coordonnées polaires est le plus souvent employé, où l'angle polaire θ est mesuré relativement à l'axe z et l'angle azimutal ϕ pris dans le sens des aiguilles d'une montre autour de l'axe z, avec le plan du Tevatron comme point de départ. La *rapidité* y est définie comme $y = \tanh^{-1}\left(\frac{p_z}{E}\right)$ et, pour des particules relativistes, est égale à la *pseudorapidité* η, définie comme $\eta = -\ln(\tan(\theta/2))$. Le plan transverse est le plan perpendiculaire au faisceau et la coordonnée longitudinale correspond à l'axe z.

Dans la partie centrale, le système de détection de muons est composé de trois sous-systèmes, capables de détecter des muons avec $p_T \geq 1.4$ GeV/c et $|\eta| < 1.0$. Situées en dehors des calorimètres hadroniques, les chambres à muons identifient les muons par leur fort pouvoir de pénétration. Le premier de ces systèmes, appelé CMU (*Central Muon Chamber*), couvrant la région $|\eta| < 0.6$, est constitué de quatre plans de chambres à dérive. Celles-ci permettent de reconstruire des segments de traces, qui pourront être associés ultérieurement aux traces reconstruites dans la CTC. En dehors du CMU, quatre plans de chambres à dérive supplémentaires sont placés derrière 60 cm d'acier (*Central Muon Uprgrade - CMP*). Ces trois longueurs d'absorption supplémentaires d'acier, s'ajoutant aux cinq longueurs d'absorption du calorimètre, permettent une meilleure réjection du bruit de fond hadronique détecté dans le CMP.

Finalement, le système CMX (*Central Muon Extension*) étend partiellement la couverture à la région $0.6 < |\eta| < 1.0$. Les muons détectés dans les plans de chambres à dérive composant le CMX auront traversé, selon leur angle d'incidence, l'équivalent de six à neuf longueurs d'absorption.

Le système de déclenchement est divisé en trois niveaux consécutifs. Les deux premiers sont constitués de systèmes électroniques dédiés, tandis que le troisième niveau est constitué d'un système informatique utilisant des programmes similaires aux programmes de reconstructions 'offline'. Les événements étudiés dans la présente analyse sont collectés par les déclenchements recherchant des paires de muons (*dimuons*) de basse impulsion transverse. Pour ces déclenchements, au premier niveau, la présence de deux segments de traces dans les chambres à muons est requise. Au deuxième niveau, les segments de traces sont associés aux traces trouvées dans la CTC par un système de reconnaissance de traces rapide (*Central Fast Tracker - CFT*). Au troisième niveau, les deux muons sont reconstruits en utilisant l'ensemble des mesures prises par tous les systèmes, à l'exclusion du SVX.

Pendant le Run 1A, seules les paires de muons dont les muons sont détectés dans le CMU ou le CMP sont sélectionnés par le déclenchement requis. Pendant le Run 1B, les muons détectés dans le CMX sont admis, mais un des deux muons au moins doit être détecté dans le CMP.

1.3. La recherche des désintégrations $B_d^0 \to \mu^+\mu^-$ et $B_s^0 \to \mu^+\mu^-$

Dans le Modèle Standard, les désintégrations $B_d^0 \to \mu^+\mu^-$ et $B_s^0 \to \mu^+\mu^-$[2] procèdent au travers de diagrammes 'pingouins' verticaux électromagnétiques et faibles et de diagrammes de W de type 'boîte'. La prédiction théorique des rapports de branchement est $\mathcal{B}(B_d^0 \to \mu^+\mu^-) = (1.5 \pm 0.9) \cdot 10^{-10}$ et $\mathcal{B}(B_s^0 \to \mu^+\mu^-) = (3.5 \pm 1.0) \cdot 10^{-9}$.

Lors de la recherche effectuée précédemment à CDF, des limites supérieures à un niveau de confiance de 90% de $\mathcal{B}(B_d^0 \to \mu^+\mu^-) < 1.6 \cdot 10^{-6}$ et $\mathcal{B}(B_s^0 \to \mu^+\mu^-) < 8.4 \cdot 10^{-6}$ furent mesurées. Cette recherche fut effectuée sur un échantillon de données, collecté pendant

[2]Bien que le nom officiel du méson B_d^0 soit B^0, la première des deux notations sera utilisée dans la présente thèse, et la notation B_s^0 sera utilisé pour le B_s. Pour référer sans faire de distinction entre elles aux deux désintégrations $B_d^0 \to \mu^+\mu^-$ et $B_s^0 \to \mu^+\mu^-$, la notation $B^0 \to \mu^+\mu^-$ sera utilisée. La conjugaison de charge est toujours sous-entendue.

le Run 1A, correspondant à une luminosité intégrée de 17.8 ± 0.6 pb^{-1}. Pour la présente recherche, un second échantillon de données, collecté pendant le Run 1B et correspondant à une luminosité intégrée de 80.4 ± 6.4 pb^{-1}, est utilisé.

Pour reconstruire un candidat B_d^0 ou B_s^0 ayant subi une désintégration du type $B^0 \to \mu^+\mu^-$, deux muons, sélectionnés par un des déclenchements à dimuons, sont choisis. Chacun de ces muons doit satisfaire à des coupures de qualité pour s'assurer qu'il ne s'agit pas d'un hadron ayant traversé les calorimètres et faussant un muons dans les chambres à muons.

Un fit cinématique des moindres-carrés est effectué, dans lequel les deux traces sont contraintes de provenir d'un même vertex. Ceci permet d'éliminer les candidats dont les traces sont proches dans l'espace mais ne proviennent pas d'un même vertex. Toutes les quantités utilisées par la suite sont dérivées des paramètres issus du fit. Le χ^2 du fit doit être inférieur à 12.

L'impulsion transverse p_T de chaque muon doit être supérieure à 2 GeV/c, et celle de la paire de muons doit être supérieure à 6 GeV/c, de manière à normaliser le résultat avec la mesure de la section efficace de production de B_d^0 effectuée précédemment.

Pour diminuer le bruit de fond, des coupures sont appliquées sur la longueur de désintégrations propre, l'isolation et l'angle d'ouverture. Ces coupures sont choisies en demandant le *rapport signal/bruit* le plus élevé. Ce rapport est donné par $\epsilon_S^2 \cdot R_B$, où ϵ_S est l'efficacité des coupures pour les désintégrations $B^0 \to \mu^+\mu^-$ et R_B le facteur de réjection du bruit de fond. Deux échantillons, supposés être similaires au bruit de fond observé dans la sélection, sont utilisés pour estimer R_B. Le premier est un échantillon de paires de muons de même signe (de masse invariante entre 5 et 6 GeV/c^2) et le second un échantillon de paires de signe opposé (de masse invariante entre 5.0 et 5.2 GeV/c^2 et entre 5.5 et 6.0 GeV/c^2).

Le long temps de vie des mésons B permet d'utiliser la longueur de désintégration propre comme critère de réjection, permettant ainsi d'éliminer une grande proportion du bruit de fond de temps de vie court. Ceci requiert une détermination précise de la distance de vol du méson B et donc de la position du vertex de désintégration du méson (appelé vertex secondaire). Pour cette raison, chacun des deux muons est requis d'être reconstruit dans le SVX dans au moins trois des quatre couches. La longueur de désintégration transverse est définie comme $L_{xy} = \frac{\vec{l}_{xy} \cdot \vec{p}_T^B}{p_T^B}$, où $\vec{l}_{xy}$ est le vecteur pointant du vertex d'interaction $p\bar{p}$ (appelé vertex primaire) au vertex secondaire et p_T^B l'impulsion transverse du B reconstruit. L'incertitude sur la longueur de désintégration transverse doit être inférieure à 150 μm. L'incertitude moyenne sur L_{xy} est d'environ 60 μm, alors que la longueur de désintégration transverse L_{xy} moyenne attendue pour le signal est d'environ 860 μm. La longueur de désintégration propre, définie comme $c\tau = L_{xy} \cdot \frac{m_{B^0}}{p_T^B}$, est requise d'être supérieure à 100 μm.

Lors de la fragmentation d'un quark b, la majeure partie de l'impulsion du quark initial est transmise au méson B issu du quark b. Ainsi, une grande proportion de l'impulsion mesurée dans un cône autour du méson B est portée par les particules issues de la désintégrations du B. La fraction d'impulsion I du méson candidat (appelée l'*isolation*), définie comme $I = \frac{p_T^B}{p_T^B + \sum p_T}$, est requise d'être supérieure à 0.75. La somme est la somme scalaire de l'impulsion transverse de toutes les traces (exceptées celles composant le méson candidat) se trouvant dans un cône de $\Delta R = \sqrt{(\Delta\eta)^2 + (\Delta\phi)^2} = 1$ autour du vecteur d'impulsion du

Coupure	Efficacité en %
Acceptance géométrique pour $p_T(B) > 6$ GeV/c et $\|y(B)\| < 1$	10.72 ± 0.06
Impulsion transverse $p_T(\mu) > 2$ GeV/c	89.6 ± 0.2
Déclenchements de dimuons	58.3 ± 3.4
Recherche des muons dans les chambres	96.6 ± 0.7
Reconstruction des traces dans la CTC	89.8 ± 3.6
Sélection des muons	97.2 ± 1.2
Qualité des traces et du vertex	77.1 ± 0.2
Incertitude sur la longueur de désintégration transverse ($\sigma_{L_{xy}} < 150$ μm)	94.7 ± 0.5
Longueur de désintégration propre ($c\tau > 100$ μm) $\left\{ \begin{array}{l} \tau_{B_d} = 468 \pm 18 \ \mu\text{m} \\ \tau_{B_s} = 483^{+30}_{-27} \ \mu\text{m} \end{array} \right.$	80.9 ± 1.0 81.8 ± 1.6
Angle d'ouverture $\Phi < 0.1$	85.1 ± 2.2
Isolation $I > 0.75$	72.8 ± 3.0
Fenêtre de sélection	91.6 ± 4.0
Correction du taux de J/ψ	84.6 ± 3.8
Acceptance × efficacité totale $\left\{ \begin{array}{l} \text{pour les } B_d \\ \text{pour les } B_s \end{array} \right.$	1.34 ± 0.15 1.37 ± 0.15

Table 1.1: *Liste des efficacités pour les désintégrations* $B_d^0 \to \mu^+\mu^-$ *et* $B_s^0 \to \mu^+\mu^-$.

candidat. La coordonnée z des traces inclues dans la somme doit être à moins de 5 cm du vertex de désintégration du méson candidat, de manière à exclure de la somme les traces provenant d'autres collisions $p\bar{p}$ ayant lieu lors du même croisement de faisceau.

Finalement, l'angle d'ouverture Φ entre les vecteurs $\vec{p}_T^{\,B}$ et $\vec{l}_{xy}$ est requis d'être inférieur à 0.1 radians, contraignant ainsi les deux vecteurs à être parallèles.

L'acceptance et l'efficacité des coupures de sélection sont données dans la table 1.1. Différents déclenchements ont été utilisés durant différentes périodes pour collecter l'échantillon de données utilisé dans cette recherche. De plus, deux différentes périodes de mesure sont combinées. Chacune des deux périodes et chacun des déclenchements ont une acceptance et des efficacités diverses. Les efficacités données dans la table 1.1 sont donc pondérées par la luminosité et la contribution du déclenchement à l'échantillon total.

Une simulation Monte Carlo des désintégrations recherchées est utilisée pour estimer l'acceptance du signal. Pour cette simulation, des quarks b sont générés selon la corrélation entre $p_T(b)$ et $y(b)$ calculée par Nason, Dawson et Ellis (NDE) à l'ordre $\mathcal{O}(\alpha_s^3)$ (*next-to-leading order*). Les fonctions de structures utilisées sont celles calculées par Martin, Roberts et Stirling (MRSD0). L'échelle de renormalisation choisie est $\mu = \mu_0 \equiv \sqrt{m_b^2 + p_T^2(b)}$, et la masse du quark b est fixée à $m_b = 4.75$ GeV/c^2. Les quarks ainsi produits sont ensuite fragmentés en mésons B selon le modèle de fragmentation de Peterson avec $\epsilon_b = 0.006$. Seuls les mésons de $p_T(B) > 6$ GeV/c et $|y(B)| < 1$ sont retenus. Après désintégration, le passage des muons dans le détecteur, en tenant compte du système de déclenchement, est simulé.

Les efficacités des coupures sur la longueur de désintégration propre et sur l'incertitude sur la longueur de désintégration transverse sont estimées en utilisant la simulation Monte

Carlo. Les efficacités des coupures sur l'isolation et l'angle d'ouverture sont estimées en utilisant un échantillon de mésons B reconstruits au travers des désintégrations $B^+ \to J/\psi K^+$ et $B^0 \to J/\psi K^{*0}$. L'incertitude sur ces dernières efficacités est donnée par l'incertitude statistique due aux échantillons utilisés. Mise à part l'efficacité de la coupure sur la longueur de désintégration propre, les efficacités sont supposées être identiques pour les mésons B_d^0 et B_s^0.

La résolution de la masse du méson reconstruit dans les désintégrations $B^0 \to \mu^+\mu^-$ est estimée à 33 MeV/c^2. Cette résolution est confirmée par l'extrapolation des résolutions mesurées dans les désintégrations $J/\psi \to \mu^+\mu^-$, $\psi(2S) \to \mu^+\mu^-$ et $\Upsilon(1S) \to \mu^+\mu^-$. La fenêtre de recherche du signal est prise comme une région de 150 MeV/c^2 centrée sur la masse-moyenne du méson correspondant. Avec une masse-moyenne de $m(B_d^0) = 5279.2 \pm 1.8$ MeV/c^2 et $m(B_s^0) = 5369.3 \pm 2.0$ MeV/c^2, ces fenêtres correspondent aux régions de masse invariante de la paire de muons entre 5.205 et 5.355 GeV/c^2 pour le B_d^0 et entre 5.295 et 5.445 GeV/c^2 pour le B_s^0.

Les efficacités des coupures de qualité sur les muons et du système de déclenchement sont estimées à partir d'échantillons de J/ψ. L'efficacité de reconstruction des traces dans la CTC est estimée en insérant deux traces générées par Monte Carlo dans des événements J/ψ réels.

Les sections efficaces de production de J/ψ et de Υ étant mesurées plus basses pendant le Run 1B que pendant le Run 1A, une baisse du taux de désintégration $B_s^0 \to \mu^+\mu^-$ reconstruites peut être attendue. Cette baisse est attribuée à la haute densité de traces et au vieillissement de la CTC pendant le Run 1B, mais aucune réponse définitive n'a pu être apportée. Une inefficacité supplémentaire doit donc être ajoutée pour les données du Run 1B pour tenir compte de cette baisse, de manière à ramener le taux de J/ψ observé au taux observé pendant le Run 1A. Cette inefficacité est estimée en utilisant un échantillon de J/ψ provenant de désintégrations de hadrons B, en tenant compte des acceptances, de la luminosité et des efficacités de tracking et de déclenchement des échantillons. La perte de J/ψ est ainsi estimée à $(18.8 \pm 4.6)\%$.

L'acceptance et l'efficacité totale est de $(1.34 \pm 0.15)\%$ pour le B_d^0 et $(1.37 \pm 0.15)\%$ pour le B_s^0, en sommant les incertitudes statistiques et systématiques quadratiquement.

La distribution de la masse invariante des paires de muons après toutes les coupures de sélection est montrée en Figure 1.1. Un événement, avec une masse invariante de 5.344 ± 0.016 GeV/c^2, est trouvé dans la région de signal. Se trouvant dans la partie commune des deux fenêtres de recherche, cet événement résulte en un candidat pour chacun des B_d^0 et B_s^0. Une estimation du nombre d'événements de bruit de fond, basée sur les paires de muons de même signe (de masse invariante entre 5 et 6 GeV/c^2) et de signe opposé (de masse invariante entre 5.0 et 5.2 GeV/c^2 et entre 5.5 et 6.0 GeV/c^2), rend cet événement compatible avec un événement de bruit de fond.

N'observant aucune indication de la présence des désintégrations recherchées dans l'échantillon de données, une limite supérieure est placée sur les rapports de branchement. Au vu du faible nombre de candidats et d'événements de bruit de fond observé, aucune soustraction du bruit de fond n'est effectuée et le candidat est considéré comme un événement de signal.

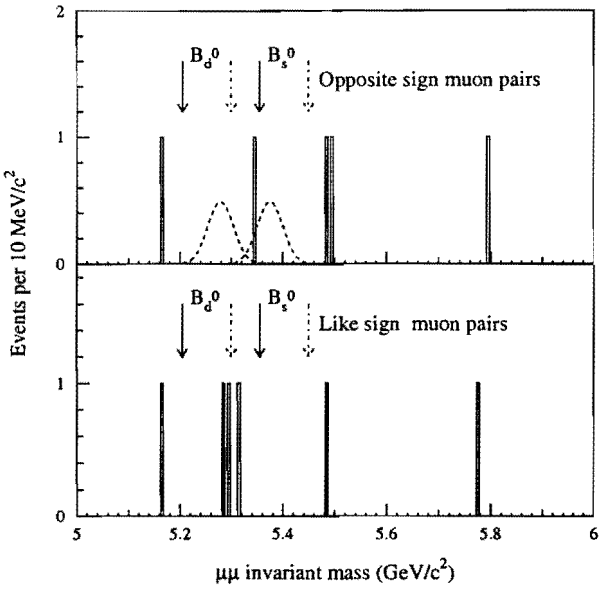

Figure 1.1: *Distribution de la masse invariante des paires de muons de signe opposé (haut) et de même signe (bas) après toutes les coupures de sélection. Les deux fonctions représentent la limite supérieure du signal à un niveau de confiance de 90%.*

La limite supérieure du rapport de branchement est donnée par

$$\mathcal{B}(B^0 \to \mu^+\mu^-) < \frac{N_{limite}(B^0 \to \mu^+\mu^-)}{2\sigma(B) \cdot \left(\int \mathcal{L}^A dt \cdot \epsilon^A \cdot \alpha^A + \sum_t^B \int \mathcal{L}_t^B dt \cdot C_t^B \cdot \epsilon_t^B \cdot \alpha_t^B\right)}, \qquad (1.1)$$

où la somme porte sur tous les déclenchements et les échantillons de données composant l'échantillon total. Pour chaque déclenchement, $\int \mathcal{L}dt$ représente la luminosité intégrée, C_t la contribution à l'échantillon total, ϵ_i l'efficacité des coupures de sélection et α_i l'acceptance géométrique. La section efficace de production du méson B_d^0, mesurée à CDF pour des mésons de $p_T(B) > 6$ GeV/c^2 et de rapidité $|y(B)| < 1$, est $\sigma(B_d^0) = 2.39 \pm 0.32 \pm 0.44\ \mu b$. La fragmentation des quarks b en mésons B_s^0 est supposée résulter en un rapport de sections efficaces de production de $\frac{\sigma(B_d^0)}{\sigma(B_s^0)} = 3$, ce qui est compatible avec la mesure effectuée à CDF. Le facteur deux dans le dénominateur de l'équation 1.1 provient du fait qu'aucune distinction n'est faite entre le méson B^0 et son anti–particule $\bar{B}^0$.

La limite supérieure de Poisson du nombre de candidats à un niveau de confiance de 90% (respectivement 95%) est de 3.89 (respectivement 4.74). Les incertitudes systématiques sont inclues dans le résultat final grâce à la prescription présentée dans la référence. Avec une incertitude systématique totale de 26.1% pour la désintégration $B_d^0 \to \mu^+\mu^-$ et de 26.0% pour la désintégration $B_s^0 \to \mu^+\mu^-$, la limite supérieure du nombre de candidats à un niveau de confiance de 90% (respectivement 95%) est de 4.31 (respectivement 5.48).

Les limites supérieures des rapports de branchement des désintégrations recherchées à des niveaux de confiance de 90 et 95% sont ainsi

$$\mathcal{B}(B_d^0 \to \mu^+\mu^-) < 6.8 \cdot 10^{-7}\ (90\%\ CL)$$
$$\mathcal{B}(B_s^0 \to \mu^+\mu^-) < 2.0 \cdot 10^{-6}\ (90\%\ CL)$$

$$\mathcal{B}(B_d^0 \to \mu^+\mu^-) < 8.6 \cdot 10^{-7}\ (95\%\ CL)$$
$$\mathcal{B}(B_s^0 \to \mu^+\mu^-) < 2.6 \cdot 10^{-6}\ (95\%\ CL)$$

Ces limites, publiées dans la référence [97], sont sensiblement plus strictes que les limites obtenues précédemment, mais sont plus grandes de plusieurs ordres de grandeurs que les rapports de branchement prévus par le Modèle Standard. Une première observation de ces désintégrations sera possible dans les expériences au LHC.

1.4. La recherche de la désintégration $B_s^0 \to \mu^+\mu^-\phi$

Dans le Modèle Standard, la désintégrations $B_s^0 \to \mu^+\mu^-\phi$ peut procéder au travers de processus de courte et de longue distance interférant. A l'ordre le plus élevé, les processus de courte distance sont des diagrammes électromagnétiques et faibles de type 'pingouins' et des diagrammes de W de type 'boîte'. Les processus de longue distance sont de type $b \to s(c\bar{c}) \to sl^+l^-$, avec des états intermédiaires résonnants (les résonances J/ψ et $\psi(2S)$) et non-résonnants. La prédiction théorique du rapport de branchement est $\mathcal{B}(B_s^0 \to \mu^+\mu^-\phi) = (1.21 \pm 0.32) \cdot 10^{-6}$.

Aucune recherche de cette désintégration n'a été publiée. Pour la présente recherche, un échantillon de données, collecté pendant les Run 1A et Run 1B et correspondant approximativement à une luminosité intégrée de 90 pb^{-1}, est utilisé.

Dans cette recherche, le rapport de branchement de la désintégration $B_s^0 \to \mu^+\mu^-\phi$ est mesuré par rapport à la désintégration $B_s^0 \to J/\psi\,\phi$. Ceci permet d'éliminer la luminosité et la section efficace de production du méson B_s^0 de l'expression du rapport des rapports de branchement, et les incertitudes sur ces facteurs n'affectent ainsi plus le résultat. Les ϕ et J/ψ sont reconstruits au travers des désintégrations $\phi \to K^+K^-$ et $J/\psi \to \mu^+\mu^-$, et les deux désintégrations sont ainsi observées dans le même état final. La similitude des deux désintégrations permet en outre d'éliminer certaines efficacités de reconstruction et de sélection. La désintégration $B_s^0 \to J/\psi\,\phi$, suivie de la désintégration $J/\psi \to \mu^+\mu^-$, a lieu au travers des processus de longue distance.

La sélection des candidats $B_s^0 \to \mu^+\mu^-\phi$ et $B_s^0 \to J/\psi\,\phi$ procède de manière similaire à la sélection effectuée lors de la recherche des désintégrations $B^0 \to \mu^+\mu^-$. Pour reconstruire un candidat B_s^0, deux muons, sélectionnés pas un des déclenchements à dimuons, et deux traces supplémentaires sont choisis. Etant donné que CDF ne possède pas de système d'identification de particules, toute trace supplémentaire observée doit être considérée comme un kaon. Ceci ajoute à la sélection un bruit de fond combinatoire non négligeable. Chacune des traces, muons et kaons doivent satisfaire à des coupures de qualité.

Un fit cinématique des moindres-carrés des quatre traces est effectué, dans lequel les traces sont contraintes de provenir d'un même vertex et où le vecteur impulsion du B $\vec{p}_T^B$ est contraint d'être parallèle au vecteur pointant du vertex primaire au vertex secondaire $\vec{l}_{xy}$. De plus, pour les candidats $B_s^0 \to J/\psi\,\phi$, la masse invariante des deux muons est contrainte d'être égale à la masse-moyenne du J/ψ. Toutes les quantités utilisées par la suite sont dérivées des paramètres issus du fit. Le niveau de confiance du χ^2 du fit est requis d'être supérieur à 1%. Les deux muons et au moins un des deux kaons doivent être reconstruits dans le SVX.

Suivant le déclenchement avec lequel l'événement a été sélectionné, l'impulsion transverse de chacun des deux muons doit être supérieure à 2 GeV/c, ou celle du muon de plus haute impulsion être supérieure à 2.8 GeV/c et celle du second supérieure à 1.8 GeV/c. L'impulsion transverse de chacun des kaons doit être supérieure à 400 MeV/c et l'impulsion transverse du ϕ doit être supérieure à 2 GeV/c. La masse invariante des deux kaons est requise d'être à moins de 10 MeV/c^2 de la masse-moyenne du ϕ. Ceci diminue sensiblement le bruit de fond combinatoire. L'impulsion transverse du B_s^0 candidat est requise d'être supérieure à 6 GeV/c. La fenêtre de recherche du signal est prise comme une région de 100 MeV/c^2 centrée sur la masse-moyenne du méson B_s^0, correspondant à la région de masse invariante entre 5.320 et 5.420 GeV/c^2 pour le B_s^0.

En outre, un fit cinématique des deux muons est effectué, et la masse invariante ainsi obtenue est utilisée pour distinguer les deux désintégrations. Pour la désintégration $B_s^0 \to J/\psi\,\phi$, la masse invariante est requise d'être à moins de 80 MeV/c^2 de la masse-moyenne du J/ψ. Pour la désintégration $B_s^0 \to \mu^+\mu^-\phi$, la masse invariante est requise d'être dans les régions $0-2.9$ GeV/c^2, $3.3-3.6$ GeV/c^2 ou $3.8-4.4$ GeV/c^2, de manière à éliminer les résonances J/ψ et $\psi(2S)$.

La longueur de désintégration propre $c\tau$ est requise d'être supérieure à 100 μm et la fraction d'impulsion I est requise d'être supérieure à 0.75. Ces coupures sont choisies de manière à minimiser la limite supérieure moyenne pouvant être obtenue en l'absence de candidats. Le bruit de fond attendu est estimé en extrapolant le nombre d'événements observés dans les régions latérales, de masse invariante entre 5.169 et 5.319 GeV/c^2 et entre 5.419 et 5.569 GeV/c^2. Dans cette sélection, la coupure sur l'angle d'ouverture est superflue car les vecteurs $\vec{p}_T^B$ et $\vec{l}_{xy}$ sont contraints d'être parallèles dans le fit.

Les distributions des masses invariantes des candidats $B_s^0 \to J/\psi\,\phi$ et $B_s^0 \to \mu^+\mu^-\phi$ satisfaisant à toutes les coupures sont montrées en figure 1.2. 11.0 ± 2.2 candidats $B_s^0 \to J/\psi\,\phi$ sont observés, résultant d'un fit de maximum de vraisemblance d'une Gaussienne et d'une droite sur la distribution. Deux candidats $B_s^0 \to \mu^+\mu^-\phi$ sont observés dans la région de signal. Observant trois événements dans les régions latérales, un événement de bruit de fond peut être attendu dans la région de signal.

Le rapport des rapports de branchement des deux désintégrations est donné par

$$\frac{\mathcal{B}(B_s^0 \to \mu^+\mu^-\phi)}{\mathcal{B}(B_s^0 \to J/\psi\,\phi, J/\psi \to \mu^+\mu^-)} = \frac{N_{obs}(B_s^0 \to \mu^+\mu^-\phi)}{N_{obs}(B_s^0 \to J/\psi\,\phi, J/\psi \to \mu^+\mu^-)} \cdot \frac{1}{\epsilon_{rel}} \tag{1.2}$$

Le rapport de branchement de la désintégration $B_s^0 \to J/\psi\,\phi$ mesuré à CDF est $\mathcal{B}(B_s^0 \to J/\psi\,\phi) = (9.3 \pm 3.3) \cdot 10^{-4}$. Avec le rapport de branchement moyen du J/ψ, le rapport de branchement du signal de référence est $\mathcal{B}(B_s^0 \to J/\psi\,\phi, J/\psi \to \mu^+\mu^-) = (5.6 \pm 2.0) \cdot 10^{-5}$.

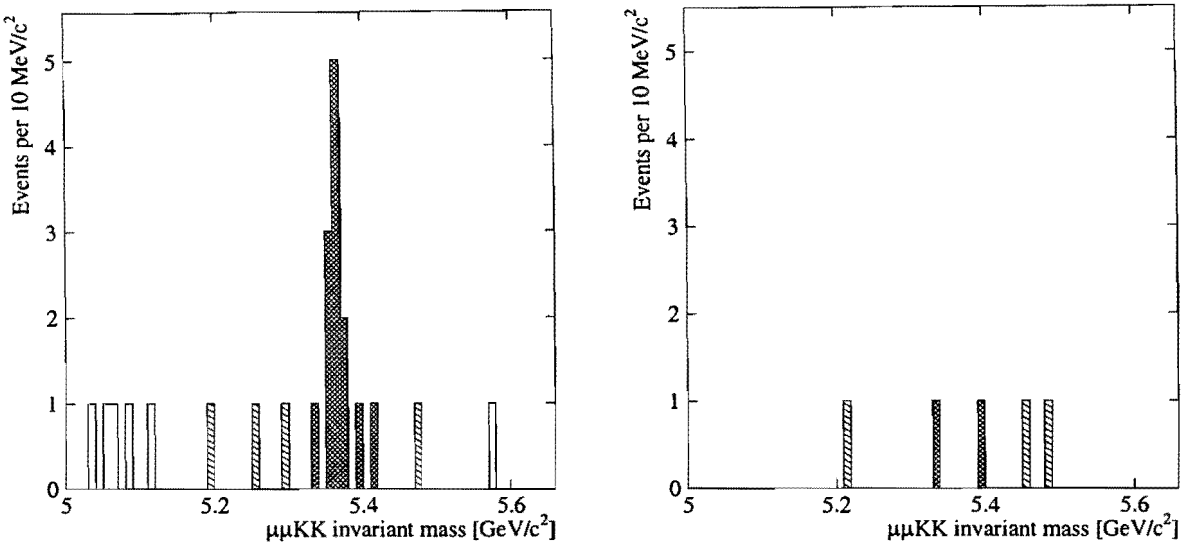

Figure 1.2: *Distribution de la masse invariante des candidats $B_s^0 \to J/\psi\,\phi$ (gauche) et $B_s^0 \to \mu^+\mu^-\phi$ (droite) après toutes les coupures de sélection. La zone quadrillée représente la région de signal et la zone hachurée la région utilisée dans l'estimation du bruit de fond.*

Etant donné que les deux désintégrations sont reconstruites via la même désintégration du ϕ, le rapport de branchement de cette désintégration ne doit bien entendu pas être inclus.

Le facteur ϵ_{rel} contient trois contributions. La première est le rapport de l'acceptance et des efficacités des désintégrations qui ne s'annulent pas. Ce rapport est obtenu par une simulation Monte Carlo similaire à celle effectuée précédemment, où la désintégration $B_s^0 \to \mu^+\mu^-\phi$ est simulée selon l'élément de matrice de désintégration. Comme une partie seulement de l'intervalle de masse invariante de la paire de muons est utilisée dans cette recherche, un facteur de correction doit être inclu pour extrapoler le résultat trouvé à l'intervalle de masse invariante entier.

Comme la valeur recherchée est le rapport de branchement dû aux processus de courte distance uniquement, un facteur de correction est inclus pour tenir compte du fait que même dans la zone de recherche, les processus de longue distance contribuent à la désintégration. Ce facteur de correction est le rapport des largeurs partielles de désintégration avec et sans les processus de longue distance.

N'observant aucune indication de la présence des désintégrations recherchées dans l'échantillon de données, une limite supérieure est placée sur le rapport de branchement. Au vu du faible nombre de candidats et d'événements de bruit de fond observé, aucune soustraction du bruit de fond n'est effectuée et les candidats sont considérés comme des événements de signal.

La limite supérieure de Poisson du nombre de candidats à un niveau de confiance de 90% (respectivement 95%) est de 5.32 (respectivement 6.30). Avec une incertitude systématique totale de 41.4%, la limite supérieure du nombre de candidats à un niveau de confiance de

90% (respectivement 95%) est de 7.55 (respectivement 10.46). Les principales incertitudes systématiques sont les incertitudes sur le rapport de branchement et le nombre de candidats observés de la désintégration $B_s^0 \to J/\psi\,\phi$. La dépendance des facteurs de correction sur le modèle de désintégration est estimée en utilisant des facteurs de forme calculés par une autre méthode.

Les limites supérieures du rapport de branchement de la désintégration recherchée à des niveaux de confiance de 90 et 95% sont ainsi

$$\mathcal{B}(B_s^0 \to \mu^+\mu^-\phi) < 4.2 \cdot 10^{-5}\ (90\%CL)$$

$$\mathcal{B}(B_s^0 \to \mu^+\mu^-\phi) < 5.8 \cdot 10^{-5}\ (95\%CL)$$

Ce résultat constitue la première limite placée sur le rapport de branchement de la désintégration $B_s^0 \to \mu^+\mu^-\phi$. Une publication est en préparation. Si cette désintégration n'est pas observée dans le prochain run de CDF, elle le sera sans aucun doute dans les expériences au LHC.

Part I

Theoretical Motivation

Chapter 2

The Standard Model

The aim of particle physics is to understand the fundamental forces governing Nature and discover the basic constituents of matter. In short, it tries to answer one question: what is the world made of and how does it work? In attempting to answer this question, it studies three of the four fundamental forces of Nature: the electromagnetic force, the weak force and the strong force. The effects of the fourth force, gravity, are negligible at the atomic and sub-atomic level at the energy scale achievable with current and near-term future accelerators.

The best description to date is contained in a model now called the *Standard Model*[1]. It is in fact composed of two theories: the *Glashow-Weinberg-Salam (GSW)* model of electroweak interactions, describing the electromagnetic and weak forces, and *Quantum Chromodynamics (QCD)*, describing the strong force. Gravitation is still well separated from the other forces, as a quantum field theory has not yet been formulated to describe it. It is best described by Einstein's General Relativity theory. The present aim is to truly unify strong interactions with the electroweak interactions.

The GSW model unifies two of the four forces, the electromagnetic force, described by the quantum electrodynamic (QED) theory, and the weak force. It was developed by S.L. Glashow [8], S. Weinberg [9] and A. Salam [10] in the 1960's. It is a spontaneously broken non-Abelian gauge theory with local gauge invariance $SU(2)_L \times U(1)_Y$. It is the most precise theory known to date describing these interactions, and its predictions have been extensively verified. It has successfully predicted the existence of neutral currents and of the W and Z^0 bosons, all of which have been experimentally observed. Until now, no experimental evidence has shown any hint that this model may not be complete, although one crucial component, the Higgs boson, has still eluded detection.

QCD is based on an unbroken non-Abelian $SU(3)$ colour symmetry gauge theory. With the fundamental representation of a $SU(3)$ group a triplet, three charges, called *colour*, and taken as *red*, *green* and *blue*, can be defined.

The fundamental particles are classified in two categories. In the first particles, called *bosons* have integer spin and obey the Bose-Einstein statistics. *Gauge bosons* mediate the

[1]Many textbooks present the Standard Model in detail. References [2, 3, 4, 5, 6, 7] have been used in this section.

interactions between the fundamental particles. These are the gauge fields of the above-mentioned gauge groups. The QCD $SU(3)_C$ colour gauge group requires eight massless spin one gauge bosons, called *gluons* $(g_1, \ldots, g_8)$. These mediate the strong force between quarks, and hold the quarks together in baryons. The $SU(2)_L$ weak isospin group will have three gauge bosons (W^1_μ, W^2_μ and W^3_μ) and the $U(1)_Y$ weak hypercharge group one gauge gauge boson B_μ. After spontaneous symmetry breaking, these latter four gauge bosons will give rise to the three massive spin one gauge bosons mediating the weak interaction ($W^\pm$ and Z^0) and the massless spin one boson mediating the electromagnetic interaction, the *photon* (γ). A further spin 0 boson is found in the Standard Model: the *Higgs* boson, which arises in the spontaneous symmetry breaking of the $SU(2)_L \times U(1)_Y$ group. This boson has not yet been discovered. Although not included in this framework, gravitation is thought to be mediated by a massless spin two boson, called the *graviton.*

In the second category, particles have half-integer spin and obey the Fermi-Dirac statistic, and hence are called *fermions*[2]. These are the basic constituents of matter. Each fermion has an associated anti-particle with equal mass and lifetime but opposite charge and quantum numbers. Fermions are classified in a sequence of generations of rising mass, in all points identical with regard to their $SU(3)_C$, $SU(2)_L$ and $U(1)_Y$ quantum numbers and interactions. The Standard Model imposes no constraint on the number of generations and does not permit to predict this number. Until now, three generations have been observed[3], shown in Table 2.1. Two types of fermions exist, *leptons* and *quarks*, characterised by the interactions to which they are sensitive.

Leptons have integer charge, and subject to electromagnetic and weak interactions, but not to strong interactions. Each generation of lepton is composed of a negatively charged and a neutral particle, called *neutrino*, thought to be massless in the Standard Model[4]. Not subject to the strong interaction, leptons do not bear colour and are $SU(3)_C$ colour-singlets.

Quarks have fractional electric charge, and, in addition to electromagnetic and weak interactions, are also subject to strong interactions. As such, they hold a further quantum number, colour, and are $SU(3)_C$ colour-triplets. The coloured quarks cannot exist free, but confined in *hadrons*, a colour-singlet combination of quarks and anti-quarks. These are either *mesons*, formed by a quark–anti-quark pair ($q\bar{q}$), or *baryons*, formed of three quarks of complementary colour (qqq). Nevertheless, at very small scale, quarks may be considered as quasi-free particles inside hadrons, a property known as *asymptotic freedom.*

As all elementary fermions are subject to weak and, for charged fermions, electromagnetic interactions, their left- and right-handed components will be arranged in left-handed *weak isospin* doublets and right-handed weak isospin singlets. This weak isospin I is defined

[2]In the following discussion, the term *fermion* will designate the elementary spin 1/2 particles, although it is clear that *all* half-integer spin states, elementary or composed, are fermions.

[3]Measurements of the properties of the Z^0 boson made at the LEP experiments indicate that only three types of light neutrinos (with a mass below $m(Z^0)/2 \simeq 45.6$ GeV/c^2) exist [1]. As it is considered unlikely that heavier neutrinos exist, since these would affect precisely measured quantities by radiative corrections and contradict further limits on the masses of 'heavy' neutrinos derived from astrophysical observations, this suggests that only three generations of fermions exist.

[4]Although it is usual to consider the neutrino as massless, there is no theoretical requirement for this. Even in the Standard Model, a 'massive' neutrino could be accommodated with minimal modifications.

Lepton	Mass [MeV/c^2]	Charge
e	0.511	-1
ν_e	$< 15 \cdot 10^{-6}$([6])	0
μ	105.6	-1
ν_μ	< 0.17 (90%CL)	0
τ	1777.0	-1
ν_τ[7]	< 18.2 (90%CL)	0

Quark	Mass[8]	Charge
up - u	$1.5 - 5$ MeV/c^2	+2/3
down - d	$3 - 9$ MeV/c^2	-1/3
charm - c	$1.1 - 1.4$ GeV/c^2	+2/3
strange - s	$60 - 170$ MeV/c^2	-1/3
top - t	$4.1 - 4.4$ GeV/c^2	+2/3
bottom - b	173.8 ± 5.2 GeV/c^2	-1/3

Table 2.1: *Fermions in the Standard Model [1].*

in analogy with the nucleon isospin. Being massless, the neutrino will of course not have a right-handed component. Each generation of leptons and quarks will be assigned to form a doublet. The first generation can be represented

$$\begin{pmatrix} e \\ \nu \end{pmatrix}_L , \; e_R \quad \text{and} \quad \begin{pmatrix} u \\ d \end{pmatrix}_L , \; u_R , \; d_R \tag{2.1}$$

This classification insures that the parity-violating $V - A$ structure of the weak interactions will be obtained. The doublet will be the fundamental representation of the $SU(2)_L$ symmetry group[5] .

Furthermore, a *weak hypercharge* group $U(1)_Y$ is defined, such that the generators of these groups satisfy the Gell-Mann-Nishijima relation:

$$Q = I_3 + \frac{Y}{2} , \tag{2.2}$$

where Q is the generator of the electromagnetic $U(1)_{EM}$ symmetry group.

2.1. The GSW model of electroweak interactions

The GSW gauge theory is obtained by imposing local gauge invariance of the product of the weak isospin symmetry $SU(2)_L$ and of the weak hypercharge symmetry $U(1)_Y$, denoted

[5]The L subscripts indicates that only the left-handed doublets are transform in this group, and that the right-handed singlets are invariant.

[6]The square of the electron neutrino mass $m^2_{\nu_e}$, measured in tritium beta decays experiments, has been found to be significantly negative [1]. With these results, the Particle Data Group was not able to set a meaningful upper limit on m_{ν_e}, but estimates that a mass larger than 15 eV would cause observable effects in the experiments.

[7]Until very recently, the existence of the ν_τ was not directly established, but inferred from all observations of τ decays and ν reactions. However, on July 21 2000, an experiment at Fermilab announced the first evidence on the direct observation of the ν_τ.

[8]Quarks, unlike leptons, are not observed free but are confined inside hadrons. Their masses can therefore not be measured directly, but inferred from the properties of the hadron. As a result, the masses will be dependent on the model used in the measurement. All masses quoted above are given in the $\overline{\text{MS}}$ QCD renormalisation scheme, except for the *top* quark, for which the pole mass is quoted, which definition is "the same as for the leptons. Reference [1] gives good summary of the different mass definitions used. It can be noted that the mass of the b quark quoted later in this dissertation is the mass defined in the framework of the Heavy Quark Effective Theory (HQET).

$SU(2)_L \times U(1)_Y$. The $SU(2)_L$ weak isospin gauge group will have three gauge bosons, called W^1_μ, W^2_μ and, W^3_μ, with a coupling constant g. The $U(1)_Y$ weak hypercharge gauge group will have one gauge boson B_μ, with a coupling constant $g'/2$.

The Lagrangian obtained by requiring this gauge invariance does not describe the electroweak interactions correctly. Indeed, all the gauge bosons and fermions in the theory are massless, which is obviously not the case in reality. Simply adding a non-invariant mass term for the gauge bosons to the Lagrangian, which is said to be an *explicit* breaking of the symmetry, would make the theory non-renormalizable. Furthermore, the global $SU(2)$ gauge invariance forbids the addition of mass terms for the fermions, as $SU(2)_L$ only transforms the left-handed doublets and not the right-handed singlets.

A mechanism has therefore to be implemented to generate the mass terms required while conserving a single quantity (the electric charge), which would be associated with the massless photon.

The solution is to start with a Lagrangian without mass terms, with a built-in symmetry. This Lagrangian can be the one obtained above with the $SU(2)_L \times U(1)_Y$ gauge groups. Then, the Higgs mechanism would break the symmetry dynamically, thereby generating mass terms for the weak bosons.

In the Higgs mechanism, a new complex doublet of scalar fields ϕ,

$$\phi \equiv \begin{pmatrix} \phi^+ \\ \phi^0 \end{pmatrix}, \tag{2.3}$$

which transforms as a $SU(2)_L$ doublet is introduced. This doublet couples to both the gauge bosons and the fermions, and the appropriate interaction terms are added to the Lagrangian. Furthermore, a potential of the form

$$V(\phi^\dagger\phi) = \mu^2(\phi^\dagger\phi) + |\lambda|\,(\phi^\dagger\phi)^2 \tag{2.4}$$

is also added.

By choosing $\mu^2 > 0$, the potential has a unique minimum at $\phi = 0$ and the exact symmetry of the Lagrangian is preserved. By choosing $\mu^2 < 0$, the potential will have new non-zero minima. As a consequence of the symmetry of the potential, the minima will be continuous and degenerate in energy. The physical vacuum (the state of least energy, called the *vacuum expectation value*) will be displaced with respect to the original minimum. This can be chosen arbitrarily from the non-zero minima,

$$\langle\phi\rangle = \begin{pmatrix} 0 \\ v/\sqrt{2} \end{pmatrix}, \tag{2.5}$$

where $v = \sqrt{-\mu^2/|\lambda|}$. By rewriting the Lagrangian in terms of the displacement of the physical vacuum, both the $SU(2)_L$ and $U(1)_Y$ symmetries are broken. The $U(1)_{EM}$ symmetry generated by the electric charge operator is nevertheless conserved.

Goldstone's theorem states that one massless spin 0 boson, called a *Goldstone boson*, is created for each broken generator (i.e. not leaving the vacuum invariant) of the original symmetry group. In Higgs's mechanism, none of the four generators of the $SU(2)_L \times U(1)_Y$

groups leave the vacuum invariant, but the generator of the $U(1)_{EM}$ group does. Three massless Goldstone bosons and a massive spin 0 boson, called a *Higgs boson*, are therefore generated.

By defining the orthogonal combinations

$$W_\mu^+ = \frac{1}{\sqrt{2}}(W_\mu^1 - iW_\mu^2) \tag{2.6}$$

$$W_\mu^- = \frac{1}{\sqrt{2}}(W_\mu^1 + iW_\mu^2) \tag{2.7}$$

$$Z_\mu = W_\mu^3 \cos\vartheta_W - B_\mu \sin\vartheta_W \tag{2.8}$$

$$A_\mu = W_\mu^3 \sin\vartheta_W + B_\mu \cos\vartheta_W \tag{2.9}$$

the W_μ^+ and W_μ^- fields can be identified with the charged W bosons, the Z_μ field with the neutral Z^0 and the A_μ field with the photon. The weak mixing angle ϑ_W, also called the Weinberg angle, parameterises the mixing of the neutral gauge bosons and is defined as

$$\tan\vartheta_W = \frac{g'}{g} \tag{2.10}$$

The rewritten Lagrangian will now feature a mass term for the W and Z^0 bosons and the newly created Higgs boson, with the photon remaining massless. By an appropriate gauge transformation, the Goldstone bosons will be 'absorbed' by the massive gauge fields, giving rise to the longitudinal components of the $W^\pm$ and Z^0[9]. The masses of the bosons are given by

$$M_W = \frac{gv}{2} \tag{2.11}$$

$$M_Z = \frac{v}{2}\sqrt{g^2 + g'^2} \tag{2.12}$$

$$M_H = -\sqrt{2}\,\mu^2 = \frac{4\lambda}{g^2}M_W^2\,, \tag{2.13}$$

The interacting terms in the Lagrangian will indeed give the electromagnetic and weak interactions, which coupling constants are given as

$$e = \frac{gg'}{\sqrt{g^2 + g'^2}} \tag{2.14}$$

$$G_F = \frac{v}{\sqrt{2}}\,, \tag{2.15}$$

In addition to the boson masses, this mechanism is also able to generate masses for the fermions[10]. Indeed the fermion scalar interaction term added to the Lagrangian transforms

[9] A massless gauge field has only two components corresponding to two transverse polarizations, whereas a massive gauge field has one additional component, corresponding to the longitudinal polarization.

[10] The same mechanism is able to generate the masses of both leptons and quarks, although for quarks, a scalar doublet with opposite weak hypercharge has to be used. Using $\bar{\phi} \equiv \begin{pmatrix} \bar{\phi}^0 \\ -\bar{\phi}^+ \end{pmatrix}$, which transforms under $SU(2)_L$ in the same way as ϕ, the same Higgs field is found after spontaneous symmetry breaking.

after symmetry breaking into a fermionic mass term and an interaction term between the Higgs boson and the fermions.

All features of the electroweak interactions have been described, both in terms of interactions and elementary particles. In particular, the neutral weak currents, mediated by the Z^0, were predicted by this model several years before their discovery. This theory was shown to be renormalizable by 't Hooft in 1974 [11].

2.2. The quark model

> Three *quarks* for Muster Mark
> Sure he hasn't got much of a bark
> And sure any he has it's all beside the mark.
> But O, Wreneagle Almighty, wouldn't un be a sky of a lark
> *James Joyce*, Finnegan's Wake

With the advent of particle accelerators of much higher energy in the 50s, a host of new particles (now called hadrons) were discovered. In addition to the pion, discovered in 1947 in cosmic rays, a new class of hadrons were discovered, which did not fit in the scheme of particle classification. These particles were termed *strange*, as they would be produced by strong interactions in fixed target experiments, but, compared to the time-scale of strong interactions, would have a very long lifetime, indicating that they decay through the weak interaction. Gell-Mann and Nishijima assigned these particles a new additive quantum number, called *strangeness*. This quantum number would be conserved in strong and electromagnetic interactions, explaining why they are always produced in pairs of opposite-strangeness, and could not decay through strong interaction, while weak interaction would not conserve it, thus allowing its weak decay.

While the proton and the neutron, then regarded as 'fundamental' particles, could be classified in the $SU(2)$ group of isospin, it was much more difficult to classify all the new states in one group. Eventually, a $SU(3)$ group was proposed in 1961, which would group several strange and non-strange states into one representation.

The regularity of hadron states and the patterns in the classification were interpreted in terms of a higher symmetry. Various classification schemes have been proposed, until Gell-Mann postulated [20] that hadrons are not elementary particles, but that they have a substructure.

The new class of elementary particles of fractional charge would be called *quarks* and come in three flavours, *up*, *down* and *strange*. All observed hadrons could be built by either the combination of a quark–anti-quark pair (for mesons) or the combination of three quarks (for baryons). These hadrons would be described by the proposed $SU(3)$ group, now called $SU(3)$ *flavour* ($SU(3)_F$), where the three quarks correspond to the fundamental representation of the group.

It is now obvious that with six quarks, $SU(3)_F$ is not an exact symmetry, although it works reasonably well when restricted to the lightest quarks. It has been replaced by another $SU(3)$ symmetry, $SU(3)$-*colour*, which is an exact symmetry of nature. Even in

the absence of flavour symmetry, this quark model correctly predicts the quantum numbers of hadrons, and that one hadron (the Ω^-) could even be predicted using $SU(3)_F$.

2.3. The Cabibbo angle

The low-energy phenomenological $V - A$ theory proposed by Feynman and Gell-Mann in 1958 [12], before the advent of the Standard Model, was designed to incorporate the property that the lepton number is conserved in weak interactions. Hence, by applying the same theory to the three quarks discovered at the time (the u, d and s), strangeness changing processes should be forbidden. But, with $\Delta S = 1$ strangeness changing decays (like the decay $K^+ \to \mu^- \nu_\mu$) unambiguously observed, this obviously cannot be the right description. A second problem is that the Fermi constant G_F measured in the purely leptonic decays of the muon $\mu^- \to e^- \nu_\mu \bar{\nu}_e$ and in nuclear beta and neutron decays differ.

Cabibbo's idea [13] was that the down-type quark d and s involved in weak interactions were not the physical quark, but rotated states d' and s':

$$\begin{array}{rcrcl} d' & = & d\cos\vartheta_C & + s\sin\vartheta_C \\ s' & = & -d\sin\vartheta_C & + s\cos\vartheta_C \end{array} , \tag{2.16}$$

where ϑ_C is the quark mixing angle, known as the Cabibbo angle. This successfully permits to describe strangeness-changing charged currents with $\Delta S = 1$ and the fact that these decays are suppressed relative to those with no change of strangeness ($\Delta S = 0$). ϑ_C can be determined by comparing the rates of $\Delta S = 1$ and $\Delta S = 0$ decays, yielding $\vartheta_C \sim 13°$. The d' and s' quarks are thus orthogonal combinations of the physical quarks:

$$\begin{pmatrix} d' \\ s' \end{pmatrix} = U \begin{pmatrix} d \\ s \end{pmatrix} = \begin{pmatrix} \cos\vartheta_C & \sin\vartheta_C \\ -\sin\vartheta_C & \cos\vartheta_C \end{pmatrix} \begin{pmatrix} d \\ s \end{pmatrix} . \tag{2.17}$$

This also solves the problem of the Fermi constant. As the lepton doublets are not rotated, the constant measured in purely leptonic decays is the true Fermi constant, whereas the constant measured in the nuclear β-decay is $G_F \cos\vartheta_C$. With the measured value of ϑ_C, both constants agree within the measurements uncertainties.

2.4. The GIM mechanism

With the GSW model describing the electroweak interactions, a further problem arose. In addition to the observed charged currents, the theory predicts weak neutral currents, mediated by the Z^0. With only three observed quarks, the strange quark could not be in a doublet. Hence, the neutral currents would also be capable of changing strangeness, which was not experimentally observed. Indeed, if the charged current decay $K^+ \to \mu^+ \nu_\mu$ has a branching fraction of $(63.5 \pm 0.18)\%$, the neutral current decay $K_L \to \mu^+ \mu^-$ has a branching fraction of $(7.2 \pm 0.5) \cdot 10^{-9}$ [1].

A mechanism to suppress the strangeness-changing neutral currents would be suggested in 1970 by Glashow, Iliopoulos and Maiani [14], and has subsequently been called the *GIM*

mechanism. They proposed that the s quark would be in a second doublet, along with a new undiscovered quark of charge +2/3, called the *charm* quark. The weak s' quark would be the same quark as defined in Equation 2.16, and the doublet would be

$$\begin{pmatrix} c \\ s' \end{pmatrix} = \begin{pmatrix} c \\ -d \sin\vartheta_C + s \cos\vartheta_C \end{pmatrix} . \tag{2.18}$$

With this doublet, the strangeness-changing terms in the neutral current cancel, and the strangeness-changing neutral current decays as the one given above would only proceed at second order through box diagrams (these will be defined in more details in Section 4.2.1). In addition, the new quark would restore the symmetry between leptons and quarks, with four flavours of each.

From the measured branching fraction of the decay $K_L \rightarrow \mu^+\mu^-$, Gaillard and Lee predicted in 1974 that the mass of the charm quark should be between 1 and 3 GeV/c^2. The subsequent discovery of this quark in the predicted range provided a further success for the theory.

2.5. The discovery of the J/ψ and the *charm* quark

In 1974, two independent groups simultaneously discovered a new resonance, the J/ψ. The first discovered a resonance in the e^+e^- mass spectrum in 28 GeV proton fixed target collisions at Brookhaven [21]. The second observed the resonance in e^+e^- collisions at SLAC, in e^+e^-, $\mu^+\mu^-$and all-hadron final states [22].

The J/ψ's quantum numbers are $J^{PC} = 1^{--}$, and other resonances with different spin and radial excitation were subsequently observed. It was interpreted to be a bound quark–anti-quark state of a new flavour of quark, the *charm* quark, which was postulated by Glashow, Iliopoulos and Maiani to explain the non-existence of strangeness-changing neutral weak current.

With a mass of 3.097 GeV/c^2, the J/ψ is below the threshold of charm particle production. The only hadronic decay modes would be to lower mass hadrons without charm, via diagrams suppressed by the OZI rule[23]. This suppression causes the resonance to be very narrow, around 87 keV.

2.6. The CKM matrix

Following the demonstration that both C and P were violated in weak interactions, it was thought that the combined operation of C and P (CP) was exactly conserved. However, in 1964, Christenson, Cronin, Fitch and Turlay established that CP was violated in the K^0 system [16].

To introduce into the Standard Model a mechanism to generate CP violation without introducing a new interaction, Kobayashi and Maskawa proposed [17] in 1973 to introduce two new quarks. This had the purpose of extending the existing mixing matrix (Equation 2.17) from two to three generations, even though there was evidence at that time for the existence of only three quarks.

As the quark mixing matrix has to be unitary, the complex $n \times n$ matrix is initially defined by n^2 parameters. After redefining the quark phases, $(n-1)^2$ independent parameters are left, $n(n-1)/2$ angles and $(n-1)(n-2)/2$ phases.

With two quark generations, the matrix is parameterized by a single angle, the Cabibbo angle. With three generations, the matrix, now called the *Cabibbo-Kobayashi-Maskawa* (*CKM*) matrix, is parameterized by three angles and a phase. This matrix is not limited to three generations and could be extended should more generations be discovered.

While 36 different parameterizations of the CKM matrix exist [18], the Particle Data Group recommends a standard parameterization [1], where the matrix is the product of three complex rotation matrices, of which only one of them has a non-null phase:

$$V_{CKM} = \begin{pmatrix} V_{ud} & V_{us} & V_{ub} \\ V_{cd} & V_{cs} & V_{cb} \\ V_{td} & V_{ts} & V_{tb} \end{pmatrix} = \begin{pmatrix} c_{12}c_{13} & s_{12}c_{13} & s_{13}e^{-i\delta} \\ -s_{12}c_{23} - c_{12}s_{23}s_{13}e^{i\delta} & c_{12}c_{23} - s_{12}s_{23}s_{13}e^{i\delta} & s_{23}c_{13} \\ s_{12}c_{23} - c_{12}c_{23}s_{13}e^{i\delta} & -c_{12}s_{23} - s_{12}c_{23}s_{13}e^{i\delta} & c_{23}c_{13} \end{pmatrix}, \tag{2.19}$$

where $c_{ij} = \cos\vartheta_{ij}$ and $s_{ij} = \sin\vartheta_{ij}$. This has the advantage that each of these rotation angles $(\vartheta_{12}, \vartheta_{23}, \vartheta_{13})$ relates to the mixing of two specific generations. If one of these angles is null, no mixing between the generations occurs. It is the phase (δ_{13}), when non-zero, that would break CP invariance for the weak interactions.

The diagonal terms of the matrix correspond to transitions within a given generation and the off-diagonal terms correspond to transitions between different generations. Observing that the diagonal terms are close to one and that the non-diagonal terms decrease with increasing distance from the diagonal, Wolfenstein proposed a new parameterization, which is in fact an expansion in term of $\sin\vartheta_C$. At the order $\mathcal{O}(\lambda^3)$, the matrix can be written as

$$V_{CKM} = \begin{pmatrix} 1 - \lambda^2/2 & \lambda & A\lambda^3(\rho - i\eta) \\ -\lambda & 1 - \lambda^2/2 & A\lambda^2 \\ A\lambda^3(1 - \rho - i\eta) & -A\lambda^2 & 1 \end{pmatrix}, \tag{2.20}$$

where $\lambda = \sin\vartheta_C$, with A, ρ and η real numbers close to unity.

The unitarity of the matrix ($VV^\dagger = V^\dagger V = 1$) yields twelve relations between the different elements. Each of these relations can be represented as a triangle in the complex plane. Most of the relations yield flat triangles, except for the relation involving the first and the third columns, where the terms are of the same order:

$$V_{ud}V_{ub}^* + V_{cd}V_{cb}^* + V_{td}V_{tb}^* = 0\,. \tag{2.21}$$

As $V_{cd}V_{cb}^*$ is nearly real, the sides are usually rescaled by a factor $(V_{cd}V_{cb}^*)^{-1}$, and a triangle, called the *unitarity triangle* with a unity base is obtained, as shown in Figure 2.1. In the Wolfenstein parameterization, the coordinate of the apex is simply (ρ, η).

A precise measurement of the angles and sides of this triangle is required to verify the unitarity of the CKM matrix. Inconsistencies between the measurements of the triangle would reveal the inadequacy of the Standard Model in its present form, as different extensions predict different properties of the mixing matrix. Although the CKM matrix allows

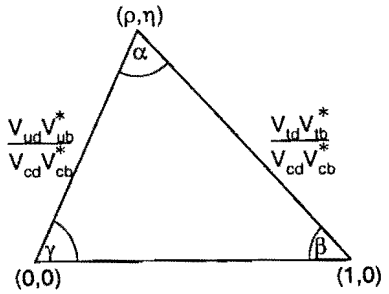

Figure 2.1: *The unitarity triangle.*

within the Standard Model a mechanism to generate CP violation, the phase δ_{13} could still be null, and the Standard Model would not have any CP violating term[11].

The possibility of having mixed quark states for the electroweak interactions is present in the GSW model, although it is not specifically predicted. As seen previously, the masses of the fermions are generated at symmetry breaking through the coupling of the fermion to the scalar doublet. After symmetry breaking, this interaction term can be rewritten as a mass term and an interaction term between the Higgs boson and the fermions. The so-called *mass matrices*, which contain the coupling constants, featured in front of both the mass and interaction terms, are not necessarily diagonal. Two mass matrices are found for each of the quark and lepton terms, for each of the $I_3 = +1/2$ and $I_3 = -1/2$ components of the doublets.

If they were diagonal, no mixing would occur for the weak interactions. As it is known that the weak quark eigenstates are not the physical eigenstates, the mass matrices are non-diagonal[12]. To obtain the physical quarks, the mass matrices have to be diagonalized, which is done using a pair of unitary matrices, one for each mass matrix, and the diagonalized matrices feature the masses of the quarks.

By writing the Lagrangian in terms of the physical fields obtained with the diagonalizing matrices, the weak neutral and electromagnetic current interaction terms will not be modified, and therefore still be diagonal in flavour. The charged current terms will now feature the physical fields, connected by a new non-diagonal matrix, and will therefore allow flavour changing currents. This new matrix is the CKM matrix.

[11]It is argued that even with a non-null phase, the Standard Model CP violation may not be sufficient to account for the observed baryon asymmetry (the predominance of baryons over anti-baryons) in the universe [19].

[12]The discrepancy between the expected and observed flux of solar and atmospheric neutrinos observed by several experiments could be due to neutrino oscillations. In this hypothesis, these oscillations would be due to the fact that neutrinos indeed would have a mass, which would cause leptons to undergo mixing in the same way as quarks.

Particle	Mass [MeV/c^2]	Width
$\Upsilon(1S)$	9460.37 $\pm$ 0.21	52.5 $\pm$ 1.8 keV
$\Upsilon(2S)$	10023.30 $\pm$ 0.31	44 $\pm$ 7 keV
$\Upsilon(3S)$	10355.3 $\pm$ 0.5	26.3 $\pm$ 3.5 keV
$\Upsilon(4S)$ ($\Upsilon(10580)$)	10580.0 $\pm$ 3.5	10 $\pm$ 4 MeV
$\Upsilon(10860)$	10865 $\pm$ 8	110 $\pm$ 13 MeV
$\Upsilon(11020)$	11019 $\pm$ 8	79 $\pm$ 16 MeV

Table 2.2: Υ *resonances with their mass and width [1].*

2.7. The discovery of the *b* quark

Like the charm quark, the bottom quark was predicted on theoretical grounds before it was actually observed. A third generation of quarks was predicted by Kobayashi and Maskawa, as a three-generation mixing matrix would include a CP violating phase. Furthermore, with the discovery of the τ lepton in 1975 [24], a third quark generation was necessary to satisfy lepton-quark universality.

In 1977, the Columbia-Fermilab-Stoney Brook collaboration (CFS) discovered at Fermilab a new resonance in 400 GeV/c proton-nucleus collision in the process $p + N \rightarrow \mu^+\mu^- + X$ [25]. This narrow resonance, at a mass of 9.46 GeV/c^2, was called Υ. With more data, further resonances were found at Fermilab, and in e^+e^- collisions at DORIS and CESR. They are summarised in Table 2.2. The Υ resonances are interpreted to be a new $q\bar{q}$ bound states, with $J^{PC} = 1^{--}$. Both the leptonic width, which is proportional to Q_b^2, and the ratio $R = \frac{\sigma(e^+e^- \rightarrow hadrons)}{\sigma(e^+e^- \rightarrow \mu^+\mu^-)}$, which is increased by $3Q_q^2$ above each new $q\bar{q}$ threshold, are consistent with a quark of charge $-1/3$. It is hence the *bottom* (also called *beauty*) and not the *top* quark, the $+2/3$-charge partner of the b in the predicted new doublet.

The $\Upsilon(4S)$ and the higher-mass resonances are much broader than the lower-mass resonances, as they are above the $B\bar{B}$ threshold and their decays are not OZI suppressed. $\Upsilon(4S)$ decays to $B_d^0\bar{B}_d^0$ and B^+B^- pairs. All dedicated e^+e^- B-factories operate at the $\Upsilon(4S)$ energy. In this case, the b production cross-section is acceptable and the track multiplicity is low (c.f. Section 3.1.1).

The Υ spectroscopy is similar to the J/ψ, and was anticipated even before the discovery of the Υ [26]. It can be reproduced reasonably successfully by applying a non-relativistic potential model to the $b\bar{b}$ bound system, in analogy to the positronium in the e^+e^- system [7].

2.8. After *beauty, truth*

> Beauty is truth, truth beauty,–that is all
> Ye know on earth, and all ye need to know.
> *John Keats*, Ode on a Grecian Urn.

After the discovery of the b quark, the focus became the search for its partner, the *top*

quark (sometimes called *truth*). As the weak isospin of the b quark has been measured to be $I_3 = -1/2$, and not zero, it is indeed part of a weak isospin doublet and not alone in a singlet. Only a doublet structure permits the cancelation of flavour-changing neutral currents (c.f. Section 2.4 and 2.6). Furthermore, the renormalization of the Standard Model requires the same number of leptons and quarks in order to cancel triangle anomalies (triangular fermion loops coupled to two photons).

It has been acknowledged early that the *top* quark should be much heavier than the other quarks, as is indicated by the rapid oscillations between the B and the $\bar{B}$ and the radiative corrections to electroweak observables. A fit to the Standard Model parameters measured in e^+e^- collisions, mainly at the LEP experiments, predict that it should be at a mass of $170 \pm 7 \pm 14$ GeV/c^2 [1, 30].

After years of unsuccessful search, it was finally found at the Fermilab Tevatron, in $p\bar{p}$ collisions at $\sqrt{s} = 1.8$ TeV, at the CDF and D0 experiments [27, 28, 29]. Its mass of 174.3 ± 5.1 GeV/c^2 is the most precisely measured quark mass.

2.9. The free parameters

The GSW model of electroweak interactions includes a relatively large number of free parameters. Due to the relations found between several of the parameters, the choice as to which are free parameters is somewhat arbitrary:

- The two gauge coupling constants, g, g', or alternatively e and ϑ_W (Equations 2.10 and 2.14).
- The Fermi constant G_F, or alternatively v (Equation 2.15).
- The mass of the Higgs boson M_H.
- The parameters of the mixing matrix (four in the case of three generations: three angles and the CP-violating phase).
- The masses of the fermions (six quark masses and three lepton masses, with the neutrinos being massless, in case of three generations).

Therefore, with three generations, a total of 17 free parameters appear in the model, to which the QCD coupling constant g_s should be added. If neutrinos are massive, a further seven parameters would be introduced, the three masses and the four parameters of the lepton mixing matrix. In addition, no prediction is made on the number of fermion generations. More generations could in principle exist, augmenting the number of free parameters!

Chapter 3

B production

3.1. b quark production

Most experiments with a B physics programme are collision experiments, with either e^+e^- collisions or hadron collisions, although fixed target experiments are also persuing researches in this field. With a centre of mass energy in the order of $10 - 40$ GeV, the latter have a low b production cross section compared to collider experiments, and now study mainly the property of the c quark. A detailed description of b quark production and fragmentation can be found in References [31, 32].

3.1.1. b quark production at e^+e^- colliders

In e^+e^- collisions, $b\bar{b}$ pairs are produced through the exchange of either a γ or a Z^0 (Figure 3.1). For centre of mass energies below 30 GeV, the photon exchange dominates, while at higher energies, the Z^0 exchange dominates.

At the lowest order, the production cross section at a centre of mass energy $\sqrt{s}$ above the production threshold ($\sqrt{s} > 2m_b$) is calculated by [1, 33]:

$$\sigma(e^+e^- \to b\bar{b}) = \frac{4\pi\alpha^2}{3s}\left\{3\,Q_b^2 + \frac{(v_e^2+a_e^2)(v_b^2+a_b^2)}{\sin^4(2\vartheta_W)}\frac{s^2}{\left(s-M_Z^2\right)^2+s^2\Gamma_Z^2/M_Z^2} - \frac{6\,s\,Q_b v_e v_b}{\sin^2(2\vartheta_W)}\frac{s-M_Z^2}{\left(s-M_Z^2\right)^2+s^2\Gamma_Z^2/M_Z^2}\right\}, \quad (3.1)$$

where α is the electromagnetic coupling constant, Q_b the charge of the b quark ($Q_b = -1/3$), ϑ_W the Weinberg angle, v_e and a_e (respectively v_b and a_b) the vector and axial-vector coupling constants of the neutral weak corrent to the electron (respectively b quark), and Γ_Z and M_Z the width and mass of the Z^0.

The first term of Equation 3.1 represents the photon exchange, the second term the Z^0 exchange and the third term the interference of the two amplitudes. Equation 3.1 describes only the lowest order electroweak exchange without higher order corrections, and does not include either strong interactions in the final state, or the production of the Υ resonances.

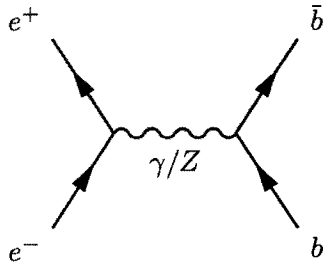

Figure 3.1: b *production diagrams in* e^+e^- *collisions.*

In e^+e^- collision, the highest $b\bar{b}$ production cross-section and the highest fraction of hadronic events containing a $b\bar{b}$ pair can be reached at a centre of mass energy at the $\Upsilon(4S)$ and at the Z^0 resonance. At $\Upsilon(4S)$, the cross section is 1.15 nb, and the cross section ratio $\frac{\sigma(b\bar{b})}{\sigma(q\bar{q})} \simeq 0.25$. At the Z^0 peak, the cross section is 7.7 nb, and $\frac{\sigma(b\bar{b})}{\sigma(q\bar{q})} \simeq 0.215$. The disadvantage of running in the continuum, i.e. not at the Υ or Z^0 resonances, is that the cross section is lower and the signal-to-background ratio is not favourable.

It should be stressed that the $\Upsilon(4S)$ resonance is only 20 MeV above the $B\bar{B}$ threshold, and can therefore only decay to $B^0_d\bar{B}^0_d$ or B^+B^- pairs. At accelerators operating at a centre of mass energy ($\sqrt{s}$) at the $\Upsilon(4S)$ resonance, heavier states, such as B^0_s, B_c, b-flavoured baryons or excited states, cannot be produced. At these low energies, the centre of mass energy would have to be at the $\Upsilon(5S)$ resonance to produce the B^0_s, where the $b\bar{b}$ production cross section is far less than at $\Upsilon(4S)$. The production of b-flavoured hadrons having higher mass can only occur at higher centre of mass energies.

The advantage of running at higher collision energies is that B's are boosted with respect to the centre of mass, which allows a better separation of the production and decay vertices. This is essential to measure the decay-time of the B. The measurement is extremely difficult at $\sqrt{s} = \Upsilon(4S)$, since the decay length is in the order of 30 μm. The separation at high energy can also be used to enhance the purity of the data sample, the background being mostly short-lived.

The advantage of e^+e^- collisions is the cleanliness of the final state. Indeed, apart from the $b\bar{b}$ pair, no other particle is produced, which allows a good tagging efficiency. The reconstruction efficiency is large, as on average 10 charged particles and 10 photons are produced in the event. At $\Upsilon(4S)$, the B candidate can be constrained to the energy of the beam, thereby improving the measurement of the B mass; furthermore, the produced B mesons are mono-energetic ($p_B \simeq 300$ MeV/c), and this can be used for background rejection. Due to this low momentum, events are more spherical, and this topological feature can be used to distinguish B's from the more jet-like background. At the Z^0 resonance, these tracks are in two back-to-back jets.

The PEP-II and KEKB B-factories run with asymmetric beam energies, where the centre of mass is be boosted with respect to the laboratory frame. This permits longer decay lengths and a good separation of the decay vertices of both B mesons.

At $\Upsilon(4S)$, the B meson pair is produced in a coherent quantum state. As a consequence, until one of the two Bs decays, they will evolve coherently, and their flavour can only be defined after the first decay. The time dependent transition amplitudes, and hence the

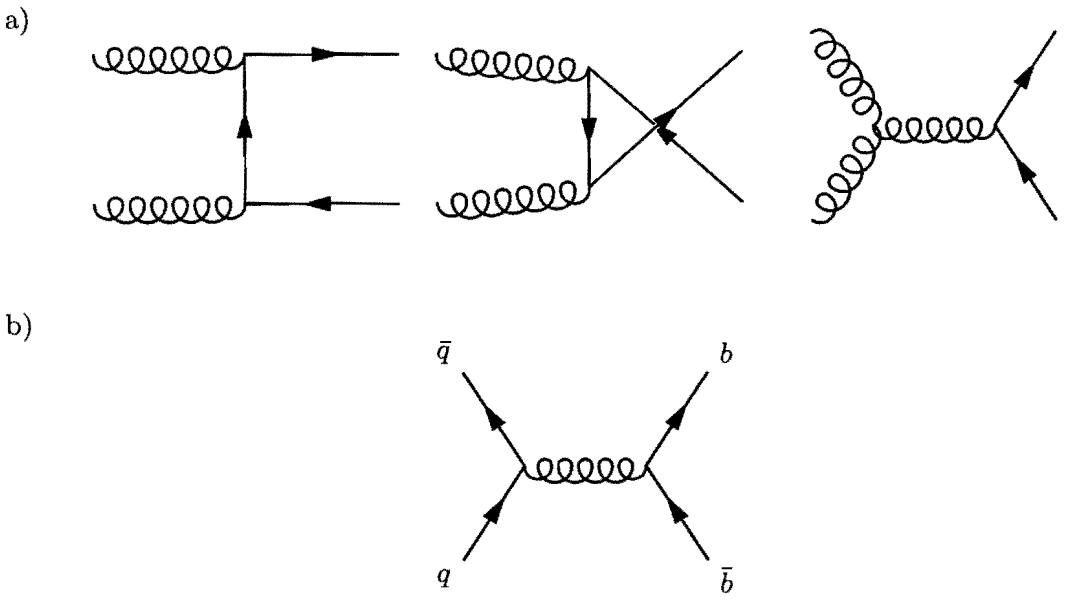

Figure 3.2: *Leading order $b\bar{b}$ production diagrams in hadron collisions.*

sought CP violation asymmetry, will depend on the time between the first and the second decay.

3.1.2. b quark production at hadron colliders

In hadron collisions, $b\bar{b}$ pairs are produced by interactions between the partons composing the proton or the anti-proton: the valance and sea quarks and the gluons. The differential cross section is given by

$$d^3\sigma = \sum_{i,j} \int dx_1 dx_2 \; d^3\hat{\sigma}_{ij}(x_1 P_A, x_2 P_B, m_b, Q^2) f_i^A(x_1, Q^2) f_j^B(x_2, Q^2) \; . \tag{3.2}$$

The sum is made on all partons i (respectively j) composing hadron A (respectively B). x_1 (respectively x_2) is the fraction of the total momentum of hadron A, P_A (respectively the fraction of P_B).

The parton distribution function, f_i (respectively f_j), describes the distribution of the momentum of the parton i (respectively j) inside the hadron when probed at momentum transfer Q^2. This function is measured in deep inelastic scattering experiments such as ep, eN, μN or νN. These measurements are made at low Q^2. For higher values of Q^2, the functions are extrapolated using QCD, for example the Altarelli-Parisi evolution equations [34]. The uncertainty of the cross section due to the difference in the parameterization of the different models is limited, as they are well constrained by the different measurements.

The parton scattering cross section $\hat{\sigma}_{ij}$, can be calculated for heavy quarks as a perturbative expansion in $\alpha_s(\mu^2)$. The energy (renormalization) scale at which α_s is evaluated, μ^2, is thought to be of the order of the mass of the produced quark. It is usually equated with the momentum transfer Q^2, referred to as μ_0 ($\mu = \mu_0 \equiv \sqrt{m_b^2 + p_T^2}$). This uncertainty

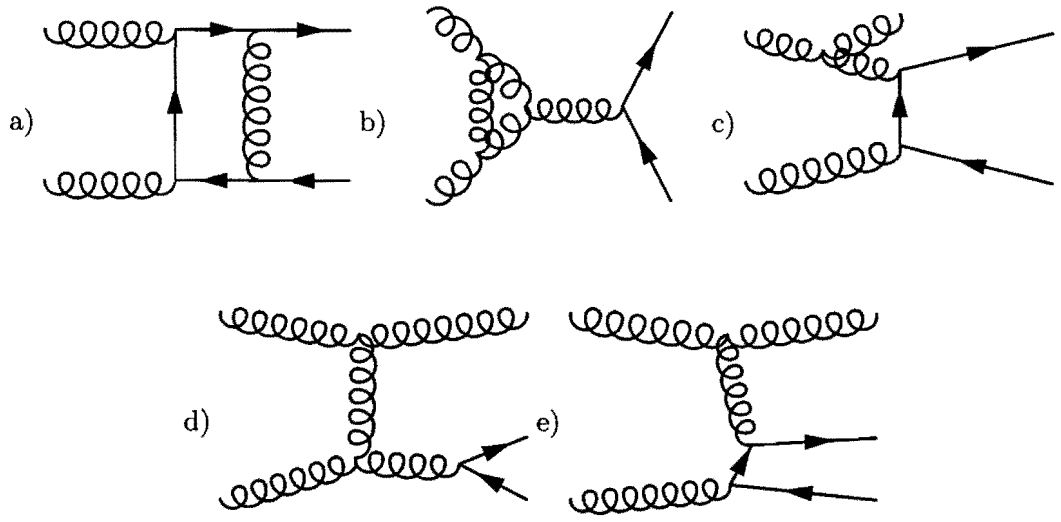

Figure 3.3: *Some next-to-leading order $b\bar{b}$ production diagrams in hadron collisions.*

on the choice of the μ scale is a large source of uncertainty on the calculation of the cross section, which is usually estimated by taking the uncertainty bounds $\mu_0/2 \leq \mu \leq 2\mu_0$.

Another difficulty is the choice of the b-mass, m_b, which is estimated to be between 4.5 and 5 GeV/c^2. The value used for most theoretical predictions is $m_b = 4.75$ GeV/c^2. As the transverse momentum of the produced quarks is large, the uncertainty caused by the choice of m_b is small.

At leading order (LO), $b\bar{b}$ pairs are produced by gluon-gluon fusion ($g + g \rightarrow Q + \bar{Q}$, Figure 3.2a) or quark–anti-quark annihilation ($q + \bar{q} \rightarrow Q + \bar{Q}$, Figure 3.?b), contributing at $\mathcal{O}(\alpha_s^2)$ in the perturbation series. The full calculation for the LO cross section can be found in References [35, 36, 37].

Some next-to-leading-order (NLO) terms in the expansion are, even if at $\mathcal{O}(\alpha_s^3)$, numerically as important as the LO terms. The process $g + g \rightarrow g + g$, followed by $g \rightarrow Q + \bar{Q}$ is of special importance, since the cross section of the $g + g \rightarrow g + g$ process is some hundred times larger than the LO $g + g \rightarrow Q + \bar{Q}$ cross section. Some NLO diagrams are shown in Figure 3.3. These include virtual (Figure 3.3a, b) and real (Figure 3.3c) gluon emission, gluon splitting (Figure 3.3d) and flavour excitation (Figure 3.3d).

The complete NLO calculations have been performed both of the single inclusive (e.g. [38]) and of the full differential heavy quark production cross sections [39]. In the single inclusive cross section calculation, the momentum of the second anti-quark is integrated out. This permits only to calculate the total cross section and the momentum distribution of a single quark, and no prediction is possible for the second quark.

It is noted that the same formalism and methods apply to all 'heavy' quarks, *charm*, *bottom* and *top*. Their large mass permits the use of perturbative QCD models as the importance of non-perturbative effects decrease with increased mass. As such, the top quark is the best suited for these calculations, where there is the best agreement between the cross-section measurements and the predictions, with theoretical uncertainties in the

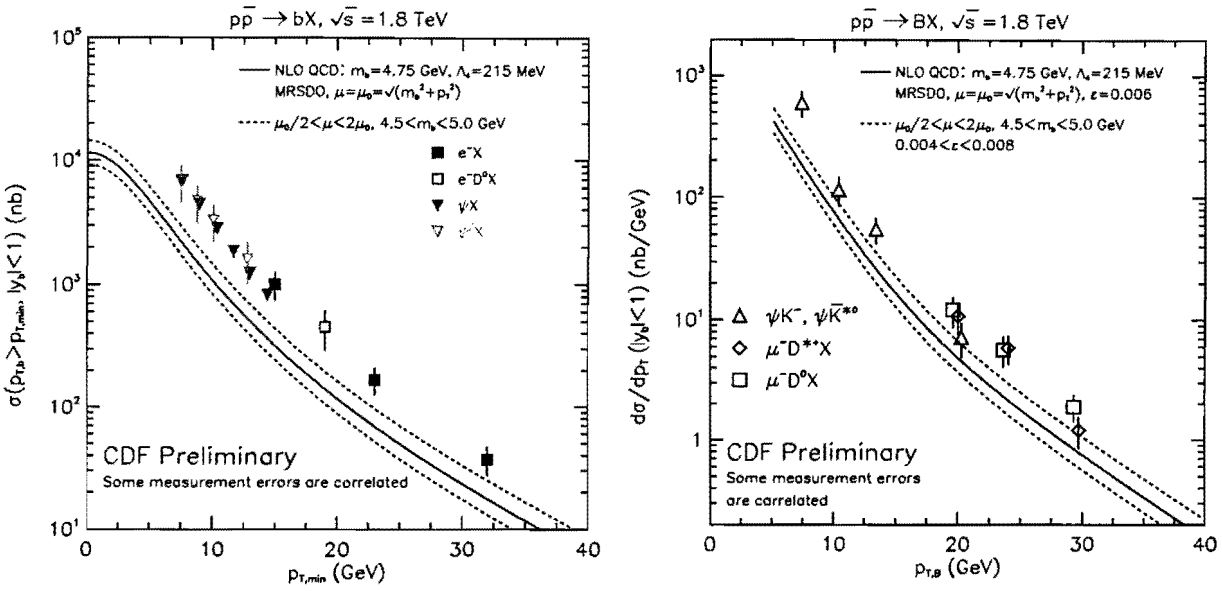

Figure 3.4: *CDF measurement (at 1.8 TeV) of the p_T-integrated* b *quark production cross section (left) and of the differential B meson cross section (right).*

order of 10%. On the other hand, the charm quark, the lightest of the heavy quarks, is the most sensitive to these effects.

The inclusive b quark production cross section has been measured at CDF at centre of mass energies of 630 GeV [40] and 1.8 TeV [41, 42]. Figure 3.4(left) compares the integrated b quark p_T distribution with the NLO QCD predictions. This is the differential p_T distribution integrated above a given p_T threshold (p_T^{min}) within a fixed rapidity range:

$$\sigma(p_T^{min}) = \int_{|y|<y_{max}} dy \int_{p_T>p_T^{min}} dp_T \frac{d^2\sigma}{dy\, dp_T} . \tag{3.3}$$

As can be seen, while the shape of the predictions and of the measurements agree well, the measurements are a factor two higher than the theoretical predictions. The difference could be due to non-perturbative effects or to uncertainties on the choice of theoretical parameters. Nevertheless, the measurements are close to the bounds given by the uncertainties on the theory, when accounting for the uncertainties due to the choice of m_b, μ and of the parton distribution function.

The production of $b\bar{b}$ pairs has also been studied at CDF [43, 44], where the correlation between the quark and the anti-quark is measured. Experimentally, this correlation is important in the study of b-tagging, since, when both b's are tagged, the tagging efficiencies depend on the momentum of both quarks.

Table 3.1 shows the $b\bar{b}$ production cross section at the Tevatron and at LHC, compared to e^+e^- collisions. The main advantage of hadron colliders over e^+e^- colliders for B physics is the much higher production cross section, albeit with a much lower fraction of the total cross section. Furthermore, a large fragmentation background has to be contended with, due to the underlying event.

Accelerator	CESR, PEP-II, KEKB, DORIS	LEP, SLC	Tevatron	LHC
Production	$e^+e^- \to \Upsilon(4S) \to B\bar{B}$	$e^+e^- \to Z^0 \to b\bar{b}$	$p\bar{p} \to b\bar{b} + X$	$pp \to b\bar{b} + X$
CM Energy	10.58 GeV	91.2 GeV	1.8 TeV	14 TeV
$\sigma(b\bar{b})$	1.15 nb	7.7 nb	$\approx 50\ \mu b$	$\approx 500\ \mu b$
$\sigma(b\bar{b})/\sigma(tot)$	0.25	0.215	$\approx 6 \cdot 10^{-4}$	$\approx 2 \cdot 10^{-3}$

Table 3.1: *Comparison of the main B production characteristics at the accelerators featuring experiments studying B physics [45, 46].*

3.2. The hadronization process

After production, b quarks are hadronized (or fragmented) into B mesons. It is a low Q^2 process, to which perturbative QCD cannot be applied, and only phenomenological models exist. The hadronization of heavy quarks displays a different behaviour than light quarks. The *top* quark is not expected to form hadrons, as, due to its high mass, it decays before hadronization occurs.

The most commonly used model to describe the fragmentation process of heavy quarks, *charm* and *bottom*, was developed by Peterson *et al.* [47]. In this model, the fraction of the momentum of the initial b quark transferred to the produced B meson, z, is parameterized by a function, called the fragmentation function:

$$D(z) = \frac{N}{z\left(1 - \frac{1}{z} - \frac{\epsilon_b}{1-z}\right)^2} . \tag{3.4}$$

N is given by the normalization condition $\int D(z)dz = 1$. The quantity z is defined as

$$z = \frac{E(Hadron) + p_{\parallel}(Hadron)}{E(b) + p(b)} , \tag{3.5}$$

where $p_{\parallel}(Hadron)$ is the momentum component parallel to the fragmentation direction and $E(b)$ and $p(b)$ are the energy and momentum of the initial quark after accounting for initial and final state radiation and gluon bremsstrahlung. The quantity z is relativistically invariant with respect to the boost in the direction of the heavy quark. As z is not accessible experimentally, it is often replaced by other variables, such as

$$x^+ = \frac{E(Hadron) + p_{\parallel}(Hadron)}{E(max) + p_{\parallel}(max)} , \tag{3.6}$$

$$x_p = p(Hadron)/p(max) , \tag{3.7}$$

$$\text{or } x_E = E(hadron)/E(beam) , \tag{3.8}$$

which are close approximations of z [1]. The function has a single parameter, different for each heavy quark flavour (ϵ_b for the b), which is called the Peterson fragmentation parameter. The latest measurement, performed by the OPAL collaboration, yield $\epsilon_b = 0.0047^{+0.0010}_{-0.0008}$ [1, 48].

The B meson production cross section can then be found by convoluting the b production cross section with the fragmentation function. The differential production cross section measured at CDF [49] is shown in Figure 3.4(right). Obviously, the discrepancies between the measurements and the predictions observed for the b quark production are present for the B meson production as well.

Some measurements suggest that this model, initially developed to describe fragmentation processes in heavy quarks produced in e^+e^- collision, is not suited for hadron collisions [32]. Several alternative models are proposed, such as the perturbative gluon bremsstrahlung model or the non-perturbative string fragmentation. An overview of these models is given in References [31, 30] and references therein.

Chapter 4

Flavour Changing Neutral Current decays of B mesons

A thing of beauty is a joy forever;
Its loveliness increases; it will never
Pass into nothingness.
John Keats, Endymion. Book I.

4.1. Introduction

Flavour Changing Neutral Current (FCNC) processes are forbidden in the Standard Model of Electroweak Interactions at tree level. They can proceed at very low rate at higher orders through box and penguin diagrams.

In the Standard Model, neutral currents are flavour conserving, as is ensured by the unitarity of the Cabibbo-Kobayashi-Maskawa (CKM) matrix. There is no direct coupling between the b and the s or d quarks. Were all quarks of same isospin of equal mass, higher order processes would also cancel, as is explained in the GIM mechanism, and FCNC processes would not exist. Thus, in the B system, it is due to the high mass of the *top* quark and the fact that the coupling of the b quark to the t quark is close to unity, that these processes are not entirely negligible. Moreover, their relative importance is enhanced by the low value of the coupling of the b quark to the c quark, V_{cb}, which suppresses the otherwise CKM-favoured tree diagram decays.

FCNC processes provide a fertile testing ground for the Standard Model, and its extensions. A comparison of measured and predicted decay rates provide a test of the validity of the Standard Model, as many processes of extensions to the Standard Model enhance or suppress FCNC decay rates. This permits an indirect probe of these models while direct effects would still be beyond reach.

In the Standard Model, the decay rates allow to access many of the fundamental parameters, such as the CKM matrix elements (in particular $|V_{td}|$, $|V_{ts}|$, ρ and η) and the quark

masses. In addition, as many required factors cannot be calculated from first principles but require non-perturbative QCD calculations, the phenomenological models used for these calculations can also be tested.

These characteristics also present the main difficulties of FCNC decays. Theoretical uncertainties are large, as strong interaction effects, being at low q^2, do not permit perturbative QCD calculations, and many parameters entering the calculations are only poorly known. Indeed, not enough observations are available to constrain the parameters present in the calculations.

Furthermore, the scarcity of FCNC measurements themselves, and their limited accuracy, provide little quantitative information at this stage. Their very low rates place most of these decays outside of reach of the present generation of experiments. The advent of B-factories and the high luminosity of hadron colliders is expected to provide several further observations and measurements of new FCNC decays in the B sector.

The field of FCNC B decays has undergone profound changes in the last few years. FCNC have initially been seen as a way to probe the *top* quark mass. With the discovery of *top* quark and its direct mass measurement, emphasis has shifted towards determination of the CKM matrix elements and physics beyond the Standard Model.

A brief overview of the theoretical framework of FCNC decays will be given, followed by a review of several classes of FCNC B decays. References [50, 51] are excellent in-depth reviews, with further references, on this vast subject.

4.2. The theoretical framework

4.2.1. Effective FCNC vertices

As already mentioned, due to the GIM mechanism, FCNC transitions do not occur at tree level, but only through higher order processes. The most important of these processes are one-loop diagrams, called penguin diagrams (Figure 4.1), and box diagrams (Figure 4.2).

Electromagnetic penguin diagrams are responsible for the radiative decays $b \to s\gamma$. As the hard photon provides a good experimental signature, the decay $B \to K^*\gamma$[1] was the first radiative penguin decay to be discovered [52], being observed in 1993 by the CLEO collaboration.

Unlike the electromagnetic penguins, gluonic penguins $b \to sg^*$ do not have such a good experimental signature. For most of these decays, the branching fractions are small, and most of the final states receive contributions from other diagrams. Furthermore, hadronization effects are difficult to calculate. Nevertheless, the CLEO collaboration has observed several two-body decays (such as $B^+ \to K^0\pi^+$ or $B \to \omega K^+$) to which gluonic penguin diagrams are believed to contribute significantly, or, as in the case of the decay $B^+ \to K^0\pi^+$, which can only be reached through gluonic penguins [53].

Box diagrams are responsible for particle–anti-particle mixing, which has been observed both in the B_d^0 and in the K^0 system, and of course for the $K^0 \to \mu^+\mu^-$ decay, which led

[1] Charge conjugate states are always implied throughout this dissertation, unless specifically stated.

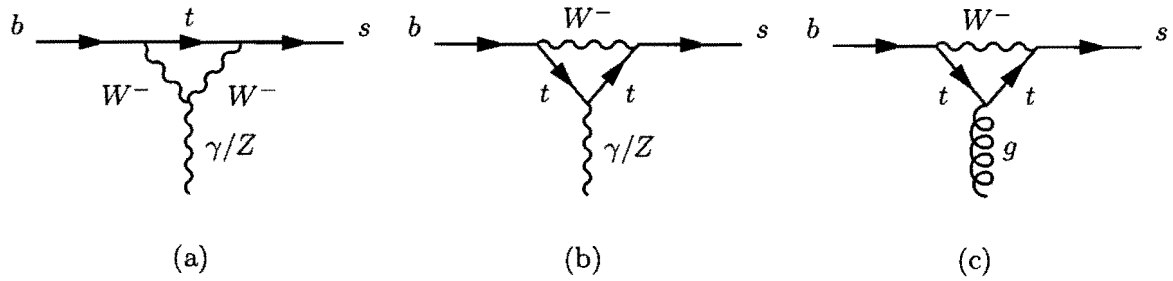

Figure 4.1: *Examples of penguin diagrams.*

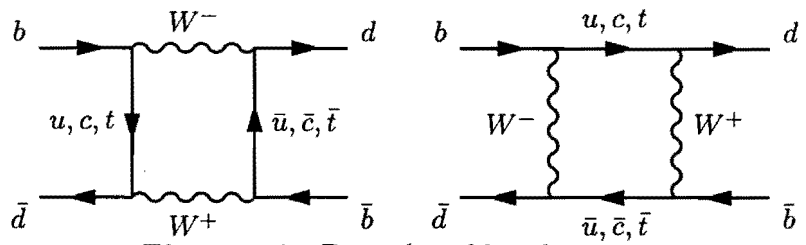

Figure 4.2: *Examples of box diagrams.*

to the proposal of the GIM mechanism.

These effective vertices can be calculated by using the elementary vertices and propagators commonly used, and effective 'Feynman rules' can be derived [50], as will be seen later.

The higher order in the gauge couplings contributes to the suppression of these diagrams. Their relative importance depends on the mass of the internal fermion lines, explaining the importance of the contribution of the *top* quark, and obviously on the relevant CKM matrix elements.

4.2.2. The Operator Product Expansion approach

To calculate the decay rates for FCNC decays, the most often used model is the Operator Product Expansion (OPE) model [54]. This model provides an effective low-energy model describing weak and strong interactions of quarks. An extensive review of the OPE approach and its application to FCNC processes is given in References [50, 51].

The central idea behind the OPE approach is that the scale of the relevant interactions, of the order of a few GeV, is low compared to the mass of the propagator, the W. As the W propagator is of the form $\frac{1}{k^2-M_W^2}$ (k being the momentum transferred by the W), the amplitude can be written as an expansion in powers of k^2/M_W^2. Thus, when calculating an amplitude, the $\mathcal{O}(k^2/M_W^2)$ terms can be neglected.

This is equivalent to writing an effective local Hamiltonian, $\mathcal{H}_{eff}$, where the short range exchange of a heavy boson can be replaced locally by a point-like interaction, as in the classic Fermi current-current theory of weak interactions. To write $\mathcal{H}_{eff}$, the product of the two charged-current operators is expanded into a series of local operators. The contribution of these operators is weighted by effective coupling terms, called the Wilson coefficients. $\mathcal{H}_{eff}$

can then be written as

$$\mathcal{H}_{eff} = \sum_i C_i(\mu) O_i(\mu) \,, \tag{4.1}$$

where O_i are the local operators and C_i the Wilson coefficients. The dominant contribution to this expansion is given by four fermion operators, and higher-order operators can be neglected.

This approach factorizes the problem into two parts. Low-energy (long-distance) interactions (such as hadronization effects) are contained in the operators, while high-energy (short-distance) contributions (such as hard gluon exchanges) are given by the Wilson coefficients. The limit between the two regimes is represented by the renormalization scale μ, chosen to be of the order of a few GeV for B decays. It should be noted that QCD corrections, which are inherently difficult to calculate, arise at both long- and short-distance and constitute one of the largest uncertainties of the theoretical predictions. They are known to modify the decay rates significantly in several cases, and cannot be neglected.

The Wilson coefficients are functions of α_s, M_W and μ. They are usually calculated perturbatively at $\mu_W = M_W$, by matching the full theory onto the effective theory, and then evolved to the chosen low-energy scale μ using renormalization group equations. Perturbative calculations can be made, as at this scale the effective QCD coupling is small. The renormalization group is a group of transformations between different choices of renormalization scales. This evolution of the coefficients has the effect of mixing the operators

$$C_i(\mu) = \sum_j U_{ij}(\mu, \mu_W) C_j(\mu_W) \,, \tag{4.2}$$

where $U_{ij}(\mu, \mu_W)$ is the evolution matrix given by the renormalization group equations.

Finally, the matrix elements $\langle O_i(\mu) \rangle$ have to be calculated at the low-energy scale μ. As long distance QCD effects are involved, non-perturbative methods, such as lattice calculation or QCD sum rules, have to be used.

Ideally, the μ dependence of the coefficients will cancel the μ dependence of the operators, since obviously the physical amplitude can not depend on μ. However, since perturbative calculations are involved, the truncation of the perturbative series will leave a scale dependence. At leading order, in the so-called leading logarithmic approximation (LLA), only terms of the form $\alpha_s^n \ln^n(M_W/m_b)$ are summed. one of the ali papers. At next-to-leading order (next-to-leading order logarithmic approximation – NLLA), also terms of the form $\alpha_s^n \ln^{n-1}(M_W/m_b)$ are added in the sum.

A further dependence is therefore added by the choice of the renormalization scheme, since different renormalization schemes will feature different perturbative series. Quantities like the Wilson coefficients will be dependent on the scheme used, and add a further uncertainty to the results. To minimize the effect of the scheme dependence, both the Wilson coefficients and the matrix elements have to be calculated in the same scheme. The two most commonly used schemes for FCNC calculations are the 'naive dimensional regularization' (NDR) scheme and the 't Hooft-Veltman (HV) scheme [55].

With the above described procedure, the heavy degrees of freedom are integrated out, i.e. the operators will not be dependent on masses larger than μ, such as the *top* quark and the W and Z^0 masses. These large masses would cause the operators to include large

logarithms ($\mathcal{O}(\ln(M_W/m_b))$). By calculating the coefficients at a high scale, such as μ_W, where the light masses are negligible in front of the high masses, and scaling them down to μ, the high masses are removed from the matrix elements and put into the coefficients.

This approach can be viewed as the construction of a non-renormalizable low-energy effective field theory consisting of only five quarks. Being non-renormalizable, this effective theory will only be valid for momenta below M_W. Since the numerical value of the Wilson coefficients is independent of the final state, the operators can be viewed as the effective interaction vertices and the Wilson coefficients as the effective coupling constants of the effective theory.

4.2.3. The effective Hamiltonian

The similarity of FCNC processes, decays or mixing, allows us to describe all FCNC processes with a set of basic effective vertices. The effective Hamiltonian for FCNC decays can then be written as an expansion in terms of the four-fermion local operators describing these effective vertices.

These local operators can be classified in six classes [50]:

a) Current-current operators (Figure 4.3a):

$$\begin{aligned} O_1 &= (\bar{c}_\alpha b_\beta)_{V-A}(\bar{u}_\beta s_\alpha)_{V-A} \\ O_2 &= (\bar{c}b)_{V-A}(\bar{u}s)_{V-A} \end{aligned}$$

b) QCD penguin operators (Figure 4.3b):

$$\begin{aligned} O_3 &= (\bar{s}b)_{V-A} \sum_{q=u,d,s,c,b} (\bar{q}q)_{V-A} \\ O_4 &= (\bar{s}_\alpha b_\beta)_{V-A} \sum_{q=u,d,s,c,b} (\bar{q}_\beta q_\alpha)_{V-A} \\ O_5 &= (\bar{s}b)_{V-A} \sum_{q=u,d,s,c,b} (\bar{q}q)_{V+A} \\ O_6 &= (\bar{s}_\alpha b_\beta)_{V-A} \sum_{q=u,d,s,c,b} (\bar{q}_\beta q_\alpha)_{V+A} \end{aligned}$$

c) Electroweak penguin operators (Figure 4.3c):

$$\begin{aligned} O_7 &= \frac{3}{2}(\bar{s}b)_{V-A} \sum_{q=u,d,s,c,b} e_q(\bar{q}q)_{V+A} \\ O_8 &= \frac{3}{2}(\bar{s}_\alpha b_\beta)_{V-A} \sum_{q=u,d,s,c,b} e_q(\bar{q}_\beta q_\alpha)_{V+A} \\ O_9 &= \frac{3}{2}(\bar{s}b)_{V-A} \sum_{q=u,d,s,c,b} e_q(\bar{q}q)_{V-A} \\ O_{10} &= \frac{3}{2}(\bar{s}_\alpha b_\beta)_{V-A} \sum_{q=u,d,s,c,b} e_q(\bar{q}_\beta q_\alpha)_{V-A} \end{aligned}$$

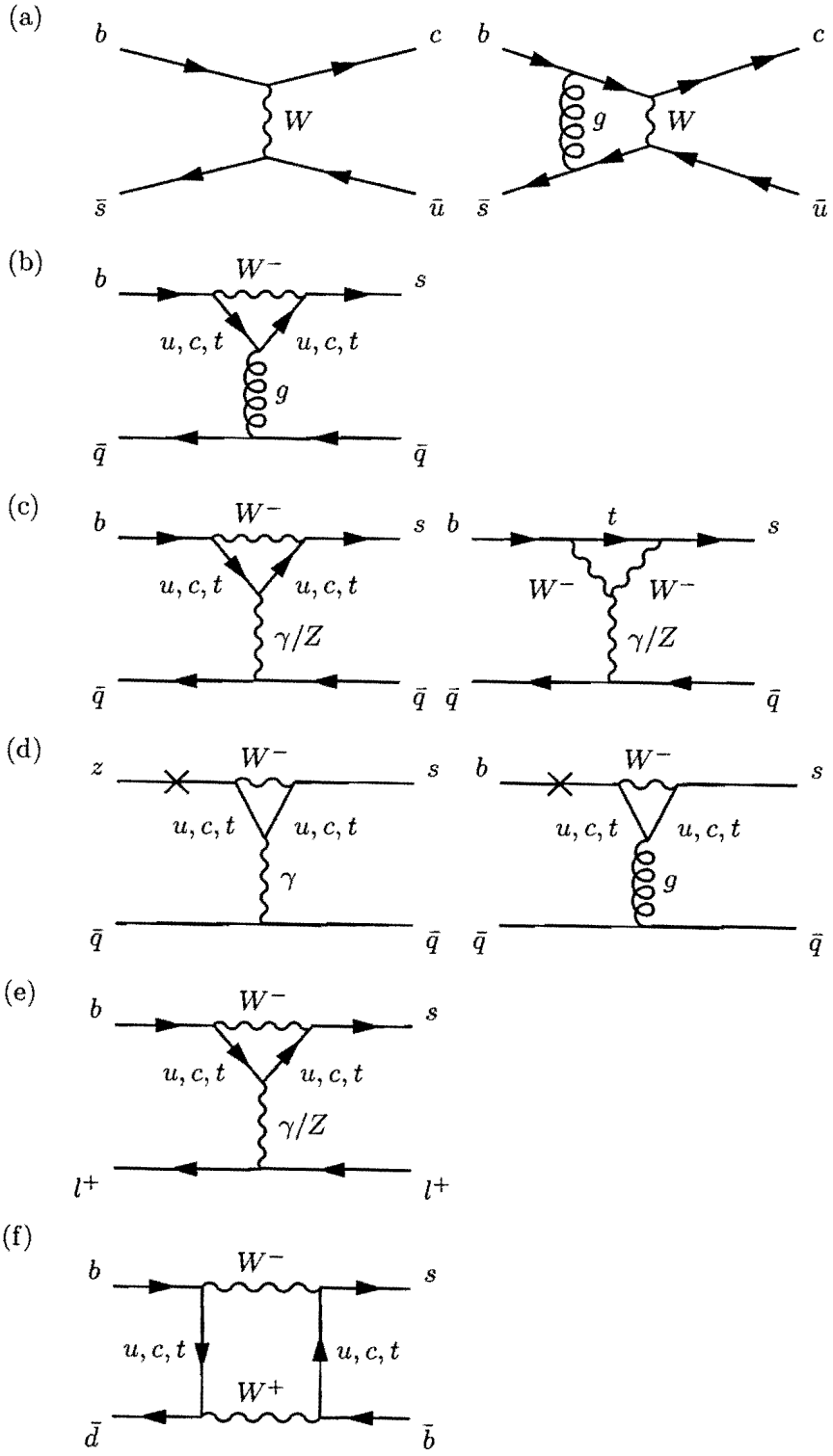

Figure 4.3: *The effective vertices governing FCNC decays.*

d) 'Magnetic penguin' operators (Figure 4.3d):

$$\begin{aligned} O_{7\gamma} &= \frac{e}{8\pi^2} m_b \bar{s}_\alpha \sigma^{\mu\nu}(1+\gamma_5) b_\alpha F_{\mu\nu} \\ O_{8G} &= \frac{g}{8\pi^2} m_b \bar{s}_\alpha \sigma^{\mu\nu}(1+\gamma_5) T^a_{\alpha\beta} b_\beta G^a_{\mu\nu} \end{aligned}$$

e) Semi-leptonic electroweak penguin operators (Figure 4.3e):

$$\begin{aligned} O_{9V} &= (\bar{s}b)_{V-A}(\bar{l}l)_V \\ O_{10A} &= (\bar{s}b)_{V-A}(\bar{l}l)_A \\ O_{\nu\bar{\nu}} &= (\bar{s}b)_{V-A}(\bar{\nu}\nu)_{V-A} \\ O_{l\bar{l}} &= (\bar{s}b)_{V-A}(\bar{l}l)_{V-A} \end{aligned}$$

f) $\Delta B = 2$ operators (Figure 4.3f):

$$O(\Delta B = 2) = (\bar{b}d)_{V-A}(\bar{b}d)_{V-A}$$

The notations

$$(\bar{c}b)_{V-A} = [\bar{c}\gamma_\mu(1-\gamma_5)b] \tag{4.3}$$

$$(\bar{l}l)_V = [\bar{l}\gamma_\mu l] \tag{4.4}$$

$$(\bar{l}l)_A = [\bar{l}\gamma_\mu\gamma_5 l] \tag{4.5}$$

are used, and α and β denote colour indices that are omitted for colour singlet currents, $F_{\mu\nu}$ and $G^a_{\mu\nu}$ are the electromagnetic and strong interaction tensors, and e_q is the electric charge of the relevant quark.

For these effective vertices, the mass of the external fermions can be set to 0, as this mass is small compared to the mass of the propagator. The influence of a non-zero mass would be felt only in the cases of QCD and photon penguin diagrams. To include the effect of this mass, a new diagram, called 'magnetic penguins' (Figure 4.3d), is added, which introduces a first order correction in m_{ext}/M_W. Only the b quark has a large enough mass to require such terms. The external mass taken into account is indicated by a cross on the propagator.

Not all processes are sensitive to all of the Wilson coefficients, even after they have been mixed by the renormalization. The decay $b \to s\gamma$ is only sensitive to the absolute value of C_7 and, to a lesser extent, C_8, while $b \to sl^+l^-$ will be sensitive to the value and sign of C_7, C_9 and C_{10}. Measurements of these processes will impose limits on the permitted values of the Wilson coefficients, which translate into bounds on extensions to the Standard Model. The decay $b \to s\nu\bar{\nu}$ is the easiest to calculate, since only Z^0 and box diagrams contribute.

4.3. The radiative decays $b \to s\gamma$ and $b \to d\gamma$

After the initial observation of the decay $B \to K^*\gamma$, the CLEO collaboration measured the branching fraction of these exclusive decays to be $\mathcal{B}(B^0 \to K^{*0}\gamma) = (4.55^{+0.72}_{-0.68} \pm 0.34) \cdot 10^{-5}$ and $\mathcal{B}(B^+ \to K^{*+}\gamma) = (3.76^{+0.89}_{-0.83} \pm 0.28) \cdot 10^{-5}$ [56].

The inclusive $b \to s\gamma$ decay rate was later measured by the CLEO collaboration ($\mathcal{B}(b \to s\gamma) = (3.15 \pm 0.35 \pm 0.32 \pm 0.26) \cdot 10^{-4}$ [57]), and by the ALEPH collaboration ($\mathcal{B}(b \to s\gamma) = (3.11 \pm 0.80 \pm 0.72) \cdot 10^{-4}$ [58]).

This decay rate is among the easiest of the FCNC B decay rates to calculate, as it involves mainly short distance contributions and long distance processes are estimated to contribute less than 10%, Furthermore, uncertainties due to hadronization effects are reduced. The Standard Model predictions at next-to-leading order for the inclusive rate is $\mathcal{B}(b \to s\gamma) = (3.48 \pm 0.31) \cdot 10^{-4}$ [59].

This is currently the only FCNC B decay for which both reliable predictions and a direct measurement of the branching fraction exist. As such, these results can now be used to estimate the CKM matrix element V_{ts} (c.f. Section 4.7.1), and to impose constraints on extensions to the Standard Model [60, 61].

With the CKM-suppressed inclusive $b \to d\gamma$ decay, which is expected to be one to two orders of magnitude lower than the inclusive $b \to s\gamma$ decay, the ratio of branching fractions $\mathcal{B}(b \to d\gamma)/\mathcal{B}(b \to s\gamma)$ would yield the parameters ρ and η from the Wolfenstein parameterization of the CKM matrix [62].

Exclusive decays have the disadvantage that they require knowledge of the hadronization process probabilities, which cannot be calculated from first principles. The ratio of $B \to K^*\gamma$ decays to $b \to s\gamma$ is predicted to be $(16 \pm 4)\%$ [63]. With the latest measurements, the mean of the measured ratios for B^+ and B^0 is $(13.2 \pm 3.5)\%$ ($B \to K\gamma$ is forbidden by angular momentum conservation). Experimentally, they have the advantage that additional kinematic constraints can be imposed on the final state, which leads to a lower background.

The large number of B decays that B-factories should collect will allow the measurement of the branching fractions of inclusive and exclusive radiative $b \to s\gamma$ decays with reduced systematic uncertainties. This will permit better constraints on theoretical models. The recent observation of the decay $B \to K_3^*(1430)\gamma$ could already be used to rule out one specific theoretical model [56].

4.4. The decays $b \to sl^+l^-$

The decays $b \to sl^+l^-$ receive short-distance contributions from electromagnetic and Z^0penguin diagrams and W box diagrams (Figure 4.4(a) and Figure 4.4(b)) and long-distance contributions from the process $b \to s(c\bar{c}) \to sl^+l^-$, with both resonant (mainly J/ψ and $\psi(2S)$) and continuum intermediate ($c\bar{c}$) states (Figure 4.4(c)). Figure 4.4 shows the main diagrams responsible for the exclusive decay $B_s^0 \to \mu^+\mu^-\phi$.

The operators contributing to the effective Hamiltonian are the current-current operators (O_1, O_2), the QCD penguin operators ($O_3, \ldots, O_6$), the magnetic penguin operators ($O_{7\gamma}, O_{8G}$) and the semi-leptonic Z^0 and γ penguin operators (O_{9V}, O_{10A}) [64]. The effective Hamiltonian will then be

$$\mathcal{H}_{eff} = -\frac{4G_F}{\sqrt{2}} V_{tb}V_{ts}^* \sum_{i=1}^{10} C_i(\mu)O_i \,, \tag{4.6}$$

where G_F is the Fermi constant, C_i the Wilson coefficients and O_i the four fermion operators.

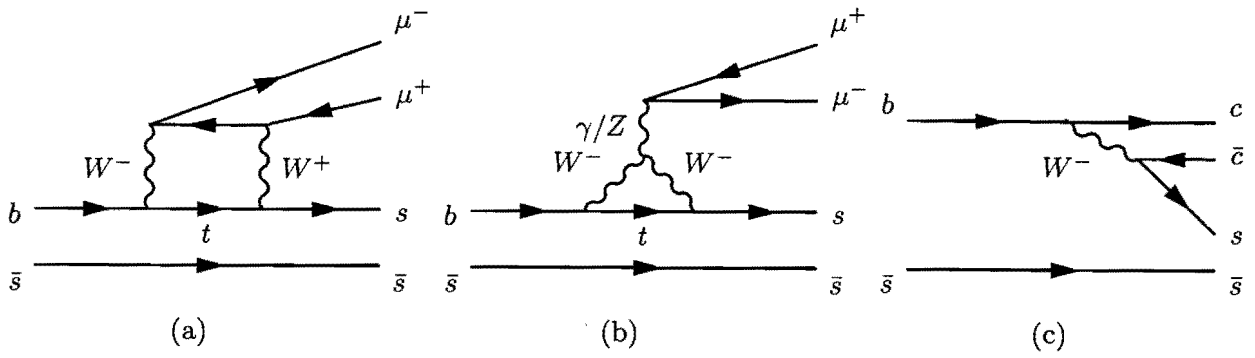

Figure 4.4: *Main diagrams contributing to the $B_s^0 \to \mu^+\mu^-\phi$ decay. (a) and (b) are short distance processes and (c) the long distance process leading to $c\bar{c}$ intermediate states.*

Diagrams where the internal virtual quark is a *top* quark are, due to its large mass, largely dominant over diagrams with virtual *up* or *charm* quarks. Diagrams with an internal *up* quark are entirely negligible, due to both its small mass and small value of the relevant CKM matrix elements ($|V_{ub}V_{us}^*/V_{tb}V_{ts}^*| < 0.02$). Diagrams with an internal *charm* quark represent small corrections, and the untitarity constraint $V_{us}V_{ub}^* + V_{cs}V_{cb}^* + V_{ts}V_{tb}^* = 0$ allows the replacement of $V_{cs}V_{cb}^*$ by $-V_{ts}V_{tb}^*$.

The long-distance contributions are generated by the current-current operators O_1 and O_2. In the dimuon invariant mass regions around the J/ψ and $\psi(2S)$ resonances, the decay is largely dominated by the long-distance contributions, while away from these resonances, the short-distance contributions dominate. The branching fraction of the long-distance decay is around two to three orders of magnitude larger than the short-distance decay. For most final states, the long-distance decay $B \to X_s J/\psi$[2] is well established (with the J/ψ usually seen via its decay to two muons), and the main interest lies in the observation of the short distance processes.

The main contribution to the short-distance processes comes from the semi-leptonic penguin operators O_{9V}, with the Z^0 penguin inducing a strong dependence on the *top* mass [65]. The other operators are only of relevance at next-to-leading order (NLO).

The complete calculation of the Wilson coefficients at NLO for the short-distance processes contributing to $B \to X_s l^+ l^-$ decays is presented in References [66] and [67]. It is also shown in Reference [66] that the scale dependence of the Wilson coefficients is indeed cancelled by the scale dependence of the matrix elements.

An accurate description of $B \to X_s l^+ l^-$ decays has to include the long-distance contributions, as, even away from the resonances, these contributions are not negligible, and both contributions interfere. The $J^{PC} = 1^{--}$ $c\bar{c}$ resonance contributions are included by adding a Breit-Wigner to the propagators, while the $c\bar{c}$ continuum contribution is obtained from the electromagnetic penguin diagram [68, 69, 70]. These contributions are contained entirely in the Wilson coefficients when replacing the $C_{9V}(m_b)$ coefficient by an effective coefficient $C_{9V}^{eff}(m_b, q^2)$ [71]. The experimental masses of the resonances and of the branching fractions $\mathcal{B}(B \to X_s\psi^{(n)})$ and $\mathcal{B}(\psi^{(n)} \to l^+l^-)$ (with $\psi^{(n)} = J/\psi, \psi(2S), \ldots$) are used to constrain the contributions arising from the resonance contributions [72]. It is uncertain

[2]The term X_s refers to any final state with an s quark.

whether this approach describes accurately the long-distance contributions away from the resonances, especially at low q^2, but there are no theoretical arguments to support other approaches [70, 73].

It is useful to present the differential decay rate as a function of the invariant mass of the lepton pair $\frac{d\Gamma}{d\hat{s}}$([3]), as the lepton pair can originate from a $c\bar{c}$ pair. The contributions of the long-distance $c\bar{c}$ resonances can then easily be visualised, and, if needed, the lepton pair invariant mass regions around the resonances can easily be omitted from the decay rate.

The discovery of both inclusive and exclusive decays and the measurement of their branching fraction and dilepton invariant mass distribution will already yield precious informations on the dynamics of the processes involved, but additional information can be obtained from the forward-backward asymmetry and lepton polarization asymmetry. The different dependence on the Wilson coefficients of the different distributions would help to disentangle the contributions of the Wilson coefficient and their dynamical behaviour.

The forward-backward charge asymmetry [71] is defined as

$$A_{FB}(\hat{s}) = \frac{1}{d\Gamma/d\hat{s}} \cdot \left\{ \int_0^1 d\cos(\vartheta)\, \frac{d^2\Gamma}{d\hat{s}\, d\cos(\vartheta)} - \int_{-1}^0 d\cos(\vartheta)\, \frac{d^2\Gamma}{d\hat{s}\, d\cos(\vartheta)} \right\} , \tag{4.7}$$

where ϑ is the angle between the anti-lepton l^+ and B meson in the rest frame of the lepton pair. Flavour tagging of the B meson is not necessary, as the definition is the same for B and $\bar{B}$ mesons.

The longitudinal lepton polarization asymmetry [74], defined as

$$P_L(\hat{s}) = \frac{1}{d\Gamma/d\hat{s}} \cdot \left\{ \frac{d\Gamma(\lambda=-1)}{d\hat{s}} - \frac{d\Gamma(\lambda=+1)}{d\hat{s}} \right\} , \tag{4.8}$$

where the $\lambda = -1(+1)$ refers to the right- (left-) handed lepton l^-, is of interest in the decays with a τ lepton, as the polarization of the τ can be determined through its decay products (e.g. momentum distributions).

In the dilepton invariant mass distribution, only two small regions, at low and high q^2, can be used to measure the Wilson coefficients describing the short distance contributions, due to the non-negligible interference with the long distance contributions elsewhere. For the lepton polarization asymmetry, long distance contributions add a sharp peak at the resonances, but away from these, do not seem to affect significantly the distribution [75]. This feature would permit to use this quantity to measure the Wilson coefficients in a model independent way, as the model describing the long-distance contributions is still uncertain.

4.4.1. Inclusive decays

For inclusive decays such as $b \to s l^+ l^-$, the spectator model can be used. In this model, the decay of a B meson can be approximated by the decay of free b quark, the mass of the b quark being large compared to the second quark. The matrix elements of the decay can be

[3]The standard dimensionless kinematic variables $\hat{s} = s/M_B^2$, with $s = (p_{l-} + p_{l+})^2 = q^2$ (q^2 is the invariant mass of the two leptons), and $\hat{t} = t/M_B^2 = (p_B - p_{l+})^2/M_B^2$ are used throughout this dissertation.

	Prediction	Upper limit
$\mathcal{B}(b \to se^+e^-)_{SD}$	$(8.4 \pm 2.3) \cdot 10^{-6}$	$< 5.7 \cdot 10^{-5}$
$\mathcal{B}(b \to s\mu^+\mu^-)_{SD}$	$(5.7 \pm 1.2) \cdot 10^{-6}$	$< 5.8 \cdot 10^{-5}$
$\mathcal{B}(b \to s\tau^+\tau^-)_{SD}$	$(2.6 \pm 0.5) \cdot 10^{-7}$	-
$\mathcal{B}(b \to se^\pm\mu^\mp)_{SD}$	forbidden in SM	$< 2.2 \cdot 10^{-5}$

Table 4.1: *Branching fraction predictions [70] and experimental upper limits (at 90%C.L.) [77] for the inclusive $b \to sl^+l^-$ decays.*

written as an expansion in powers of $1/m_b$ (Heavy Quark Expansion – HQE [76]). At leading order, $\mathcal{O}(1/m_b)$, the hadronic matrix element $\langle X_s|O_i|B\rangle$ corresponds to the matrix element of the free quarks, $\langle s|O_i|b\rangle$, which is easier to calculate, as it can be done perturbatively. Correction terms for real and virtual gluons are usually added. The next-to-leading order corrections of this expansion will be $\mathcal{O}(1/m_b^2)$, which, thanks to the high mass of the b quark, are small. It is estimated that $1/m_b^2$ corrections cause a suppression of the decay rate of the order of 1.5% [70].

The inclusive decay has the advantage that it does not require for the calculations of the decay rate the probability of forming a specific hadronic final state. The theoretical uncertainties are therefore much reduced.

The calculation of the differential decay rate at NLO has been presented in Reference [66], to which the long-distance contributions have to be added [70]. The theoretical predictions of the branching fractions are given in Table 4.1, with the experimental upper limits. The most stringent limits on the branching fractions have been reached by CLEO [77]. As can be seen, the experimental upper limits are an order of magnitude above the branching fractions predicted by the Standard Model. CLEO has also searched for the lepton number violating decay $b \to se^\pm\mu^\mp$, which is forbidden in the Standard Model.

4.4.2. Exclusive decays

For the calculation of the decay rates of semi-leptonic exclusive decays, the matrix elements of $\mathcal{H}_{eff}$ can be factorized into a hadronic and a leptonic current:

$$\langle hL|O_i|B\rangle = \langle h|J_h|B\rangle \cdot \langle L|J_l|0\rangle \ . \tag{4.9}$$

The leptonic current can be written explicitly and the hadronic current can be expressed in terms of the relativistic invariant meson transition form factors [78], which will contain the dynamic information of the decay process.

Based on these, the analytical expressions of the differential partial width $\frac{d^2\Gamma}{d\hat{s}\,d\hat{t}}$ and of $\frac{d\Gamma}{d\hat{s}}$, obtained after integrating $\frac{d^2\Gamma}{d\hat{s}\,d\hat{t}}$ over $\hat{t}$, can be calculated [75]. While Reference [75] calculates the form factors for $B \to (K, K^*)l^+l^-$, the expressions of the partial widths can be used for any decay of the form $B \to X_s l^+l^-$, with either a pseudo-scalar or a vector meson in the final state, provided the appropriate form factors are known.

As these form factors describe all strong interaction effects, they have to be calculated using non-perturbative models, for each individual configuration of initial and final states

mesons. Different models yield the form factors in different kinematic regions. The form factors are usually calculated in a small region, then extrapolated to the entire region, providing a parameterization of these. No single model can calculate the form factors accurately over the entire allowed kinematic region.

The theoretical predictions are therefore dependent on the model used. The main uncertainties in these models is the imprecise knowledge of the hadron structure and formation mechanism, as the quarks are of course not free but contained in a hadron, and of the quark masses.

It is hoped that the measurement of the decay rates will yield a measurement of the CKM matrix element V_{ts}, and the precise knowledge of the form factors is thus essential. Exclusive decays have the disadvantage over the inclusive $b \to sl^+l^-$ decays, that the formation mechanism of the specific final state hadron, contained in the form factors, has to be known.

Each measured decay would constrain the form factors relevant to that decay and result in a refinement of the models used to calculate these form factors. This, in turn, would decrease the uncertainties on the form factors of related decays.

The decays $B^+ \to l^+l^-K^+$ and $B^0 \to l^+l^-K^{*0}$

The decays $B^+ \to l^+l^-K^+$ and $B^0 \to l^+l^-K^{*0}$ are the most studied exclusive $b \to sl^+l^-$ decays. Each of the two decays is expected to constitute 10% of the total $b \to sl^+l^-$ rate. The $B \to K, K^*$ transition form factors have been calculated in several models, among which are lattice QCD, three-point QCD sum rules [79], light-cone QCD sum rules [80, 81, 82], quark models [75, 83, 84], and potential models [85]. The comparison between the different sets of form factors is usually done at $q^2 = 0$. Most recent calculations show an agreement to within 20%, which is generally the estimated accuracy.

The differential partial width of the decay $B^0 \to l^+l^-K^{*0}$ shows a stronger dependence on the q^2 behaviour of the form factors than the decay $B^+ \to l^+l^-K^+$ [83]. For the latter decay, the decay rate is expected to be the same for $B^+ \to e^+e^-K^+$ and $B^+ \to \mu^+\mu^-K^+$. For the decays with a τ lepton, the decay rate is much reduced, as the phase space is much more restricted.

The theoretical predictions of the branching fractions are given in Table 4.2 for different form factor calculations. As the branching fractions obtained with the different form factor calculations can differ significantly, it is expected that exclusive decays cannot be used to test the Standard Model or determine its fundamental parameters, such as the CKM matrix elements, but rather can be used to constrain the different QCD models. It is nevertheless hoped that some model-independent quantities can be extracted and used for the purpose of testing the Standard Model.

The most stringent limits on the branching fractions of these decays have been placed by CDF and CLEO. These limits are shown in Table 4.3. The experimental upper limits are about an order of magnitude above the branching fractions predicted by the Standard Model, with the noteworthy exception of the limit on the decay $B^0 \to \mu^+\mu^-K^{*0}$, which is less than a factor three higher than the expected value!

Reference	$\mathcal{B}(B^+ \to l^+l^-K^+)$	$\mathcal{B}(B^+ \to \tau^+\tau^-K^+)$
[75]	$4.4 \cdot 10^{-7}$	-
[79]	$3 \cdot 10^{-7}$	-
[80]	$(3.2 \pm 0.7) \cdot 10^{-7}$	$(1.77 \pm 0.40) \cdot 10^{-7}$
[82]	$(5.7^{+1.6}_{-1.0}) \cdot 10^{-7}$	$(1.3^{+0.3}_{-0.1}) \cdot 10^{-7}$
[84]	$5 \cdot 10^{-7}$	$1.3 \cdot 10^{-7}$
[86]	$(5.9 \pm 2.3) \cdot 10^{-7}$	-

Reference	$\mathcal{B}(B^0 \to e^+e^-K^{*0})$	$\mathcal{B}(B^0 \to \mu^+\mu^-K^{*0})$	$\mathcal{B}(B^0 \to \tau^+\tau^-K^{*0})$
[75]	$1.50 \cdot 10^{-6}$	$1.15 \cdot 10^{-6}$	-
[79]	$1 \cdot 10^{-6}$	$1 \cdot 10^{-6}$	-
[80]	-	$1.4 \cdot 10^{-6}$	$2.5 \cdot 10^{-8}$
[82]	$(2.3^{+7.3}_{-0.5}) \cdot 10^{-6}$	$(1.9^{+0.5}_{-0.2}) \cdot 10^{-6}$	$(1.9 \pm 0.3) \cdot 10^{-7}$
[84]	-	$1.4 \cdot 10^{-6}$	$2.2 \cdot 10^{-7}$
[86]	$(2.3 \pm 0.9) \cdot 10^{-6}$	$(1.5 \pm 0.6) \cdot 10^{-6}$	-

Table 4.2: *Standard Model branching fraction predictions for the exclusive decays* $B^+ \to l^+l^-K^+$ *and* $B^0 \to l^+l^-K^{*0}$.

	$\mathcal{B}(B^+ \to l^+l^-K^+)$	$\mathcal{B}(B^0 \to l^+l^-K^{*0})$
$l = e$	$< 1.1 \cdot 10^{-5}$ [87]	$< 1.4 \cdot 10^{-5}$ [87]
$l = \mu$	$< 5.2 \cdot 10^{-6}$ [88]	$< 4.0 \cdot 10^{-6}$ [88]
$l = \tau$	-	-

Table 4.3: *Experimental upper limits on the branching fraction for the exclusive decays* $B^+ \to l^+l^-K^+$ *and* $B^0 \to l^+l^-K^{*0}$ *(at 90 % C.L.).*

The decay $B_s^0 \to \mu^+\mu^-\phi$

Two different calculations of the $B_s^0 \to \phi$ form factors have been published. The first available calculation is based on the *Light Cone Sum Rule* (LCSR) model [81], and the second, more recent, is based on the *Constituent Quark Model* (CQM) model [83]. A comparison of the form factors at $q^2 = 0$ shows that the two calculations agree within the estimated accuracy of the models (15%) [83].

No numerical value of the expected branching fraction has been found in the literature. It can nevertheless be computed easily as it is given by the relation

$$\mathcal{B}(B_s^0 \to \mu^+\mu^-\phi) = \frac{\Gamma(B_s^0 \to \mu^+\mu^-\phi)}{\Gamma_{tot}(B_s^0)} = \Gamma(B_s^0 \to \mu^+\mu^-\phi) \cdot \tau(B_s^0) \,. \tag{4.10}$$

The partial width $\Gamma(B_s^0 \to \mu^+\mu^-\phi)$ due to the decay is obtained by performing a numerical integration of the differential partial width $\frac{d\Gamma}{d\hat{s}}$ (Equation 35 in Reference [75]) over $\hat{s}$. The results[4] for the two sets of form factors are shown in Table 4.4.

[4]For the B_s^0 mass and lifetime, the world-average values are used, $m(B_s^0) = 5369.3 \pm 2.0$ MeV/c^2 and $c\tau(B_s^0) = 1.54 \pm 0.07$ ps [1]. For $|V_{ts}|$, the value derived in Reference [75] ($|V_{ts}| = 0.038 \pm 0.005(exp)$) is used, which is consistent with the value derived in Section 4.7.1. Furthermore, $|V_{tb}| = 1$ is assumed.

Form Factors	$\Gamma(B_s^0 \to \mu^+\mu^-\phi)$ [GeV]	$\mathcal{B}(B_s^0 \to \mu^+\mu^-\phi)$
CQM	$(5.2 \pm 1.4) \cdot 10^{-19}$	$(1.21 \pm 0.32) \cdot 10^{-6}$
LCSR	$(4.6 \pm 1.2) \cdot 10^{-19}$	$(1.08 \pm 0.30) \cdot 10^{-6}$

Table 4.4: *Standard Model Partial width and branching fraction predictions for the exclusive decay $B_s^0 \to \mu^+\mu^-\phi$ for the two sets of form factors.*

The uncertainty on the partial width is due to the uncertainty on the CKM matrix element $|V_{ts}|$([5]). All other uncertainties are found to be negligible, and no uncertainties on the form factors have been included. The uncertainty on the lifetime (4.5%) is then added quadratically to yield the uncertainty on the branching fraction.

There has been no published result on the search for the decay $B_s^0 \to \mu^+\mu^-\phi$. This work presents the first search for this decay.

4.5. The decays $b \to s\nu\bar{\nu}$

These decays are theoretically the cleanest to calculate, as the only diagrams contributing to the decay are Z^0 penguins and box diagrams. Furthermore, contrary to the $B \to X_s l^+ l^-$ decay, there are nearly no long-distance contributions, as there are no intermediate states that can decay into a neutrino pair. By summing over the three neutrino flavours, the predicted branching fraction is $\mathcal{B}(b \to s\nu\bar{\nu}) = (3.8 \pm 0.8) \cdot 10^{-5}$ [89]. They are however among the most difficult to detect experimentally, the neutrinos escaping detection. The experimental signature of these decays is a large missing energy around the B meson, which is characteristic of a neutrino.

Only LEP experiments have searched for these decays, as, at the Z^0 peak, the final state multiplicity is low, the B hadrons are well separated and the energy of the $b\bar{b}$ system can be constrained to the Z^0 mass, thus allowing the measurement of the missing energy and its association with the B. It would be very difficult, if not impossible, to observe these decays at hadron colliders. In hadron collisions, the high track multiplicity would make it difficult to identify the B meson only from the remaining meson produced in the decay. Furthermore, the missing energy due to the neutrino pair is small compared to the missing energies typically observed, and would not be high enough to fire a dedicated missing energy trigger.

The ALEPH collaboration extracted, from their search for the leptonic decay $B^+ \to \tau^+\nu_\tau$ [90], an upper limit on the inclusive decay rate, $\mathcal{B}(b \to s\nu\bar{\nu}) < 7.7 \cdot 10^{-4}$ (at 90% C.L.) [91]. The DELPHI collaboration set upper limits on exclusive decays $\mathcal{B}(B^0 \to K^{*0}\nu\bar{\nu}) < 1.0 \cdot 10^{-3}$ and $\mathcal{B}(B_s^0 \to \phi\nu\bar{\nu}) < 5.4 \cdot 10^{-3}$ (at 90% C.L.) [92].

As this is theoretically the cleanest decay to calculate, the measurement of the branching fraction would permit a very good comparison with the Standard Model prediction. In addition, with the measurement of the decay rate of the CKM-suppressed decay $b \to d\nu\bar{\nu}$,

[5]The uncertainty on $|V_{ts}|$ quoted in Reference [75] ($\pm$13.2%) includes only the experimental uncertainty (from the CLEO measurement of $\mathcal{B}(B \to K^*\gamma)$) and no theoretical uncertainty. The uncertainty derived in Section 4.7.1, when not including the uncertainty on $|V_{tb}|$, is comparable to this value.

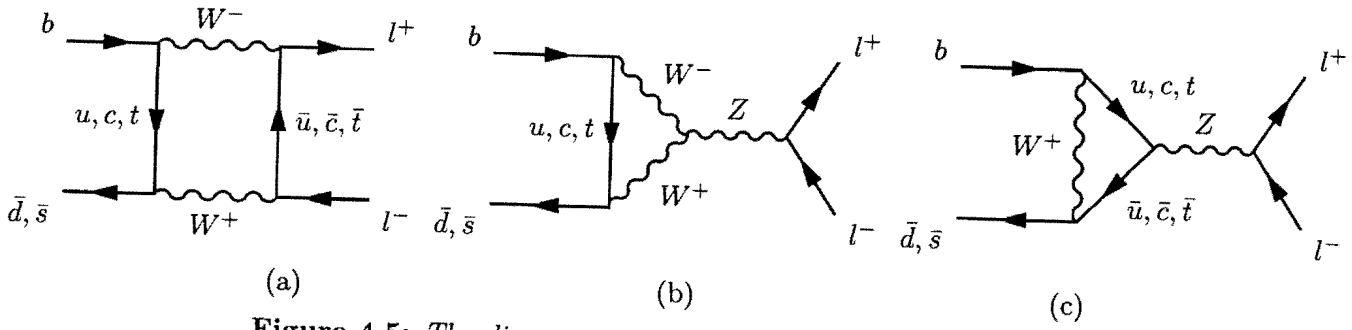

Figure 4.5: *The diagrams contributing to the decays* $B^0 \to l^+l^-$.

Standard Model contribute to the decay. As the predictions of the branching fractions are still uncertain, a result of the same order of magnitude would neither confirm the Standard Model calculations, nor rule out any additional contribution which predicts a comparable result. Nevertheless, several measurements and limits already provide constraints on new models.

The loop diagrams involved in FCNC processes are very sensitive to the mass of the internal virtual states, as the predominance of diagrams with a virtual *top* quark over diagrams with other quarks show. Loops featuring heavy particles from extensions to the Standard Model would make a significant contribution to the usual Standard Model diagrams and affect the result. These could be charged Higgs, SUSY particles or fourth generation quarks. In the same way as the large mass difference of the B^0 mass eigenstates points to a heavy *top* quark, the effects of heavy particles, which would still be outside of reach of accelerators, could be seen at these low energies.

4.7.1. The CKM matrix

As seen, several FCNC B decays provide access to the CKM matrix elements. The values of the matrix elements extracted from these decays can then be compared to the values measured in other processes, such as CP asymmetry, particle–anti-particle mixing, FCNC K decays or direct measurements in *top* quark decays. A discrepancy between the values obtained by the different methods would indicate that the Standard Model does not describe the relevant processes correctly.

In several Standard Model extensions, the CKM matrix may be very different from the Standard Model CKM matrix, either being extended, non-unitarian or have several phases in addition to the current one [100]. With either different CKM matrix elements or additional diagrams contributing to the processes mentioned above, the values measured may then not be the pure CKM matrix elements.

The measurement of the branching fraction of the inclusive decay $b \to s\gamma$ can already yield a direct measurement of $|V_{ts}|$. It is found by dividing the weighted average of the branching fractions measurements ($\mathcal{B}(b \to s\gamma) = (3.14 \pm 0.48) \cdot 10^{-4}$, c.f. Section 4.3) by the Standard Model prediction[6] [59], yielding

$$\left|\frac{V_{ts}^*}{V_{cb}}V_{tb}\right| = 0.927 \pm 0.041\ (th) \pm 0.071\ (exp)\ . \tag{4.16}$$

$$|V_{ts}| = 0.0376 \pm 0.0120 \,. \tag{4.19}$$

Similar values can be derived from the measurement of the branching fraction of the exclusive decays $B \to K^*\gamma$ (c.f. Footnotes 4 and 5 in Section 4.4.2). In the same way, $|V_{td}|$ could be measured in the $b \to d\gamma$ decays. This determination of the matrix elements is model-dependent, since it is assumed that the dominant contribution to the decays is given by a *top* quark loop, rather than processes beyond the Standard Model. These matrix elements would be very difficult to measure directly in *top* decays, since light-quark jets are very difficult to tag and samples of *top* quarks are (still) limited.

4.7.2. Beyond the Standard Model

Contributions from extensions to the Standard Model affect, sometimes dramatically, the branching fractions expected for several FCNC decays. In addition, these models will also affect CP asymmetries, FCNC K decays and particle–anti-article mixing. The observation of the inclusive decay $b \to s\gamma$ and of several related exclusive decays permits already to constrain several models, since the small difference between the measured and the predicted branching fraction does not permit to accommodate large effects from non-Standard Model processes.

In this respect, the leptonic decays $B^0 \to l^+l^-$ and $B^0 \to \nu\bar{\nu}$ are particularly interesting. Because of their low rates in the Standard Model, due to the strong helicity suppression, non-Standard Model processes could represent a significant, if not dominant, contribution. Many models indeed predict large increases of the decay rates. The decay $B^0 \to \nu\bar{\nu}$ is forbidden by helicity conservation for mass-less neutrinos, and, as the decay into charged leptons, would be suppressed by a factor m_ν^2 if the neutrino had a mass. However, with the present limits on the neutrino mass, the Standard Model rates would be insignificant. Furthermore, as massive neutrinos would induce mixing in the lepton sector (as is now the case only in the quark sector), lepton flavour violating decays (e.g. $B^0 \to e^\pm\mu^\mp$) would in principle be allowed.

The sometimes large uncertainties of the Standard Model predictions should always be kept in mind. For some choices of parameters, the predicted branching fraction would be close to the Standard Model predictions, or even within the quoted uncertainties. In this case, the measurement of a branching fraction close to either of the predictions would not permit to distinguish between the Standard Model and the tested model.

The Wilson coefficients

Effects of additional non-Standard Model diagrams would modify the Wilson coefficients, both their magnitude and sign and their q^2 behaviour. Measurements of the decay rates of rare B decays and, for both the inclusive and exclusive decays $B \to X_s l^+l^-$, of the muon-pair kinematic distribution, forward-backward asymmetry, τ polarization asymmetry and Dalitz plots, would permit to derive the values of the Wilson coefficients in a model-independent way. In turn, this would allow the disentanglement of the contributions of the different parameters of the tested model [102].

The decay $b \to s\gamma$ is only sensitive to the absolute values of C_7 and, to a lesser extent, of C_8, through the operator mixing induced by the renormalization. With the measurement of the inclusive $b \to s\gamma$ branching fraction, some constraints could already be placed on these coefficients [103], although large deviations of C_8 are still allowed. C_8 could be constrained by experimental bounds on gluonic decays $b \to sg$.

The decays $b \to sl^+l^-$ are sensitive to both the absolute value and the sign of C_7, C_9 and C_{10}, and the decays $B^0 \to l^+l^-$ and $b \to s\nu\bar{\nu}$ to C_{10}. References [102, 103] show the effect several models could have on the Wilson coefficients, and the bounds which could be placed on these coefficients in the near future.

Four fermion generation model

In this model, an additional generation of fermions, in all points similar to the already existing ones, would exist. It could be accommodated in the present Standard Model with minimal modifications, by requiring only an extension of the CKM matrix. This 4×4 matrix would be parametrized by six angles and three phases and the unitarity relations would yield a quadrangle instead of the present triangle. The present model-independent lower limits on the masses of the new quarks are $m(Z^0)/2$ for both the t' and b', which are the quarks of charge $+2/3$ and $-1/3$ respectively, with higher model-dependent limits. However, the mass limit imposed on the neutrino belonging to this generation by the LEP experiments ($m(\nu') > m(Z^0)/2$) renders this model somewhat implausible [1].

FCNC processes would receive an additional contribution involving internal t' quarks, which would affect both mixing and decay rates. The additional CKM phases would be a further source of CP violation, and affect CP asymmetries.

By adjusting the parameters of the model ($m(t')$ and the CKM elements) to reproduce the measured $b \to s\gamma$ branching fraction, the $b \to d\gamma$ branching fraction would be reduced by a factor four[8] [104]. The decays $B_d^0 \to l^+l^-$ would be enhanced by a factor eight, which is well above the uncertainties of the Standard Model predictions, with little change for the decays $B_s^0 \to l^+l^-$. The decays $b \to s\nu\bar{\nu}$ would be enhanced by approximately an order of magnitude, as well as the decays $b \to sl^+l^-$, albeit slightly less [105].

Z mediated FCNC model

In this model, an additional vector-singlet quark of charge $-1/3$ is introduced, with an isospin different than the usual quarks. FCNC could then be mediated by the Z^0 at tree level. The coupling between the down-type quarks would be described by three parameters, each of which could contain a phase generating CP violation.

Constraints on these couplings can already be imposed from the upper limit on $\mathcal{B}(B \to \mu^+\mu^- X)$ [106] and $\mathcal{B}(b \to s\nu\bar{\nu})$. By choosing the highest allowed values for the couplings, the rates of the decays $B \to X_s l^+l^-$ and $B \to X_d l^+l^-$ would be increased by one and two orders of magnitude respectively [104]. The rates of the decays $B_d^0 \to l^+l^-$ and $B_s^0 \to l^+l^-$ would be increased by a factor 20 and 300-400 respectively, and that of the decays $b \to s\nu\bar{\nu}$

[8]Increases or reductions are quoted with respect to the rates predicted in the Standard Model.

by an order of magnitude [105].

These increases would place the branching fraction for the inclusive decay $b \to sl^+l^-$ and several exclusive decays at their present experimental upper limits. With the upper limit of the branching fraction of the decay $B^0 \to \mu^+\mu^- K^{*0}$ only a factor three above the Standard Model predictions, such high values for the couplings would nevertheless be forbidden.

Multi-Higgs doublets models

Several models predict more than one Higgs doublets. In these models, charged Higgs bosons can be exchanged instead of the W in the loop diagrams. Two types of models exist. In the first model (Model I), the up- and down-type quarks receive their mass from the same Higgs doublet, while in the second (Model II), they receive their mass from different Higgs doublets [60].

In the first model, the rate of the inclusive decay $b \to s\gamma$ is reduced and in the second, the rate is increased. As such, the present measurement of a slightly lower branching fraction would be more compatible with the first model. The previous measurement of the branching fraction [107], which resulted in a still lower value[9], already placed a lower limit on the mass of the charged Higgs at $M_H > 490$ GeV for $\tan\beta = 2$.

In the allowed parameter space, the largest effect would be an increase of the $B^0 \to l^+l^-$ decay rate by approximately one order of magnitude [104]. Other FCNC decays would be much less affected, with only modest increases of the decay rates, of the order of a factor two to three for the decays $b \to sl^+l^-$. The effect on the forward-backward asymmetry would be large [108, 109, 105].

Anomalous gauge boson coupling models

In addition to the measurements performed at the Tevatron and LEP experiments, the measurement of the $b \to s\gamma$ decay rate constrains the contributions from anomalous gauge boson couplings.

From the measured $b \to s\gamma$ decay rate, the parameter describing the anomalous $WW\gamma$ coupling, $\Delta\kappa_\gamma$, is constrained to lie within 0.20 units of the Standard Model value of 0 [110]. This rules out the pure $U(1)$ theory, in which the weak and electromagnetic neutral bosons do not mix [60].

With these bounds, the largest variation of the $B \to X_s l^+l^-$ decay rate would be of the order of 20% [110]. A larger effect could be seen for anomalous $W^+W^-Z^0$ couplings, which could induce variations of the branching fraction between +250% and −60% and raise the $b \to s\nu\bar{\nu}$ decay rate by an order of magnitude [105].

Here as well, the effect on the forward-backward asymmetry would be large, and the contributions of the different parameters could be disentangled by the measurements of the different observables, as presented above.

[9] $\mathcal{B}(b \to s\gamma) = (2.32 \pm 0.57 \pm 0.35) \cdot 10^{-4}$ [107]

Supersymmetric models

With several different supersymmetric (SUSY) models, each with a large number of new parameters, the effects on FCNC processes are quite diverse, and several of these models can accommodate the present measurement of $\mathcal{B}(b \to s\gamma)$. An overview of the effect of SUSY models on FCNC processes is given in Reference [111].

References [103, 111] show that the measurement of $\mathcal{B}(b \to s\gamma)$ nevertheless allows the constrait of the parameter space of several SUSY models, although not in a simple way. Within these bounds, the $B \to X_s l^+ l^-$ decay rates could show variations between 12% and 300%, depending on the model considered.

References [103, 112] point out that in the minimal supersymmetric extension of the Standard Model (MSSM), large values of $\tan\beta$([10]) are compatible with the observed $b \to s\gamma$ decay rate. Since a chargino-stop loop could destructively interfere with the charged Higgs, the sensitivity of this branching fraction to the mass of the charged Higgs is diminished, and the limit quoted above does not apply to the MSSM charged Higgs. At large $\tan\beta$, the branching fraction of the decays $B \to X_s l^+ l^-$ would be increased by a factor two. More interestingly, the $B_s^0 \to l^+ l^-$ decay rate could be as high as 10^{-6} [112], which would place this decay within reach of the present experiments.

The largest effects on the decays $B \to X_s l^+ l^-$ and $b \to s\nu\bar{\nu}$ would occur at small $\tan\beta$, but the decay $b \to s\gamma$ would be affected as well, with decay rates beyond the measured values. Only a precise fine-tuning of the many MSSM parameters would allow the keep the $b \to s\gamma$ decay rate unchanged while allowing large variations of the former two [105].

[10] $\tan\beta$ is the ratio of the vacuum expectation values of the two neutral Higgs fields, as the MSSM has two Higgs doublets.

Part II

The Experimental Setup

Chapter 5

The Tevatron

The Tevatron at the 'Fermi National Accelerator Laboratory' (Fermilab) in Batavia, Illinois, USA, is a proton–anti-proton collider. With a centre of mass energy $\sqrt{s} = 1.8$ TeV during the last run, it is the collider that provides the highest centre of mass energy, and will remain so until the advent of the Large Hadron Collider (LHC) at CERN.

After introducing the concept of Luminosity, the accelerator complex needed to accelerate the protons and anti-protons to reach such a high energy will be described, with a description of the upgrades being made for Run 2.

5.1. The luminosity

In high energy collisions, the *instantaneous luminosity* $\mathcal{L}$ is defined as the interaction rate per unit cross section of the colliding beams (collisions/(cm^2 · s)). When studying a given process, the number of interactions per second (N) would consequently be given by

$$N = \sigma \cdot \mathcal{L} \,, \tag{5.1}$$

where σ is the cross section of the process (in units of cm^2).

This instantaneous luminosity is given by

$$\mathcal{L} = \frac{f B N_p N_{\bar{p}}}{2\pi(\sigma_p^2 + \sigma_{\bar{p}}^2)} F(\sigma_l, \beta^*) \,, \tag{5.2}$$

where f is the revolution frequency, B the number of bunches in each beam, N_p ($N_{\bar{p}}$) the number of protons (anti-protons) in a bunch, σ_p ($\sigma_{\bar{p}}$) the r.m.s. of the radius of the proton (anti-proton) beam at the interaction point, and F a form factor which depends on the bunch length (σ_l) and the amplitude function at the interaction point (β^*). The beta function is a measure of the beam width and its evolution around the accelerator.

The first collision at the Tevatron took place in October 1985 and the first physics data-taking period, called Run 0, between 1988 and 1989. The Run 1 data-taking period, on which this study is based, can be subdivided in two periods. The first, called Run 1A, took place in 1992, and the second, called Run 1B, took place between 1994 and 1996. The

		Run 0	Run 1A	Run 1B	Run 2
f	kHz	47.7	47.7	47.7	47.7
Bunches		6	6	6	36 – 108
N_p		$1.0 \cdot 10^{11}$	$1.2 \cdot 10^{11}$	$2.3 \cdot 10^{11}$	$2.7 \cdot 10^{11}$
$N_{\bar{p}}$		$7 \cdot 10^{9}$	$0.3 \cdot 10^{11}$	$0.6 \cdot 10^{11}$	$0.3 \cdot 10^{11}$
$\sigma_p, \sigma_{\bar{p}}$	μm	~ 40	~ 40	~ 40	34/ 29
σ_l	cm	50	60	60	38
β^*	cm	50	35	35	35
$F(\sigma_l, \beta^*)$			0.65	0.65	0.72
$\mathcal{L}$	$\mathrm{cm^{-2}s^{-1}}$	$2 \cdot 10^{30}$	$0.54 \cdot 10^{31}$	$1.6 \cdot 10^{31}$	$8.6 \cdot 10^{31} - 2 \cdot 10^{32}$
$\int \mathcal{L}dt$	pb−1	~ 4.5	~ 30	~ 126	~ 2000

Table 5.1: *Run 0, Run 1 and expected Run 2 Tevatron operating parameters [1, 113, 114, 115].*

typical values for the parameters of Equation 5.2 for the different data-taking periods are given in Table 5.1.

During Run 1A, the typical luminosity was of $0.54 \cdot 10^{31}$ $\mathrm{cm^{-2}s^{-1}}$, with a peak luminosity of $1.0 \cdot 10^{31}$ $\mathrm{cm^{-2}s^{-1}}$. The upgrades made to the accelerator complex between Run 1A and Run 1B permitted to more than double the instantaneous luminosity for Run 1B. The typical luminosity was then of $1.6 \cdot 10^{31}$ $\mathrm{cm^{-2}s^{-1}}$, with a peak luminosity of $2.8 \cdot 10^{31}$ $\mathrm{cm^{-2}s^{-1}}$.

Cross sections are usually given in units of *barn*, corresponding to 10^{-24} $\mathrm{cm^2}$. The integrated luminosity ($\int \mathcal{L}dt$) is then given in $\mathrm{barn^{-1}}$. The total integrated luminosity seen at the CDF interaction region in Run 1A was about 30 $\mathrm{pb^{-1}}$ ($1\ \mathrm{pb^{-1}} = 10^{36}\ \mathrm{cm^{-2}}$) and in Run 1B 126 $\mathrm{pb^{-1}}$. The integrated luminosity recorded by the CDF detector is lower due to inefficiencies of the data acquisition system.

5.2. The Tevatron in Run 1

To reach a beam energy of 900 GeV, several accelerators are needed. Figure 5.1 shows the Fermilab accelerator complex as it was during Run 1 [114].

The first step is collectively called the 'Preaccelerator', where negatively charged hydrogen ions (H^-) are accelerated up to an energy of 750 keV. Gaseous hydrogen molecules (H_2) are transformed into hydrogen ions in a magnetron surface-plasma source. This is an oval-shaped cathode surrounded by an anode, distant about 1 mm, with a constant magnetic field. The ions are produced at the cathode and extracted through an aperture in the anode, and accelerated to an energy of 18 keV. These are then accelerated to 750 keV in a five-stage Cockroft-Walton generator.

Next, a two-staged 150 m linear accelerator, the Linac, accelerates the ions up to an energy of 200 MeV in Run 1A and 400 MeV in Run 1B. The Linac is composed of electrically-resonant cylindrical high-conductivity copper clad steel tanks, each composed of a line of drift tubes between which the ions are accelerated by the RF field. The upgrade undertaken on the second stage of the Linac between Run 1A and Run 1B raised the energy from

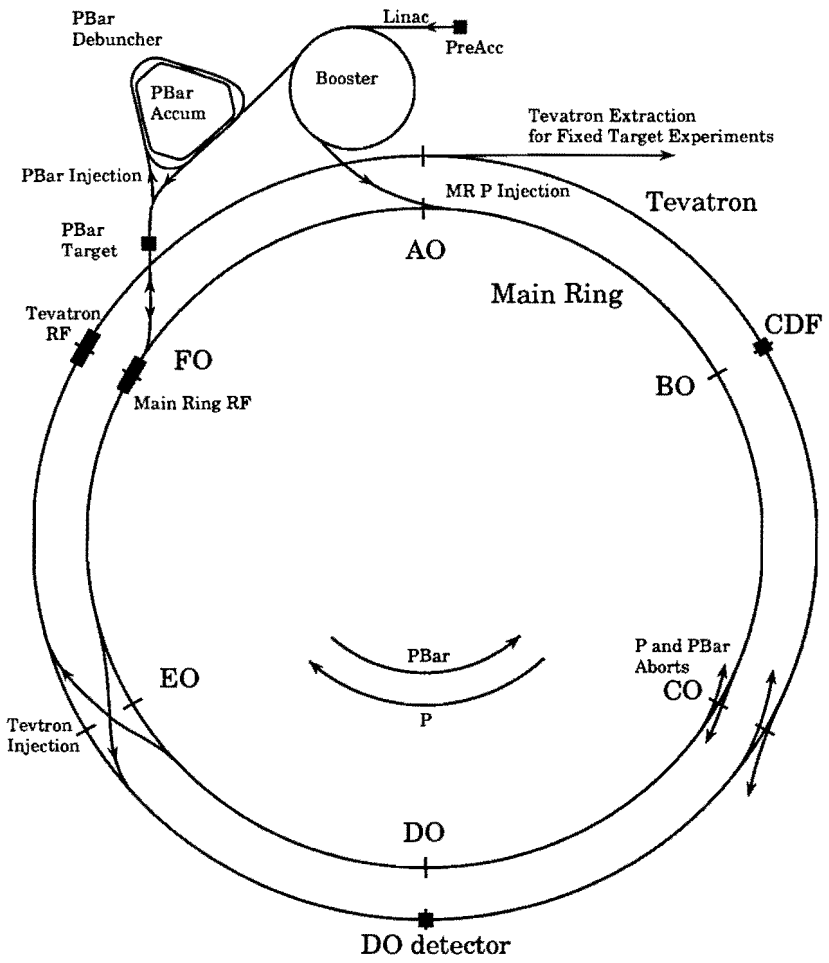

Figure 5.1: *Schematic diagram of the Fermilab accelerator complex (the diagram is not drawn to scale).*

200 MeV to 400 MeV and improved the transfer efficiency to the next stage.

From the Linac, the ions are transferred to the Booster, an 8 GeV alternating gradient proton synchrotron with a radius of 75.5 m. This accelerator is composed of 96 combined function dipole/quadrupole magnets and 17 cavity resonators. Before entering the Booster, the ions are merged with any proton remaining in the Booster, and both are passed through a carbon foil to remove the electrons from the ions.

The 8 GeV protons are then injected into the Main Ring. The Main Ring is a 400 GeV 1 km radius synchrotron, composed of 774 dipole and 240 quadrupole magnets and 18 RF accelerating cavities. Initially conceived to accelerate protons to 400 GeV for fixed-target experiments, it is used in this context both to accelerate the protons used to create the anti-protons and accelerate the protons and anti-protons before injecting them into the Tevatron.

For protons used in the collisions, the Main Ring will coalesce 15 8 GeV bunches from the

Booster into one bunch, and accelerate it to 150 GeV before injecting it into the Tevatron.

The Tevatron is a 1 km radius synchrotron located in the same tunnel as the Main Ring, only 65 cm below the latter. It is used both for proton–anti-proton collisions with a centre of mass energy of 1.8 TeV and to accelerate protons to an energy of 800 GeV for fixed target experiments. It is composed of 774 dipole and 240 quadrupole superconducting magnets, operating at a temperature of 4.6 K, and 8 RF accelerating cavities. The quadrupole magnets are used to focus the beam, with so-called 'low-beta quadrupoles' used next to the interaction regions (see also Figure 6.1) to reduce the beam spot-size to less than 40 μm. Out of the interaction regions, electrostatic separators keep the proton and anti-proton beams in different helical orbits to minimize the beam-beam interaction rate.

Anti-protons are produced in an inelastic collision of 120 GeV proton beams, accelerated in the Main Ring, with a Nickel target. This process produces about one anti-proton per 10^5 collisions. The produced particles are focused by a liquid lithium lens with an azimuthal magnetic field (produced by a pulsed current) and 8 GeV anti-protons are selected. These are then directed to the Debuncher, a rounded triangular-shaped synchrotron with a mean radius of 90 m. The Debuncher reduces the momentum spread of the beam by adiabatic debunching and RF bunch rotation, and the transverse profile by stochastic cooling.

The anti-protons are then stored in the Accumulator, a roughly triangular-shaped synchrotron with a mean radius of 75 m, concentric to the Debuncher, and maintained at 8 GeV until they are needed for collisions. The anti-protons are produced continuously during a collider store, and several hours (typically 10 to 12) are needed to produce enough anti-protons for one store.

After the 150 GeV proton bunches have been injected into the Tevatron, anti-protons are transferred to the Main Ring and accelerated to 150 GeV. They are then injected into the Tevatron, counter-clockwise to the protons, and both the proton and the anti-proton beams are accelerated to an energy of 900 GeV.

In the collision mode, six bunches of protons and anti-protons are collided in two luminous regions, called B0 (where the CDF detector is located) and D0 (where the D0 detector is located), with 3.5 μs between two bunch crossings. In these regions, the Main Ring is raised with respect to the Tevatron to permit to place a detector around the interaction point. This enables the Main Ring to be used during collision runs to accelerate the protons used in the anti-proton production (called Pbar stacking). While at B0, the Main Ring passes well above the CDF detector, this separation is not sufficient at D0, where the Main Ring has to pass through the detector.

The beams are usually kept in the collider for 10 to 12 hours (called a store), after which the instantaneous luminosity has decreased by an order of magnitude, due to collisions both at and outside the interaction regions (beam-beam interactions) and transverse spreading of the beam. The typical downtime between two stores is around two hours.

5.3. The Tevatron in Run 2

The initial goal for Run 2 is to achieve a typical instantaneous luminosity of the order of $5 \cdot 10^{31}$ cm^{-2}s^{-1}, with a peak of $2 \cdot 10^{32}$ cm^{-2}s^{-1}, and an integrated luminosity of 2 fb^{-1} over

two years. With some further improvements, an instantaneous luminosity of $1 \cdot 10^{33}$ cm^{-2}s^{-1} is thought to be achievable in the long term, and an integrated luminosity of up to 20 fb^{-1} remains possible before the start of LHC. Furthermore, the centre of mass energy will be raised to 2 TeV. This increase of energy would raise the $t\bar{t}$ production cross section by 40%.

To reach this high luminosity, several upgrades to the accelerator complex are underway [115]. The main changes are the construction of two new accelerators, the Main Injector, which would replace the Main Ring and the Recycler, both located in the same tunnel. The removal of the Main Ring will reduce the background on the collider experiments due to its use to accelerate the protons needed for the anti-proton production during collider operation.

The Main Injector is a 150 GeV 3.3 Km-long elliptical synchrotron which will take over all duties of the Main Ring. The performances of the Main Injector will be much higher than those of the Main Ring, both in terms of protons delivered per cycle, and in terms of acceptance and transmission efficiencies. The anti-proton transfer efficiency and acceleration will also be improved, lowering the losses of anti-protons. In addition, the Main Injector will also be capable of providing 120 GeV proton beams to the fixed target experimental areas during collider operations, which was not possible with the Main Ring.

The main limitation on the luminosity is the low yield of the anti-proton production, resulting in anti-proton beams of low intensity. The higher intensity of the primary proton beam and its faster repetition rate, due to the increased capability of the Main Injector, will permit to reach higher stacking rates, and improvements in the Debuncher and Accumulator will permit to increase the number of anti-protons cooled and stored.

A further synchrotron is added to the anti-proton complex, the Recycler [116]. This will permit, in combination with the Accumulator, to further increase the number of anti-protons stacked. Furthermore, the Recycler will be able to recover the unused anti-protons remaining in the beam at the end of a store, to reuse them in the next store. It is estimated that as much as 75% of the initial anti-protons are still present in the beam at the end of a store, of which 50% are expected to be recycled. All these improvements will result in the increase in the total number of anti-protons in a beam from $3.3 \cdot 10^{11}$ to $1.1 \cdot 10^{12}$.

The increase of the available number of protons and anti-protons for each beam would raise the number of simultaneous interactions per bunch crossing beyond the capability of the experiments, causing pile-up, high channel-occupancy and high trigger rates. To maintain the number of interactions per bunch crossing between one and two, the number of bunches per beam has been raised to 36, reducing the particle density per bunch. The time between two bunch crossings is thus 396 ns.

Many of these upgrades are already in place. The Main Injector commissioning run was successfully completed in April 2000. The Tevatron engineering run is expected to begin in August 2000, but the Recycler will first not be used. Run 2 is expected to begin in March 2001.

Chapter 6

The CDF experiment

The Collider Detector at Fermilab (the CDF detector) is the first of the two detectors built to study high-energy proton–anti-proton collisions at the Tevatron. While its original purpose was the study of high transverse momentum phenomena ($W^{\pm}$ and Z^0 boson properties, discovery of the top quark, search for phenomena beyond the Standard Model), it also proved to be very successful in the field of B-physics.

It is a general-purpose detector with a cylindrical and forward-backward symmetry, designed for a maximum solid angle coverage. An isometric view of the CDF detector in Run 1 is shown in Figure 6.1 and a cross-section of one quarter of the detector is shown in Figure 6.2.

6.1. The CDF coordinate system

CDF uses a right-handed coordinate system (as illustrated in Figure 6.2), with the origin at the centre of the detector, which is also the nominal $p\bar{p}$ interaction point. The z-axis is pointing along the proton beam-line (the protons circling clockwise in the Tevatron), the y-axis is pointing upwards and the x-axis is pointing radially outwards in the horizontal plane of the Tevatron.

The spherical coordinate system is usually preferred with the polar angle θ measured with respect to the proton direction, the azimuthal angle ϕ measured anti-clockwise from the positive x-axis in the horizontal plane of the Tevatron and the radial distance r measured from the centre of the beam-line.

A more natural unit of measurement in collider physics is the *rapidity*, y, defined as

$$y = \frac{1}{2} \ln \left(\frac{E + p_z}{E - p_z} \right) = \tanh^{-1} \left(\frac{p_z}{E} \right) \tag{6.1}$$

since, when viewed in the laboratory frame, a Lorentz transformation along the z-axis to an inertial frame with velocity β transforms the rapidity as $y \rightarrow y + \tanh^{-1} \beta$. The shape of the particle density distribution in rapidity, dN/dy, is thus invariant under Lorentz transformation.

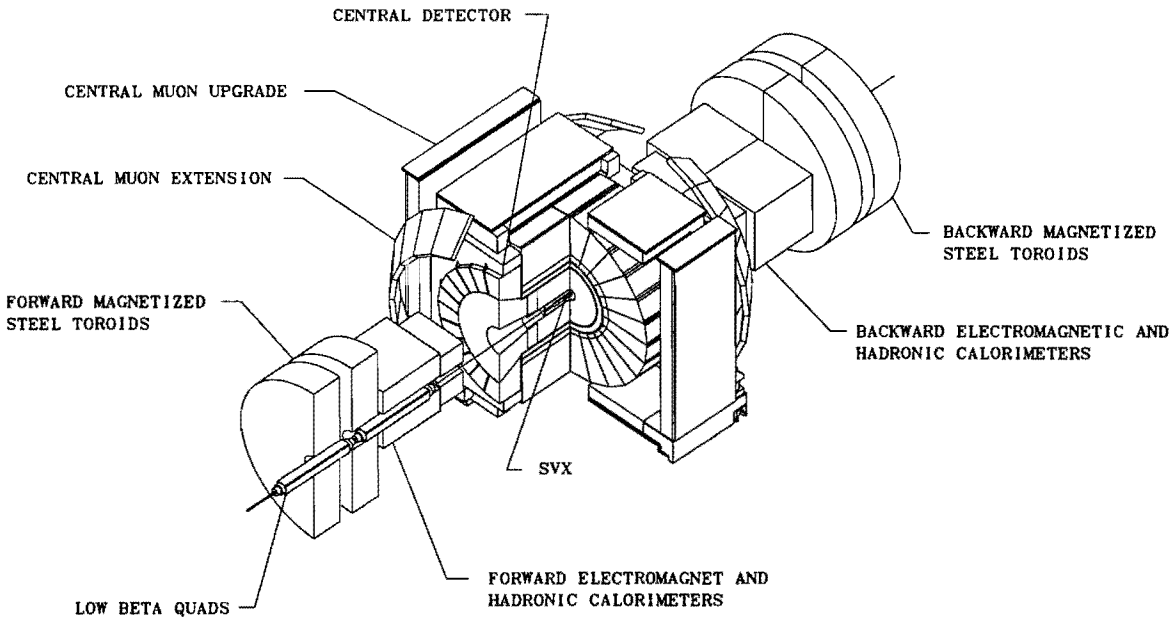

Figure 6.1: *Isometric view of the Run 1 configuration of the CDF detector.*

For highly relativistic particles, where $p \gg mc$, which is the case at CDF, the rapidity is approximately equal to the *pseudorapidity*, η, defined as

$$\eta = -\ln \tan\left(\frac{\theta}{2}\right) \tag{6.2}$$

Because of its simple relation with the polar angle and its independence of the particle type, this is the unit normally used at CDF.

In hadron collisions, such as the ones taking place at the Tevatron, interactions occur between the partons forming the hadrons. Interactions with a high momentum transfer generate particles with a high momentum transverse to the beam-line. This *transverse momentum*, p_T, is, with the *transverse energy*, E_T, defined as

$$p_T = p \times \sin\theta = \sqrt{p_x^2 + p_y^2} \tag{6.3}$$

$$E_T = E \times \sin\theta \tag{6.4}$$

At high energy, the transverse energy is approximately equal to $E_T \simeq c \cdot p_T$. At CDF, the transverse momentum is used when measuring a track momentum in the tracking system, and the transverse energy when measuring the energy deposited by a particle in the calorimeters.

Along with the high-momentum-transfer interactions, the spectator quarks will also interact and hadronize, resulting in low-p_T jets. Genuine low-momentum interactions, called *minimum bias events*, will also have a low-p_T, with $\langle p_T \rangle \simeq 0.5$ GeV/c. In both cases, most of the energy is directed longitudinally along the beam-pipe, and will not be measured by the detector. While the total momentum in a collision as measured by the detector is not

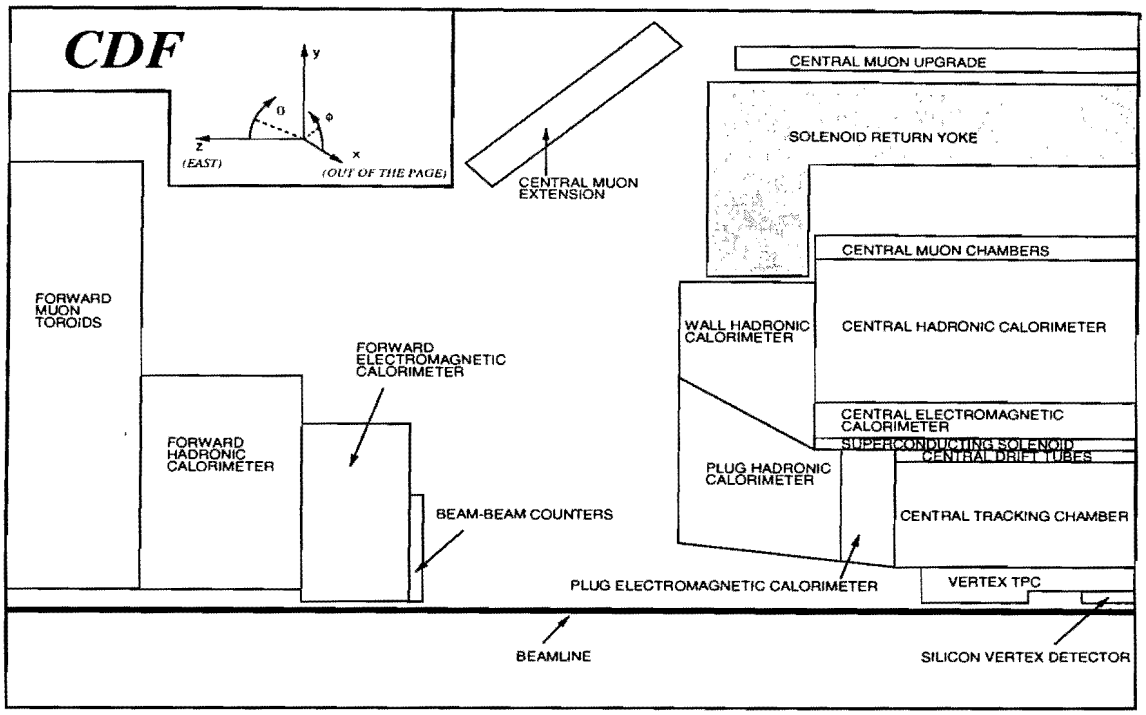

Figure 6.2: *Cross-section of one quadrant of the Run 1 configuration of the CDF detector. The interaction point is located at the lower-right corner.*

expected to balance, the transverse momentum, mostly carried by the particles originating in the high-momentum transfer interactions, should be balanced. The imbalance of the transverse energy, termed *missing energy*, is mostly due to non-interacting particles, such as neutrinos, or minimum ionizing particles. This imbalance may also be caused by detector inefficiencies and particles passing through uninstrumented regions (called *cracks*). A good coverage (hermeticity) of the calorimeters is thus essential.

6.2. An overview of the experiment

To study interactions with a high momentum transfer and identify the individual processes taking place, the momentum, energy, vertex and identity of the particles produced have to be measured over the largest possible solid angle.

The CDF detector can be subdivided into several subsystems [117], each with a particular task and employing different detection techniques. Three regions can be identified in η, the central region ($|\eta| < 1.1$) the end-plug region ($1.1 < |\eta| < 2.4$) and the forward region ($2.2 < |\eta| < 4.2$). With the nominal interaction point at the centre of the detector, the different subsystems are layered around the interaction point.

In the central region, the tracking systems, designed to measure the track parameters and vertices of charged particles, are the closest to the interaction point. These systems are located inside a superconducting solenoid magnet producing a 1.412 T field. Closest

to the beam-pipe, the Silicon Vertex Detector (SVX), a four-layered silicon microstrip detector, permits a precise measurement of primary and eventual secondary vertices. Around the SVX, the vertex drift chamber (VTX) will locate the primary vertex and the Central Tracking Chamber (CTC), a cylindrical drift chamber, will measure the track parameters.

Around the tracking systems, calorimeters provide a measurement of the energy of both charged and neutral particles (except neutrinos of course) in all three regions. An electromagnetic calorimeter measures the energy of electrons and photons, followed by a hadronic calorimeter measuring the energy of hadrons.

In the central and the forward regions, muons are identified by further tracking chambers located outside of the calorimeters, as they will not be absorbed by the calorimeters.

The luminosity is measured by the beam-beam counters (BBC), two planes of scintillation counters located on the front of each of the two forward calorimeters.

These systems will be described in more detail below. Since in this analysis we rely on measurements made in the tracking systems and in the central region muon chambers, emphasis will be put on the these systems.

6.3. The tracking systems

The task of the tracking systems, all located in the central region, is a precise determination of track parameters, momenta and vertices of both isolated tracks and tracks contained in jets. Also, the interaction vertex should be determined and secondary decay vertices of eventual long-lived particles identified.

As the momentum and charge of charged particles is measured through their curvature in a magnetic field, the tracking systems are surrounded by a 1.5 m radius, 4.8 m long superconducting solenoidal coil producing a 1.412 T solenoidal magnetic field oriented along the incident beam direction [118]. In the tracking region ($|z| < 150$ cm), the field is constant within 0.1%. The thickness of the solenoid is 0.85 radiation length (X_0) at normal incidence.

In order to minimize secondary interactions and multiple scattering, which would downgrade the measurements, the amount of material composing these systems has been kept as low as possible. Before reaching the detector, particles have to traverse a 2 mm thick beryllium beam-pipe with an inner radius of 1.9 cm.

The main tracking device at CDF is the CTC. Tracks are first found in the $r - \phi$ plane using the hits recorded in the axial superlayers. To reconstruct the track in three dimensions, the z coordinate of the track has to be measured in the VTX. Only once the track has been reconstructed in three dimensions in the CTC, can it be extrapolated to the SVX to search for matching hits. If hits are found in the SVX, the track parameters are recalculated, with a higher precision than the original parameters.

As the position resolution of the SVX is significantly better than that of the CTC, the impact parameter and azimuth of a track is essentially determined by the SVX. The SVX measurements also increase the momentum resolution, as the inclusion of the SVX hits to the CTC hits increases the lever arm.

The minimum p_T for a track found by the pattern recognition algorithms is 250 MeV/c,

	SVX	SVX'
Channels	46080	46080
Power	DC	AC, FOXFET Bias
Passivation	none	silox
Atmosphere	argon/ethane + alcohol	dry nitrogen
Readout Chip	SVX IC Rev. D	SVX IC Rev. H3
Sampling	quadruple	double
Noise	2200 electrons	1300 electrons
Gain	15 mV/fC	21 mV/fC
Signal/Noise:		
Begin of Run	9	16
End of Run	6.5	8
Reset/integrate time	3.5 μs	3.5 μs
readout time	2.7 μs	2.1 μs
Radiation limit	15-20 kRad	> 1 MRad
Bad Channels	1.59%	1.73%
Typical occupancy	7-10%	5%
Maximum occupancy	12-20%	25%

Table 6.1: *Main parameters of the SVX and the SVX' detectors.*

	Radius [cm]	Crystal Width [μm]	Active Width [μm]	Readout strips	η coverage	ϕ overlap
Layer 0 (SVX)	3.005	16040	15360	256	± 2.9	$-1.26°$ (gap)
Layer 0 (SVX')	2.861	16040	15360	256	± 2.9	0.17°
Layer 1	4.256	23720	23040	384	± 2.5	0.32°
Layer 2	5.678	31400	30720	512	± 2.2	0.30°
Layer 3	7.866	42930	42240	768	± 1.9	0.04°

Table 6.2: *Main dimensions of the silicon detectors.*

as tracks are requested to exit the CTC through the outer radius.

6.3.1. The Silicon Vertex Detector

The Silicon Vertex Detector (SVX) [119] is a silicon microstrip detector designed to precisely measure track coordinates in the $r-\phi$ plane and reconstruct the decay vertices of the long-lived b and c hadrons. The first detector was installed in 1992 for Run 1A, and was the first such detector successfully operating in a hadron collider. Due to degradation from radiation damage, it was replaced for Run 1B by the more resistant SVX' (*SVX prime*) [120]. Both detectors are very similar, and the description following applies to both, unless otherwise noted. The main parameters of both detectors are summarised in Table 6.1.

The SVX consists of two independent cylindrical modules (barrels), one of which is shown in Figure 6.3. They are placed end-to-end, separated by a gap of 2.15 cm at the centre of the detector, at $z = 0$. The total active length in z is 51 cm. As, due to

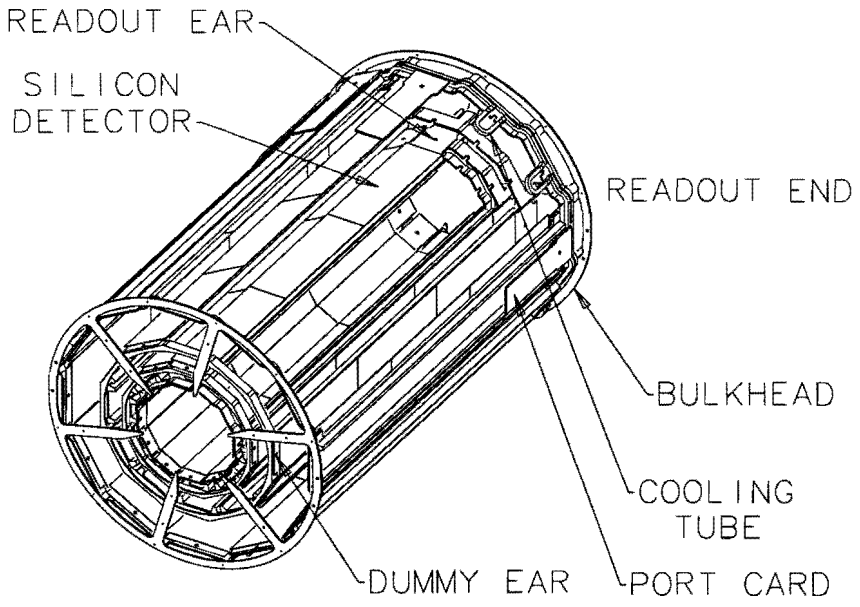

Figure 6.3: *Isometric view of one of the two SVX barrels.*

the longitudinal size of the proton and anti-proton bunches, the z distribution of the $p\bar{p}$ interaction vertices follows a Gaussian distribution centred at $z = 0$ with a r.m.s. width of $\sigma = 30$ cm, about 60% of the $p\bar{p}$ interactions are in the acceptance region of the SVX.

Each barrel consists of four concentric cylindrical layers (numbered 0 to 3 in increasing radius). To obtain the best impact parameter resolution, the inner layer has to be as close as possible to the interaction vertex. The inner layer is, for the SVX, at a radius of 3.005 cm and, for the SVX', at a radius of 2.861 cm. The outer layer is positioned as close as possible to the outer tracker to increase the lever arm and permit for a good matching between the two systems. The outer radius is in both cases 7.866 cm.

The four layers of each barrel are segmented in twelve modules (called *ladders*) oriented parallel to the beam axis, subtending 30° in ϕ. On each ladder (Figure 6.4), three single-sided 8.5 cm long silicon microstrip detectors are wire-bonded together, forming a 25.5 cm active silicon region. The length is limited by the increased input capacitance and leakage current of the detectors. The ladder substrates are fabricated from a light-weight foam (Rohacell) and reinforced with carbon-fibre strips. At the outer extremity of each ladder, a ceramic readout hybrid circuit board (ear card) holds the readout chips, which are wire-bonded to the detectors.

The ladders are of increasing width from the inner to the outer layer, and each ladder is rotated by 3° about its major axis on its position on the face of the barrels, to permit for a complete coverage in ϕ and allow for some overlap between adjacent ladders. The innermost layer (layer 0) of the SVX is the only layer where a complete coverage in ϕ was not possible, leaving a 1.26° gap between each ladder. The geometry of this layer has been significantly changed for the SVX' to permit a complete coverage. The inner layer has been brought

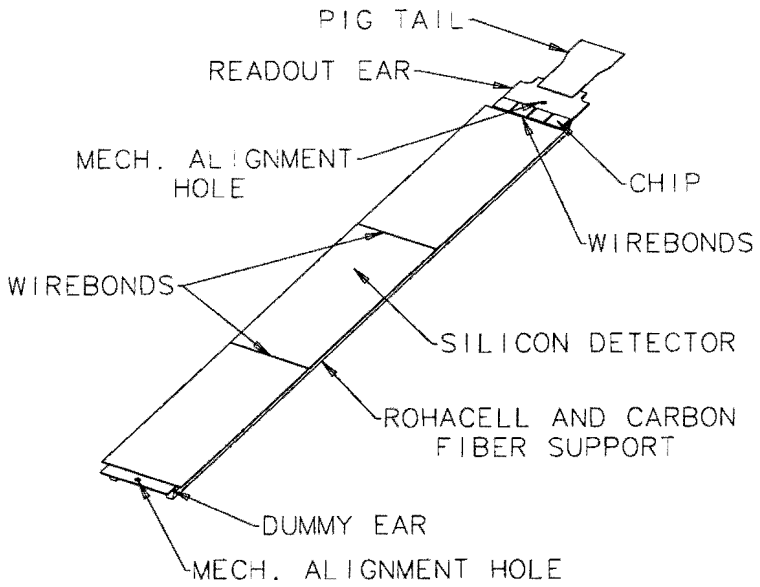

Figure 6.4: *Schematic drawing of a SVX ladder.*

approximately 1.5 mm closer to the beam-line, to a radius of 2.86 cm, and a 1° rotation of each ladder allows an overlap of 0.17° between adjacent ladders. The characteristics of each layer for both detectors are given in Table 6.2.

The SVX uses DC coupled silicon detectors [121], while the SVX' uses AC-coupled FOXFET[1] biased silicon detectors [122]. Each detector is 300 μm thick, and the strip pitch is 60 μm for layers 0, 1 and 2, and 55 μm for layer 3.

The readout chips feature 128 readout channels permitting an unbiased threshold comparison for each channel, with charge integration, sample and hold and voltage amplification functions. Comparator/latch and priority encoding circuits allow the multiplexed analog readout to select only the channels above threshold (sparse mode). This reduces both the readout time and the data size, which will be proportional to the occupancy. Typical values for the occupancy were between 7% and 10%, with peak values around 25%.

The SVX readout chip (SVX IC revision D, or SVXD) is made in a radiation soft 3 μm CMOS technology. With a DC-coupled detector, the readout chip has to operate in a *quadruple sample and hold* mode, as the baseline shift due to strip-to-strip leakage current variations, which will be integrated during the sampling time, has to be subtracted. In this mode, an on-beam and an off-beam charge integration are subtracted, and the signal is given by an on-beam charge excess.

The SVX' readout chip (SVX IC revision H, or SVXH3) is made in a radiation hard 1.2 μm CMOS technology. With an AC-coupled detector, the leakage current does not appear at the preamplifier, and only one (on-beam) charge integration is needed to de-

[1]Field oxide field-effect transistor

termine the signal. This mode is called *double sample and hold.* As only one integration is performed, the noise is reduced by a factor $\sqrt{2}$ compared to the SVXD, resulting in a significantly higher Signal-to-Noise (S/N) ratio. The absence of leakage current at the preamplifier has the further advantage that the latter will not be saturated when leakage currents increase due to radiation damages. This increase will nevertheless be seen as shot noise.

Being so close to the beams, the SVX is exposed to a high level of radiation. During Run 1A, the SVX received about 15 krad of radiation. This caused bulk damage in the silicon detector, resulting in increased leakage current, and to the radiation soft SVXD chips, which showed a marked decrease in gain at the end of the run.

To minimize leakage currents in the silicon detectors and prevent damage to the front-end electronics, the detectors are maintained at an operating temperature of 20° C. This is achieved by cooling the readout electronics (generating about 50 W of heat) with 13° C de-ionized water and the detectors with a flow of chilled gas. This also ensures the mechanical stability of the support structure, as thermal variations are reduced.

The hit efficiencies (the probability for a reconstructed track to leave a hit in a particular layer) are affected by S/N ratio, pedestal, clustering, pattern recognition, bad regions and geometrical acceptance. The inefficiencies are mainly due to bonding gaps between the silicon crystals (1.7% for the SVX') and dead strips (1.7% for the SVX'). The geometric acceptance affects mostly the inner and outer layers due to the gap at $z = 0$ and the edges of the detector. For the SVX, layer 0 is furthermore affected by the incomplete ϕ coverage. The efficiencies measured at the beginning of the run, are, from the inner to the outer layer, 92.01%, 96.8%, 96.9% and 95% for the SVX'. For the SVX, these were of 93% for layer 0, 1 and 2 and 91% for layer 3. The values measured at the end of the run were approximately 4% lower due to radiation damage.

Once the track has been reconstructed in the CTC and extrapolated to the SVX, the subsequent track finding efficiency was about 98% for the SVX, and slightly higher for the SVX'. At the beginning of the run, 70% of the tracks could be reconstructed with four hits and 23% with 3 hits. This decreased to 60% and 30% respectively at the end of the run, without affecting the overall track finding efficiency.

After alignment, both mechanical during construction and subsequently using high-p_T CTC tracks, the maximum misalignments were measured to be less than 10 μm. The global misalignment of the SVX with respect to the CTC is approximately 40 μm, which has no significant effect on position or impact parameter resolutions. The average position resolution for a fitted track is 13 μm for the SVX and 11.6 μm for the SVX'. The impact parameter resolution is $(16 + 40/p_T)$ μm, where the p_T of the track is measured in GeV/c. By fitting all the tracks seen in an event, the primary vertex position is measured with a resolution of 40 μm in the $x - y$ plane. This resolution is dominated by the size of the beam spot, which is of this order.

6.3.2. The Vertex Time Projection Chamber

The Vertex Time Projection Chamber (VTX) system measures track coordinates in the $r - z$ plane. It is composed of 28 separate time projection modules mounted end-to-end

parallel to the beam axis. The system has a total length of 264 cm, with an outer radius of 22 cm, which permits the VTX to measure tracks up to $|\eta| < 3.25$. The inner radius is of 6.5 cm for the 10 outer modules ($85 < |z| < 132$ cm) and, due to the space needed for the SVX, 11.5 cm for the 18 inner modules ($|z| < 85$ cm).

Each 9.4 cm long module is segmented in octants subtending 45° in ϕ and divided into two drift regions by a high voltage grid. Within each octant, sense wires, 16 in the 18 inner modules and 24 in the 10 outer modules, are strung tangentially on either side of the grid. Adjacent modules are rotated by 15° with respect to each other to eliminate inefficiencies near octant boundaries and to provide rudimentary ϕ information for tracks crossing more than one module.

Track coordinates are measured in the $r - z$ plane with a spatial resolution per hit of 200 μm, yielding a measurement of the z coordinate of the track vertex with a resolution of 2 mm. These tracks permit to reconstruct the z coordinate of the primary vertex with a resolution of 1 mm and separate multiple vertices in the same beam crossing. The track vertex z coordinate is also used as seed for the three-dimensional track reconstruction in the CTC.

In the forward region ($\theta < 10°$), the VTX is the only tracking system in front of the forward calorimeters. The VTX is also used to identify electrons from photon conversions in the CTC inner cylinder.

6.3.3. The Central Tracking Chamber

The Central Tracking Chamber (CTC) [123] is a cylindrical gas drift chamber with an inner radius of 0.28 m, an outer radius of 1.38 m and a length of 3.20 m. It provides precise track parameter measurements in the region $|\eta| < 1.0$. The momentum and the charge are derived from the track curvature in the magnetic field.

The chamber contains 6156 40 μm diameter gold-plated tungsten sense wires arranged into 84 layers. These layers are grouped into nine alternating axial and stereo superlayers. Five of the superlayers contain 12 layers of axial sense wires, providing a measurement in the $r - \phi$ plane. The four stereo superlayers, containing 6 layers of sense wires tilted by ±3° relative to the beam-line, permit to infer the z-coordinate of a track.

The superlayers are divided into open drift cells, each made of a row of alternating (anode) sense and potential wires bounded by two rows of field shaping (cathode) wires. Shaper and guard wires are placed at the outer edges of the cells to keep the field uniform over the fiducial volume of the cell. The cells are tilted at an angle of 45° in the radial direction to correct for the Lorentz angle of the electron drift in the magnetic field. This tilt permits furthermore to resolve the left-right ambiguity, as only one of the two track possibilities will point to the interaction vertex. The overlap of the cells will ensure that even stiff high-p_T tracks will pass within a very short drift distance of at least one sense wire in each superlayer. Figure 6.5 shows the endplate of the CTC, with the disposition of the cells.

With a 1350 V/cm electric field, the drift velocity in the 49.6%/49.6%/0.8% admixture of argon/ethane/ethanol is 51 μm/ns. To minimize the drift time, the maximum drift

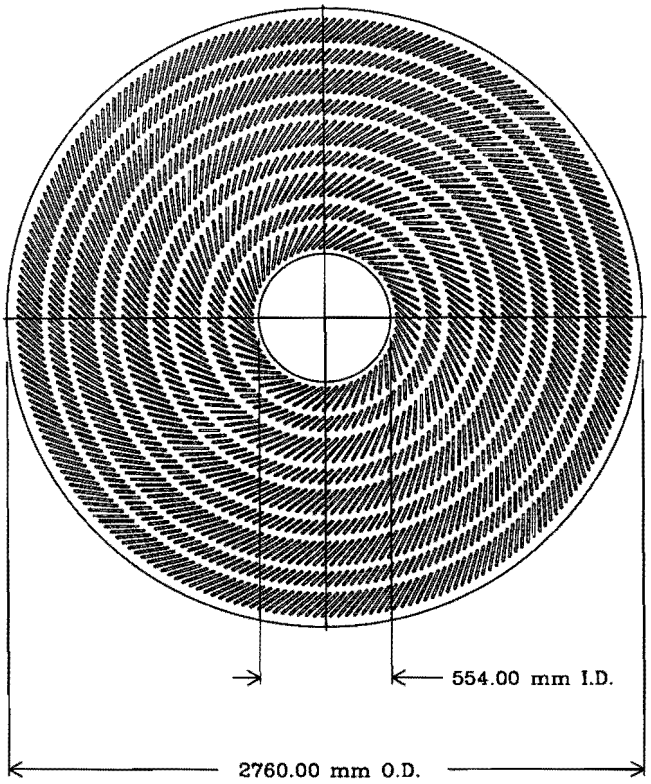

Figure 6.5: *End view of the Central Tracking Chamber, showing the disposition of cells and superlayers.*

distance is 40 mm, corresponding to a drift time of about 800 ns.

The spatial resolution in the transverse plane is between 250 μm in the inner layers and 160 μm in the outer layers, and 3.8 mm ($= 0.2$ mm$/\sin 3°$) in the z direction. The momentum resolution of CTC tracks is better than $\delta p_T/p_T < 0.002 \cdot p_T(\mathrm{GeV}/c)^{-1}$, where p_T is measured in GeV/c. For tracks measured both in the CTC and the SVX, the momentum resolution improves to $\delta p_T/p_T = [(0.0009 \cdot p_T)^2 + (0.0066)^2]^{1/2}$.

6.4. The calorimetry

The calorimetric system is composed of three independent electromagnetic and hadronic calorimeters, located in each of the main regions. All of these calorimeters are segmented in pseudorapidity and azimuth, with a projective tower geometry pointing to the interaction point. A segmentation uniform in pseudorapidity instead of the polar angle is chosen as in high-energy collisions, the number of charged particles per unit of rapidity is constant in the central region. The towers cover 0.1 units of η by 15° in ϕ in the central region, and 0.1 units of η by 5° in ϕ in the plus and forward regions.

Both electromagnetic and hadronic calorimeters have the same geometry and disposition

Calorimeter	$\|\eta\|$ coverage	Energy resolution $\sigma(E)/E$	Position resolution (σ_x, σ_y) [cm]	Thickness
Central EM	0 – 1.1	$13.5\%/\sqrt{E_T} \oplus 1.7\%$	(0.2, 0.2)	18 X_0, $\sim 1\ \lambda_0$
Central HAD	0 – 0.9	$75\%/\sqrt{E_T} \oplus 3\%$	(10, 5)	4.5 λ_0
Wall HAD	0.7–1.3	$75\%/\sqrt{E_T} \oplus 3\%$	(10, 5)	4.5 λ_0
Plug EM	1.1–2.4	$28\%/\sqrt{E_T} \oplus 2\%$	(0.2, 0.2)	$18 - 21\ X_0$, $\sim 1\ \lambda_0$
Plug HAD	1.3–2.4	$130\%/\sqrt{E_T} \oplus 3\%$	(2, 2)	5.7 λ_0
Forward EM	2.2–4.2	$25\%/\sqrt{E_T} \oplus 0.5\%$	(0.2, 0.2)	25 X_0, $\sim 1.3\ \lambda_0$
Forward HAD	2.3–4.2	$130\%/\sqrt{E_T} \oplus 4\%$	(3, 3)	7.7 λ_0

Table 6.3: *Coverage, resolution and thickness of the CDF calorimeters. When quoting the energy resolution, the first term is the (energy dependent) stochastic term and the second the constant term, and both are added in quadrature. The thickness is given in radiation length (X_0) for the electromagnetic calorimeters and interaction lengths (λ_0) for the hadronic calorimeters.*

of the towers, such that a comparison of the energy deposition in each element can be made for any individual tower, helping to discriminate between electrons and pions. By further matching a track from the CTC, electrons and photons can be separated.

The coverage, energy and position resolution and radiation thickness of the different calorimeters are given in Table 6.3. When quoting the energy resolution, the first term is the (energy dependent) stochastic term and the second the constant term, and both are added in quadrature. The thickness is given in radiation length (X_0) for the electromagnetic calorimeters and pion interaction lengths (λ_0) for the hadronic calorimeters.

In the central region, the electromagnetic calorimeter [124] (CEM) is composed of passive layers of 3.2 mm thick lead sheets alternating with active layers of 5 mm thick polystyrene scintillators. In the plug (PEM) [125] and the forward (FEM) [126] electromagnetic calorimeters, the active sampling detectors are proportional chambers with cathode pad readout. In the CEM, in each tower, the signals of all counters are added to give a single measurement, and a proportional chamber [127] (called the Central Electromagnetic Strip Chamber – CES) is located at a depth of 6 X_0 (approximately where a typical EM shower reaches its maximum transverse development) to measure the lateral profile of the shower with a high spatial resolution. In the other regions, to give a more detailed profile of the shower, each tower is read out in several samples (three for PEM and two for the FEM) in depth and the strip layers around the shower maximum are more finely segmented and read out by quadrant.

Due to the geometry of the solenoid, the central region is covered by two hadronic calorimeters, the Central (CHA) and the Wall (WHA) hadronic calorimeters [128]. In all of the hadronic calorimeters the absorbing layers are steel plates. The active detectors are plastic scintillators in the central region (CHA and WHA) and gas proportional chambers in the plug (PHA) and the forward (FHA) [129] region. In all of these calorimeters, the towers are read out in one sample. In the PHA and FHA, the wires in each wire plane are read out individually to provide information on the shower profile.

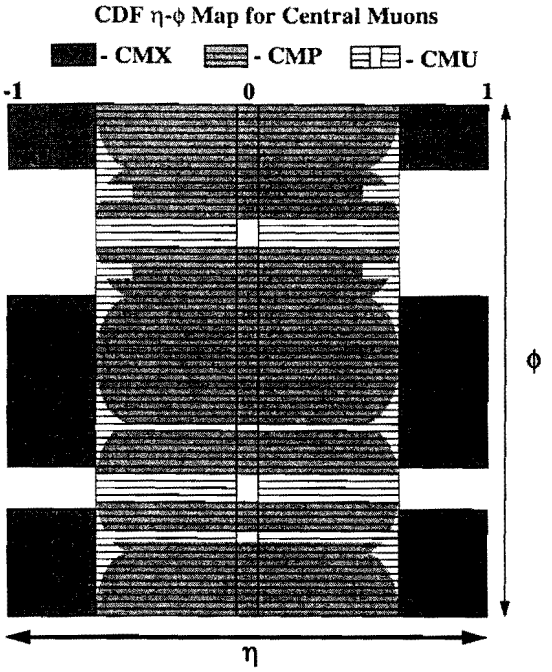

Figure 6.6: *Map of the central muon chamber $\eta - \phi$ coverage.*

6.5. The muon detectors

The muons system is composed of four sub-systems: the Central Muon System (CMU), the Central Muon Upgrade (CMP) and the Central Muon Extension (CMX) in the central region, and the Forward Muon Spectrometer (FMU, not used in this analysis) in the forward region.

Muons are identified by tracking chambers located after the hadronic calorimeters. While most of the hadrons, and the particles formed in the hadronic showers, will be absorbed in the calorimeters, muons, with a critical energy much higher than the energy at which they are produced at CDF, will not be absorbed, and leave only little energy.

6.5.1. The central muon detectors

Figure 6.6 shows the $\eta - \phi$ coverage of the different muon systems in the central region, and Figure 6.7 shows the quantity of material in front of the detectors at $\phi = 0$.

Located immediately behind the CHA, the CMU is the first muon detector as seen from the interaction point. With the calorimeters in front of the CMU presenting an average of 5.4 pion interaction lengths, about 1 in 220 hadrons, both interacting (called *punch-through*) and non-interacting (called *sail-through*), will reach the CMU and fake a muon signal. These hadrons are a significant source of background, dominating the trigger rates and hindering the identification of muons in or near jets.

To improve the rejection of the hadronic background, the CMP has been added behind

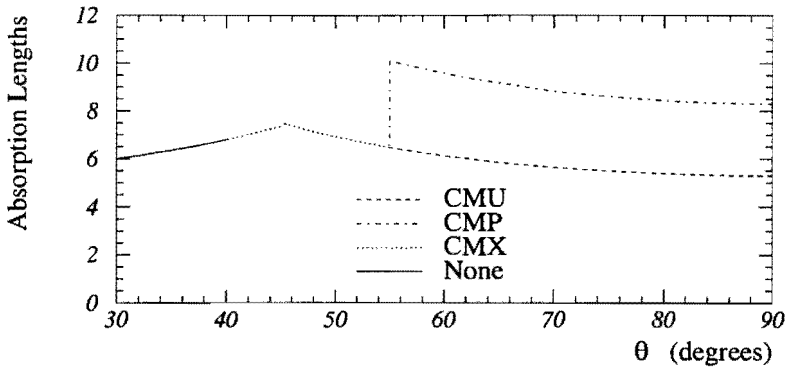

Figure 6.7: *Absorption lengths of material in front of the central muon detectors at* $\phi = 0$.

the CMU, where four layers of drift chambers are placed behind an additional 60 cm of steel. Averaged over θ, this layer of steel adds 3.0 interaction lengths in the central region, reducing the background from hadronic punch-through reaching the CMP by a factor 20.

With the CMU and CMP coverage limited to $|\eta| < 0.63$, the CMX has been added to extend the coverage to $|\eta| < 1.0$, thereby increasing the acceptance for many of the studied processes. Compared to the CMU, the addition of the CMX increases the acceptance of $W \rightarrow \mu\nu$ by 50%, $t\bar{t} \rightarrow \mu +$ jets by 25% and similarly for muons produced in the decay of the b daughters of a top quark, and 30% for J/ψ originating from B mesons.

With the lower polar angle, the hadron calorimeter and magnet return yoke present more material to particles reaching the CMX (6.8 λ_0 on average), and no additional steel has been added.

The minimum momentum for a muon to reach these systems is 1.4 GeV/c for the CMU, 2.2 GeV/c for the CMP and 1.7 GeV/c for the CMX.

A muon track is identified by matching a track found in the CTC with a track reconstructed from the hits in the muon chambers (called a *track stub*). The CTC tracks are extrapolated to the muon chambers and matched in position and in angle to the muon stubs. As the muon chambers are located outside of the magnetic field, these have only a limited momentum resolution. The momentum measurement has therefore to be made, as for all other charged tracks, only on the track parameters measured in the tracking systems.

The Central Muon System

The Central Muon System (CMU) [130] is composed of four layers of single wire drift cells located outside of the central hadron calorimeter, at a radius of 3.47 m. The CMU is segmented in ϕ in 12.6° wedges which are attached to the 15°-wide calorimeter wedges, leaving thus a gap of 2.4° between each CMU wedge. Figure 6.8 shows the location of the muon chambers in the central calorimeter wedge. With two 2.26 m long drift cells placed end-to-end, separated by a gap of 3° in ϕ, centred at $z = 0$, the CMU covers the region $|\eta| < 0.63$. Due to all these gaps, the total coverage in this region is 84%.

The CMU wedges are further segmented in ϕ in three modules of 4.2°. A module, shown

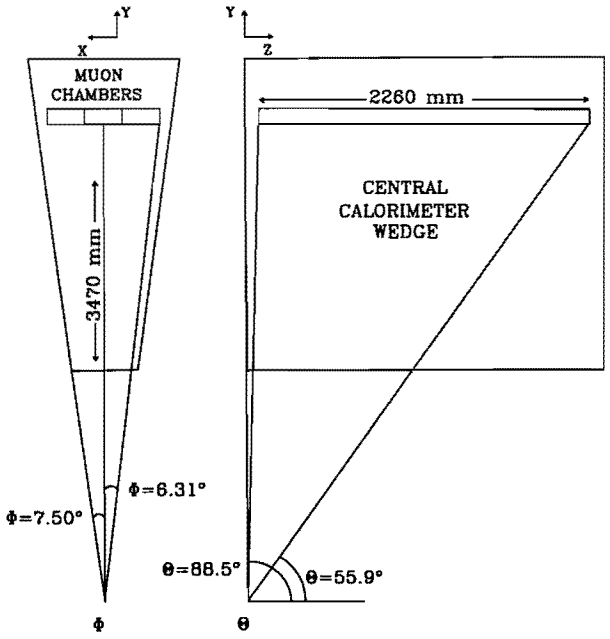

Figure 6.8: *Location of the CMU wedge within a central calorimeter wedge.*

in Figure 6.9, is composed of four adjacent towers of four layers of drift cells. The drift cells have a width of 63.5 mm, a height of 26.8 mm and a length of 2261 mm, with a 50 μm sense wire strung at the centre of the cell. The wires are held at a potential of +3150 V and the beams separating two adjacent cells are held at -2500 V. In a 49.65%/49.65%/0.7% admixture of argon/ethane/ethanol, the cells operate in a limited streamer mode. The maximum drift time in a cell is 1.2 μs.

In a tower, two of the four sense wires, on the second and the fourth layer, lie on a radial line pointing to the interaction point, with the two other sense wires offset by 2 mm from this radial centre-line. This geometry permits to resolve any ambiguity as to which side of the radial centre-line the track lies (left-right ambiguity). The difference between the drift times of two alternating layers (drift times t_2 and t_4 in Figure 6.9) determines the angle α between the track and the radial centre-line. The two other layers provide a second independent measurement of the same angle. This angle can be related to the deflection angle of the track in the magnetic field, yielding thus an estimate of its transverse momentum. With a track angle given by $\alpha = 0.14 \cdot {p_T}^{-1}$, drift time differences range between 160 ns for $p_T = 1$ GeV/c and 16 ns for $p_T = 10$ GeV/c. The difference in drift times is used in the Level 1 trigger to select muon tracks above a certain threshold, as this is a very fast measurement. Furthermore, at calibration, the drift velocity can be determined by comparing the drift times for alternating layers of cosmic ray muons.

Drift time measurements permit to measure positions on the $r-\phi$ plane with a resolution of 250 μm, and charge division yields a resolution of 1.2 mm on the z coordinate.

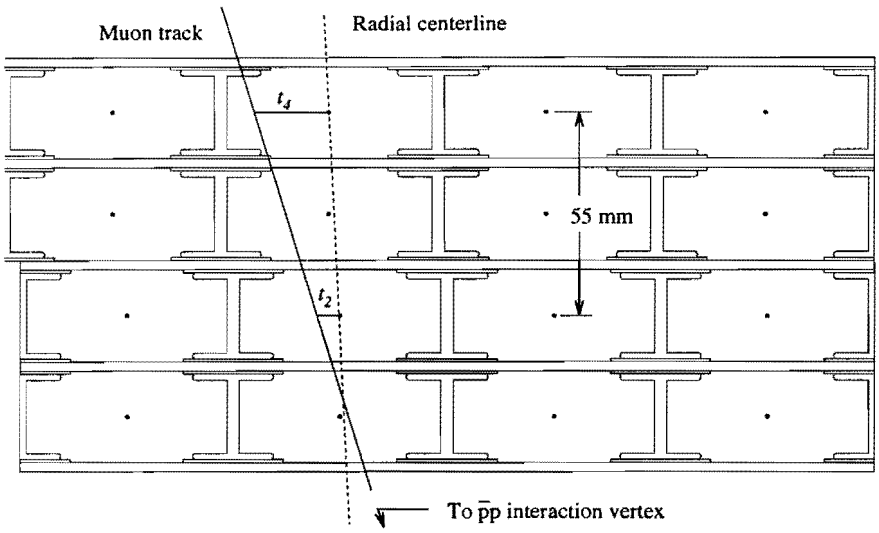

Figure 6.9: *Layout of a CMU module showing the four towers of four layers of drift cells. The dotted line represents the radial centre-line pointing to the interaction vertex and the solid line a muon track. The difference of the drift times t_2 and t_4 determines the angle between the track and the radial centre-line, and can be used as an estimate of the transverse momentum.*

The Central Muon Upgrade

The Central Muon Upgrade (CMP) [131] is composed of four layers of drift chambers placed behind 60 cm of steel. It forms a rectangular box with open ends surrounding the CMU (as can be seen on Figure 6.1). On the top and bottom of the detector, the absorber is provided by the magnet return yoke, while on the sides, steel panels had to be added.

Due to this box-like geometry, the pseudorapidity coverage varies with the angle, with a maximum coverage of $|\eta| < 0.63$, as is shown on Figure 6.6. With further uninstrumented areas still reducing the coverage, the CMP only covers 60% of the area covered by the CMU.

Single wire drift tubes, shown in Figure 6.10, are arranged in four layers, staggered by half a cell to resolve left-right ambiguities. Each drift cell is 25.4 mm wide by 152.4 mm high and typically 6400 mm long, with shorter cells on the bottom plane. A 50 μm anode sense wire strung at the centre of the cell is held at a potential of +5600 V. On the upper and lower wall of the tube, a thick central shaping strip is held at a potential of +3000 V, with eight narrow shaping strips on either side held at potentials decreasing in steps of 375 V, providing a nearly uniform field in the drift volume. With a 50%/50% admixture of argon/ethane bubbled through isopropyl alcohol, the cells operate in proportional mode. The maximum drift time in a cell is 1.2 μs.

The Central Muon Extension

The Central Muon Extension (CMX) [131] and the Central Muon Extension Scintillators (CSX) [132] have been added to extend the coverage of the muon detectors to the region

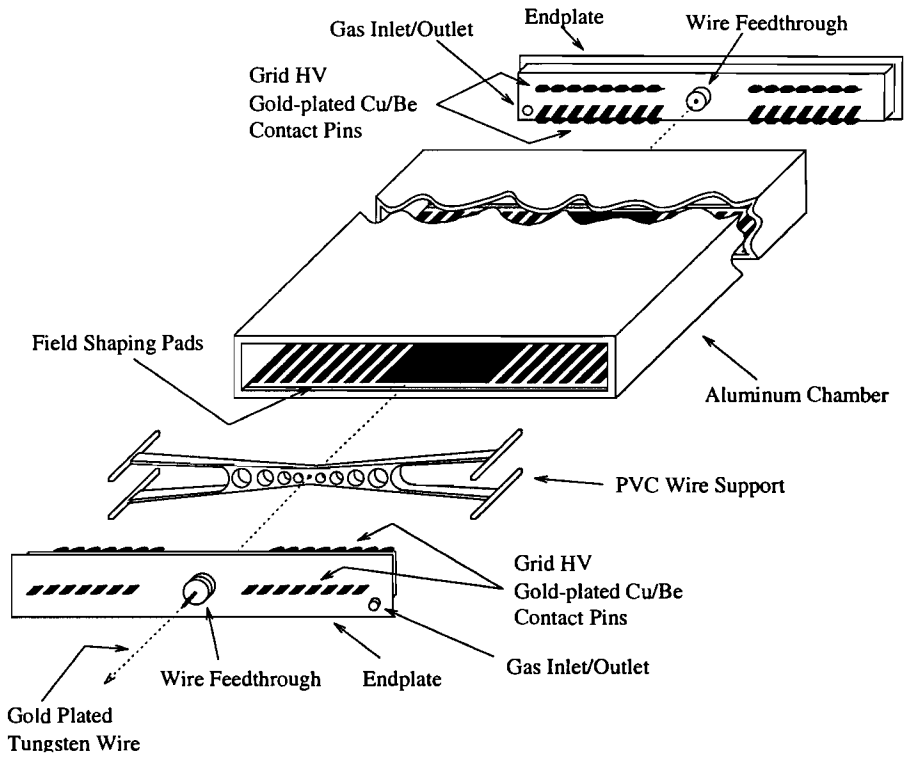

Figure 6.10: *Schematic view of a CMP/CMX drift tube.*

$0.6 < |\eta| < 1.0$.

The CMX consists of eight layers of rectangular drift tubes. The drift tubes are identical to the tubes used in the CMP, albeit with a length of only 180 cm. Each layer is half-cell staggered with respect to the previous one to eliminate ambiguities, such that a muon typically traverses four to six tubes. The tubes are arranged in four arch-shaped structures, lying on the surface of a virtual cone with an opening angle of 41.4° and a vertex 10 m from the interaction point. The layout of a 15°-module is shown in Figure 6.11. The CMX cover in total 240° in azimuth, with a 30° gap at the top of the detector, due to the Main Ring bypass beam-pipe and the magnet refrigerator, and a 90° gap at the bottom of the detector where the cone meets the floor.

To provide accurate timing information for muons, two planes of four layers of scintillators (the CSX) are placed on either side of the CMX modules. These scintillators were required as most of the tracks seen in the CMX were not due to muons produced in the primary interaction, but particles produced in interactions with the beam-pipe and scattering off the forward and plug calorimeters into the CMX. As these particles would reach the CMX some 14 ns after the muons produced in the primary interaction, muons are selected by requiring that the timing of the CSX pulses associated with the CMX track stub be compatible with the expected timing of a muon.

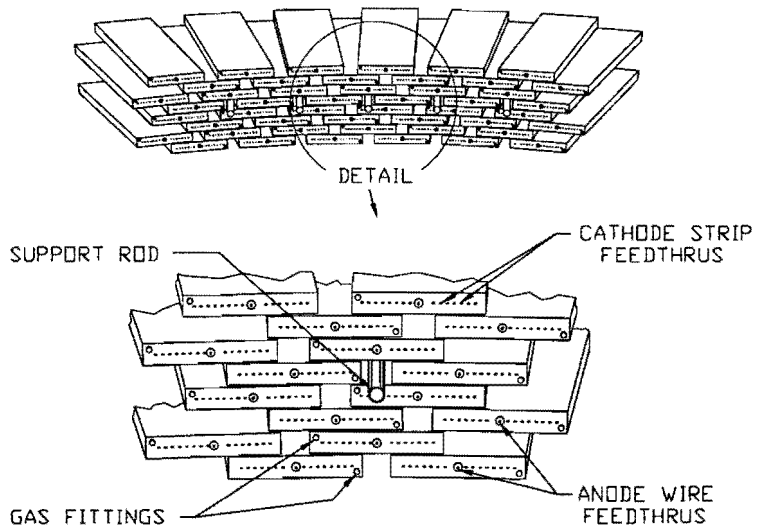

Figure 6.11: *Layout of drift tubes in the CMX. The upper drawing shows the layout of a CMX module, subtending* 15° *in* ϕ*, with eight layers of six drift tubes.*

6.5.2. The Forward Muon Spectrometer

The Forward Muon Spectrometer (FMU) [133] measures the trajectory and momentum of muons in the region $2.0 < |\eta| < 3.6$ ($3° < \theta < 16°$). They are composed of two 1 m-thick magnetized steel toroids, with an inner radius of 0.5 m and an outer radius of 2.8 m. The magnetic field ranges from 2.0 T at the inner radius to 1.6 T at the outer radius. Three layers of drift chambers segmented in $r - \phi$ measure the muon trajectory with a resolution of 200 μm on r and 5° on ϕ, yielding a momentum resolution of 13%. Two layers of scintillation counters in coincidence, one on either side of the system, are used for the trigger. The Forward Muon Spectrometer is not used in this study.

6.6. The Beam-Beam Counters

The beam-beam counters (BBC) [117] are two planes of scintillation counters located on the front of each of the forward calorimeters, in both halves of the detector ($z < 0$ and $z > 0$) at a distance of 5.8 m from the interaction point. The counters are arranged in a rectangle around the beam-pipe, covering the region $3.24 < |\eta| < 5.9$ ($0.32° < \phi < 4.47°$). At least one hit in each plane in a 15 ns window centred on the beam crossing time is required.

With a timing resolution better than 200 ps, they provide the best measurement of the interaction timing. This timing is essential for the CTC, providing the start-time of the drift time measurements. In addition, the timing of the arrival times of particles in the two counters yields a crude measurement of the z-coordinate of the interaction vertex ($\sigma_z \sim \pm 4$ cm).

The BBC are used as the primary luminosity monitors, where the instantaneous (respectively integrated) luminosity is given by the rate (respectively number) of coincidences in

the counters, divided by their effective cross section. As a coincidence in the BBC's indicate only that at least one interaction has occurred, but not the absolute number of interactions per beam crossing, the rate and number of BBC coincidences cannot be obtained by a simple count. It is instead given by the product of the number of beam crossing and the mean number of interactions per beam crossing, which can be obtained by measuring the rates of the individual counters [134]. The BBC are also part of the *minimum-bias* trigger.

6.7. The trigger system

The total $p\bar{p}$ cross section at a centre of mass energy of $\sqrt{s} = 1.8$ TeV has been measured to be 80 mb [135], of which the inelastic cross section[2] is 50 mb. At a typical instantaneous luminosity of $\mathcal{L} = 10^{31}$ cm^{-2}s^{-1} during Run 1B, a inelastic interaction rate of 500 kHz is expected, with an average of 1.6 interactions per bunch crossing. As the rate at which these events can be written to tape is of the order of 10 Hz, a trigger system is needed to select the small fraction of potentially interesting events.

CDF uses a three level trigger system, designed to select interesting events with a high efficiency and reject uninteresting events as early as possible to minimize detector dead-time, as during the time that a trigger decision is taken and the event is read out, the detector is unable to observe interactions. The Level 1 and Level 2 triggers [136] are implemented in dedicated FASTBUS electronic boards and based on analog 'fast-output' signals from different sub-systems. Only at the last level is the complete detector information read out, as this is a very time consuming process, taking of the order of 3 ms. The complete event information is then used in the Level 3 trigger, which is implemented in software running on dedicated processor farms.

With a total b production cross section of the order of 50 μb, the triggers have to be carefully designed to select B candidates with a high efficiency while minimizing the background. Being interested in final states containing two muons, the events used for this analysis have been selected by the low-p_T central dimuon triggers. Along with a general description of the trigger system, the latter triggers will be described in more detail.

It should be noted that for several triggers, the acceptance rate is reduced by applying an acceptance (*prescale*) factor. This permits to limit the trigger rate without raising the trigger thresholds. These triggers, either with a very high rate or deemed of less interest, are reduced in order not to saturate the data acquisition bandwidth, and thereby limiting the acceptance of rarer or more interesting processes. Some of the prescale factors are continuously altered during a run (*dynamic prescaling*) to allow for a optimal usage of the available bandwidth.

6.7.1. Level 1

The Level 1 trigger decision is made in the 3.5 μs between two beam crossings, thus incurring no deadtime. At a luminosity of $5 \cdot 10^{30}$ cm^{-2}s^{-1}, the Level 1 trigger rate is approximately

[2] An inelastic event is observed by a signal at small angle in both BBC's. In elastic collisions, the polar angle of the proton and anti-proton is too small to be detected by the BBC's.

1 kHz [27]. The Level 1 trigger relies on 'fast-output' signals from the calorimeters for electron and jet triggers and from the central muon detectors for the muon triggers, receiving information on the global features on the energy deposition in the calorimeters without information on the energy flow in the detector.

In Run 1A, a signal was required in the BBC, to ensure that a $p\bar{p}$ interaction has taken place in the bunch crossing. This requirement was dropped in Run 1B, as the high luminosity yielded at least one interaction per bunch crossing.

For the purpose of the Level 1 and Level 2 triggers, the calorimeters are segmented into logical trigger towers of 0.2 in η and 15° in ϕ to reduce the number of signals. At this level, the electromagnetic, hadronic and total trigger tower energies which are above a programmable threshold are weighted by the polar angle θ, yielding the transverse energy $E_T = E \cdot \sin\theta$. The transverse energy imbalance in the electromagnetic and hadronic calorimeters are also calculated, given by the sum of $E_T \sin\phi$ and $E_T \cos\phi$ over the towers above threshold. One or more of the trigger towers signals (E_T, $E_T \sin\phi$ or $E_T \cos\phi$) are then required to be above a given threshold, dependent on the relevant trigger.

With no tracking information from the CTC available at this point, the Level 1 muon triggers rely solely on information from the muon chambers [137]. The transverse momentum of a muon candidate can be related to the angle α between the track stub and the radial line, and α is obtained from the difference between the drift times for wires in two alternating layers, as seen in Section 6.5.1. The requirement on a minimum p_T is made by requiring this drift time difference to be below a given threshold. A muon stub is so defined by any wire pair from alternating layers in a tower satisfying the p_T requirement. The nominal p_T requirement is 3.3 GeV/c for low-p_T and 6.0 GeV/c for high-p_T muons stubs. Only the CMU and the CMX can be used for this measurement, as the CMP does not have a natural projective geometry. In addition, a signal in the hadron calorimeter tower corresponding to the muon trigger tower is required, to confirm that the particles reaching the muon chambers project to the interaction region and are synchronous with the beam crossing. For high-p_T muons, in the regions covered by the CMP, a CMP hit corresponding to the CMU stub is required instead. For CMX muons, an appropriate CSX scintillators signal is further required to reject out-of-time background.

Three low-p_T dimuon triggers are defined, each requiring two low-p_T muon stubs in non-contiguous trigger towers, when the muon chambers are segmented in 5° logical trigger towers, with both detector halves ($z < 0$ and $z > 0$) counted independently. Two muon stubs in contiguous trigger towers in the same half of the detector would be counted as a single muon for these triggers. The TWO_CMU_3PT3 trigger requires two or more CMU stubs, the TWO_CMU_CMX_3PT3 trigger one or more stubs in each CMU and CMX and the TWO_CMX_3PT3 trigger requires two or more CMX stubs.

6.7.2. Level 2

The Level 2 trigger takes between 20 and 30 μs, depending on the complexity of the event. Given the Level 1 rate, the incurred deadtime is approximately of 5%. The Level 2 trigger rate is approximately 12 Hz.

At this stage, more complex operations are possible, and basic topological features of

the event are determined. Using the same calorimeter signals as Level 1, a hardware cluster finder provides a list of calorimeter clusters, and determines their E_T, average position and width in η and ϕ, and total E_T and E_T imbalances are calculated. Simple calculations, such as finding the invariant mass of a group of clusters, can also be performed

A dedicated high-speed hardware processor, the *Central Fast Tracker* (CFT) [138] has been designed to find tracks with $p_T > 2$ GeV/c, relying on fast timing information from the CTC. The CFT will first search for hits in the five axial superlayers, classifying them into *prompt* hits, with drift times less than 90 ns, and *delayed* hits, with drift times between 500 ns and 650 ns. Prompt hits occur very near (less then 4.5 mm) to a sense wire, when the charged particle crosses the plane of sense wires in a superlayer. Delayed hits will occur at large drift distances, around 2/3 of the cell size, on either sides of the prompt hit sense wire. Stiff tracks have typically one prompt and two delayed hits per superlayer, yielding a total of 15 expected hits per track.

For each prompt hit found in the outer superlayer, a lookup table is used to find a predefined hit pattern with the same combinations of prompt and delayed hits as observed. For each prompt hit in the outer superlayer, 32 hit patterns are defined, arranged in eight p_T bins and two ϕ bins for each sign of curvature. Different p_T bins were used for Run 1A and Run 1B.

The track-finding efficiency with the CFT is $(93.5 \pm 0.3)\%$ for tracks above 10 GeV/c, with a resolution of $\delta p_T/p_T = 0.035 \cdot p_T$ in p_T (with p_T in units of GeV/c) and 5° in ϕ.

CFT tracks, muon stubs and energy clusters are then combined into Level 2-clusters related to physics objects, such as electron-, jet-, muon- or photon-clusters, on which a Level 2 processor takes the Level 2 trigger decision.

At Level 2, muons are identified by matching a CFT track with a muon stub in a dedicated module, called CTCX. It contains a lookup table with two maps, matching each valid p_T and ϕ CFT bin to the muon trigger towers and to the calorimeter trigger towers. Via this map, each found CFT track is extrapolated to the muon chambers. If the trigger tower that is pointed at by the CFT track was already set at Level 1, the tower is said to contain a *gold* muon. The Level 2 muon cluster is then formed by associating to this muon tower the calorimeter tower already found at Level 1 and all contiguous groups of towers above threshold, including typically three calorimeter towers. The azimuthal separation between the CFT track and the muon stub was required to be within 15° in Run 1A, while in Run 1B, the map was optimized to account for the multiple scattering of muons and the maximum separation reduced to 5° on average, permitting to reduce the minimum p_T requirement.

Two gold muons in adjacent wedges of the same muon system (either CMU or CMX), would be counted as a single Level 2 muon cluster, formed of six calorimeter towers. Similarly, a single CFT track associated with both a CMU and a CMX Level 1 muon stub in the same wedge on the same half of the detector would yield a single five-tower Level 2 muon cluster.

In Run 1A, the dimuon trigger used (TWO_CMU_ONE_CFT) requires one CMU Level 2 muon cluster and a second Level 1 muon stub in the CMU. This trigger is dynamically prescaled.

In Run 1B, there are five different Level 2 low-p_T dimuon triggers:

- TWO_CMU_TWO_CFT_2_2:
  Unprescaled trigger, requiring two CMU Level 2 muon clusters. Two muon clusters in the same half of the detector are required to be separated by at least one empty wedge, while two muon cluster in the opposite halves are required to be in different azimuth, without requiring an empty wedge separation.
- CMX_CMU_TWO_CFT_2_2:
  Dynamically prescaled trigger, requiring one CMU and one CMX Level 2 muon cluster, without wedge-separation requirement. A single five-tower cluster would be counted as both the CMU and the CMX cluster, effectively passing this trigger on its own.
- TWO_CMX_TWO_CFT_2_2:
  Dynamically prescaled trigger, requiring two CMX Level 2 muon clusters. Two muon clusters in the same half of the detector are required to be separated by at least one empty wedge. For two muon cluster in the opposite halves, no ϕ-separation requirement exists.
- TWO_CMU_CMX_ONE_CFT_3_4:
  Dynamically prescaled trigger, requiring one CMU Level 2 muon cluster and a second Level 1 stub in either CMU or CMX, without wedge-separation requirement. The p_T bin of the CFT track of the muon cluster is required to be greater than 1 ($p_T >$ 3.4 GeV/c). In the later stages of Run 1B, the CMU cluster is required to be confirmed by a CMP hit (then renamed TWO_CMU_CMX_ONE_CMUP_3_4).
- TWO_CMU_ONE_CFT_2_2_6TOW:
  Dynamically prescaled trigger, included only in the later stages of Run 1B. It requires one six-tower Level 2 muon cluster. This trigger is intended to compensate for the losses incurred by the TWO_CMU_TWO_CFT_2_2 trigger due to the azimuthal separation requirement, when two muon stubs are combined in a single cluster.

6.7.3. Level 3

Once an event is accepted by Level 2, the complete detector is digitized and read out. This operation takes approximately 3 ms, resulting in a further deadtime of 4%. After read out, the detector and the Level 1 and Level 2 trigger systems are free again to observe new interactions, and no further deadtime occurs. The information of the read-out events is buffered until it can be processed by the Level 3 trigger system. Level 3 is a software trigger running on a farm of commercial computers. The Level 3 trigger takes approximately 1 CPU second, and the buffered events are processed in parallel. The Level 3 trigger rate is between 5 and 10 Hz, the rate at which these events can be written to tape. Events passing Level 3 will be written to tape for offline processing, and a fraction of these events will be monitored in real time to monitor the detector performances, the trigger rates and the luminosity conditions.

The Level 3 farm was composed of commercial Silicon Graphics multiprocessor systems running the IRIX operating system. The Level 3 hardware has undergone significant modifications between Run 1A and Run 1B. 48 MIPS R3000 processors were available in Run 1A. These have been replaced by R4000 and R4400 processors for Run 1B, and several of these have been upgraded in the course of the run.

The Level 3 software performs a full event reconstruction, where physics quantities such as track parameters or energy clusters are derived from the raw detector measurements. Three-dimensional track-reconstruction is made on potentially interesting tracks (*regional tracking*), such as high-p_T tracks or muon candidates, using the VTX and CTC information. The SVX is not used at this stage to limit processing time. The trigger decision is then taken on these reconstructed quantities. The algorithms used in Level 3 are identical to those used in the offline reconstruction, albeit with a few modifications, notably to the track-reconstruction, to improve the processing speed.

According to the Level 3 trigger they passed, accepted events will be directed to three output *streams*, each with a different level of priority. Approximately 4% of events are directed to *Stream A*, also called 'express line' as it is the stream of highest priority. These events are cached to disk and, after reconstruction, available for analysis within a few hours of being recorded. *Stream B* events (approximately 67% of all events) are available within two weeks, whereas *Stream C* events (the remaining 29%) were reconstructed some two years after the end of the run.

At Level 3, the muon reconstruction is refined, and a match between the muon chamber track stubs and the CTC track is required. The CTC track is extrapolated to the muon chambers, accounting for energy loss and multiple scattering. A requirement is imposed on the match between the extrapolated track and the muon stub, in both the $r-\phi$ plane and the z direction.

In Run 1A, a matching requirement of 4σ is placed for the general dimuon triggers and a looser requirement of 5σ for the J/ψ and $\psi(2S)$ trigger. In Run 1B, a looser matching requirement (4σ) is placed for the Stream A and Stream C triggers and a tighter requirement (between 3 and 4σ) for the Stream B triggers.

The Level 3 dimuon triggers will select events mainly according to the invariant mass range of the the muons, with slightly different detector and quality requirements on the muon candidates.

In Run 1A, the dimuon trigger used (PSI1_DIMUON_CMUCMU) requires both muons to be in the CMU, each with a minimum transverse momentum of 2.0 GeV/c. The Level 2 TWO_CMU_ONE_CFT trigger is required and no requirement is made on the charge of the muons or their invariant mass.

In Run 1B, the only momentum requirement placed on the muons at this level is very loose ($p_T > 1.4$ GeV/c), ensuring that their momentum is large enough for them to traverse the calorimeters and reach the muon chambers. As most of the Level 3 dimuon triggers do not require specifically a Level 2 dimuon trigger (except the Stream A trigger), events with two muons which do not meet the strict Level 2 dimuon requirements can be selected by the Level 3 dimuon triggers. These events are called volunteers.

The low-p_T dimuon triggers are the following:

- PSIA_DIMUON_JPSI_DOUBLE:
  Stream A trigger, designed to select $J/\psi \to \mu^+\mu^-$ candidates. Requires two opposite charge muons with an invariant mass between 2.8 and 3.4 GeV/c^2. Requires any of the TWO_CFT triggers or the TWO_CMU_CMX_ONE_CFT_3_4 trigger.

- PSIB_DIMUON_JPSI:
  Stream B trigger, designed to select J/ψ and $\psi(2S)$ candidates. Requires two opposite charge muons with an invariant mass between 2.7 and 4.1 GeV/c^2.

- PSIB_DIMUON_UPSILON:
  Stream B trigger, designed to select $\Upsilon(1S)$, $\Upsilon(2S)$ and $\Upsilon(3S)$ candidates. Requires two opposite charge muons with an invariant mass between between 8.5 and 11.4 GeV/c^2.

- PSIB_DIMUON_LOWMASS:
  Stream B trigger, requiring two muons of any charge in the SVX acceptance region with an invariant mass below 2.8 GeV/c^2. Both muons are required to be confirmed by CMP hits.

- PSIB_DIMUON_HIGHMASS:
  Stream B trigger, requiring two muons of any charge in the SVX acceptance region with an invariant mass above 2.7 GeV/c^2. One of the two muons is required to be confirmed by a CMP hit.

- PSIB_DIMUON_SEQUENTIAL:
  Stream B trigger, designed to select muons from sequential semileptonic B decays[3]. Requires two muons of any charge in the SVX acceptance region, seen in any of the central muon detectors, each with $p_T > 2.1$ GeV/c. Their invariant mass is required to be between 1.0 and 2.8 GeV/c^2.

- PSIC_DIMUON:
  Stream C trigger, requiring two muons of any charge seen in any of the central muon detectors, without invariant mass requirement. Events already accepted with the PSIB_DIMUON_JPSI or PSIB_DIMUON_HIGHMASS are vetoed.

Not all of these triggers will be used in this analysis, as will be explained in Section 8.1.

[3] $b \to c\mu^-\bar{\nu}$, $c \to s\mu^+\nu$

Part III

The Analysis

Chapter 7

The principle of the measurement

When observing the decay of a B meson to a specific final state f, the expected number of observed events N_{obs} is given by

$$N_{obs}(f) = \int \mathcal{L}dt \cdot \sigma(B) \cdot \mathcal{B}(B \to f) \cdot \epsilon \cdot \alpha \,, \tag{7.1}$$

where $\int \mathcal{L}dt$ is the total integrated luminosity of the collected data sample, $\sigma(B)$ the B meson production cross section, $\mathcal{B}(B \to f)$ the branching fraction of the specific decay, α the acceptance and ϵ the total efficiency. The latter two factors contain the geometric acceptance factor of the detector for the given process and the efficiency of recording and reconstructing the specific final state and the efficiencies of all selection requirements.

In a *direct* measurement, all these factors have to be measured independently, and all acceptance, reconstruction and selection efficiencies have to be taken into account. Furthermore, the systematic uncertainties on these factors will all contribute to the total systematic uncertainty.

By doing a measurement relative to a decay of similar final state f', the B production cross section and several common reconstruction and selection efficiencies will cancel. By using the same data sample for both decay modes, the integrated luminosity will (ideally) cancel as well. In turn, the uncertainties on these factors will no longer affect the result. The branching fraction will thus be given by

$$\frac{\mathcal{B}(B \to f)}{\mathcal{B}(B \to f')} = \frac{N_{obs}(B \to f)}{N_{obs}(B \to f')} \cdot \frac{1}{\epsilon_{rel}} \tag{7.2}$$

where ϵ_{rel} will include the ratio of the acceptance and efficiencies of the two processes that do not cancel.

In the absence of a signal, upper limits on the branching fraction can be set.

7.1. The search for the decays $B_d^0 \to \mu^+\mu^-$ and $B_s^0 \to \mu^+\mu^-$

The theoretical Standard Model predictions for the branching fractions of the decays $B_d^0 \to \mu^+\mu^-$ and $B_s^0 \to \mu^+\mu^-$[1] are $\mathcal{B}(B_d^0 \to \mu^+\mu^-) = (1.5 \pm 0.9) \cdot 10^{-10}$ and $\mathcal{B}(B_s^0 \to \mu^+\mu^-) = (3.5 \pm 1.0) \cdot 10^{-9}$ [94] (c.f. Section 4.6). With a data sample of integrated luminosity of the order of 100 pb^{-1}, no event is expected and the sensitivity of the experiment is several orders of magnitude above the predicted branching fractions. Nevertheless, non-Standard Model processes can increase the branching fraction significantly, and the observation of a signal would indicate contributions from physics beyond the Standard Model.

In the MSSM model, the branching fraction of the decay $B_s^0 \to \mu^+\mu^-$ could be as high as 10^{-6} for large values of $\tan\beta$ (c.f. Section 4.7.2). Such a branching fraction is estimated to be at the limit of the present study. In this case, with the total luminosity on which this study is based, approximately 160 B_s^0 mesons would undergo this decay. Taking into account the acceptance and all selection efficiencies, only one or two such decays may be observed.

The previous search for these decays performed at CDF [139] obtained upper limits on the branching fractions of $\mathcal{B}(B_d^0 \to \mu^+\mu^-) < 1.6 \cdot 10^{-6}$ and $\mathcal{B}(B_s^0 \to \mu^+\mu^-) < 8.4 \cdot 10^{-6}$ at a 90% confidence level. It was performed on the Run 1A dataset, corresponding to an integrated luminosity of 17.8 ± 0.6 pb^{-1}. These were the most stringent experimental limits prior to the results of this study. Compared to the previous measurement, an additional 81.2 ± 6.5 pb^{-1} from Run 1B is used in the present search, and both data sets are combined for the final result.

In the search for these decays, a direct measurement of the branching fraction will be made. A measurement relative to the inclusive decay $B \to J/\psi X$ was attempted, but was inconclusive, since the partially reconstructed B mesons do not allow the use of several of the selection requirements, resulting in a very high background.

The branching fractions will therefore be measured using Equation 7.1, for which all factors will be estimated. As in these measurements, the B and $\bar{B}$ will not be distinguished, the right-hand side of Equation 7.1 has to be multiplied by a factor two. As such, charge conjugation of final states will always be implied, unless otherwise noted.

The B_d^0 production cross section has been measured at CDF for B mesons with $p_T(B) > 6$ GeV/c and rapidity $|y(B)| < 1$ [140]. The integrated production cross section has been measured to be $\sigma(B_d^0) = 2.39 \pm 0.32 \pm 0.44$ μb.

The fragmentation of b quarks into B mesons will be assumed to yield $\frac{\sigma(B_d^0)}{\sigma(B_s^0)} = 3$ which is consistent with the measurement presented in Reference [141]. In this measurement, the ratio of the fragmentation fractions has been found to be

$$\frac{f_s}{(f_u, f_d)} = 0.34 \pm 0.10 \pm 0.03 \,. \tag{7.3}$$

A new measurement of the ratio of the fragmentation fractions [142], published after the

[1] Although the official name of the B_d^0 is B^0 the first notation will be used when referring to it, and the B_s will be referred to as B_s^0. The decays $B_d^0 \to \mu^+\mu^-$ and $B_s^0 \to \mu^+\mu^-$ will in the following be collectively referred to as $B^0 \to \mu^+\mu^-$, and charge conjugation is implied.

publication of the results of the $B^0 \to \mu^+\mu^-$ searches, found

$$\frac{f_s}{(f_u, f_d)} = 0.426 \pm 0.076 \,, \tag{7.4}$$

indicating that this fraction may have been underestimated.

7.2. The search for the decay $B_s^0 \to \mu^+\mu^-\phi$

There is no previous publication on the search for this decay, and no limit on the branching fraction has been set. This is the first measurement attempted. The theoretical Standard Model predictions for the branching fractions is $\mathcal{B}(B_s^0 \to \mu^+\mu^-\phi) = (1.21 \pm 0.32) \cdot 10^{-6}$ for the CQM form factors (c.f. Section 4.4.2). With a data sample of integrated luminosity of the order of 90 pb^{-1}, approximately 190 B_s^0 mesons would undergo this decay in the region of acceptance. Nevertheless, once the acceptance and all selection efficiencies have been accounted for, less than one of these decays is expected to be observed.

In this search, the branching fraction can be measured relative to the branching fraction of the decay $B_s^0 \to J/\psi\,\phi$. The branching fraction will therefore be given by Equation 7.2. With the ϕ reconstructed in the decay $\phi \to K^+K^-$ and the J/ψ in the decay $J/\psi \to \mu^+\mu^-$, the same final state will be observed for both decays. The similarities between the two decays allows the cancellation of most of the reconstruction and selection efficiencies.

The reference decay is well established, and its branching fraction has been measured at CDF to be $\mathcal{B}(B_s^0 \to J/\psi\,\phi) = (9.3 \pm 3.3) \cdot 10^{-4}$ [141]. Using for the J/ψ decay the world-average branching fraction[2], the branching fraction for the reference signal is $\mathcal{B}(B_s^0 \to J/\psi\,\phi, J/\psi \to \mu^+\mu^-) = (5.6 \pm 2.0) \cdot 10^{-5}$. As for both the sought and the reference decays, the ϕ is reconstructed through the same decay, this branching fraction[3] should of course not be included in the reference branching fraction.

7.3. A note on the decay $B_s^0 \to J/\psi\,\phi$

The B_s^0 was first observed by the CUSB collaboration in 1990 in $\Upsilon(5S)$ resonances [143] and was later confirmed by the ALEPH collaboration [144]. The decay $B_s^0 \to J/\psi\,\phi$ has first been observed at CDF in June 1993 [145], where its branching fraction has subsequently been measured [141].

The decay proceeds (c.f. Section 4.4) through long-distance contributions with a resonant $c\bar{c}$ intermediate state, mainly through the tree spectator diagram (Figure 4.4(c)). It permits, through the decays $J/\psi \to \mu^+\mu^-$ and $\phi \to K^+K^-$, a full reconstruction of the B_s^0 meson, and is an ideal channel to study many properties of the B_s^0 system[4].

[2] $\mathcal{B}(J/\psi \to \mu^+\mu^-) = (6.01 \pm 0.19)\%$ [1].

[3] $\mathcal{B}(\phi \to K^+K^-) = (49.1 \pm 0.8)\%$ [1].

[4] This is in principle also true for the decay channels $B_s^0 \to D_s^+ D_s^-$ and $B_s^0 \to D_s^{*+} D_s^{*-}$, but as the branching fractions are even lower, the available samples have not permitted any quantitative measurement. Only the ALEPH collaboration has made use of these decays, by performing only a partial reconstruction of the final state [146].

It is in principle the best suited to measure the lifetime of the B_s^0 meson. However, as the branching ratios of these modes are low, the available samples are small, and the semi-leptonic inclusive decays $B_s^0 \to D_s^- l^+ \nu + X$ still provide a more precise measurement.

Having the largest $B_s^0 \to J/\psi\,\phi$ sample, CDF could measure the mass of the B_s^0 meson with the most precision[5]. OPAL derives the mass from one such candidate [148], ALEPH used the very similar $B_s^0 \to \psi(2S)\phi$ decay, of which it saw one event [149], and DELPHI uses one event for each of the decays $B_s^0 \to D_s^- \pi^+$, $B_s^0 \to D_s^- a_1^+(1260)$ and $B_s^0 \to J/\psi\,\phi$ [150].

This decay provides one of the best ways to determine the height of the Unitarity Triangle, η in the Wolfenstein parameterization [151, 152]. At first order of the Wolfenstein parameterization, the CP-violating weak phase $\phi_{CKM} = [\arg(V_{cs}^* V_{cb}) - \arg(V_{ts}^* V_{tb})]$, measured in the rate asymmetry, cancels, and higher order terms have to be taken, yielding a weak phase $\phi_{CKM} = 2\lambda^2\eta$ [50]. Because of the orbital angular momentum, the final state is a mixture of CP-even and CP-odd states, and the total rate asymmetry will suffers from a partial cancellation. As the CP-even and CP-odd components have different angular dependence, an analysis of the angular correlation of the decay will permit to separate the CP-even and CP-odd states, thereby permitting to access the fundamental asymmetry.

It is predicted that in the B_s^0 system, the difference between the widths $\Delta\Gamma_s$ of the two mass eigenstates[6], B_s^H and B_s^L, is large, with a relative difference $\Delta\Gamma_s/\Gamma_s$ in the range $10 - 30\%$ [153]. By separating the CP-even and CP-odd states using the angular analysis, the different lifetimes of the states would yield the width difference [154]. The lifetime measured in semi-leptonic decays would be the mean lifetime.

The mass difference between two eigenstates, Δm_s, could until now not be measured directly, and its lower limit is $\Delta m_s > 9.1\ \mathrm{ps}^{-1}$ [1]. Time-integrated measurements are not possible, as the time-integrated mixing probability χ saturates in this range of mass differences, and in time-dependent measurements, the rapid oscillations generated could not be observed until now. As in the B_s^0 system the ratio $\Delta m_s/\Delta\Gamma_s$ depends on the ratio $|V_{cb}V_{cs}|/|V_{tb}V_{ts}|$, which is quite well known, and on QCD corrections, a measurement of $\Delta\Gamma_s$ would therefore yield Δm_s.

[5] $m(B_s^0) = 5369.9 \pm 2.3 \pm 1.3$ [147]

[6] The mass eigenstates B_s^H and B_s^L are *not* CP eigenstates. They are mixtures of the two CP-conjugate states $|\bar{b}s\rangle$ and $|b\bar{s}\rangle$. It is only when neglecting CP violation that the mass eigenstates can be considered CP eigenstates CP-even (B_s^L) and CP-odd (B_s^H).

Chapter 8

The event selection

8.1. The data samples

The data samples used in this study were collected at CDF in $p\bar{p}$ collisions at a centre of mass energy of $\sqrt{s} = 1.8$ TeV, during the Run 1 data taking period. As seen in Section 5, Run 1 is subdivided in two separate data taking periods, referred to as Run 1A and Run 1B. In Run 1A, which lasted from August 1992 to May 1993, a total integrated luminosity of $\int \mathcal{L}dt = (19.5 \pm 1.0)\ \mathrm{pb}^{-1}$ of data were collected. With the much higher instantaneous luminosity delivered by the accelerator in Run 1B, a total integrated luminosity of $\int \mathcal{L}dt = (89 \pm 7)\ \mathrm{pb}^{-1}$ was recorded between January 1994 and July 1995. The total Run 1 data corresponds to an integrated luminosity of $\int \mathcal{L}dt = (109 \pm 7)\ \mathrm{pb}^{-1}$.

Between Run 1A and Run 1B, CDF underwent several important modifications. The main modifications were the replacement of the SVX by the more robust SVX' (c.f. Section 6.3.1) and the significant improvement of the data acquisition system and the trigger hardware. As a result, the trigger requirements have been substantially modified, as described in Section 6.7.

8.1.1. The datasets

After being accepted by Level 3 and written to the appropriate streams, the data were be reconstructed offline and *split* into datasets. The reconstruction programs used offline at the production stage are more sophisticated than the programs used at Level 3 and permit a more detailed reconstruction of the event, utilising the full information provided by all subdetector systems. The tracking algorithm is notably improved, and SVX information is included. Furthermore, run dependent conditions, such as calibration and alignment constants, not available at Level 3, are known at this stage and can be included. The datasets are defined using physics analysis criteria, and are related to one or more of the Level 3 triggers.

Events analysed in this study were collected by the dimuon triggers. The relevant datasets are organised according to the invariant mass of the muon pair, and are closely associated with the Level 3 triggers, described in Section 6.7.3.

Due to the large range of invariant mass of the muon pair searched, several datasets were required. In the search for the decays $B^0 \to \mu^+\mu^-$, muon pairs with an invariant mass between 5 and 6 GeV/c^2 are used. For the decay $B_s^0 \to \mu^+\mu^-\phi$, the invariant mass of the muon pair ranges from nearly 0 to 4.4 GeV/c^2. For the resonant reference decay $B_s^0 \to J/\psi\,\phi$, the searched mass range (around the J/ψ peak) is included in the latter.

For Run 1A, the events collected with the PSI1_DIMUON_CMUCMU Level 3 trigger were split into several datasets, according to their dimuon mass. The four datasets used for these analyses are given in Table 8.1.

Dataset	Dimuon mass range
Dimuon 1	0.0 to 2.8 GeV/c^2
Dimuon 2	2.8 to 3.2 GeV/c^2
Dimuon 3	3.2 to 4.6 GeV/c^2
Dimuon 4	above 4.6 GeV/c^2

Table 8.1: *Run 1A datasets used in this study.*

For Run 1B, four datasets, from Stream B and Stream C will be used:

- PSAB:
  Stream B dataset, covering the $J/\psi \to \mu^+\mu^-$ invariant mass range, collected with the PSIB_DIMUON_JPSI Level 3 trigger.

- PSPB:
  Stream B dataset, covering the $\psi(2S) \to \mu^+\mu^-$ invariant mass range, collected with the PSIB_DIMUON_JPSI Level 3 trigger.

- BHMB:
  High-mass Stream B dimuon dataset, covering the dimuon masses above 2.7 GeV/c^2, collected with the PSIB_DIMUON_HIGHMASS Level 3 trigger. One of the muons is required to have a CMP stub.

- MMPHI:
  Stream C dataset, collected with the PSIC_DIMUON Level 3 trigger. It is a subset of the entire Stream C dimuon dataset, selected with the requirements described in Section 10.1.1. It starts only at Run 61051, and after Run 63924, as the Level 3 trigger vetoes the PSIB_DIMUON_JPSI and PSIB_DIMUON_HIGHMASS triggers, the events selected for the J/ψ, $\psi(2S)$ and high-mass datasets are excluded.

It should be noted that neither the low-mass dimuon (named BLMB) nor the sequential (named SQLM) Stream B datasets could be used, as the requirements imposed on these datasets are unacceptable for the searches. The low-mass dataset requires both muons to have a CMP stub, thus reducing the acceptance of the sought signal below an acceptable level, and the sequential dataset does not accept muon pairs with an invariant mass below 1.0 GeV/c^2.

The $B^0 \to \mu^+\mu^-$ candidates will be found exclusively in the Dimuon 4 Run 1A dataset and the BHMB Run 1B dataset, and these will be the only ones considered for this decay.

$B_s^0 \to \mu^+\mu^-\phi$ candidates will be found in the Dimuon 1, Dimuon 2 and Dimuon 3 Run 1A datasets and all of the four above-mentioned Run 1B datasets. The resonant $B_s^0 \to J/\psi\,\phi$ candidates will be found in the Dimuon 2 Run 1A dataset and the PSAB Run 1B dataset.

Selection requirements common to the two searches will be given in this section. Requirements specific to each decay will be given in the relevant sections.

8.1.2. Detector and trigger requirements

The muon detectors used in this study are mostly conditioned by the requirements imposed by the Level 3 triggers.

The Run 1A Level 3 trigger used requires both muons to be observed in the CMU, and CMX muons are therefore excluded from the Run 1A datasets.

In Run 1B, the BHMB dataset requires that at least one of the two muons have a stub in the CMP. CMX muons are allowed, but the CMP requirement discards muon pairs with both muons observed in the CMX. As in the $B_s^0 \to \mu^+\mu^-\phi$ search the four datasets are combined, this requirement will be imposed on all the datasets in order to have a consistent data sample.

As can be seen, these datasets (and the other samples used in B physics) only use the central muon detectors. The FMU is not used as its coverage does not overlap the CTC and the SVX, precluding a vertex measurement. Furthermore, the momentum resolution of the FMU is significantly worse than that of the CTC.

In Run 1B, none of the Level 3 triggers required in the datasets specifically request a Level 2 dimuon trigger. As some of the constraints imposed on the muon pair at Level 3 are looser than at Level 2, a muon pair not satisfying the Level 2 dimuon trigger requirements could still be accepted by one of the Level 3 dimuon triggers. These events are called *volunteers*.

In both searches, the trigger selection efficiencies for the sought decays have to be determined precisely. These are determined using a Monte Carlo simulation of the dimuon triggers, which will be described in Appendix A.4. As volunteers do not pass the Level 1 and Level 2 dimuon triggers but some other trigger, their efficiency is difficult to determine. Therefore, only events with a well defined trigger path are retained, and volunteers are rejected.

The triggers requested are the TWO_CMU_ONE_CFT trigger for the Run 1A data, and the TWO_CMU_TWO_CFT_2_2, CMX_CMU_TWO_CFT_2_2, TWO_CMU_CMX_ONE_CFT_3_4 and TWO_CMU_ONE_CFT_2_2_6TOW triggers for the Run 1B data[1].

Even for events having passed one of the requested Level 2 triggers, no information is given on which of the muon pairs, if several are present, have satisfied the trigger requirements. To confirm that the two muon candidates selected are the ones that have fired the triggers, and not two random muons from the underlying event, the same trigger simulation is required to confirm that the candidate muons satisfy the trigger requirements.

[1]Other dimuon triggers could not be used, as the measured efficiency curves of these triggers have not been implemented in the dimuon trigger simulation used.

Runs for which the central muon chambers were not declared operational or for which the trigger efficiencies were not deemed to be reliable were discarded for this study [155].

8.1.3. The primary vertex

The location of the primary interaction vertex is used in several instances in this study, as will be described in the following sections. Therefore, runs for which the beam position is not available are discarded.

The z-coordinate of the vertex was determined for each event using the tracks measured in the VTX. The uncertainty on this coordinate has been fixed at $\sigma_z = 3\,\text{mm}$, as the calculated uncertainty was deemed unreliable.

The transverse $(x - y)$ coordinates were determined using SVX and CTC tracks. They were not measured for each event separately, but averaged over the course of each run, as they would vary by less than 10 μm over the course of a run. The slope and intercept of the beam position were obtained using all measured tracks over the course of a run. The transverse coordinates for each event would then by obtained by using the z-coordinate measured in the VTX. The coordinates obtained in this way were attributed an uncertainty of 25 μm in the x and the y direction. This method is preferred over using transverse coordinates determined separately for each event, since in this case, the resolution would be dominated by low track multiplicities and individual event topologies.

8.2. Track quality requirements

To reduce uncertainties on track parameters and derived quantities due to poor track measurements, quality requirements are imposed on the tracks used in this study.

The primary tracking system at CDF is the CTC. First, track segments of several consecutive hits are located in the axial superlayers, and, starting from the outer superlayer, linked together to form a two-dimensional (2D) track in the $r - \phi$ plane. Then, with the z_0 parameter supplied by the VTX, stereo hits are added to form a full three-dimensional (3D) parameterization.

To include the SVX [156], the CTC track is extrapolated to the outer layer of the SVX, accounting for multiple scattering and energy losses in the material crossed. A road in the $r - \phi$ plane is then calculated in which to look for hit clusters. Starting on the outer layer, hit clusters are added and the track parameters are recalculated for every layer, accounting for multiple scattering effects in all materials crossed. The track is declared an SVX track if a minimum of hits, three for the SVX and two for the SVX', could be included in the fit.

For this study, tracks are required to be reconstructed in the CTC with at least four hits in each of at least two axial superlayers and at least two hits in each of at least two stereo superlayers. No requirement on which of the superlayers had to feature the hits was made. These requirements, referred to as *CTC hit selection*, ensure that tracks are reconstructed with a minimal pattern of hits, permitting a good determination of their parameters.

For tracks measured in the SVX, SVX information will only be used for tracks with at least three hits in the SVX and a requirement on the SVX-χ^2/hit is imposed. The

SVX-χ^2/hit is the increase of the track-fit-χ^2 per SVX hit when including SVX hits to the CTC track fit, accounting for the detector resolution and multiple scattering. These requirements are designed to reject accidental combination of hits in the SVX and associate to the CTC information only hits consistent with the track reconstructed in the CTC. At event selection, all SVX tracks are refitted using the best set of alignment constants.

In the search for the decays $B^0 \to \mu^+\mu^-$, both muons are required to be measured in the SVX, and for each track, the SVX-χ^2/hit is required to be less than 5.0.

In the search for the decay $B_s^0 \to \mu^+\mu^-\phi$, both muons and at least one of the two kaon tracks are required to be measured in the SVX. For each track, the SVX-χ^2/hit is required to be less than 6.0.

The tracking algorithm employed at CDF begins by locating track segments in the outer axial superlayer of the CTC, the occupancy of this superlayer being much lower than the inner ones. Tracks with a transverse momentum below 250 MeV/c would not exit the CTC through the outer cylinder, but loop in the CTC until they exit through the endplates (hence their name, *loopers*). Lower momentum tracks are produced in large numbers, and their reconstruction would have been difficult due to the large number of helixes intersecting. The pattern recognition algorithm therefore only finds tracks with $p_T > 250$ MeV/c, and a high track-finding efficiency and good resolution of the track parameters is only reached for tracks with $p_T > 400$ MeV/c.

In this study, tracks will thus be required to have a transverse momentum greater than 400 MeV/c, to ensure a high and reliable efficiency and a good resolution of the track parameters.

8.3. Muon selection requirement

A central muon is identified by extrapolating a CTC track to the muon chambers and matching it with a muon stub. Correcting the difference between the extrapolated CTC track and the muon stub for p_T-dependent effects such as multiple scattering and energy losses, and accounting for measurement uncertainties, a p_T-independent χ^2 matching quantity is constructed. The square root of the matching-χ^2 has a Gaussian distribution with $\sigma = 1$. This matching-χ^2 is independently calculated in both the transverse and longitudinal planes for CMU and CMX muons, while for CMP muons, it is only calculated in the transverse plane.

For this study, the muons selected are required to have the relevant matching-χ^2 less than 3σ from zero (i.e. smaller than 9). This is tighter than the requirement imposed at Level 3, where the maximum matching-χ^2 ranges from 3σ to 5σ, according to the trigger.

Furthermore, the energy deposition in the hadronic calorimeter associated with the candidate muon is required to be greater than 0.5 GeV, which is 3σ lower (based on the RMS of the Landau distribution below the peak) than the average expected energy loss of a minimum ionizing particle.

These requirements are designed to reduce the background due to punch-through hadrons and light hadrons decaying to muons. Not being absorbed in the hadronic calorimeter, punch-through hadrons would reach the muon systems, faking a muon signal. Charged

pions or kaons, with a lifetime of 7.8 m and 3.7 m respectively [1], could decay before reaching the calorimeters and the produced muon would be observed in the muon systems. In both cases, the measured muon stub would show a significant displacement relative to the extrapolated CTC track of the hadron.

The minimum momentum for a muon to reach the muon systems ranges from 1.4 GeV/c for the CMU to 2.2 GeV/c for the CMP at $\eta = 0$. The events used in this study were collected with the low-p_T dimuon triggers, detailed in Section 6.7.2. As the measurements of the branching fractions require the calculation of the trigger efficiencies, a reliable modelling of the trigger behaviour is thus essential.

As the intrinsic width of the turn-on region of the trigger efficiency parameterization and measurement uncertainties result in large effects on the signal-efficiencies, a requirement on the minimum transverse momenta of the muon is imposed. In Run 1B, for positive CMU muons in the CFT, the 50% point in the turn-on of the lowest p_T bin is $1/p_{T\,50} = 0.51283 \pm 0.00078(\text{ GeV}/c)^{-1}$ (≈ 1.95 GeV/c) and the width of the turn-on is $\sigma^0_{1/p_T} = 0.0394 \pm 0.0010(\text{ GeV}/c)^{-1}$ [157] (values for negative muons are similar). Furthermore, below 1.8 GeV, the measured Level 1 efficiencies are not deemed reliable.

In the search for the decays $B^0 \to \mu^+\mu^-$, both muons are required to have a transverse momentum greater than 2.0 GeV, for both Run 1A and Run 1B.

In the search for the decay $B_s^0 \to \mu^+\mu^-\phi$, for Run 1A, both muons are required to have a transverse momentum greater than 2.0 GeV. For Run 1B, when both muons match a CFT track, both muons are required to have $p_T > 2$ GeV/c. When only one muon matches a CFT track, the high-p_T muon is required to have $p_T > 2.8$ GeV/c and the low-p_T muon $p_T > 1.8$ GeV/c.

8.4. B mesons selection requirement

For this study, three different decay channels are selected. The similarities between the channels allow the reconstruction of the B meson candidate in a similar way while imposing similar selection requirements.

The B meson candidate is reconstructed using a least-squares kinematic fit of the candidate tracks, where the tracks are constrained to come from a common secondary vertex (*vertex-constrained fit*). Candidates failing the fit procedure are discarded by imposing a requirement on the confidence level of the fit. This eliminates candidates with tracks that are spatially close but are not consistent with a common vertex.

All tracks used are required to pass the CTC hit selection. The track parameters derived from the combined SVX-CTC information are used in the fit for tracks passing the SVX quality requirements. Otherwise, only track parameters derived from the CTC measurements are used. To permit the reconstruction of the decay vertex of the B candidate with a good precision, a minimum number of daughter tracks are required to be measured in the SVX.

All quantities used subsequently will be based on the track parameters derived from the fit, both for the B meson and for its daughter tracks.

8.4.1. $B^0 \to \mu^+\mu^-$ reconstruction

In the search for the decay $B^0 \to \mu^+\mu^-$, two muons of opposite charge, both measured in the SVX are required. The probability of the vertex-constrained fit is required to be greater than 0.0005 ($P(\chi^2) > 0.05\%$). As the fit has one degree of freedom, the upper bound on the χ^2 is 12.

8.4.2. $B_s^0 \to \mu^+\mu^-\phi$ and $B_s^0 \to J/\psi\,\phi$ reconstruction

First, as in the $B^0 \to \mu^+\mu^-$ reconstruction, two muons of opposite charge, both required to be measured in the SVX, are fitted to a common vertex. The invariant mass derived from this fit is subsequently used to determine whether the B_s^0 candidate underwent a resonant or a non-resonant decay.

As both decays are observed with two oppositely charged muons and two oppositely charged kaons, two further tracks of opposite charge are then associated to the muon pair. At least one of the tracks is required to be measured in the SVX. As CDF lacks the ability to identify observed tracks (with the obvious exception of muons), all measured charged tracks have to be considered as kaon candidates. This adds to the candidate sample a significant contribution of combinatorial background.

Assigning a kaon mass to the two additional tracks, the four tracks are fitted to a common vertex. In addition to the vertex constraint, the momentum vector of the B meson is constrained to be parallel to its flight path in the transverse ($r-\phi$) plane (*2D-pointing constraint*). This momentum vector is thus required to point back from the secondary decay vertex to the primary vertex.

The pointing constraint was not imposed in the longitudinal (z) direction, due to the limited precision of both the primary vertex and the track parameters in this direction. Contrary to the transverse plane, where individual coordinates are measured by the SVX with hit resolutions of the order of 10 μm and secondary vertices are reconstructed with a resolution of the order of 40 μm, track reconstruction in the z-direction rely on measurements made in the stereo wires of the CTC, where the resolution is of a few millimetres. Similarly, the primary vertex is measured in the transverse plane with a resolution of 40 μm, whereas it is measured in the z-direction in the VTX with a resolution of 1 mm.

For $B_s^0 \to J/\psi\,\phi$ candidates, the two muons are constrained to have an invariant mass equal to the world-average J/ψ mass[2] (*mass-constraint*). As, compared to the mass measurement resolution at CDF, the J/ψ has a narrow width[3], the mass-constraint permits to improve the quality of the global fit.

The confidence level of the global fit is required to be greater than 0.01 ($P(\chi^2) > 1\%$). For $B_s^0 \to \mu^+\mu^-\phi$ candidates, where the vertex- and pointing-constrained fit has six degrees of freedom, the upper bound on the χ^2 is 16.81. For $B_s^0 \to J/\psi\,\phi$ candidates, where the vertex-, pointing- and mass- constrained fit has seven degrees of freedom, the upper bound on the χ^2 is 18.47.

[2] $m(J/\psi) = 3.096.88 \pm 0.04$ MeV/c^2 [1].

[3] $\Gamma(J/\psi) = 87 \pm 5$ keV/c^2 [1].

The small width of the ϕ[4] permits to require the invariant mass of the kaon pair to fall within 10 MeV/c^2 of the world-average ϕ mass[5]. This requirement significantly reduces the combinatorial background arising from the blind mass assignment.

8.4.3. The proper decay length requirement

The long lifetime of B mesons allows the use of the proper decay length as a strong rejection criteria against the mostly short-lived background. The proper decay length $c\tau$ is defined as

$$c\tau = L_{xy} \cdot \frac{m_{B^0}}{p_T^B} , \tag{8.1}$$

where the transverse decay length L_{xy} is the projection of the decay length vector on the transverse momentum

$$L_{xy} = \frac{\vec{l}_{xy} \cdot \vec{p}_T^B}{p_T^B} . \tag{8.2}$$

$\vec{l}_{xy}$ is the vector pointing from the primary interaction vertex to the secondary decay vertex and $\vec{p}_T^B$ is the transverse momentum vector of the B candidate. Both are determined using quantities derived in the vertex fit described above. As in the search for the decay $B_s^0 \to \mu^+\mu^-\phi$, the kinematic fit includes a 2D-pointing requirement, where the transverse momentum vector is required to point towards the primary vertex, L_{xy} would be equal to the magnitude of $\vec{l}_{xy}$.

The tight SVX requirements imposed on the observed tracks and the requirement that the beam position be measured are motivated by this requirement, as it requires a precise measurement of the position of the primary and secondary vertices. With a measured lifetimes of $c\tau(B_d^0) = (1.56 \pm 0.04)$ ps $= 468 \pm 12$ μm and $c\tau(B_s^0) = (1.54 \pm 0.07)$ ps $= 462 \pm 21$ μm [1], a mean transverse decay length of approximately 860 μm is expected for the signal.

In the search for the decay $B^0 \to \mu^+\mu^-$, a requirement is imposed on the error on the transverse decay length $\sigma(L_{xy})$. This error is required to be smaller then 150 μm. The mean error for $J/\psi \to \mu^+\mu^-$ candidates is approximately 60 μm, as shown in Figure 8.1.

8.4.4. The isolation requirement

Due to the hard fragmentation of b quarks [47], the B meson produced in the fragmentation process are expected to carry most of the transverse momentum of the b quark. A large fraction of the momentum of the tracks observed in a cone around the B meson is thus expected to be carried by the daughter tracks of the B meson.

The momentum fraction carried by the B candidate, the *isolation*, is defined as

$$I = \frac{p_T^B}{p_T^B + \sum p_T} . \tag{8.3}$$

[4] $\Gamma(\phi) = 4.43 \pm 0.05$ MeV/c^2 [1].

[5] $m(\phi) = 1019.413 \pm 0.004$ MeV/c^2 [1].

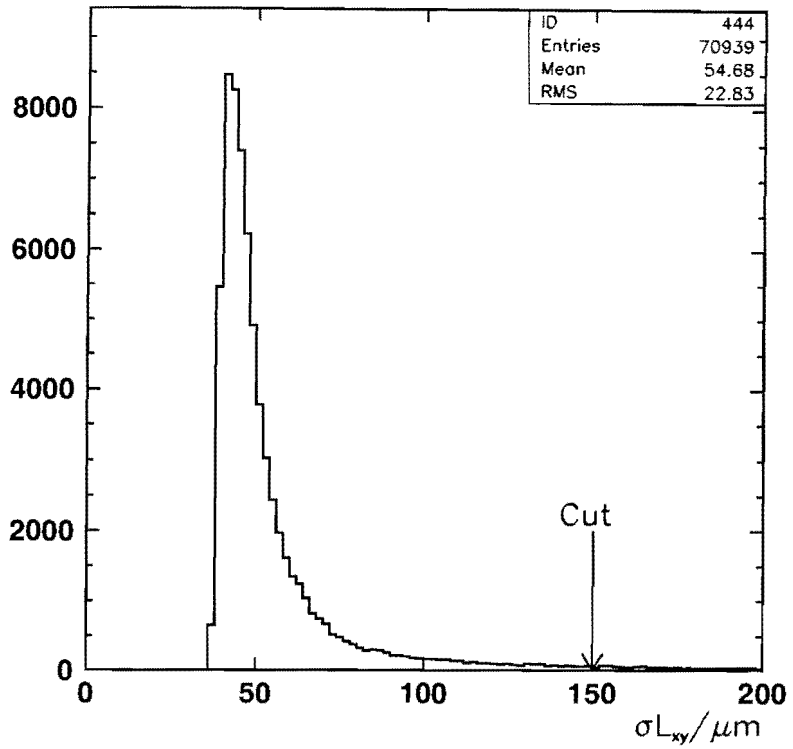

Figure 8.1: *$\sigma(L_{xy})$ distribution of oppositely charged muon pairs from $J/\psi \rightarrow \mu^+\mu^-$ decays.*

The sum ($\sum p_T$) is the scalar sum of the transverse momenta of all the tracks (except the tracks composing the B candidate) within a cone of $\Delta R = 1$ around the momentum vector of the B candidate. ΔR is defined as $\Delta R = \sqrt{(\Delta\eta)^2 + (\Delta\phi)^2}$. The z-coordinate of these tracks must be within 5 cm of the B candidate vertex so as to exclude tracks from other $p\bar{p}$ collisions that can occur during the same bunch crossing.

The isolation variable used initially in Run 1A analyses [158] did not impose a requirement on the z-coordinate of the tracks in the sum. This requirement was added after it was shown that the isolation of B candidates was significantly lower in Run 1B than in Run 1A [159]. As with the higher instantaneous luminosity of Run 1B multiple $p\bar{p}$ collisions can occur in the same bunch crossing, tracks originating from another collision than that of the B candidate can be found in the cone around the B candidate. These tracks can be removed by imposing the z-coordinate requirement. For consistency, this requirement has has also been imposed for this study on the Run 1A sample.

8.4.5. The pointing angle requirement

In the search for the decay $B^0 \rightarrow \mu^+\mu^-$, a further requirement is imposed on the opening angle Φ (called *pointing angle*) between $\vec{p}_T^B$ and $\vec{l}_{xy}$, effectively requiring the vectors $\vec{p}_T^B$ and $\vec{l}_{xy}$ to point in the same direction. The variable is well defined, since requirements on a minimum decay length and transverse momentum are imposed before calculating the angle.

This requirement is not necessary in the search for the decay $B_s^0 \to \mu^+\mu^-\phi$, as the kinematic fit includes a 2D-pointing requirement, where the transverse momentum vector is required to point towards the primary vertex.

Chapter 9

The search for the decays $B_d^0 \to \mu^+\mu^-$ and $B_s^0 \to \mu^+\mu^-$

9.1. The luminosity of the data sample

A direct measurement of the branching fraction requires the determination of the total luminosity of the data sample used (Equation 7.1). For this search, the Run 1A Dimuon 4 and the Run 1B BHMB datasets are used. Both running periods have different experimental conditions, and the efficiencies of both will be different. Furthermore, the Run 1B data sample was collected with four different triggers, each with a different efficiency. Some of the triggers were only used for part of Run 1B, and the data accumulated with them corresponds to a smaller integrated luminosity. As, with the exception of the TWO_CMU_TWO_CFT_2_2 trigger, these triggers were prescaled, their overall contribution is further reduced.

The total integrated luminosity of the Run 1B sample is given by the sum of the integrated luminosity weighted by the expected relative contribution C_t of each trigger:

$$\mathcal{L}_{total} = \sum_{t=triggers} \mathcal{L}_t \cdot C_t \,. \tag{9.1}$$

The Level 2 triggers retained are shown in Table 9.1, with their integrated luminosity before prescaling and prescale factor, as obtained from the luminosity database. In addition the expected relative contribution from each trigger to the signal, as estimated by Monte Carlo, is listed. These luminosities are calculated after removal of runs not suitable for this analysis, as detailed in Sections 8.1.2 and 8.1.3. It can be noted that, although some triggers overlap, the sum of the contributions equal 100%, since each event is assigned to only one of the triggers.

The Monte Carlo procedure followed to simulate the expected signal is detailed in Appendix A. It is worth reminding at this point that the Run 1B dimuon trigger simulation takes the prescale factors and muon chamber inefficiencies into account when modeling the trigger efficiencies.

A sample of inclusive $B \to J/\psi X$ decays is used to verify the procedure used to estimate the relative contributions. This sample is described in Section 9.5.2. Table 9.2 shows the

Trigger	$\int \mathcal{L}dt$ [pb^{-1}]	Contribution (includes prescale)	prescale factor
TWO_CMU_TWO_CFT_2_2	81.2 ± 6.7	66.5%	100 %
CMX_CMU_TWO_CFT_2_2	81.2 ± 6.7	23.7%	73.9 %
TWO_CMU_ONE_CFT_2_2_6TOW	76.8 ± 6.1	2.7%	83.7 %
TWO_CMU_CMX_ONE_CFT_3_4	71.0 ± 5.7	7.1%	34.2 %
Run 1B Weighted Total	80.4 ± 6.6		
Run 1A: TWO_CMU_ONE_CFT	17.8 ± 0.6	100%	100%

Table 9.1: *Level 2 triggers requested, with their corresponding integrated luminosity, prescale factor and expected contribution. Relative contributions include the prescale factor.*

Trigger	J/ψ data	J/ψ MC
TWO_CMU_TWO_CFT_2_2	67.02 ± 0.54	$69.62 \pm 1.5\%$
CMX_CMU_TWO_CFT_2_2	18.66 ± 0.45	$17.94 \pm 1.2\%$
TWO_CMU_ONE_CFT_2_2_6TOW	8.26 ± 0.32	$7.86 \pm 1.2\%$
TWO_CMU_CMX_ONE_CFT_3_4	6.02 ± 0.25	$4.58 \pm 1.0\%$

Table 9.2: *Relative contributions of the Level 2 triggers as measured for J/ψ data and Monte Carlo.*

relative contributions of the triggers as measured for the background subtracted J/ψ's and as estimated by Monte Carlo simulations of the inclusive decay. As can be seen, both are found to be in good agreement, confirming the procedure used.

9.2. The basic selection requirements

In the initial sample, unsuitable runs have been discarded, and only events accepted by one of the chosen dimuon triggers and for which the candidate muon pair confirms the dimuon trigger are kept.

The basic quality and selection requirements applied to the data sample were given and motivated in Section 8. As a brief reminder, they will be listed below:

- Muon matching requirements.
- CTC hit selection.
- SVX quality requirements, with both muons required to be in the SVX.
- The error on the transverse decay length $\sigma(L_{xy})$ is required to be below 150 μm.
- The transverse momentum of each muon is required to be above 2 GeV/c.
- The transverse momentum of the muon pair is required to be above 6 GeV/c, to normalize the measurement to the measured cross-section.

Requirement	Run 1A		Run 1B		1A + 1B	
	OS	LS	OS	LS	OS	LS
Initial sample	6859	5914	20018	16338	26877	22252
CTC hit selection	6854	5904	19967	16290	26821	22194
SVX tracks selection	4266	3629	14977	11900	19243	15529
$\sigma(L_{xy}) < 150$ μm	3466	2971	12578	9895	16044	12866
$p_T(\mu^+\mu^-) > 2$ GeV/c	3208	2763	10525	8193	13733	10956
$p_T(\mu^+\mu^-) > 6$ GeV/c	244	189	951	638	1195	827
SVX-χ^2/DoF< 5	237	181	898	591	1135	772
Vertex-fit $\chi^2 < 12$	232	171	862	565	1094	736

Table 9.3: *Number of events remaining in the overlapping B_d^0 and B_s^0 search region (5.205–5.450 GeV/c^2) in the different samples after each selection requirement.*

- The χ^2 of the vertex-constrained fit is required to be below 12 (1 dof).

For both decays, 150 MeV/c^2 search regions, centered on the world-average mass of the relevant B meson[1], are chosen. These are thus the muon pair-invariant mass regions $5.205 - 5.355$ GeV/c^2 for the B_d^0 and $5.295 - 5.445$ GeV/c^2 for the B_s^0.

Table 9.3 lists the number of events remaining in the search regions after each requirement, for both opposite-sign (denoted *OS*) and same-sign muon pairs (denoted *LS*). Same-sign muon pairs are used as an estimate of the background contribution in the search region. The invariant mass spectrum of the muon pairs after the basic selection requirements is shown in Figure 9.1. The proper decay length, isolation and pointing angle requirements will be chosen in the next section.

9.3. A Run 1A cross check

In order to confirm the selection procedure, the previously published search [139], based only on Run 1A data, has been repeated. In addition to the basic requirements described in the previous section, the proper decay length was required to be greater than 100 μm and the isolation greater than 0.7. The isolation variable used did not impose a z-coordinate requirement on the tracks in the sum of Equation 8.3 (Section 8.4.4).

With these selection requirements, the same result has been found. No candidates has been found in the B_d^0 search region and the one identical event has been found in the B_s^0 region.

Applying the same isolation requirement to the Run 1B data sample (now with the z-coordinate requirement), a total of ten events are left in the two overlapping search regions. Six candidates are identified in the B_d^0 search region and six in the B_s^0 search region (Figure 9.2, right). For Run 1A, the result is the same as previously (Figure 9.2, left).

[1] $m(B_d^0) = 5279.2 \pm 1.8$ MeV/c^2 and $m(B_s^0) = 5369.3 \pm 2.0$ MeV/c^2 [1].

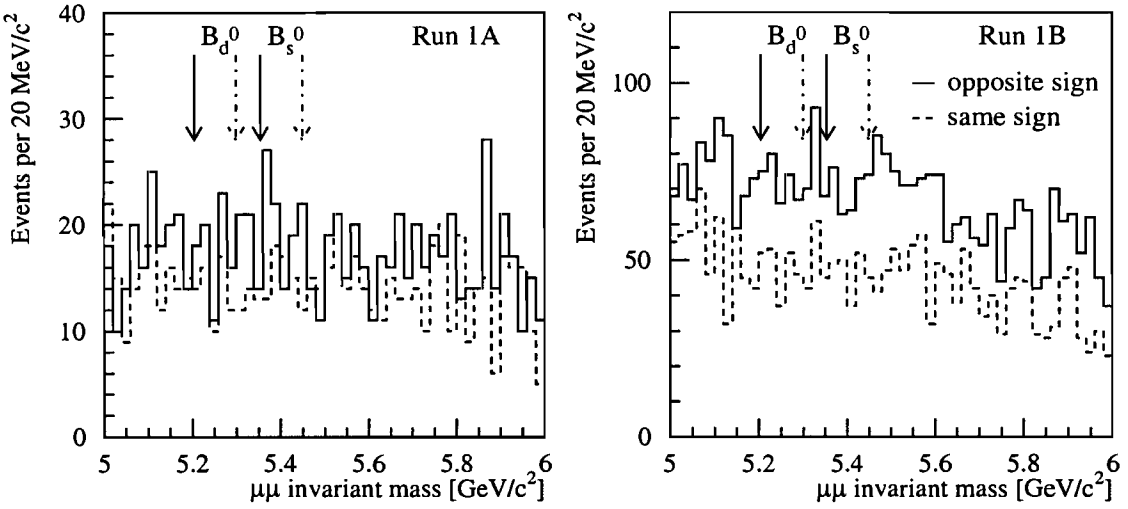

Figure 9.1: *Invariant mass distribution of opposite- and same-sign muon pairs after the basic selection requirements.*

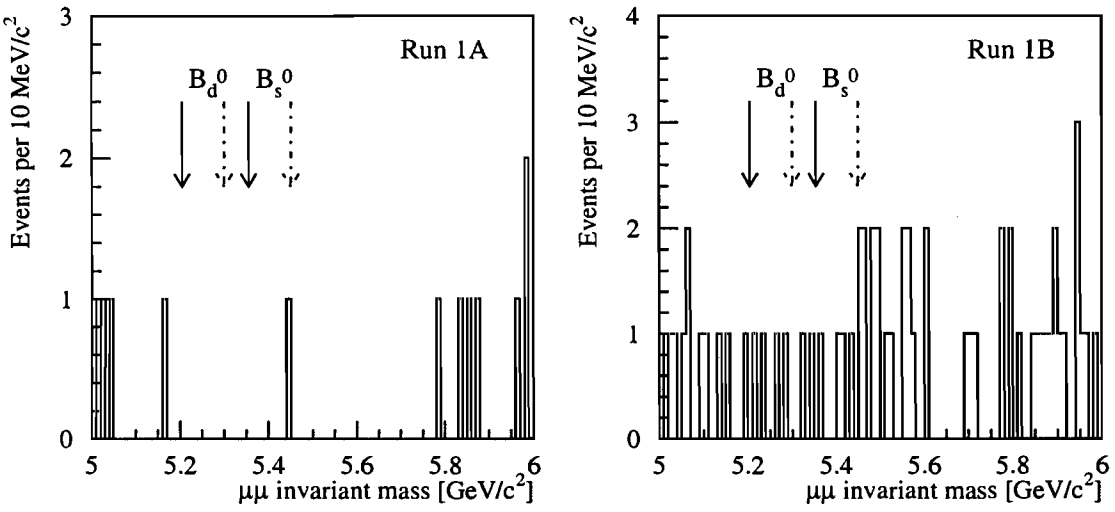

Figure 9.2: *Invariant mass distribution of oppositely charged muon pairs after the basic selection requirements and the isolation requirement in the Run 1A (left) and Run 1B (right) data samples. The "z-requirement" is imposed in both Run 1A and Run 1B.*

9.4. Optimization of the selection requirements

Three further requirements are applied to the data sample, the proper decay time, isolation and pointing angle requirements, with the aim of reducing the background, while retaining a high efficiency for the sought signal. These requirements are chosen by maximizing the *signal-to-background significance*. The optimization is conducted on the Run 1B data sample. The samples used to model the background are presented in Section 9.4.1 and the signal-to-background significance will be defined in Section 9.4.2. The requirements chosen will then be presented in Section 9.4.3.

9.4.1. The background

Two samples of pure background, believed to be similar to the background found in the search region, are used to study the rejection power of the requirements. The first sample are the same-signed muon pairs in the invariant mass range between 5 and 6 GeV/c^2. The second sample are opposite-signed muon pairs in the sideband invariant mass regions $5.0 - 5.2$ GeV/c^2 and $5.5 - 6.0$ GeV/c^2. These background events are mainly muons from hadron decays and punch-through hadrons.

In these invariant mass ranges, no contributions from sequential semileptonic B decays[2] or leptons coming from back-to-back produced B's are expected. The invariant mass of muons produced in sequential B decays is typically below 3 GeV/c^2.

Figures 9.3 and 9.4 show the distributions of the isolation and pointing angle respectively, of opposite-sign and same-sign muon pairs and of background subtracted $B^+ \to J/\psi K^+$ and $B^0 \to J/\psi K^{*0}$ candidates. The latter two decays are used to evaluate the efficiencies of the requirements. For these histograms, all selection requirements, with the exception of the pointing angle and isolation requirements, are applied. The background subtracted distributions are obtained by subtracting to the signal region distribution ($5.2 - 5.35$ GeV/c^2) the sideband region distribution ($5.0 - 5.2$ and $5.5 - 6.$ GeV/c^2) normalized to the same area.

9.4.2. The signal-to-background significance

The *signal-to-background significance* is defined as

$$sig = \frac{S^2}{B} = \frac{(\epsilon_S \cdot S_0)^2}{\epsilon_B \cdot B_0} \,. \tag{9.2}$$

S and B are the signal and background events remaining after a particular set of requirements. With S_0 and B_0 the number of signal and background events remaining after the initial selection, before the requirements to be optimized are imposed, the significance can be related to the efficiency of the requirements on each sample, ϵ_S and ϵ_B. As S_0 and B_0 will be constant for all trials, these can be omitted, and the significance can be written as

$$sig = \epsilon_S^2 \cdot R_B \,, \tag{9.3}$$

[2] of the type $b \to c\mu^-\bar{\nu}$, $c \to s\mu^+\nu$

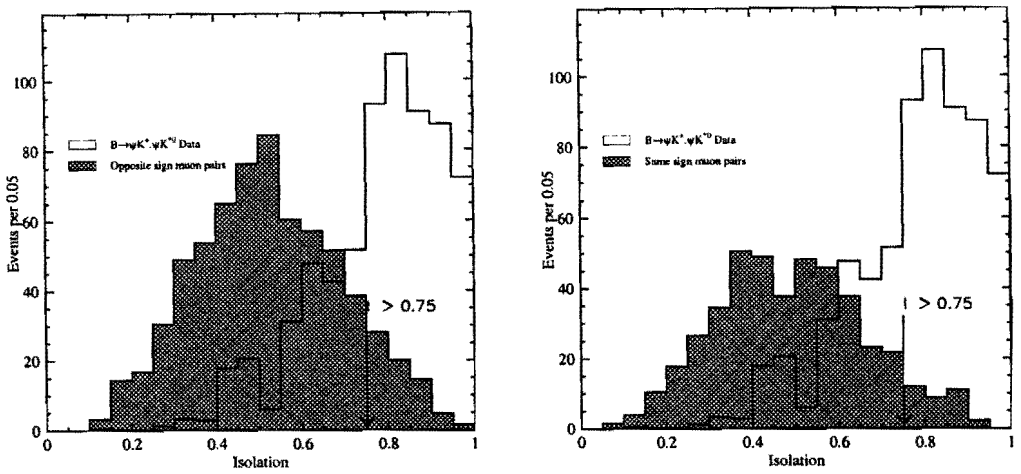

Figure 9.3: *Distribution of the isolation of opposite-sign (left) and same-sign (right) muon pairs in the 5 to 6 GeV/c^2 mass range and of background subtracted $B^+ \to J/\psi K^+$ and $B^0 \to J/\psi K^{*0}$ candidates after all selection requirements except the pointing angle and isolation selection requirements. The arrow represents the chosen cut.*

where R_B is the rejection factor of the background ($R_B = 1/\epsilon_B$) as observed in the background sample.

The efficiencies of the isolation and pointing angle requirements needed in the expression of the signal-to-background significance are measured on $B^+ \to \mu^+\mu^-K^+$ and $B^0 \to J/\psi K^{*0}$ candidates. The measurement of their efficiencies will be presented in Section 9.5.5. Since the combinatorial background is different for three or four tracks, these candidates cannot be used to check the rejection power of the cuts, and the background samples detailed above have to be used. The efficiencies of the proper decay length requirements are determined from a Monte Carlo simulation, as explained in Section 9.5.4

The value of the signal-to-background significance for the different combinations of proper decay length, isolation and pointing angle requirements are shown in Table C.1 for the same-sign sample, and in Table C.2 for the opposite-sign sideband sample. Both tables are in Appendix C. As can be seen in these tables, for some tight requirements, no background event is left, and the signal-to-background significance is infinite. As the infinite signal-to-background significances do not permit to discriminate between the different sets of requirements anymore, the final requirement will be chosen by requiring the highest non-infinite signal-to-background significance, with the highest efficiency.

9.4.3. The final requirements

The best signal-to-background significance is obtained with a proper decay length requirement of $c\tau > 100$ μm, an isolation requirement of $I > 0.75$ and a pointing angle requirement of $\Phi < 0.1$. These requirements will thus be chosen for the final selection.

The invariant mass distributions of the candidates satisfying all requirements are shown

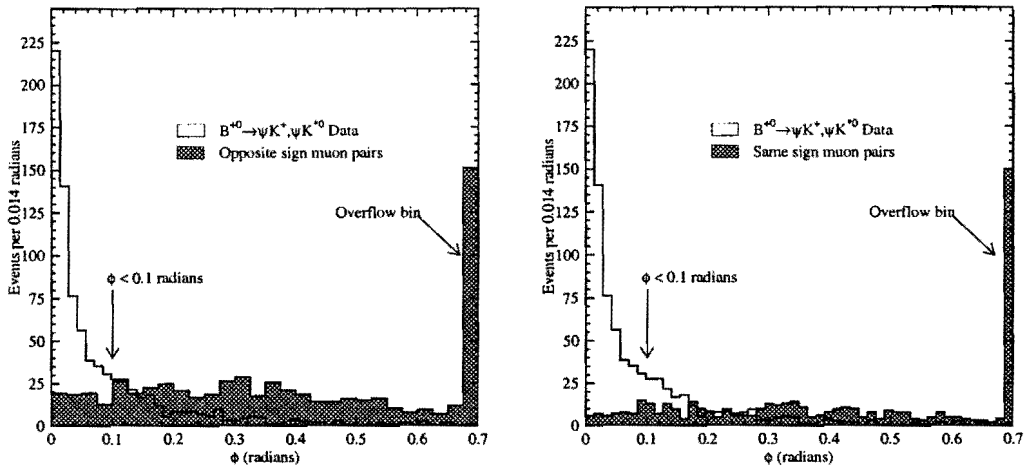

Figure 9.4: *Distribution of the pointing angle of opposite-sign (left) and same-sign (right) muon pairs in the 5 to 6 GeV/c^2 mass range and of background subtracted $J/\psi K^+$ and $J/\psi K^{*0}$ candidates after all selection requirements except the pointing angle and isolation requirements. The arrow represents the chosen cut.*

in Figure 9.5. Figure 9.6 shows the combined Run 1 invariant mass distribution. As can be seen, one event (from Run 1B), with an invariant mass of 5.344 ± 0.016 GeV/c^2 remains in the combined search region. The characteristics of this event are given in Table 9.4. As it is in the overlapping part of the B_d^0 and B_s^0 search regions, this will result in one candidate for both the B_d^0 and B_s^0 (c.f. Figure 9.5). The candidate found in the previous Run 1A analysis does not satisfy the pointing angle requirement.

In Run 1A, one same-signed muon pair is observed in the $5 - 6$ GeV/c^2 mass region and five in Run 1B. Extrapolating the observed number of events to the 0.15 GeV/c^2 wide search regions, 0.15 background event can be expected in Run 1A and 0.75 in Run 1B.

Invariant mass	5.344 ± 0.016 GeV/c^2
1^{st} Muon p_T	4.49 GeV/c
2^{nd} Muon p_T	2.20 GeV/c
Muon pair p_T	6.32 GeV/c
Lifetime	103.8 μm
Isolation	0.833
Pointing angle	0.036 radians

Table 9.4: *Run 1B candidate event.*

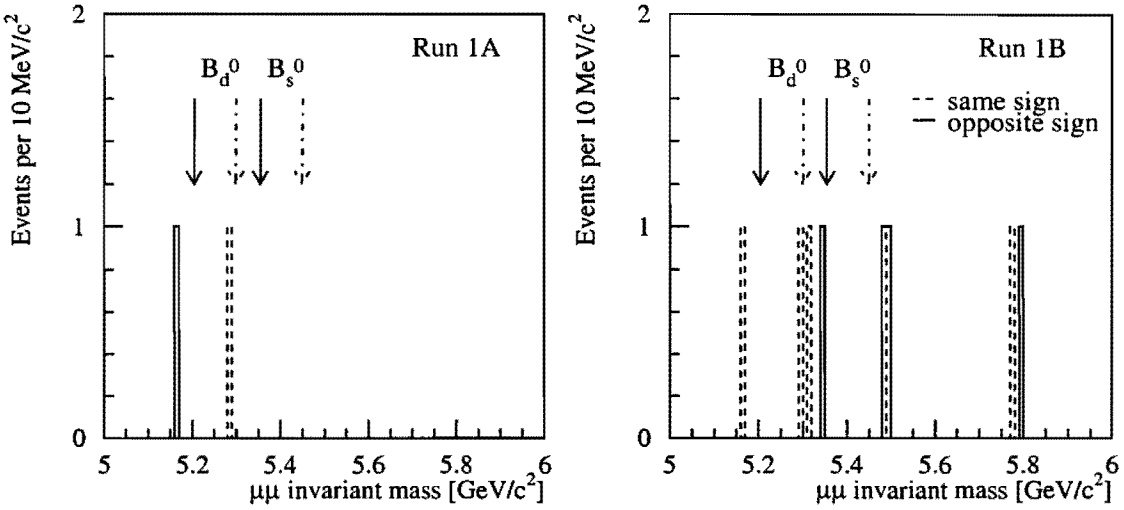

Figure 9.5: *Invariant mass distribution of oppositely charged muon pairs after all selection requirements in the Run 1A (left) and Run 1B (right) data samples. Solid lines represent opposite-signed muon pairs and dashed lines represent same-signed muon pairs.*

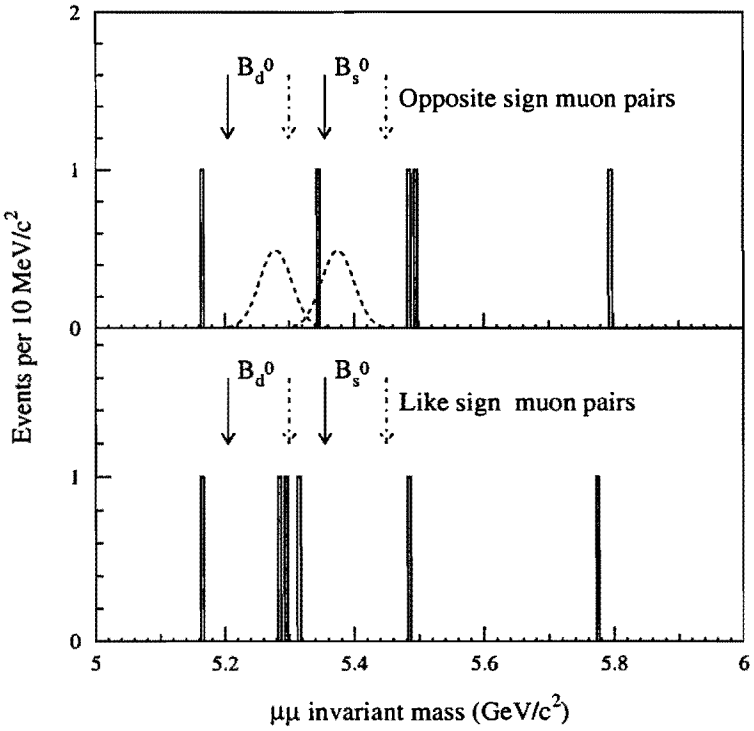

Figure 9.6: *Invariant mass distribution of opposite-signed (top) and same-signed muon pairs (bottom) muon pairs after all selection requirements in the combined Run 1 sample. The two functions represent the 90% C.L. upper limit with the expected resolution.*

9.5. Acceptance and selection efficiencies

In a direct measurement of the branching fraction, the absolute acceptance and efficiencies of the selection requirements imposed are necessary. These factors, and the measurements thereof, will be described in this section.

Although these factors will be derived from data whenever possible, Monte Carlo simulation will have to be used as well. Due to the different detector geometry and experimental conditions, different acceptance and efficiencies are expected for Run 1A and Run 1B.

9.5.1. Geometric acceptance

The geometric acceptance represents the fraction of opposite-sign muon pairs (from the $B^0 \to \mu^+\mu^-$ decay) observed in the central muon chambers, with both tracks measured in the SVX. It includes the acceptance of the SVX requiring at least 2 hits on the track, the minimum required for a track to be observed in the SVX. For Run 1A, only muons observed in the CMU are accepted, and for Run 1B, at least one of the muons is required to have a CMP stub.

The geometric acceptance of the sought process can only be determined from a Monte Carlo simulation and not from data. The acceptance is found to be $(8.31 \pm 0.06)\%$ in Run 1A and $(11.25 \pm 0.08)\%$ in Run 1B. The uncertainties quoted are due to Monte Carlo statistics alone. The difference in acceptance between Run 1A and Run 1B can be attributed to the inclusion of the CMX in Run 1B.

9.5.2. Track quality efficiencies

CTC tracking efficiency

The efficiency of reconstructing tracks in the CTC cannot be estimated reliably by the Monte Carlo simulation used, as the detector simulation does not use the same track reconstruction algorithms as the offline data reconstruction. Furthermore, the CTC pattern recognition is affected by conditions external to the simulated process. It has been shown that significant deterioration of the CTC tracking capabilities occurred in the course of Run 1B [160], due to the increase of the instantaneous luminosity and multiple interactions and CTC ageing.

The CTC pattern recognition efficiencies have been measured for Run 1A and Run 1B in References [161] and [162] respectively, in which Monte Carlo generated tracks have been embedded into real J/ψ data events, and the efficiency of reconstructing one or both tracks measured.

The efficiency of reconstructing two tracks has been found to be $(97.8 \pm 2.2)\%$ in Run 1A [161] and $(88.2 \pm 4.0)\%$ in Run 1B [162]. As this efficiency is not dependent on the type of charged particle producing the track, this factor will be applied here to the two sought muon tracks.

CTC hit selection, SVX quality and fit-χ^2 requirements

With two tracks reconstructed in the CTC and the SVX, this factor represents the efficiency of both tracks satisfying the CTC hit selection, SVX quality requirements and that their vertex-constrained fit yields a χ^2 lower than 12. This is estimated using $J/\psi \to \mu^+\mu^-$ data candidates, where the efficiency is taken as the fraction of candidates satisfying the requirements.

This efficiency is found to be $(66.7 \pm 0.4)\%$ in Run 1A and $(79.4 \pm 0.2)\%$ in Run 1B. The lower value of the Run 1A efficiency is due to the deterioration of the innermost SVX layer towards the end of the run, caused by radiation damage.

The Monte Carlo simulation for the inclusive decays $B^0 \to J/\psi X, J/\psi \to \mu^+\mu^-$ and the exclusive $B^0 \to \mu^+\mu^-$ predict efficiencies of $(75.3 \pm 0.5)\%$ and $(77.7 \pm 0.5)\%$, respectively. The efficiency found in the J/ψ data will be used.

J/ψ-yield correction

It has been observed that the production cross section of the J/ψ and Υ resonnances measured in Run 1B would on average be some 10% lower than the Run 1A measurement [163, 164]. Furthermore, the yield would drop over the course of Run 1B by 15% to 20%. even after accounting for all known run dependent corrections. This degradation is believed to be caused by high track occupancy and ageing of the CTC, which are related to the instantaneous and integrated luminosities respectively [165], although the CTC tracking efficiency study quoted previously [162] could not account for the loss of yield.

Having observed a loss in the yield of both J/ψ and Υ, it has to be expected that the sought decays would be affected as well. An additional inefficiency is added for the Run 1B sample to account for the expected decrease during the run. This correction factor is derived by estimating the loss of yield of inclusive $B \to J/\psi X$ decays incurred between Run 1A and Run 1B.

The inclusive decays will be found in the the Run 1A and Run 1B Stream A J/ψ datasets. To compare the evolution of the yield, Run 1B is divided in twelve run ranges, as shown in Table 9.5. This table shows the luminosity and tracking efficiency in each run range. As can be seen, the tracking efficiency is decreasing over the course of Run 1B.

To ensure that the J/ψ come from B decays, a vertex-constrained fit of the two muon tracks is done, and requirements similar to the search-sample are imposed. Looking at an inclusive decay, where the B meson is not fully reconstructed, the isolation and pointing angle requirements cannot be imposed.

- The position of the beam has to be measured.
- Only the TWO_CMU_TWO_CFT trigger in Run 1B and the TWO_CMU_ONE_CFT in Run 1A are accepted.
- Both tracks have to be reconstructed in the SVX, satisfying the CTC hit selection and SVX quality requirements.
- Standard Muon selection requirements.

	Begin Run Nr.	End Run Nr.	Luminosity pb^{-1}	Tracking eff. %
Run 1A	40000	48000	19.4	93.7 ± 2.8
1	55273	60000	3.5	92.5 ± 2.6
2	60001	61500	9.0	92.3 ± 2.7
3	61501	63500	5.4	88.8 ± 3.8
4	63501	64250	6.8	91.0 ± 2.3
5	64251	65000	6.7	90.2 ± 2.4
6	65001	66000	8.4	89.4 ± 2.4
7	66001	67000	7.4	87.2 ± 4.0
8	67001	67880	6.4	85.9 ± 3.3
9	67881	68500	6.5	84.6 ± 2.5
10	68501	69000	6.4	84.6 ± 3.9
11	69001	69700	4.6	80.1 ± 6.8
12	69701	72000	7.7	87.8 ± 3.5

Table 9.5: *Run ranges with luminosity and corresponding tracking efficiencies [166].*

- The lifetime $c\tau$ is required to be above 100 μm.
- The error on the transverse decay length $\sigma(L_{xy})$ is required to be below 150 μm
- The transverse momentum of each muon is required to be above 2 GeV/c.
- The transverse momentum of the muon pair is required to be above 6 GeV/c.
- The vertex-fit-χ^2 is required to be below 12.

The yield is defined as the sideband-subtracted number of J/ψ candidates corrected for the tracking and trigger efficiencies, acceptance and luminosity in each different run range. The acceptance and trigger efficiency is obtained by a Monte Carlo simulation of inclusive $B \to J/\psi X$ decays. The tracking efficiency includes the run dependent variations in the CTC track reconstruction.

For Run 1A, two different muon-p_T requirements were used. In the first case, the p_T of both muons were required to be higher than 2 GeV/c. Figure 9.7(left), shows the sideband-subtracted number of candidates in each run range and Figure 9.7(right) shows the yield. The ratio between the Run 1A yield and the luminosity-weighted Run 1B yield gives an efficiency of $81.2 \pm 4.6\%$. As this is the requirement imposed on the Run 1A search sample, this value will be used as the correction factor.

In the second case, the p_T of the first muon was required to be higher than 2.8 GeV/c and the second higher than 2.0 GeV/c. Figure 9.8(left), shows the sideband-subtracted number of candidates and Figure 9.8(right) shows the yield. Here, the ratio between the Run 1A yield and the luminosity-weighted Run 1B yield gives an efficiency of $82.6 \pm 4.7\%$.

The uncertainty on the J/ψ-yield correction is given by the statistical uncertainty of the number of J/ψ found. All other systematic uncertainties affecting the yield, as those on

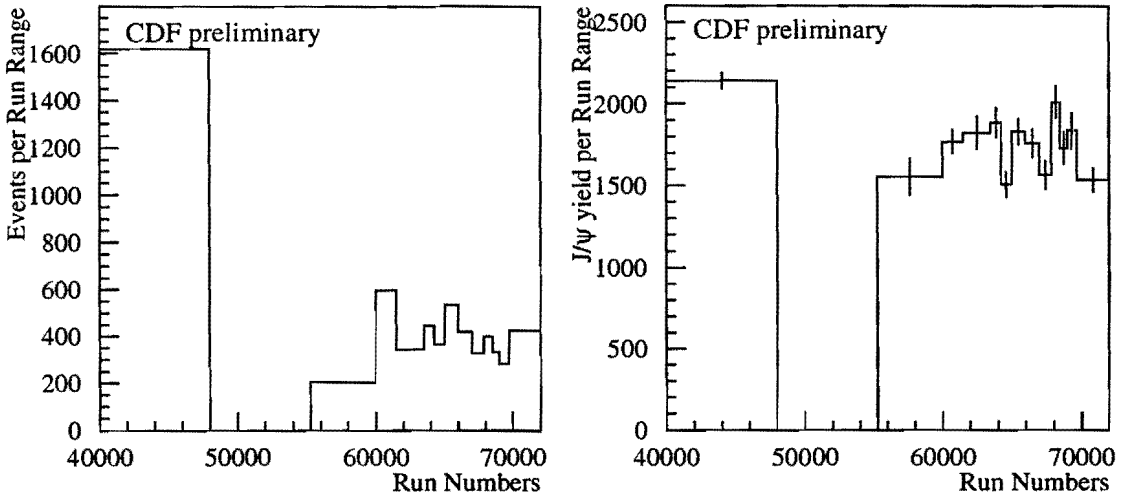

Figure 9.7: *Background subtracted number of J/ψ candidates and yield in the different run ranges. On Run 1A, the p_T requirement is of* 2.0 GeV/c *on both muons.*

the acceptance, tracking or trigger efficiencies are already accounted for in the individual efficiencies on the $B^0 \to \mu^+\mu^-$ search, and should not be included again.

It should be noted that this sample of inclusive $B \to J/\psi X$ candidates, without the Level 2 trigger requirement, has been used to verify the relative contributions of the Level 2 triggers (c.f. Section 9.1).

9.5.3. Muon reconstruction efficiencies

Muon stub finding efficiencies

The efficiency of matching a muon stub in the central muon detectors with a track, and thus identifying the muon, cannot be estimated with the Monte Carlo simulation, as the detector simulation has a built-in efficiency of 100% for this factor.

This factor can be measured in the data, using $Z^0 \to \mu^+\mu^-$ candidates, by requiring one of the muons to be observed in the CMU and confirmed in the CMP, and a second track extrapolating to either the CMU (and thus also to the CMP) or the CMX. The invariant mass of the two tracks is required to be consistent with the Z^0 mass. The efficiency is then given by the fraction of events where the second track is matched to a muon stub in the corresponding muon chamber.

The measurements of these efficiencies are presented in References [167] (CMU and CMP) and [168] (CMX). Reference [169] measures the probability of matching an incorrect muon stub to a muon track, which is found to be negligible, of the order of $2 \cdot 10^{-3}$.

The efficiency of finding two muon stubs is taken as the square of the single muon efficiency for the relevant detector. The muon-pair efficiencies are given in Table 9.6 for each of the possible detector combinations.

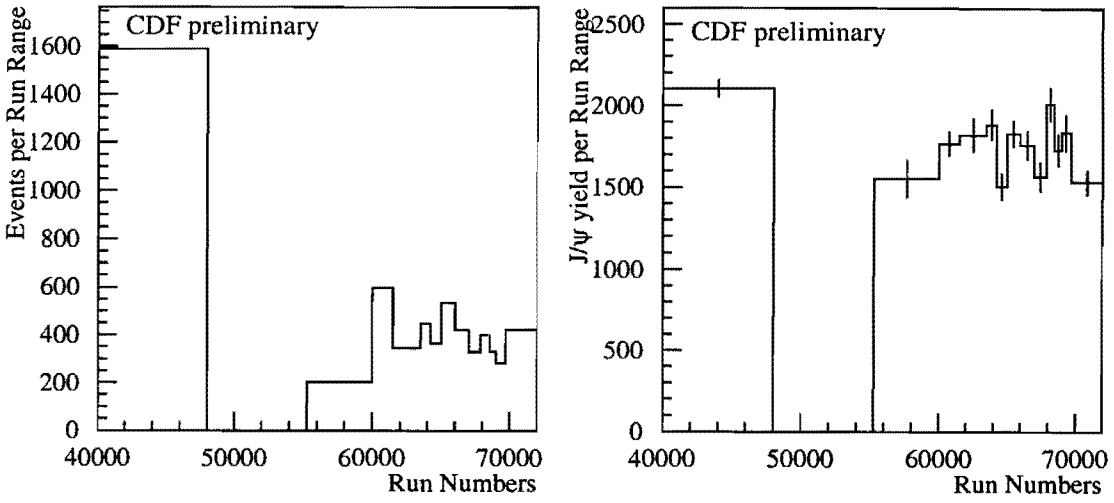

Figure 9.8: *Background subtracted number of J/ψ candidates and yield in the different run ranges. On Run 1A, the p_T requirement is of* 2.8 GeV/c *on the first muon and* 2.0 GeV/c *on the second muon.*

Muon matching requirements

The efficiency of the separation requirement between the extrapolated CTC track and the muon stub (Section 8.3) has been measured in Reference [170]. It had been estimated using $J/\psi \to \mu^+\mu^-$ data candidates, where the efficiency is taken as the background-subtracted fraction of candidates where both muons satisfy the requirements.

The efficiencies are given in Table 9.6 for each of the possible detector combinations. For CMP-CMX muon pairs, the value used is the measured value for CMU-CMX muon pairs multiplied by the measured relative single-muon efficiency between CMP and CMU: $(96.9 \pm 1.1)\%$ x R(CMP/CMU) where $R = (98.67 \pm 0.24)/(99.93 \pm 0.14)$.

Type of dimuon	Muon matching efficiency [%]	Stub finding efficiency [%]
CMU - CMU (Run 1A)	98.7 ± 0.20	96.63 ± 0.42
CMP - CMU (Run 1B)	97.5 ± 1.6	96.40 ± 0.42
CMP - CMX (Run 1B)	95.7 ± 1.1	97.0 ± 1.0

Table 9.6: *Muon matching requirement efficiencies and muon stub finding efficiencies (For a muon pair).*

Muon transverse momentum and dimuon trigger requirements

This efficiency represents the fraction of muon pairs, satisfying the transverse momentum requirement and passing one of the required triggers. It has been estimated using the Monte Carlo simulation, where the dimuon trigger simulation implements the measured

trigger efficiency curves.

The efficiency of both muons having $p_T > 2\,\mathrm{GeV}/c$ is found to be $(90.1 \pm 0.2)\%$ in Run 1A and $(88.4 \pm 0.3)\%$ in Run 1B.

The efficiency of the muon passing one of the requested dimuon triggers is found to be $(51.6 \pm 0.7 \pm 2.0)\%$ in Run 1A and $(55.0 \pm 0.4 \pm 3.2)\%$ in Run 1B. The first uncertainty quoted is due to the Monte Carlo statistic and the second due to the uncertainties on the trigger efficiency curve parameters. The latter term is estimated by varying in the trigger simulation the parameters coherently in terms of their effects on the efficiency by $\pm 1\sigma$.

Level 3 trigger efficiency

The efficiency of the Level 3 trigger is independent of the transverse momentum of the muons, hence does not need to be simulated for this specific process. It has been measured for Run 1A in Reference [171], where the efficiency is taken as the fraction of 'Level 3-accept' J/ψ candidates (candidates automatically accepted at Level 3 without requiring a specific Level 3 trigger) which were also accepted by the Level 3 dimuon trigger. The efficiency has been found to be $(97 \pm 2)\%$. In addition, in part of Run 1A, invalid CTC calibration constants were used in the Level 3 reconstruction, resulting in a degradation of the Level 3 dimuon trigger efficiency. This degradation of efficiency, averaged over the entire Run 1A, has been found to be $(98.5 \pm 0.4)\%$ [139].

The Run 1A efficiency has been verified to be the same for Run 1B using a sample of inclusive muons. A small number of events in this sample feature J/ψ candidates accepted by the Level 2 dimuon triggers and satisfying a-priori the Level 3 PSIB_DIMUON_HIGHMASS trigger requirements. The single-muon Level 3 efficiency is then calculated for the muon which was not the one that fired the inclusive muon trigger. It is taken as the fraction of J/ψ candidates effectively accepted by the Level 3 dimuon triggers, and found to be 98.4%. For a muon pair, the squared efficiency confirms the efficiency found in Run 1A.

9.5.4. B candidate requirements

Proper decay length and decay length error

The efficiencies of these requirements are estimated using the Monte Carlo simulation. The lifetimes of the B mesons used in the simulation were the world-average values as known at the time of the search[3].

The efficiency of the proper decay length requirement is found to be $(80.7 \pm 0.9 \pm 1.2)\%$ in Run 1A and $(81.0 \pm 0.7 \pm 1.0)\%$ in Run 1B for the B_d^0. For the B_s^0, the efficiency is $(82.2 \pm 0.9 \pm 1.5)\%$ in Run 1A and $(81.9 \pm 0.7 \pm 1.6)\%$ in Run 1B. The first uncertainty quoted is due to the Monte Carlo statistic and the second due to the uncertainty on the world-average lifetimes. The small difference of the proper decay length requirement efficiency between the B_d^0 and B_s^0 is due to their different lifetimes.

The efficiency of the decay length error requirement ($\sigma L_{xy} < 150\ \mu\mathrm{m}$) is found to be

[3] $\tau_{B_d} = 468 \pm 18\ \mu\mathrm{m}$ and $\tau_{B_s} = 483^{+30}_{-27}\ \mu\mathrm{m}$ [172].

	Mass MC [MeV/c^2]	σ MC [MeV/c^2]	Mass data [MeV/c^2]	σ data [MeV/c^2]	PDG value [MeV/c^2]	Number observed
J/ψ	3099.4 ± 0.2	17.8	3094.2 ± 0.2	17.2 ± 0.05	3096.88 ± 0.04	12932 ± 198
$\psi(2S)$	3688.8 ± 0.2	21.7	3682.2 ± 1.3	19.3 ± 0.7	3686.00 ± 0.09	565 ± 58
B_d^0	5282.7 ± 0.2	33.5	-	-	5279.2 ± 1.8	-
B_s^0	5372.9 ± 0.2	33.4	-	-	$5369.3. \pm 2.0$	-
$\Upsilon(1S)$	-	-	9447.6 ± 1.1	$56. \pm 2.0$	9460.37 ± 0.21	-

Table 9.7: *Fitted mass and mass resolution as predicted by the the Monte Carlo simulations and as seen in the data samples, with the number of candidates found.*

$(95.7 \pm 0.3)\%$ in Run 1A and $(94.5 \pm 0.6)\%$ in Run 1B. This coincides with the value of $(95.61 \pm 0.05)\%$ obtained from Run 1A J/ψ data in Reference [173].

B search region

The mass resolution for the decays $B^0 \to \mu^+\mu^-$ obtained in the Monte Carlo simulations can be confirmed by J/ψ, $\psi(2S)$ and $\Upsilon(1S)$ decays, as, at CDF, the mass resolutions of resonances is expected to scale with their mass. The mass resolutions for the different decays as predicted by Monte Carlo simulations and as measured in the data are shown in Table 9.7 and Figure 9.9.

The $B^0 \to \mu^+\mu^-$ mass resolution predicted by the Monte Carlo simulation can indeed be estimated from the scaling of the observed J/ψ and $\psi(2S)$ resolutions. The efficiency of requiring the mass of the B meson candidate to be within ± 75 MeV/c^2 of the world average mass is found to be $(92.9 \pm 4)\%$ in Run 1A and $(91.3 \pm 4)\%$ in Run 1B. The systematic uncertainty on this efficiency is evaluated by varying the width of the region by $\pm 10\%$. The effect of the uncertainties on the measured masses of the B mesons on the mass requirements are negligible.

9.5.5. Isolation and pointing angle requirements

The efficiency of the isolation requirement cannot be estimated using a Monte Carlo simulation, as it requires the inclusion of tracks from the underlying event, for which no reliable simulation exists. Nevertheless, as the fragmentation of the b quark is clearly independent on the subsequent decay of the B meson, any sample of fully reconstructed B meson can be used to measure the efficiency of this requirement. This efficiency has been measured previously [158, 159], albeit for an isolation variable which did not impose the z-coordinate requirement.

The efficiency for the isolation variable used is measured on fully reconstructed B's undergoing the decays $B^+ \to J/\psi K^+$ and $B^0 \to J/\psi K^{*0}$, $K^{*0} \to K^+\pi^-$, which is the largest and cleanest sample of fully reconstructed B mesons available. The same sample can also be used to measure the efficiency of the pointing angle requirement.

The B candidate is obtained from a vertex-constrained fit of the three or four candidate

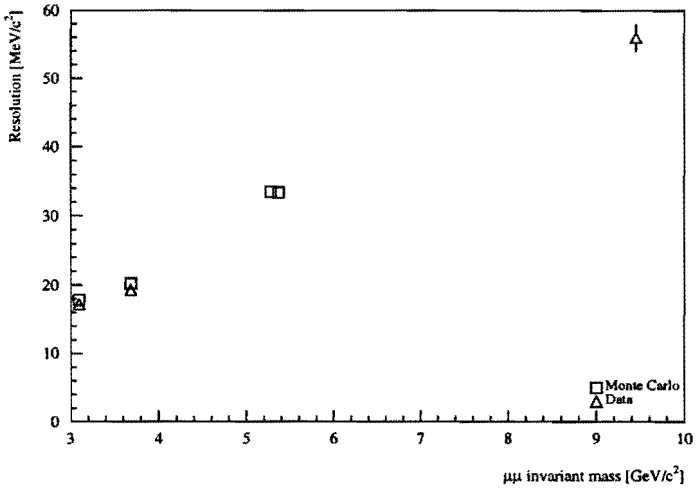

Figure 9.9: *Mass resolutions as predicted by the Monte Carlo simulations and as seen in the data samples.*

daughter tracks. All tracks are required to be reconstructed in the SVX, without imposing any additional track quality requirements in order not reduce the sample too much. The proper decay length is required to be greater than 100 μm and the error on the decay length σ_{Lxy} is required to be less than 150 μm. The invariant mass of the muon pair is required to be between 3.046 and 3.146 GeV/c^2. The observed mass resolution of the B meson is 25 MeV/c^2.

The number of candidates satisfying the imposed requirements are shown in Table 9.8, with the measured efficiency. The number of B candidates is obtained from the fit of a Gaussian signal and linear background on the invariant mass distribution of the three or four tracks. Figure 9.10 shows the invariant mass distribution of the sample after the final requirements are imposed.

The distribution of the isolation and of the pointing angle of the data candidates are shown in Figure 9.11. Figure 9.11(A) and Figure 9.11(C) show the distribution of the pointing angle and isolation variables respectively, for the signal and the sideband regions shown in Figure 9.10. The sideband distribution has been normalized to represent an invariant mass region of the same width as the signal region. Figure 9.11(B) and Figure 9.11(D) show the distribution of the same variables for the background subtracted signal.

Figure 9.12 shows the distribution of the background subtracted pointing angle of Run 1B $B^+ \to J/\psi K^+$ candidates and of the $B^+ \to J/\psi K^+$ Monte Carlo predictions. Although the distribution of the pointing angle, and hence the efficiency of the requirement, in the data coincides with its Monte Carlo predictions, the efficiencies used will be measured in the data sample.

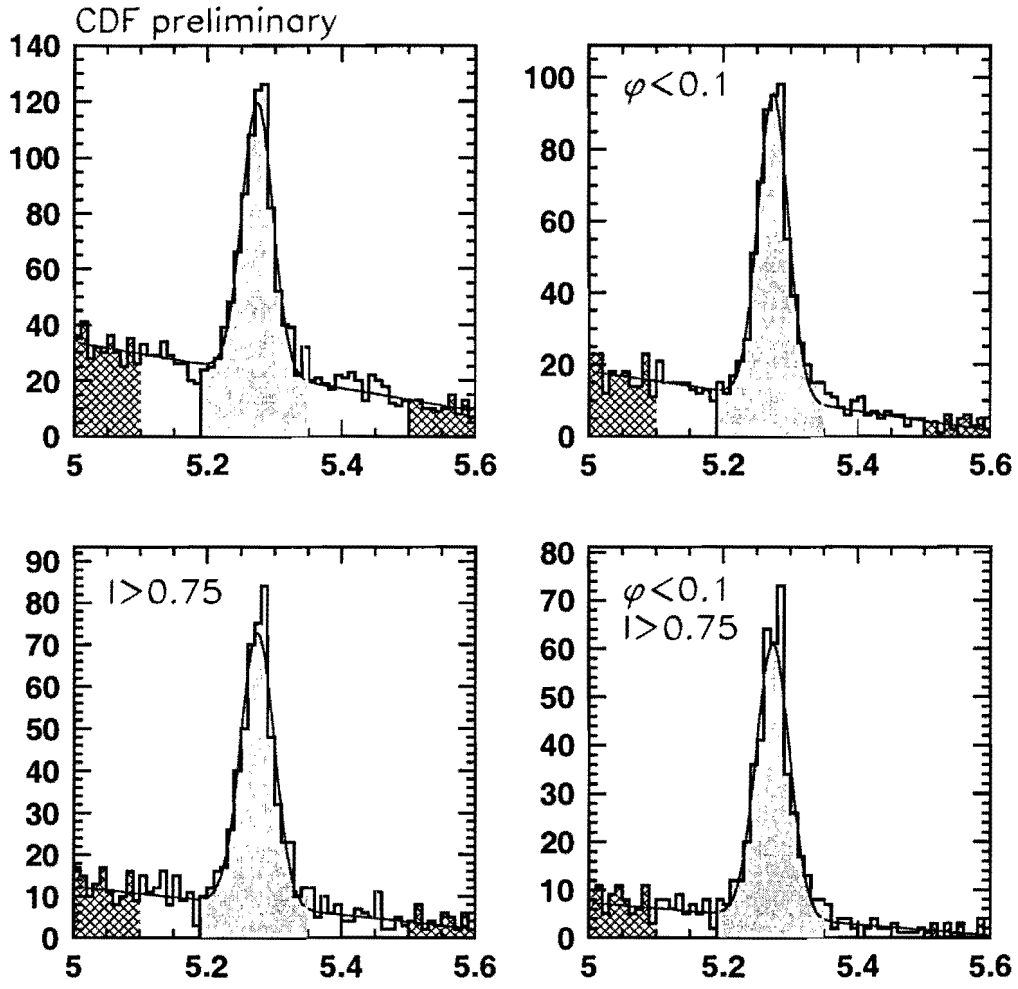

Figure 9.10: *Invariant mass distributions of Run 1B $B^+ \to J/\psi K^+$ and $B^0 \to J/\psi K^{*0}$ candidates, before (top left) and after the final isolation and pointing angle requirements. The grayed area indicate the signal region and the cross-hatched areas indicate the sideband regions used to obtain the sideband-subtracted distribution shown in Figure 9.11.*

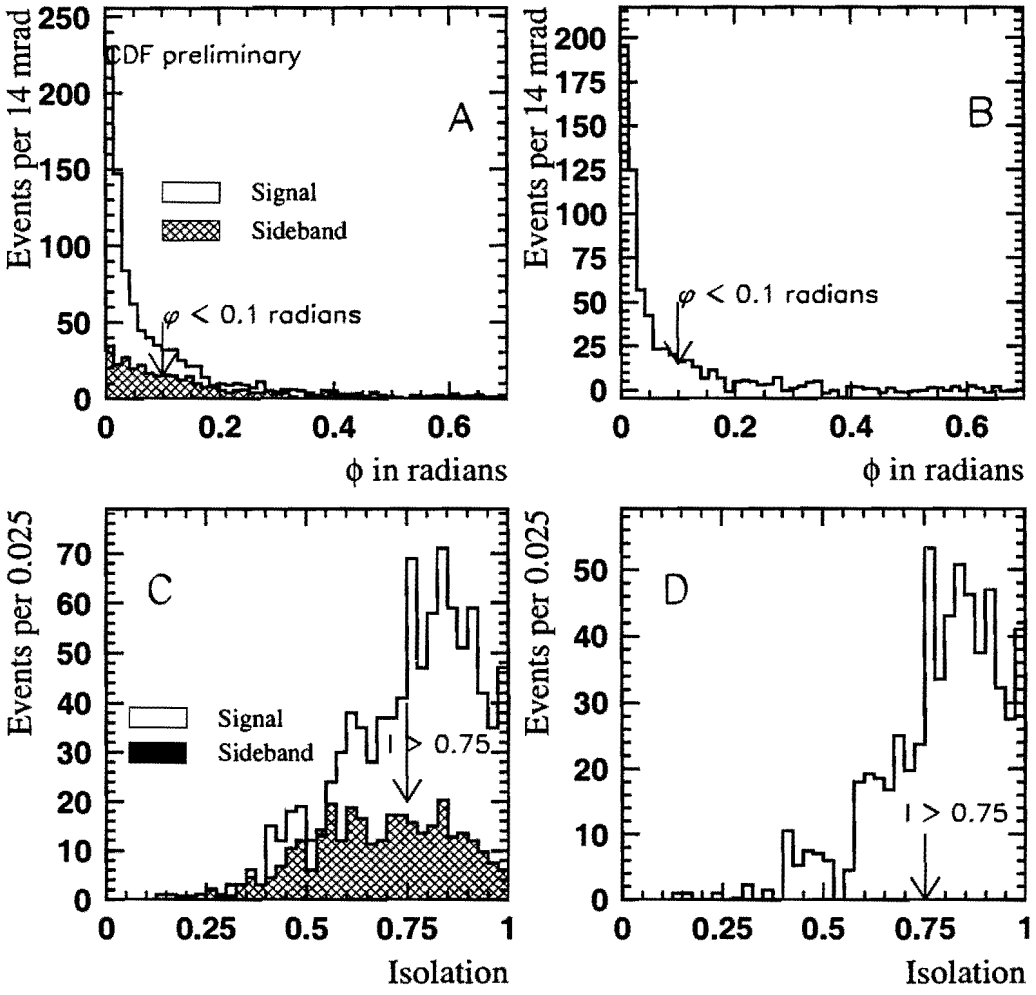

Figure 9.11: *Figure A shows the distribution of the pointing angle for the signal and sideband (hatched) Run 1B $B^+ \to J/\psi K^+$ and $B^0 \to J/\psi K^{*0}$ candidates (the invariant mass regions are defined in Figure 9.10). Figure B shows the background subtracted distributions of B candidates. Figures C and D show similar distributions for the isolation variable. The arrows represent the final selection requirement chosen.*

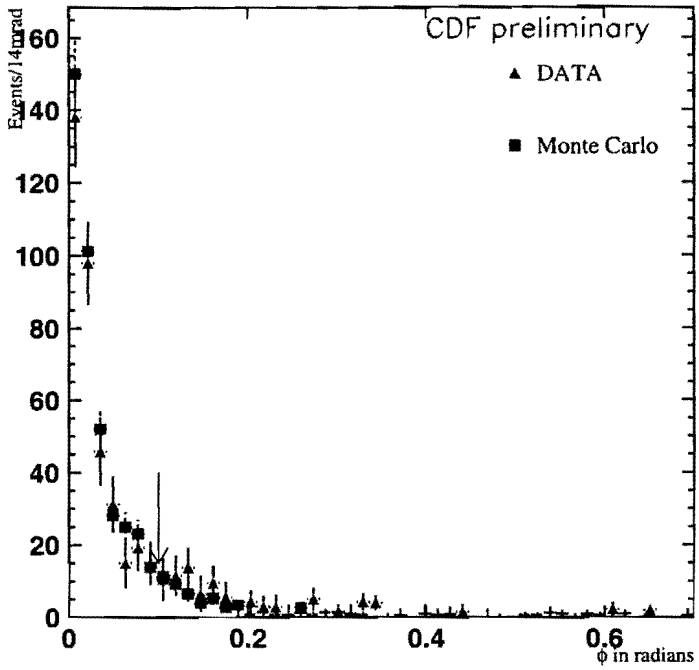

Figure 9.12: *Comparison of the distribution of the pointing angle of Run 1B $B^+ \to J/\psi K^+$ candidates and as predicted by a $B^+ \to J/\psi K^+$ Monte Carlo simulation.*

$\Delta\varphi(\vec{p}_T^{\,\mu\mu}, \vec{P}_{vtx})$ (rad)	Isolation	B candidates Run 1A	Efficiency [%] Run 1A	B candidates Run 1B	Efficiency [%] Run 1B
0.1	no cut	128± 22	85.3± 3.4	475± 48	85.1± 1.9
0.2	no cut	146± 24	97.3± 1.4	532± 42	95.3± 0.9
no cut	0.7	130± 21	86.7± 3.2	443± 46	79.3± 2.3
0.1	0.7	111± 18	74.0± 4.4	400± 44	71.7± 2.7
0.2	0.7	125± 20	83.3± 3.6	435± 43	77.9± 2.3
no cut	0.75	115± 21	76.7± 4.5	402± 44	72.0± 2.7
0.1	0.75	94± 17	62.7± 5.3	365± 41	65.3± 3.0
0.2	0.75	107± 20	71.3± 4.9	393± 42	70.4± 2.8
no cut	0.8	95± 18	63.3± 5.4	336± 35	60.1± 3.0
0.1	0.8	82± 16	54.7± 5.7	287± 33	51.4± 3.2
0.2	0.8	90± 17	60.0± 5.5	323± 36	57.8± 3.1

Table 9.8: *Efficiency of different isolation and pointing angle requirements. The uncertainties on the number of events are obtained from the fit.*

Requirement	Efficiency in %	
	Run 1A	Run 1B
Geometrical acceptance for $p_T(B) > 6$ GeV/c and $\|y(B)\| < 1$	8.31 ± 0.06	11.25 ± 0.07
$p_T(\mu) > 2$ GeV/c	88.4 ± 0.3	90.1 ± 0.2
Level 1 and Level 2 dimuon triggers	57.9 ± 2.6	61.0 ± 3.5
Muon stub finding $CMU/CMP - CMU$	96.63 ± 0.42	96.40 ± 0.42
Muon stub finding $CMP - CMX$	–	97.0 ± 1.0
CTC tracking	97.8 ± 2.2	88.2 ± 4.0
Muon matching $CMU/CMP - CMU$	98.7 ± 0.20	97.5 ± 1.6
Muon matching $CMP - CMX$	–	95.7 ± 1.1
Level 3 trigger	97 ± 2	97 ± 2
Run 1A Level 3 trigger correction	98.5 ± 0.4	-
CTC hit selection, SVX quality and fit-χ^2	66.7 ± 0.4	79.4 ± 0.2
Decay length error ($\sigma_{L_{xy}} < 150$ μm)	95.7 ± 0.3	94.5 ± 0.6
Lifetime ($c\tau > 100\mu m$) $\tau_{B_d} = 468 \pm 18$ μm	80.7 ± 1.5	81.0 ± 1.2
Lifetime ($c\tau > 100\mu m$) $\tau_{B_s} = 483^{+30}_{-27}$ μm	82.2 ± 1.8	81.9 ± 1.8
B search region	92.9 ± 4	91.3 ± 4
Pointing angle $\Phi > 0.1$	85.3 ± 3.4	85.1 ± 1.9
Isolation $I > 0.75$	76.7 ± 4.5	72.0 ± 2.7
J/ψ-yield correction	-	81.2 ± 4.6
Total B_d^0 efficiency $\times$ acceptance	1.20 ± 0.12	1.38 ± 0.18
Fractional error	$\pm$ 10.0%	$\pm$ 13.0%
Total B_s^0 efficiency $\times$ acceptance	1.22 ± 0.12	1.40 ± 0.18
Fractional error	$\pm$ 9.8%	$\pm$ 12.8%

Table 9.9: *List of Efficiencies for Run 1A and Run 1B.*

9.5.6. The total efficiency

A summary of all efficiencies is given in Table 9.9. The Run 1B data was collected with different triggers, each of which required the muons to be observed in a different combination of detectors. The total efficiency is therefore the sum of the efficiencies of each trigger sample weighted by its contribution to the final data sample:

$$\epsilon_B \times \alpha_B = \frac{\sum_t^B \int \mathcal{L}_t^B dt \cdot C_t^B \cdot \epsilon_t^B \cdot \alpha_t^B}{\sum_t^B \int \mathcal{L}_t^B dt \cdot C_t^B}, \tag{9.4}$$

where C_t is the expected relative contribution of each trigger.

The total efficiency and acceptance is $(1.20 \pm 0.12)\%$ in Run 1A and $(1.38 \pm 0.18)\%$ for Run 1B.

Table 9.10 lists the the combined Run 1 efficiencies. Each individual efficiency is the average of the Run 1A and Run 1B efficiencies weighted by the contribution of each run to the total luminosity, and the total efficiency is derived in the same way as above:

$$\epsilon \times \alpha = \frac{\int \mathcal{L}^A dt \cdot \epsilon^A \cdot \alpha^A + \sum_t^B \int \mathcal{L}_t^B dt \cdot C_t^B \cdot \epsilon_t^B \cdot \alpha_t^B}{\int \mathcal{L}^A dt + \sum_t^B \int \mathcal{L}_t^B dt \cdot C_t^B}. \tag{9.5}$$

Requirement	Efficiency in %
Geometric acceptance for $p_T(B) > 6$ GeV/c and $\|y(B)\| < 1$	10.72 ± 0.06
$p_T(\mu) > 2$ GeV/c	89.6 ± 0.2
Dimuon triggers	58.3 ± 3.4
Track finding efficiency in the muon chamber	96.6 ± 0.7
CTC tracking	89.8 ± 3.6
Muon selection	97.2 ± 1.2
Track and Vertex quality	77.1 ± 0.2
Decay length error ($\sigma_{L_{xy}} < 150$ μm)	94.7 ± 0.5
Lifetime ($c\tau > 100$ μm) $\begin{cases} \tau_{B_d} = 468 \pm 18$ μm	80.9 ± 1.0
Lifetime ($c\tau > 100$ μm) $\begin{cases} \tau_{B_s} = 483^{+30}_{-27}$ μm	81.8 ± 1.6
Pointing angle ($\Phi < 0.1$)	85.1 ± 2.2
Isolation ($I > 0.75$)	72.8 ± 3.0
B search region	91.6 ± 4.0
J/ψ-yield correction	84.6 ± 3.8
Total efficiency $\times$ acceptance $\begin{cases} for\ B_d \end{cases}$	1.34 ± 0.15
Total efficiency $\times$ acceptance $\begin{cases} for\ B_s \end{cases}$	1.37 ± 0.15

Table 9.10: *List of the combined Run 1 efficiencies.*

Source of uncertainty	Uncertainty [%]	
	Run 1A	Run 1B
B production cross section	22.6	22.6
Integrated luminosity	-	8.2
Efficiency $\times$ acceptance	10.0	13.0
Sum	24.6	27.3
Total	26.8	

Table 9.11: *List of systematic uncertainties for Run 1A and Run 1B for* B_d^0.

9.6. The systematic uncertainties

The contributions to the systematic uncertainties are given in Tables 9.11 and 9.12. Table 9.11 shows the contributions separately for Run 1A and Run 1B. Table 9.12 shows the combined Run 1 uncertainties, where, as previously, the contribution for each run is weighted by the contribution of each run to the total luminosity. The total systematic uncertainty is the quadratic sum of the individual contributions.

For the B production cross section [140], the systematic and statistical uncertainties have been added in quadrature, resulting in a fractional uncertainty of 22.6%. This uncertainty already includes the uncertainties due to Monte Carlo generation of B mesons. In addition, it also includes the uncertainty on the integrated luminosity of Run 1A.

For Run 1B, the uncertainty on the integrated luminosity has to be added separately, which, at the time of the search, has been estimated to be 8.2%. The fractional uncertainties on the efficiency $\times$ acceptance factor is given in Tables 9.9 and 9.10

Source of uncertainty	Uncertainty [%]	
	for B_d^0	for B_s^0
B production cross section	22.6	22.6
Integrated luminosity	6.7	6.7
Efficiency × acceptance	11.2	10.9
Total	26.1	26.0

Table 9.12: *List of combined Run 1 systematic uncertainties.*

9.7. The branching fraction results

One event has been found in the overlapping part of the search regions, resulting in one candidate for each of the B_d^0 and B_s^0. The observed event is consistent with the background estimates from the same-sign muon pairs and from opposite-sign sideband events. Finding no evidence for a signal, an upper limit on the branching fraction is set.

The low number of candidates and background does not warrant a background subtraction, and the observed candidate is assumed to be a signal event. This results in Poisson upper limits of 3.89 and 4.74 events at a 90% and 95% confidence level respectively. The systematic uncertainties are included using Equation B.6, yielding upper limits on the number of candidates of 4.31 and 5.48 events at a 90% and 95% confidence level respectively.

The upper limit on the branching fractions is then calculated from the formula

$$\mathcal{B}(B^0 \to \mu^+\mu^-) < \frac{N_{limit}(B^0 \to \mu^+\mu^-)}{2\sigma(B) \cdot \left(\int \mathcal{L}^A dt \cdot \epsilon^A \cdot \alpha^A + \sum_t^B \int \mathcal{L}_t^B dt \cdot C_t^B \cdot \epsilon_t^B \cdot \alpha_t^B\right)}, \tag{9.6}$$

found by inserting the expression of the efficiency, Equation 9.5, into Equation 7.1.

The 90% and 95% confidence level upper limits of the branching fractions of the sought decays are found to be

$$\mathcal{B}(B_d^0 \to \mu^+\mu^-) < 6.8 \cdot 10^{-7}\ (90\%\ CL)$$
$$\mathcal{B}(B_s^0 \to \mu^+\mu^-) < 2.0 \cdot 10^{-6}\ (90\%\ CL)$$

$$\mathcal{B}(B_d^0 \to \mu^+\mu^-) < 8.6 \cdot 10^{-7}\ (95\%\ CL)$$
$$\mathcal{B}(B_s^0 \to \mu^+\mu^-) < 2.6 \cdot 10^{-6}\ (95\%\ CL)$$

These limits, are a significant improvement over the previously published upper limits [139]:

$$\mathcal{B}(B_d^0 \to \mu^+\mu^-) < 1.6 \cdot 10^{-6}\ (90\%\ CL)$$
$$\mathcal{B}(B_s^0 \to \mu^+\mu^-) < 8.4 \cdot 10^{-6}\ (90\%\ CL)\,,$$

but still orders of magnitude above the Standard Model predictions.

Chapter 10

The search for the decay $B_s^0 \rightarrow \mu^+\mu^-\phi$

10.1. The selection process

For this search, the Run 1A Dimuon 1, Dimuon 2 and Dimuon 3 and the Run 1B PSAB, PSPB, BHMB and Stream C dimuon datasets are used. The Stream C dimuon dataset has already been produced for other analyses (e.g. [88]), but no reduced dataset satisfying the requirements of the sought decays has been split. As the Stream C dimuon dataset encompasses some 24 million events, it is not imaginable to run the selection procedure on the entire sample. The selection process has therefore to be conducted in two steps.

The task of the first selection step, the preselection, is to reduce the original Stream C dimuon dataset to a manageable size. The resulting dataset is called MMPHI. The selection requirements imposed at this level are outlined in Section 10.1.1. For consistency, the three other samples have also been subjected to the same requirements.

The second selection step, the basic selection, will then result in the sample on which the final selection requirements will be chosen and subsequently imposed. This selection is described in Section 10.1.2.

The total luminosity of the Run 1A data sample is 19.3 pb^{-1}. In the Run 1B sample, only runs present in the four datasets are retained. This ensures that the four datasets cover the same running periods and have the same integrated luminosity. With samples of different luminosities, the luminosity terms in the ratio of branching fraction would not cancel. As the Level 3 Stream C dimuon trigger did not exist for the first part of Run 1B, the total integrated luminosity of the remaining sample is 72.1 pb^{-1}.

10.1.1. The preselection

When splitting the Stream C dataset, one of the aims is to redo the SVX tracking. As this is extremely time-consuming, it cannot be done on the entire dataset, but only on the events satisfying the preselection requirements. All requirements imposed at this step will therefore be based on quantities for which the SVX informations have not been taken into

account. Some SVX acceptance requirements will nevertheless be made.

A candidate is formed by fitting two oppositely charged muons and two further oppositely charged tracks, to which a kaon mass is assigned, to a common vertex, using only CTC information. All four tracks are required to pass basic track quality requirements.The fit is deemed to be successful if the fit-χ^2 is below 100.

The two muon tracks must each have a transverse momentum above 1.5 GeV/c, a z-vertex inside the SVX acceptance, and their invariant mass must be less than 6.5 GeV/c^2. No attempt is made at this stage to separate $B_s^0 \to \mu^+\mu^-\phi$ and $B_s^0 \to J/\psi\,\phi$ candidates.

The two tracks forming the ϕ candidate must have an invariant mass within 80 MeV/c^2 of the world-average mass of the ϕ, and the transverse momentum of the ϕ candidate must be above 1.4 GeV/c.

The fitted B_s^0 candidate must have a z-vertex inside the SVX acceptance, a transverse momentum above 5.4 GeV/c and an invariant mass between 4.6 and 6.0 GeV/c^2.

To be retained, an event must have passed a Level 2 dimuon trigger, and have at least one B_s^0 candidate satisfying the above-described requirements. On these events, the SVX tracking is redone, using the latest sets of alignment constants. From the original 24 million, 535486 events are retained in this selection.

10.1.2. The basic selection

Only events accepted by one of the chosen dimuon triggers and for which the muon pair candidate confirms the dimuon trigger are kept. In both Run 1A and Run 1B, at least one muon is required have a CMP stub, as this is already the case for the BHMB data sample.

In Run 1B, when both muons match a CFT track, the transverse momentum of each muon is required to be above 2 GeV/c. When only one muon matches a CFT track, the transverse momentum of the high-p_T muon is required to be above 2.8 GeV/c and that of the low-p_T muon above 1.8 GeV/c. In Run 1A, the transverse momentum of each muon is required to be above 2 GeV/c.

At this level, the full SVX information is used and new vertex-constrained fit with a 2D-pointing constraint is performed. This is described in more detail in Section 8.4.2. For the $B_s^0 \to J/\psi\,\phi$, the two muons are furthermore constrained to the world-average J/ψ mass.

Further selection and quality requirements, as given and motivated in Section 8, are listed below:

- Muon matching requirements.
- CTC hit selection.
- SVX quality requirements, with both muons and at least one of the two kaons required to be in the SVX.
- The χ^2 confidence level of the vertex-fit is required to be above 0.01. (6 *dof* for $B_s^0 \to \mu^+\mu^-\phi$, 7 *dof* for $B_s^0 \to J/\psi\,\phi$).

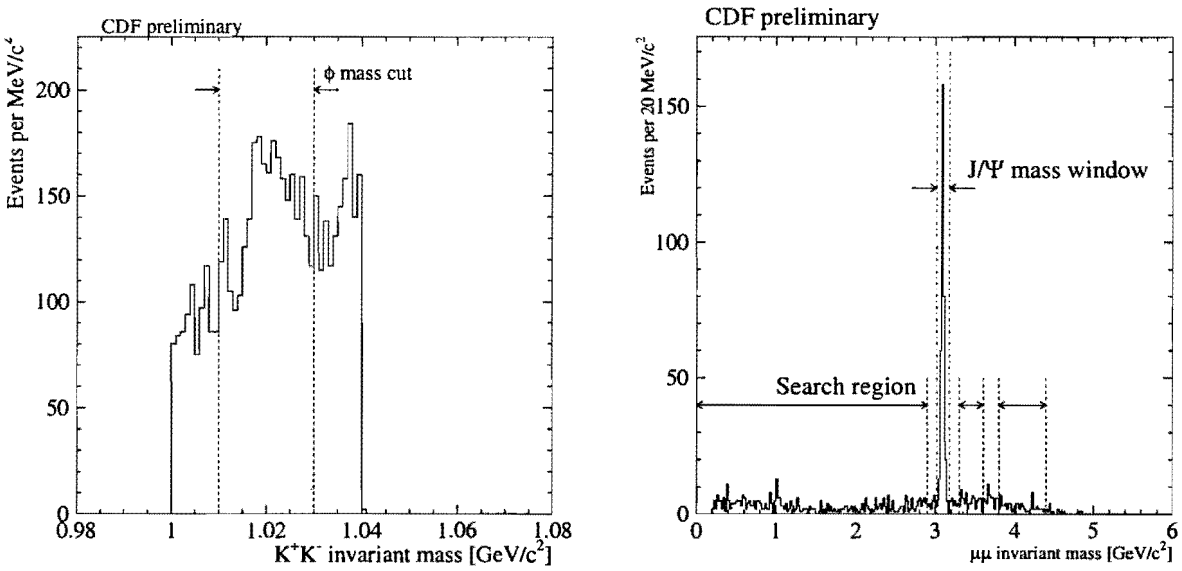

Figure 10.1: *K^+K^- (left) and $\mu^+\mu^-$ (right) invariant mass distribution after the basic selection requirements (Run 1B data sample only).*

- The transverse momentum of each kaon track is required to be above 400 MeV/c.
- The transverse momentum of the ϕ is required to be above 2 GeV/c.
- The transverse momentum of the B candidate is required to be above 6 GeV/c.
- The invariant mass of the two kaons is required to be within 10 MeV/c^2 of the world-average ϕ mass. Figure 10.1(left) shows their invariant mass distribution. The ϕ peak is visible above the rising background.

In addition, a vertex-constrained fit of the muon pair is performed. The invariant mass derived from this fit is used to determine whether the B_s^0 candidate underwent a resonant or a non-resonant decay. The following invariant mass regions are used to distinguish the two decays:

- For the resonant $B_s^0 \to J/\psi\,\phi$ candidates, the invariant mass of the muon pair is required to be within 80 MeV/c^2 of the world-average J/ψ mass.
- For the non-resonant $B_s^0 \to \mu^+\mu^-\phi$ candidates, the invariant mass of the muon pair is required to be in the ranges $0 - 2.9$ GeV/c^2, $3.3 - 3.6$ GeV/c^2 or $3.8 - 4.4$ GeV/c^2.

Figure 10.1(right) shows the invariant mass distribution observed after the basic selection requirements.

For this decay, a 100 MeV/c^2 search region, centered on the world-average mass of the B_s^0 meson[1], is chosen. This is the four-track-invariant mass region between 5.320 and

[1] $m(B_s^0) = 5369.3 \pm 2.0$ MeV/c^2 [1].

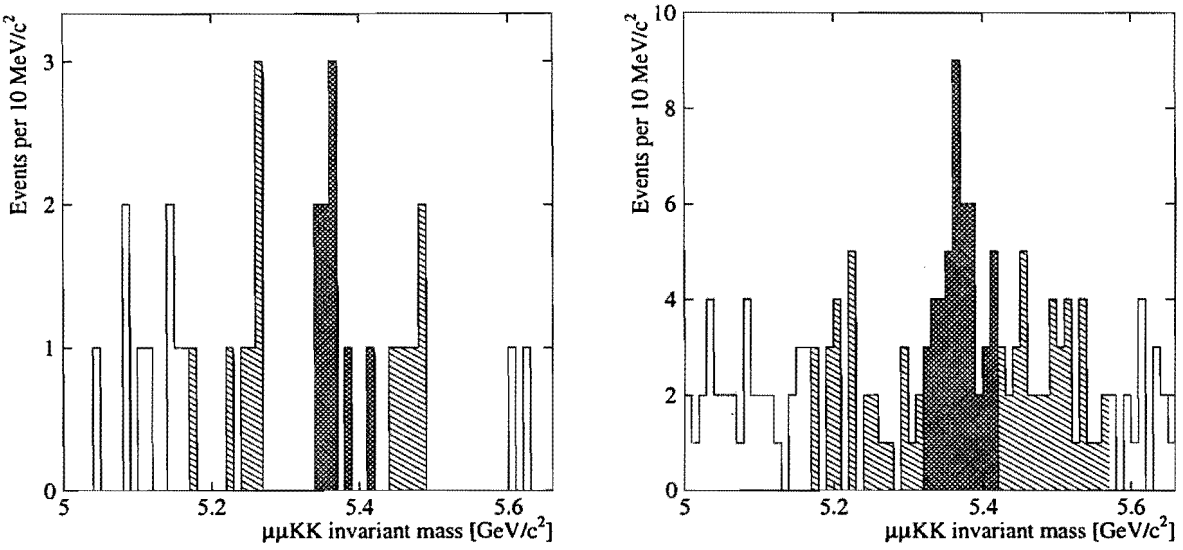

Figure 10.2: *Invariant mass distribution of $B_s^0 \to J/\psi\,\phi$ candidates after the basic selection requirements, in the Run 1A (left) and Run 1B (right) data samples. The cross-hatched area show the B_s^0 signal region and the hatched areas the sideband regions.*

5.420 GeV/c^2.

The distribution of the invariant mass of the four tracks after these requirements is shown in Figure 10.2 for the $B_s^0 \to J/\psi\,\phi$ candidates and in Figure 10.3 for the $B_s^0 \to \mu^+\mu^-\phi$ candidates. While the peak observed in the resonant selection can clearly be attributed to the $B_s^0 \to J/\psi\,\phi$ decay, no signal can be seen in the non-resonant selection at this stage.

10.2. Optimization of the selection requirements

In order to reduce the background, two further requirements are applied to the data sample, the proper decay time and the isolation requirements. The procedure to optimize these requirements is presented in Section 10.2.1 and the chosen requirements are then presented in Section 10.2.2.

10.2.1. The sensitivity

In the case of Poisson distributed data with a low number of observed events and an uncertain background, no universally accepted method of calculating and reporting a limit exists. It has therefore been suggested in References [1] and [174] that, together with the full result (numbers of recorded counts, expected background with error, normalization factor and resulting limit), a measure of the *sensitivity* be reported.

This sensitivity is defined as the average upper limit that would be attained by an ensemble of experiments with the expected background and no true signal. It permits to

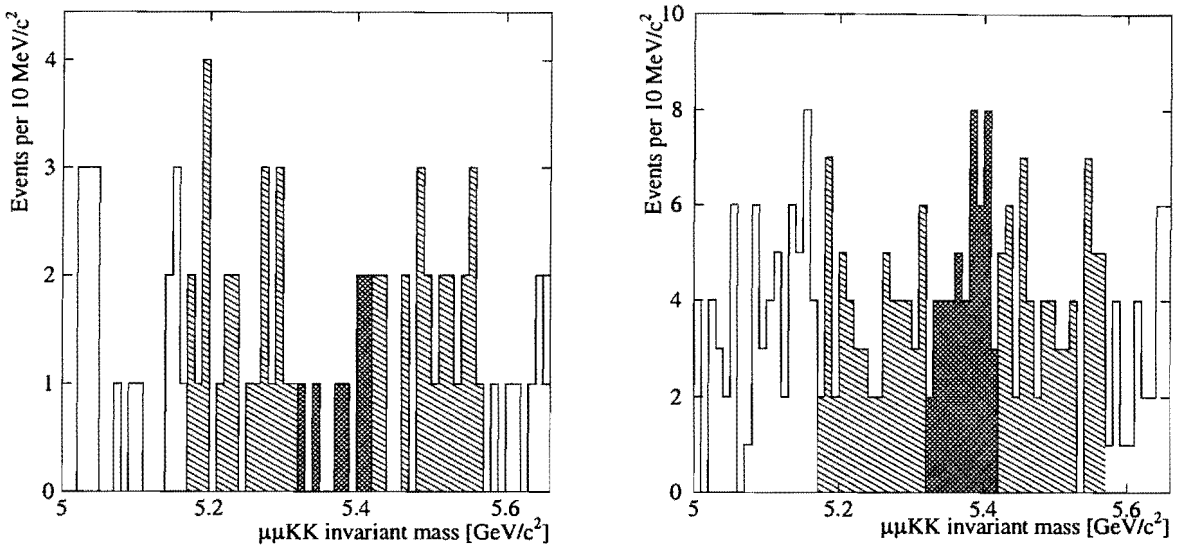

Figure 10.3: *Invariant mass distribution of $B_s^0 \to \mu^+\mu^-\phi$ candidates after the basic selection requirements, in the Run 1A (left) and Run 1B (right) data samples. The cross-hatched area show the B_s^0 signal region and the hatched areas the sideband regions.*

judge the quality of an experiment by (as its name suggests) its sensitivity to the result. It also allows to rank several experimental possibilities according to the result that could be expected from them. This quantity will thus be used to select the set of requirements that would permit to attain the best limit.

The sensitivity $\mathcal{S}$ will be given by

$$\mathcal{S} = \frac{\bar{N}(\mu_B) \cdot \mathcal{B}(B_s^0 \to J/\psi\,\phi, J/\psi \to \mu^+\mu^-)}{N_{obs}(B_s^0 \to J/\psi\,\phi, J/\psi \to \mu^+\mu^-) \cdot \epsilon_{rel}}\,, \tag{10.1}$$

$$\bar{N}(\mu_B) = \sum_{n=0}^{\infty} P(n,\mu_B) \cdot N(n,\mu_B) \tag{10.2}$$

$$= \sum_{n=0}^{\infty} \frac{\mu_B^n}{n!} e^{-\mu_B} \cdot N(n,\mu_B)\,, \tag{10.3}$$

where μ_B is the number of background events expected in the search window for the set of requirements considered and N_{obs} is the number of candidates reconstructed in the reference decay, in this case $B_s^0 \to J/\psi\,\phi$. $\bar{N}(\mu_B)$ is the average upper limit of signal events given the expected background μ_B. Since, for the measure of $\mathcal{S}$, the observed events are considered to be only background events, the probability to observe n events is given by the Poisson probability of the background to fluctuate to n events. $\bar{N}(\mu_B)$ is thus the sum of the upper limits of candidates in a sample of n events weighted by the probability to observe this number of events. As the measured quantities will be considered without any uncertainties,

the upper limit on a signal $N_S = N(n, \mu_B)$ is found by resolving

$$1 - \epsilon = \frac{\sum_{i=0}^{n} \frac{(\mu_B + N_S)^i}{i!} e^{-(\mu_B+N)}}{\sum_{i=0}^{n} \frac{\mu_B^i}{i!} e^{-\mu_B}} . \tag{10.4}$$

The derivation of this equation can be found in Section B.2.2. The confidence level is chosen to be at 95%.

The quantity ϵ_{rel} is the relative efficiency of the reference and the signal decay after the basic selection requirements have been applied. This can be estimated by Monte Carlo, but, as it will be constant for all trials (as is the branching fraction of the reference signal), it can be omitted.

The number of background events expected in the search region, μ_B, will be the number of events observed in the sidebands normalized to the 100 MeV/c^2 search region. The sidebands are chosen as the two invariant mass regions between 5.169 and 5.319 GeV/c^2 and between 5.419 and 5.569 GeV/c^2. This is the same background estimate that might be used to calculate the final branching fraction. As the procedure used will attempt to find a set of requirements which leads to the lowest background, this final estimation of the background might be underestimated. This is nevertheless a conservative bias, which would increase the upper limit in the absence of a signal.

The number of observed $B_s^0 \to J/\psi\,\phi$ candidates (N_{obs}) should be obtained from a Monte Carlo simulation, to avoid a biased result. As the isolation requirement, which cannot be simulated by Monte Carlo, is also optimized, N_{obs} will have to be obtained from the data sample.

It has been noticed that, due to the low number of $B_s^0 \to J/\psi\,\phi$ candidate events, a binned fit on the invariant mass distribution does not yield meaningful results. A maximum log-likelihood fit has therefore to be used to extract the number of $B_s^0 \to J/\psi\,\phi$ candidates from the observed distribution.

In this fit, the function $\mathcal{P}$ to maximize is the product of the probability distribution of the invariant mass of each event in the region on which the fit is performed. The probability density function chosen to describe the distribution of the invariant mass of the candidates is the sum of a Gaussian $\mathcal{G}$, representing the signal events, and a linear background $\mathcal{L}$:

$$\mathcal{P} = \prod_i \left(f_{sig} \cdot \mathcal{G}(m_i) + (1 - f_{sig}) \cdot \mathcal{L}(m_i)\right) \tag{10.5}$$

$$\mathcal{G}(m_i) = \frac{1}{\sqrt{2\pi}\sigma_B} e^{-\frac{1}{2}\left(\frac{m_i - M_b}{\sigma_B}\right)^2} \tag{10.6}$$

$$\mathcal{L}(m_i) = a \cdot m_i + b\,, \tag{10.7}$$

where m_i is of course the invariant mass of each candidate.

The parameters of these functions represent the mass and width of the B_s^0 (M_B and σ_B), the fraction of signal candidates in the sample (f_{sig}) and the two parameters of the straight line (a and b).

The mass and width of the B_s^0 peak is obtained from the fit to the largest sample, on which only the $c\tau > 0$ μm requirement is applied. This allows the measurement of these two parameters with the best resolution, as this sample has the largest number of $B_s^0 \to J/\psi\,\phi$ candidates. Both parameters and then fixed to these values for the subsequent fits.

As the probability density function has to be normalized to a fixed value, one parameter is removed from the linear background. Choosing this normalization to be 1, this function becomes

$$\mathcal{L}(m_i) = \frac{c \cdot m_i + 1}{c/2 \cdot (m_{inf} - m_{sup})^2 + (m_{inf} - m_{sup})}\,, \tag{10.8}$$

where the parameter c is simply a/b. m_{inf} and m_{sup} are the upper and lower bounds of the invariant mass distribution on which the fit is performed,. These are chosen to be 5.169 and 5.569 GeV/c^2, to include the same sideband regions as used in the decay $B_s^0 \to \mu^+\mu^-\phi$.

In some cases, when very few events remain after the imposed requirements, the fit does not return a reliable uncertainty on the parameters. In these cases, a Poisson uncertainty ($\sqrt{N_{obs}}$) would be used on the number of $B_s^0 \to J/\psi\,\phi$ candidates instead of the error returned by MINUIT.

The optimization will be conducted on the Run 1B data samples. Table C.3 in Appendix C shows, for each set of requirements, the number of background events expected in the search region, the number of $B_s^0 \to J/\psi\,\phi$ candidates, the average upper limit on the number of signal events and the sensitivity. For some tight requirements, no background event is left, and $\mathcal{S}$ will not be defined. As the undefined $\mathcal{S}$ do not permit to discriminate between the different sets of requirement anymore, the final requirement will be chosen by requiring the lowest defined $\mathcal{S}$, with the highest efficiency.

10.2.2. The final requirements

The best sensitivity (lowest $\mathcal{S}$) is obtained with a proper decay length requirement of $c\tau > 100$ μm and an isolation requirement of $I > 0.75$. These requirements will thus be chosen for the final selection. Incidentally, it can be noted that these two requirements are identical to the requirement chosen independently in the search for the decays $B^0 \to \mu^+\mu^-$.

The fit yields 11.0±2.2 $B_s^0 \to J/\psi\,\phi$ candidates in the Run 1B sample (Figure 10.4(right)). As can be seen in Figure 10.4(left), no candidate is left in the Run 1A sample. When applying the optimized requirements to the $B_s^0 \to \mu^+\mu^-\phi$ sample, two candidates are counted in the search region in Run 1B and none in Run 1A (Figure 10.5).

Two events are observed in the sidebands in Run 1A and one in Run 1B. Extrapolating the observed number of events to the 0.1 GeV/c^2-wide search region, one background event can be expected.

Fig. 10.6 shows the combined Run 1 invariant mass distribution and Fig. 10.7 shows, for all events, the distribution of the invariant mass of the four tracks versus the invariant mass of the muon pair.

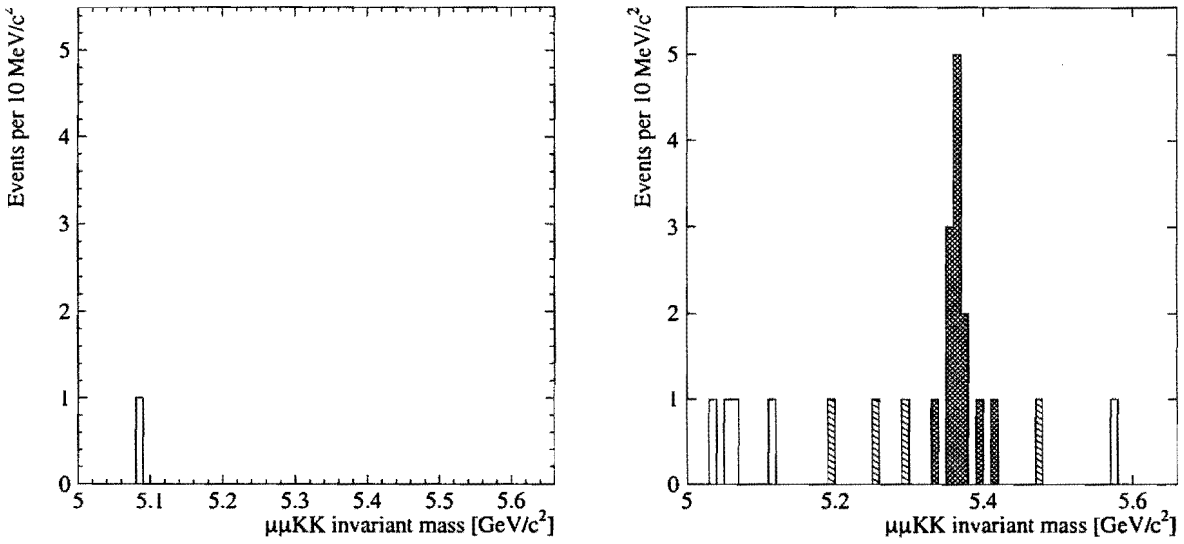

Figure 10.4: *Invariant mass distribution of $B_s^0 \to J/\psi\,\phi$ candidates imposing the optimized selection requirements, in the Run 1A (left) and Run 1B (right) data samples. The cross-hatched area show the B_s^0 signal region and the hatched areas the sideband regions.*

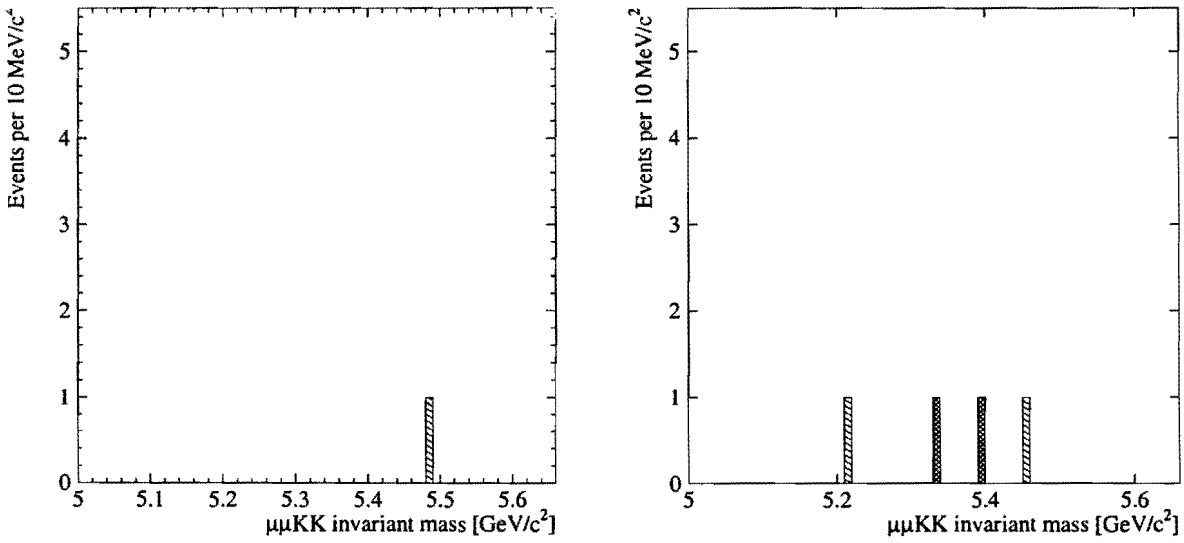

Figure 10.5: *Invariant mass distribution of $B_s^0 \to \mu^+\mu^-\phi$ candidates imposing the optimized selection requirements, in the Run 1A (left) and Run 1B (right) data samples. The cross-hatched area show the B_s^0 signal region and the hatched areas the sideband regions.*

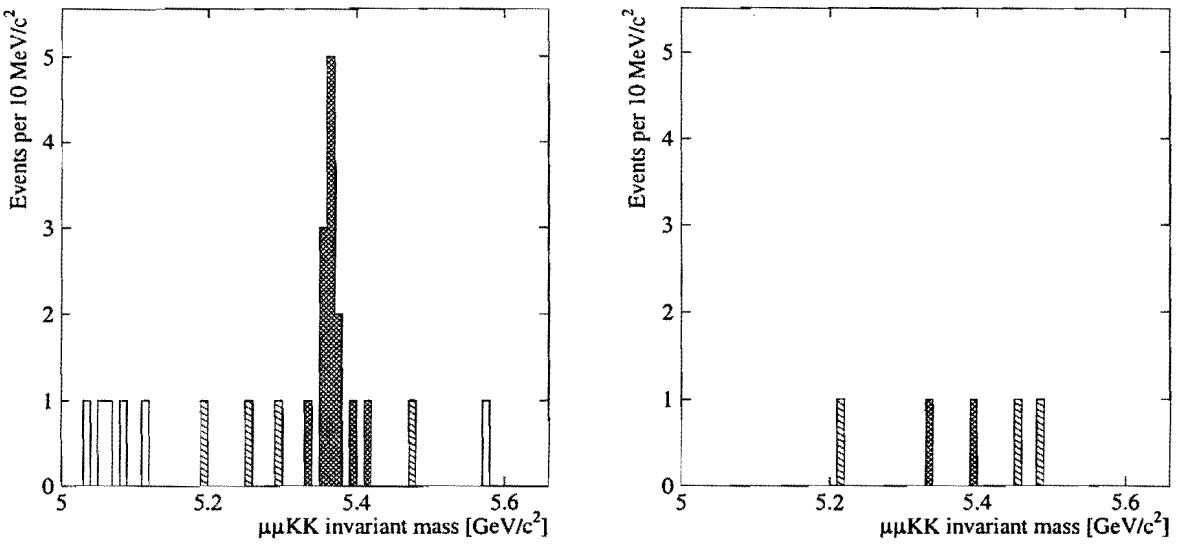

Figure 10.6: *Invariant mass distribution of $B_s^0 \to J/\psi\,\phi$ (left) and $B_s^0 \to \mu^+\mu^-\phi$ (right) candidates with optimized selection requirements, in the combined Run 1 data sample.The cross-hatched area show the B_s^0 signal region and the hatched areas the sideband regions.*

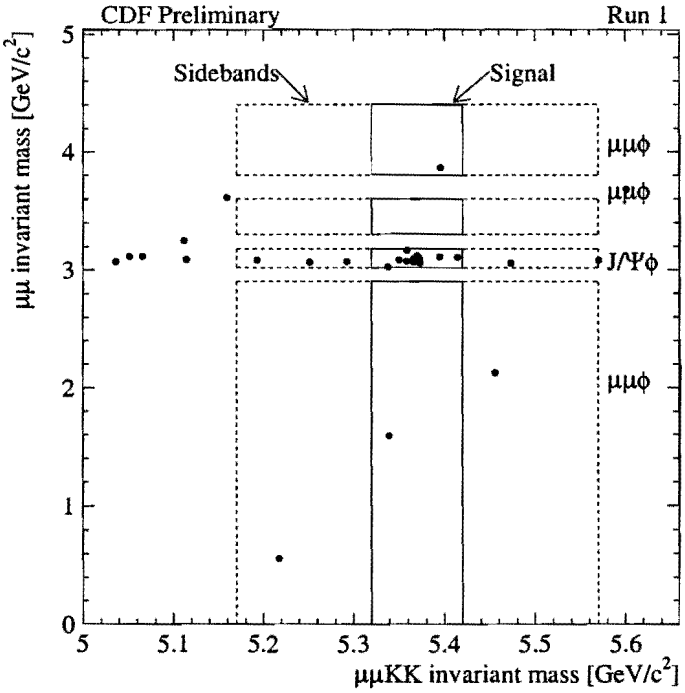

Figure 10.7: *$\mu^+\mu^-K^+K^-$ invariant mass versus $\mu^+\mu^-$ invariant mass of all candidates satisfying the optimized selection requirements for the combined Run 1 data sample*

10.3. The relative efficiency

10.3.1. The definition of ϵ_{rel}

As already seen in Section 4.4, the decay $B_s^0 \to \mu^+\mu^-\phi$ receives short-distance contributions from electromagnetic and Z penguin diagrams and W box diagrams (Figure 4.4(a) and Figure 4.4(b)) and long-distance contributions from the process $B \to \phi(c\bar{c}) \to \phi\mu^+\mu^-$, with both resonant (mainly J/ψ and $\psi(2S)$) and continuum intermediate $(c\bar{c})$ states (Figure 4.4(c)). In the dimuon invariant mass regions around the J/ψ and $\psi(2S)$ resonances, the decay is dominated by the long-distance processes, while away from these resonances, short-distance processes dominate.

The branching fraction being measured should be the branching fraction of the short-distance processes only, would it be possible to distinguish the two contributions. It is the ratio between the partial width due to short distance processes and the total width of the B_s^0[2]:

$$\mathcal{B}(B_s^0 \to \mu^+\mu^-\phi) = \frac{\Gamma(SD)}{\Gamma_{B_s^0}} . \tag{10.9}$$

However, the *total* width of the final state $\mu^+\mu^-\phi$ is the sum of the long- and short-distance amplitudes, and the interference of these two terms ($\Gamma(LD+SD) \propto |A_{SD}+A_{LD}|^2$). The number of events observed will be proportional to this width ($N_{\mu^+\mu^-\phi} = \Gamma(LD + SD)/\Gamma_{B_s^0} \cdot \mathcal{L}\sigma\epsilon$), and the observed width will not be solely the short-distance amplitude, but will also include to a certain extent the other terms. As such, $\mathcal{B}(B_s^0 \to \mu^+\mu^-\phi)$ is strictly speaking not a physical amplitude.

Even though the search is restricted to the non-resonant dimuon invariant mass regions[3] to reduce the influence of long-distance processes, the latter will still be present, and will have to be taken into account. To obtain the short-distance branching fraction (with the full dimuon mass spectrum) from the observed number of events, the corrections involved can be split in two parts:

$$\begin{aligned} N^{meas}_{\mu^+\mu^-\phi} &\propto \mathcal{L}\sigma\epsilon \cdot \frac{\Gamma(LD+SD,NR)}{\Gamma_{B_s^0}} \\ &\propto \mathcal{L}\sigma\epsilon \cdot \underbrace{\frac{\Gamma(LD+SD,NR)}{\Gamma(SD,NR)}}_{\epsilon_{SD}} \cdot \underbrace{\frac{\Gamma(SD,NR)}{\Gamma(SD,full)}}_{\epsilon_{mass}} \cdot \underbrace{\frac{\Gamma(SD,full)}{\Gamma_{B_s^0}}}_{\mathcal{B}(B_s^0\to\mu^+\mu^-\phi)} \end{aligned} \tag{10.10}$$

- ϵ_{SD}: even in the non-resonant part of the dimuon spectrum, the *measured* partial width includes a contribution of long-distance processes and of the interference. The correction can be expressed as the ratio of the full and the short-distance partial widths.

[2]In the notation used in this section, the mention *SD* and/or *LD* refers to the contribution(s) taken into account when calculating the width. In case only part of the dimuon invariant mass region is taken into account, it will be noted as *NR* for the non-resonant mass region and *full* for the full mass region.

[3]These are, as defined previously, the mass ranges $0-2.9$ GeV/c^2, $3.3-3.6$ GeV/c^2 and $3.8-4.4$ GeV/c^2, to exclude the J/ψ and $\psi(2S)$ resonances.

- ϵ_{mass}: as only the non-resonant part of the dimuon spectrum is measured, the result has to be extrapolated to the full dimuon mass region. This is simply the ratio of the partial widths of the non-resonant and full mass ranges.

Finally, as the branching fraction is measured relative to a known reference decay ($B_s^0 \to J/\psi\,\phi$), the ratio of the acceptance (α) and selection requirement efficiencies (ϵ) between the two processes has to be accounted for:

$$\epsilon_{cut} = \frac{\alpha \cdot \epsilon(B_s^0 \to \mu^+\mu^-\phi)}{\alpha \cdot \epsilon(B_s^0 \to J/\psi\,\phi, J/\psi \to \mu^+\mu^-)} \,. \tag{10.11}$$

The relative efficiency ϵ_{rel} will then be defined as the product of the three correction factors

$$\epsilon_{rel} = \epsilon_{SD} \cdot \epsilon_{mass} \cdot \epsilon_{cut} \,. \tag{10.12}$$

10.3.2. Combining Run 1A and Run 1B

In this search two data samples, from Run 1A and Run 1B, are combined and the branching fraction will be given by

$$\mathcal{B}(B_s^0 \to \mu^+\mu^-\phi) = \frac{(N^A_{\mu^+\mu^-\phi} + N^B_{\mu^+\mu^-\phi}) \cdot \mathcal{B}(B_s^0 \to J/\psi\,\phi, J/\psi \to \mu^+\mu^-)}{(N^A_{J/\psi\phi} + N^B_{J/\psi\phi}) \cdot \epsilon_{rel}} \tag{10.13}$$

Between Run 1A and Run 1B, the ratio of selection efficiencies, ϵ_{cut}, is expected to be different. The other two correction factors, ϵ_{SD} and ϵ_{mass}, will of course not change, as they depend only on the physical process involved, and not on experimental conditions. The combined Run 1 relative efficiency, as used to calculate the branching fraction (Equation 10.13), will then be given by

$$\epsilon_{rel} = \frac{N^A_{J/\psi\phi}}{N^A_{J/\psi\phi} + N^B_{J/\psi\phi}} \epsilon^A_{rel} + \frac{N^B_{J/\psi\phi}}{N^A_{J/\psi\phi} + N^B_{J/\psi\phi}} \epsilon^B_{rel} \tag{10.14}$$

10.3.3. The measurement of ϵ_{rel}

The measurement of ϵ_{cut}

As the decays $B_s^0 \to \mu^+\mu^-\phi$ and $B_s^0 \to J/\psi\,\phi$ and their selection requirements are very similar, most of their efficiencies will be identical. When calculating the ratio of the total efficiency of the two decays, all the common efficiencies cancel. The exact knowledge of the values of these efficiencies is therefore not needed. In turn, the systematic uncertainties on these efficiencies will also be removed, reducing the total systematic uncertainty.

As the same number and species of tracks (four tracks, with two muons) are selected in the two processes, all reconstruction efficiencies will cancel. Also, most selection requirement efficiencies, such those of the proper decay length or the isolation, will be identical.

Only efficiencies depending on the topology specific to one or the other decay will differ. This is notably the case of the trigger efficiencies, as the invariant mass of the two

muons, and hence their transverse momentum, is very different. The geometric acceptance and kinematic efficiency might also be affected by this difference. The ratio of selection efficiencies, ϵ_{cut}, will therefore not be unity.

The acceptance and efficiencies remaining are estimated by the Monte Carlo simulation described in Appendix A. The decay model of the decay $B_s^0 \to \mu^+\mu^-\phi$ is described in Appendix A.2.1. The CQM form factors are used for the evaluation of ϵ_{rel} and the LCSR form factors will be used to estimate the systematic uncertainty due to the choice of a particular decay model. This will be described in the next section. All other decays, $B_s^0 \to J/\psi\,\phi$, $J/\psi \to \mu^+\mu^-$ and $\phi \to K^+K^-$, are simulated by the standard CLEOMC decays [175].

The selection efficiencies derived from the simulation for B mesons with $p_T > 6$ GeV/c and $|y(B)| < 1$ and ϵ_{cut} are given in table 10.1. The uncertainties quoted are only due to the Monte Carlo statistics.

	$B_s^0 \to J/\psi\,\phi$ (%)	$B_s^0 \to \mu^+\mu^-\phi$ (%)	ϵ_{cut}
Run 1A	1.272 ± 0.014	1.466 ± 0.017	1.153 ± 0.018
Run 1B	1.119 ± 0.007	1.248 ± 0.010	1.117 ± 0.011

Table 10.1: *Selection efficiencies and relative efficiencies.*

The measurement of ϵ_{mass} and ϵ_{SD}

The correction factors ϵ_{mass} and ϵ_{SD} are obtained by performing a numerical integration over $\hat{s}$ of the analytical expression of the differential decay width $\frac{d\Gamma}{d\hat{s}}$. Equation 10.10 indicates over which invariant mass ranges the integration will be done and which contributions (LD or SD) will be included in $\frac{d\Gamma}{d\hat{s}}$. Here as well, the CQM form factors are used for the evaluation of the correction factors and the LCSR form factors will be used to estimate the systematic uncertainty due to the choice of a particular decay model. The product $\epsilon_{mass} \cdot \epsilon_{SD}$ is determined to be

$$\epsilon_{mass} \cdot \epsilon_{SD} = 81.65\%$$

10.4. The systematic uncertainties

Doing a relative measurement removes some factors as the luminosity, cross-section and some reconstruction uncertainties, but introduces new contributions, such as the branching fraction of the reference signal and its number of events. These systematic uncertainties are discussed in this section, and summarized in table 10.3.

Branching fraction

The branching fraction of the decay $B_s^0 \to J/\psi\,\phi$ has been measured at CDF [141] to be $\mathcal{B}(B_s^0 \to J/\psi\,\phi) = (9.3 \pm 3.3) \cdot 10^{-4}$. Using for the J/ψ decay the world-average branching

Variation	ϵ_{cut}
Default	1.117
Maximum	1.129
Minimum	1.070

Table 10.2: *Effect of the trigger curve variation on* ϵ_{cut}.

fraction, $\mathcal{B}(J/\psi \to \mu^+\mu^-) = (6.01 \pm 0.19) \cdot 10^{-2}$ [1], the resulting branching fraction for the reference signal is $\mathcal{B}(B_s^0 \to J/\psi\,\phi, J/\psi \to \mu^+\mu^-) = (5.6 \pm 2.0) \cdot 10^{-5}$.

It should be noted that as the measurement of $\mathcal{B}(B_s^0 \to J/\psi\,\phi)$ was also done relative to a final state containing a J/ψ, the uncertainty on $\mathcal{B}(J/\psi \to \mu^+\mu^-)$ is not included in $\mathcal{B}(B_s^0 \to J/\psi\,\phi)$.

$B_s^0 \to J/\psi\,\phi$ signal event count

The number of $B_s^0 \to J/\psi\,\phi$ candidates is obtained from the maximum-likelihood fit performed on the events remaining in the signal and sideband regions after all selection requirements. It is the product of the total number of events in both regions and the signal/background ratio (the factor f_{sig} in equation 10.5). The fit is done using MINUIT, and the error returned is taken as the uncertainty on the parameter. Sometimes, due to the low number of events, the fit does not return a reliable error. In these cases, the standard deviation of the Poisson distribution ($\sqrt{N}$) would be used instead of the error returned by MINUIT.

For the chosen selection requirements, MINUIT was able to calculate this error, which is ± 2.2 candidate.

Relative efficiency

Apart from the statistical uncertainty due to the Monte Carlo sample (1.0%), the main source of uncertainty in the ratio of selection efficiencies is the trigger efficiency. As the muons can be of low momentum, especially for the $B_s^0 \to \mu^+\mu^-\phi$ decay, they can be sensitive to the turn-on point of the trigger curves. The effect of the uncertainties on the trigger efficiency parameterizations on ϵ_{rel} can be estimated by varying in the trigger simulation the parameters coherently in terms of their effect on the efficiency by $\pm 1\sigma$. As moving the trigger efficiency curves changes the trigger efficiencies for the two decays in the same direction, the effect on the relative efficiency will be attenuated. Table 10.2 shows the variation of the relative efficiency. A 4.2% uncertainty is assigned by taking the largest variation.

Model dependence

All correction factors, ϵ_{rel}, ϵ_{mass} and ϵ_{SD}, were obtained using the form factors calculated with the CQM model. To estimate the model dependency of the result, these factors will be estimated using the form factors calculated with the LCSR model.

Source	Uncertainty in %
Branching fraction	35.7
$B_s^0 \to J/\psi\,\phi$ Signal	20.2
MC statistic	1.0
Trigger efficiency	4.2
Model dependence: ϵ_{cut}	3.1
Model dependence: $\epsilon_{mass} \cdot \epsilon_{SD}$	3.7
Total	41.4

Table 10.3: *List of systematic uncertainties of the relative measurement.*

Using this model, the Run 1B relative selection efficiency ϵ_{cut} is found to be 1.176±0.016. From the difference with the value obtained with the CQM form factors, a 3.1% systematic uncertainty is assigned to this factor.

The correction factor $\epsilon_{mass} \cdot \epsilon_{SD}$ obtained using the LCSR form factors is 78.60%, and a 3.7% systematic uncertainty is assigned to this factor.

The total systematic uncertainty

Adding the different contributions in quadrature, the total systematic uncertainty is 41.4%. As can be seen, both the uncertainties on the branching fraction and the $B_s^0 \to J/\psi\,\phi$ signal count are very large, and together dominate the total uncertainty.

10.4.1. Systematic uncertainty of a direct measurement

In view of the large total systematic uncertainty of the relative measurement of the branching fraction, the question can be asked whether a direct measurement would have a smaller systematic uncertainty. In a direct measurement, the branching fraction is given by Equation 7.1. Of the systematic uncertainties of the relative measurement, only the uncertainties form the model dependence would be the same in a direct measurement. The uncertainties of the different factors of Equation 7.1 are estimated below, and summarized in Table 10.4. When applicable, the estimates are given only for Run 1B.

- The B_s^0 production cross section $\sigma(B_s^0)$:
  The production cross section of the B_s^0 is given by the product of the B_d^0 production cross section $\sigma(B_d^0)$ [140] and of the ratio of the fragmentation fractions $\frac{f_s}{(f_u+f_d)}$ [142], both of which have been measured at CDF.

- The uncertainty on the integrated luminosity is estimated to be 4.1% [134].

- As the ϕ meson is reconstructed in the decay $\phi \to K^+K^-$, the branching fraction of this decay has to be accounted for in the denominator of Equation 7.1. In the measurement of the fragmentation fraction, the B_s^0 is reconstructed in the decay $B_s^0 \to J/\psi\,\phi$ and the uncertainty on the branching fraction of the decay $\phi \to K^+K^-$ is already included in the uncertainty of the fragmentation fraction. It should therefore not be counted again.

Source	Uncertainty in %
$\sigma(B_d^0) = 2.39 \pm 0.32 \pm 0.44$ μb [140]	22.8
$\frac{f_s}{(f_u,f_d)} = 0.426 \pm 0.076$ [142]	17.8
Integrated luminosity	4.1
Efficiency $\times$ acceptance	19.6
Model dependence: ϵ_{cut}	3.1
Model dependence: $\epsilon_{mass} \cdot \epsilon_{SD}$	3.7
Total	35.5

Table 10.4: *List of the estimated systematic uncertainties of a direct measurement.*

- The uncertainty on the absolute efficiency and acceptance is based on the uncertainty of this factor obtained in the search for the decays $B^0 \to \mu^+\mu^-$ (c.f. Section 9.5). While the values of the individual efficiencies contributing to the total efficiency could be different due to the different topologies of the decays, it is believed that their uncertainties would be similar than those for the decays $B^0 \to \mu^+\mu^-$. These are summarized in Table 9.9. Several differences can nevertheless be found:
  - As instead of two tracks in the decay $B^0 \to \mu^+\mu^-$ four tracks are reconstructed, the efficiency of reconstructing the two further tracks has to be added. This efficiency was found to be $(88.2 \pm 4.0)\%$ in Run 1B [162].
  - The pointing pointing angle requirement is not used in this search. Its efficiency has therefore to be removed.
  - Since the publication of the result of the search for the decay $B^0 \to \mu^+\mu^-$, a thorough investigation of the loss of J/ψ yield has been conducted [176]. In this analysis, the efficiency has been measured to be $(88.0 \pm 4.0)\%$. This number will be used instead of the one used in the search for the decays $B^0 \to \mu^+\mu^-$.

  With these changes, the fractional uncertainties on the efficiency $\times$ acceptance factor is estimated to be 19.6%.

Adding these uncertainties in quadrature, the total systematic uncertainty is estimated to be 35.5%. It is therefore estimated that a direct search would not yield a significantly better measurement in terms of the systematic uncertainty.

10.5. The branching fraction result

Combining the Run 1A and the Run 1B data samples, two candidates are found in the search region, with an expected background of one event. Finding no evidence for a signal, an upper limit on the branching fraction is set.

The low number of candidates and background does not warrant a background subtraction, and the observed candidates in the search region are assumed to be signal events. This results in Poisson upper limits of 5.32 and 6.30 events at a 90% and 95% confidence level repectively. The systematic uncertainties are included using Equation B.6, yielding upper

limits on the number of candidates of 7.55 and 10.46 events at a 90% and 95% confidence level respectively.

Inserting these upper limit of candidates into Equation 10.13, the 90% and 95% confidence level upper limit of the $B_s^0 \to \mu^+\mu^-\phi$ branching fraction are found to be

$$\mathcal{B}(B_s^0 \to \mu^+\mu^-\phi) < 4.2 \cdot 10^{-5} \ (90\% \ CL)$$

$$\mathcal{B}(B_s^0 \to \mu^+\mu^-\phi) < 5.8 \cdot 10^{-5} \ (95\% \ CL)$$

Chapter 11

Future prospects

The search of FCNC B decays will actively continue in the near future. Several experiments have already begun, or will begin in the next year, with the LHC expected to start in 2005. These will offer rich opportunities to study B mesons, and the prospects of observing several new decay channels is at hand.

A new generation of B factories, with dedicated experiments, has begun operation in the last year, the PEP-II accelerator at SLAC and the KEKB accelerator at KEK. With a centre of mass energy at the $\Upsilon(4S)$ resonance, these will have a large production of B mesons. Furthermore, with asymmetric beam energies, the $B\bar{B}$ system will be boosted with respect to the laboratory frame, which permits a measurement of the proper decay length of the individual B's. These experiments, BaBar at SLAC [177] and BELLE at KEK [178], are optimised to study time-dependent CP asymmetries in B decays, and will carry out a complete programme of B-physics studies.

These experiments will be complemented by the upgraded CLEO III experiment at the CESR accelerator at Cornell [179]. The successive CLEO detectors have already been extremely successful, having recorded the largest sample of $b\bar{b}$ pairs (approximately $8 \cdot 10^6$). This experiment nevertheless has the disadvantage that the $\Upsilon(4S)$ is produced at rest, and the proper decay length of the produced B's is very difficult to measure. The HERA-B experiment [180] at DESY has also started to observe $b\bar{b}$ pairs, produced at a higher energy in hadronic collisions.

With their very large b production cross section, hadron colliders will continue to retain their importance. Furthermore, they have the capability to produce higher mass b hadrons, such as the B_s^0, B_c, b-flavoured baryons or excited states. The upgraded Tevatron, with upgraded experiments, is expected to start the Run 2 physics programme in March 2001. In Run 1, CDF demonstrated that a successful B physics programme can be conducted in a hadronic environment, and, with significant upgrades made to the detector, will continue to have a rich and varied programme in Run 2. The D0 [185] experiment underwent also significant modifications, and will conduct B physics studies as well.

The LHC accelerator at CERN, a pp collider with a centre of mass energy of $\sqrt{s} = 14$ TeV, will start operations in 2005. Four experiments are constructed, two general-purpose detectors, ATLAS [181] and CMS [182], and two specialised detectors, LHCB [183],

a single-arm spectrometer dedicated to the study of B physics, and ALICE [184], to study heavy ion collisions.

11.1. CDF II

The Fermilab accelerators have recently been upgraded to operate at a centre of mass energy of $\sqrt{s} = 2.0$ TeV with instantaneous luminosities of up to $2 \cdot 10^{32}$ cm^{-2}s^{-1} (c.f. Section 5.3). The goal of the Run 2 data taking period is to accumulate data corresponding to an integrated luminosity of 2 fb^{-1}. To reduce the number of simultaneous interactions per bunch crossing, the particle density of the individual bunches is reduced, and the number of bunches is increased from six to 36, yielding a beam crossing time of 396 ns. For higher instantaneous luminosity, the number of bunches could be raised to 108, with a beam crossing time of 132 ns.

To cope with the higher instantaneous luminosity and reduced beam crossing time, the CDF detector is undergoing a major upgrade. Many of the individual subsystems are modified or replaced. The CDF II detector is extensively described in Reference [186]. The modifications relevant to B physics are summarised below.

One of the most important upgrades concerns the tracking system, which is completely revised, based on the successful approach of the Run 1 system while correcting several of its limitations.

The SVX and VTX systems are replaced by a new silicon vertex detector (SVX II) and an intermediate silicon layers system (ISL). The SVX II consists of three independent cylindrical barrels of a total length of 96 cm, covering nearly 98% of the $p\bar{p}$ interaction region. Each barrel consists of five concentric layers of double-sided silicon detectors, placed between radii of 2.4 and 10.7 cm. Three of these layers combine an $r-\phi$ measurement with a 90° stereo measurement and the other two combine an $r-\phi$ measurement with a 1.2° stereo measurement.

In the central region ($|\eta| < 1$), one ISL silicon layer is placed at a radius of 22 cm, and in the plug region ($1 < |\eta| < 2$), two ISL layers are placed at radii of 20 and 28 cm. The ISL silicon detectors are similar to the SVX II detectors, combining an $r-\phi$ measurement with a 1.2° stereo measurement. The SVX II and ISL systems form a single functional system, which will permit stand alone 3D tracking up to $|\eta| < 2$. This considerably extends the geometric acceptance of the SVX and adds further layers to improve the resolution. In the forward region, where only the SVX II and ISL systems can be used for tracking, the asymptotic resolution on the track parameters are expected to be $\delta p_T/p_T < 0.004 \cdot p_T(\text{GeV}/c)^{-1}$[1], where p_T is measured in GeV/c, $\delta d_0 = 15$ μm and $\delta\phi_0 = 0.3$.

The CTC is being replaced by a new open cell drift chamber, the Central Outer Tracker (COT). The design of the COT is similar to the CTC, with smaller drift cells and a faster gas, to limit the drift time to 100 ns, such that even with a beam crossing time of 132 ns, no pile-up will occur. Ninety-six layers of wires are arranged into eight alternating axial and stereo

[1]This can be compared to $\delta p_T/p_T < 0.002 \cdot p_T(\text{GeV}/c)^{-1}$ in Run 1 when only the CTC is used (c.f. Section 6.3.3).

B decay mode	SM $\mathcal{B}$ prediction	CDF Run I	CDF Run II
$B_d^0 \to \mu^+\mu^-$	$(1.5 \pm 0.9) \cdot 10^{-10}$	$< 6.8 \cdot 10^{-7}$	$1 \cdot 10^{-8}$
$B_s^0 \to \mu^+\mu^-$	$(3.5 \pm 1.0) \cdot 10^{-9}$	$< 2.0 \cdot 10^{-6}$	$4 \cdot 10^{-8}$
$B^+ \to \mu^+\mu^- K^+$	$(2 - 8) \cdot 10^{-7}$	$< 5.2 \cdot 10^{-6}$	$2 \cdot 10^{-7}$
$B^0 \to \mu^+\mu^- K^{*0}$	$(1 - 2.5) \cdot 10^{-6}$	$< 4.0 \cdot 10^{-6}$	$4 \cdot 10^{-7}$

Table 11.1: *Standard Model branching fraction predictions and expected CDF sensitivity (at 90% C.L.) for an integrated luminosity of* 2 fb^{-1}.

superlayers, with twelve layers in each superlayer, thus permitting a better measurement of the z coordinates. It will also add dE/dx capability, which could be employed for particle identification.

The existing central muon detectors (CMU, CMP and CMX) will be retained, and their coverage will be extended to fill several of the gaps in azimuth. While the CMU is unchanged, the CMP coverage is increased by approximately 17% and the CMX coverage by approximately 45%. With the tracking extended to $|\eta| < 2$, new systems are needed to identify muons in the forward region.

The FMU is replaced by the Intermediate Muon System (IMU), covering the region $(1 < |\eta| < 1.5)$ with fine granularity and the region $(1.5 < |\eta| < 2.0)$ with enough capability to identify isolated tracks as muons or hadrons. It is composed of three layers of drift chambers similar to those used in the CMP, with one layer of scintillators. These are located on the outer radius of the steel toroids which composed the former FMU system.

In addition to these upgrades, the calorimetric system is also being upgraded, but these are less relevant to B physics studies. The central scintillator-based calorimeters will be retained, and the forward and plug gas calorimeters will be replaced by scintillating tile calorimeters.

With a higher instantaneous luminosity and above all a much reduced beam crossing time, the trigger system has been entirely redesigned. All detector channels will be buffered while awaiting the Level 1 trigger decision. The Level 1 trigger decision is based, as in Run 1, on information from the calorimeter and muon systems, with the added capability of identifying high-p_T tracks (this was previously done only at Level 2).

The major improvement to the Level 2 trigger is the addition of the Silicon Vertex Tracker (SVT). This system is able to reconstruct tracks using measurements from the SVX II and the COT with a resolution similar to the offline reconstruction in the 20 μs allocated to the Level 2 trigger decision. This allows the selection of tracks with a large impact parameter, such as those originating from the displaced decay vertex of B meson. This can be used in B physics studies and for *top* quark, Z^0 or exotic triggers.

The Run 2 B physics programme will profit from the twentyfold increase in data, the extended coverage of the tracking and muon systems and the upgraded trigger system. These tracking upgrades will increase the mass resolution, while the 3-D silicon tracker is expected to improve the vertex measurement resolution.

The estimates of the sensitivity of several FCNC decay searches are given in Table 11.1. The predictions are made on conservative estimates on signal-to-noise ratio based on the

B decay mode	Assumed $\mathcal{B}$	Expected Signal
$B_d^0 \to K^{*0}\gamma$	$4.5 \cdot 10^{-5}$	100-300
$\Lambda_b \to \Lambda\gamma$	$4.5 \cdot 10^{-5}$	3-6
$B^0 \to \mu^+\mu^- K^{*0}$	$1.5 \cdot 10^{-6}$	30-60

Table 11.2: *Number of expected events for several FCNC decays in Run 2 at CDF for an integrated luminosity of* 2 fb^{-1}.

Run 1 studies. Assuming Standard Model branching fractions, several FCNC decays are expected to be observed in Run 2, such as $B_d^0 \to K^{*0}\gamma$, $\Lambda_b \to \Lambda\gamma$ and $B^0 \to \mu^+\mu^- K^{*0}$. The signal yield can be estimated by scaling the Run 1 analysis results with the ratio of the acceptances between Run 1 and Run 2 [187]. As the final requirements will obviously depend on experimental conditions, only an estimate of the number of expected events can be given. This is given in Table 11.2 for a data sample of 2 fb^{-1}. For the decay, $B^0 \to \mu^+\mu^- K^{*0}$, such a sample may allow to study the invariant mass distribution of the muon pair and the forward-backward charge asymmetry, although the low number of candidates may not be enough to study the Standard Model or its extensions. Based on the extrapolations from Run 1 to Run 2 presented in Tables 11.1 and 11.2, it can be estimated that the decay rates of several other decays, such as $B^+ \to \mu^+\mu^- K^+$, $B_s^0 \to \phi\gamma$ or $B_s^0 \to \mu^+\mu^-\phi$, may be just at the limit of the attainable sensitivity.

11.2. ATLAS

The LHC is scheduled to start operations in the year 2005, at an energy of $\sqrt{s} = 14$ TeV, with an initial (low) instantaneous luminosity of the order of 10^{33} $\text{cm}^{-2}\text{s}^{-1}$. Three years of data-taking at the low luminosity is expected to yield an integrated luminosity of 30 fb^{-1}, after which period, the instantaneous luminosity will be raised to 10^{34} $\text{cm}^{-2}\text{s}^{-1}$, where data corresponding to an integrated luminosity of 100 fb^{-1} could be collected per year.

The Atlas collaboration B physics program [46] will focus on the search and measurement of CP-violation through the decays $B_d^0 \to J/\psi K_S^0$, $B_d^0 \to \pi^+\pi^-$ and $B_s^0 \to J/\psi\phi$, the measurement of B_s^0 mixing, searches for FCNC decays, the study of B-baryon decay dynamics, and spectroscopy of B hadrons. B physics studies will be experimentally easiest at the initial low luminosity, where pile-up effects are small and vertex detectors very close to the beam pipe are expected to survive for several years. Much of the B physics will therefore be performed during the first few years of LHC operation, although it can also be performed at higher luminosities, albeit at the price of higher background and reduced performance and efficiency.

It is expected that the total B production cross section at $\sqrt{s} = 14$ TeV is approximately of 500 μb. Although only a fraction of the total cross section can be used for physics studies, the high production rate and the luminosity favour the search for FCNC decays. Predictions are based on simulations and the analyses are similar to those performed at CDF.

The potential of observing several FCNC B decays has been studied in Reference [46]. For the studied decays, the estimated number of signal and background events observed in the low luminosity data (30 fb^{-1}) and, if available, one year of high luminosity data

		30 fb^{-1}		100 fb^{-1}	
B decay mode	Assumed $\mathcal{B}$	Signal	Background	Signal	Background
$B_d^0 \to \mu^+\mu^-$	$1.5 \cdot 10^{-10}$	4	93	14	660
$B_s^0 \to \mu^+\mu^-$	$3.5 \cdot 10^{-9}$	27	93	92	660
$B_d^0 \to \rho^0\mu^+\mu^-$	$1 \cdot 10^{-7}$	220	950	-	-
$B^0 \to \mu^+\mu^- K^{*0}$	$1.5 \cdot 10^{-6}$	2000	290	-	-
$B_s^0 \to \mu^+\mu^-\phi$	$1 \cdot 10^{-6}$	410	140	-	-

Table 11.3: *Number of expected signal and background events for several FCNC decays at ATLAS.*

(100 fb^{-1}), is given in Table 11.3.

The decays $B_d^0 \to \rho^0\mu^+\mu^-$, $B^0 \to \mu^+\mu^- K^{*0}$ and $B_s^0 \to \mu^+\mu^-\phi$ should all be observed in the low luminosity data. The interest in observing the decay $B_d^0 \to \rho^0\mu^+\mu^-$ lies in the possibility of determining the ratio $|V_{td}|/|V_{ts}|$. Indeed, the ratio of the branching fractions of the decays $B_d^0 \to \rho^0\mu^+\mu^-$ and $B^0 \to \mu^+\mu^- K^{*0}$ is proportional to the squared ratios of the CKM matrix elements and of the respective form factors. The overall form factors still have a large theoretical uncertainty. These are nevertheless smaller in the muon pair invariant mass range $16.5(\mathrm{GeV}/c^2)^2 < q^2 < 19.25(\mathrm{GeV}/c^2)^2$, and by restricting the events to this mass range, $|V_{td}|/|V_{ts}|$ could be measured with a statistical uncertainty of 14% and a systematic uncertainty of 7%.

The high number of observed $B^0 \to \mu^+\mu^- K^{*0}$ decays will allow a detailed study of the forward-backward charge asymmetry and possible contributions from non-Standard Model processes [188]. The accuracy is expected to be sufficient to separate the effects on the asymmetry from Standard Model and from MSSM processes contributing to the decay.

After the first year of operation at low luminosity, the branching fraction sensitivity at 95% C.L. would reach $9 \cdot 10^{-10}$ for $B_d^0 \to \mu^+\mu^-$ and $3.4 \cdot 10^{-9}$ for $B_s^0 \to \mu^+\mu^-$, if no signal is seen above background. Assuming Standard Model branching fraction, the decay $B_s^0 \to \mu^+\mu^-$ could be observed in the 30 fb^{-1} of low-luminosity data, with a low signal significance of $2.8\,\sigma$. With one further year of high luminosity of data, a $4.3\,\sigma$ signal significance could be reached, assuming no deterioration of the inner detector. With this sample, the 95% C.L. upper limit on the branching fraction of the decay $B_d^0 \to \mu^+\mu^-$ would be $3 \cdot 10^{-10}$, and it could be observed if B physics studies can continue at high luminosity.

Chapter 12

Conclusion

A search for the flavour-changing neutral current decays $B_d^0 \to \mu^+\mu^-$, $B_s^0 \to \mu^+\mu^-$ and $B_s^0 \to \mu^+\mu^-\phi$ has been conducted in $p\bar{p}$ collisions at $\sqrt{s} = 1.8$ TeV produced at the Collider Detector at Fermilab (CDF). In the Standard Model, these decays are forbidden at tree-level, but proceed at low rate via higher order processes. The low predicted rates place these decays outside reach of the present study, but several extensions of the Standard Model predict substantially higher branching fractions. An observation of one of these decays would indicate contributions from processes beyond the Standard Model.

The search for the decays $B_d^0 \to \mu^+\mu^-$ and $B_s^0 \to \mu^+\mu^-$ is conducted using data corresponding to an integrated luminosity of 98 pb^{-1}. One candidate event is found for each of these decays, which is consistent with the background estimates. Finding no evidence for a signal, an upper limit on the branching fraction is set. Assuming the candidate event to be a signal event, the 95% confidence level upper limits of the branching fractions, derived from a direct measurement, are found to be

$$\mathcal{B}(B_d^0 \to \mu^+\mu^-) < 8.6 \cdot 10^{-7}$$
$$\mathcal{B}(B_s^0 \to \mu^+\mu^-) < 2.6 \cdot 10^{-6}$$

These limits, published in Reference [97], are significant improvements over the previously published results but still orders of magnitude above the Standard Model predictions. With branching fractions as predicted in the Standard Model, the first observations of these decay should be possible at the LHC experiments.

The search for the decay $B_s^0 \to \mu^+\mu^-\phi$ is conducted using data corresponding to an integrated luminosity of 91.4 pb^{-1}. Two candidates are found in the search region, with an expected background of one event. Finding no evidence for a signal, an upper limit on the branching fraction is set. Assuming the candidate events to be signal events, the 95% confidence level upper limit of the branching fraction, derived from a measurement relative to the decay $B_s^0 \to J/\psi\,\phi$, is found to be

$$\mathcal{B}(B_s^0 \to \mu^+\mu^-\phi) < 5.8 \cdot 10^{-5}$$

This study constitutes the first search for this decay, A publication is in preparation. The measured upper limit of the branching fraction is approximately a factor 30 above the Standard Model prediction. As such, if not observed in the next Run by the CDF experiment,

it will without doubt be observed by the LHC experiments, provided the Standard Model estimate of the branching fraction is correct. A measurement of the invariant mass distribution of the muon pair and of the forward-backward charge asymmetry will provide valuable information on the processes involved.

In addition to these decays, the author has participated in the search for the decays $B^+ \to \mu^+\mu^- K^+$ and $B^0 \to \mu^+\mu^- K^{*0}$. No evidence for these decays has been found in this search, and the 90% confidence level upper limit of the branching fractions is found to be

$$\mathcal{B}(B^+ \to \mu^+\mu^- K^+) < 5.2 \cdot 10^{-6}$$

$$\mathcal{B}(B^0 \to \mu^+\mu^- K^{*0}) < 4.0 \cdot 10^{-6}$$

Both these decays are expected to be observed in the near future, both at the B factories and at CDF.

In conclusion, no significant signal for the sought flavour-changing neutral current decays of B mesons has been observed in this search. However, with the next generation of experiments, observation of several new flavour-changing neutral current decays of the B meson is expected to provide a stringent test of the Standard Model, and may offer a glimpse of possible new physics effects.

Remerciements

Je tiens tout d'abord à exprimer ma gratitude envers le Professeur Allan G. Clark pour m'avoir donné la possibilité de travailler sur une expérience telle que CDF et m'avoir ainsi fait découvrir ce vaste et fascinant domaine qu'est la physique des particules. Je lui sais gré de son enseignement, de ses conseils et de la confiance qu'il m'a témoigné.

Je remercie tout particulièrement les Dr. Xin Wu et Hans Wenzel, pour leur dévouement et leur patience. Nombreuses furent les discussions au cours desquelles ils m'ont guidé dans mon travail. C'est uniquement grace à leur aide précieuse que cette recherche a pu être menée à bien.

Un grand merci également à Annie Léger, pour sa patience, ses nombreuses explications et son aide, et ce toujours avec le sourire. Mes remerciements vont aussi aux membres des groupes électronique et informatique.

Je tiens aussi à remercier nos collègues de l'INFN de Pise, en particulier le Professeur Luciano Ristori et le Dr. Stefano Belforte, pour m'avoir accueilli parmis eux. Merci également à toutes les personnes de la collaboration CDF pour leur aide, directe ou indirecte.

Je désire remercier tous mes collègues du groupe pour l'amitié qu'ils m'ont témoignée au fil des années. Les pauses-café ne seront plus les mêmes sans eux!

Finalement, jamais je ne pourrai remercier assez mes parents et ma compagne pour leur soutient sans faille, leur aide et leur amour. Sans eux, ce travail n'aurait pas été possible. C'est à eux que cette thèse est dédiée.

Part IV

Appendices

Appendix A

The Monte Carlo simulations

This section introduces the Monte Carlo simulations used to simulate the various processes studied in these searches. The simulation proceeds in several steps. First, b quarks are generated and hadronized into B mesons. These are then decayed to a specified final state, and the signature left by the final-state particles in the CDF detector are simulated. Finally, the dimuon triggers are simulated.

A.1. The B meson generation

First, b quarks are generated [189] according to the correlation between $p_T(b)$ and $y(b)$ calculated by Nason, Dawson and Ellis (NDE) [38] at next-to-leading order (c.f. Section 3.1.2). The parton distribution functions MRSD0, calculated by Martin, Roberts and Stirling [190] are used. The renormalization scale is chosen as $\mu = \mu_0 \equiv \sqrt{m_b^2 + p_T^2(b)}$, and the b-mass is chosen as $m_b = 4.75\ \mathrm{GeV}/c^2$.

The b quarks are then fragmented into the specified B meson according to the Peterson fragmentation model [47] with $\epsilon_b = 0.006$ [191].

For the purposes of this study, the b quarks are generated in the rapidity range $|y(b)| < 1.3$ and $p_T(b) > 5.5\ \mathrm{GeV}/c$. Only B mesons with $p_T > 6.0\ \mathrm{GeV}/c$ and $|y(B)| < 1.0$ are retained, as these are the minimum requirements imposed on B mesons in both searches.

A.2. The B meson decay simulation

The simulation of the decay of the B mesons is done using CLEOMC [175], a version of the QQ B decay Monte Carlo simulator developed at CLEO and modified for CDF. The kinematics of the final state particles are determined according to phase space. Properties of initial and final state particles (masses, lifetimes and intrinsic widths), were set to the world-average values at the time of the study, as given in References [1, 172].

The decay $B_s^0 \to \mu^+\mu^-\phi$ was not simulated according to three-body phase space, but according to the prediction of the decay matrix elements, which were implemented in the CLEOMC 'user' function. This is described in the following section.

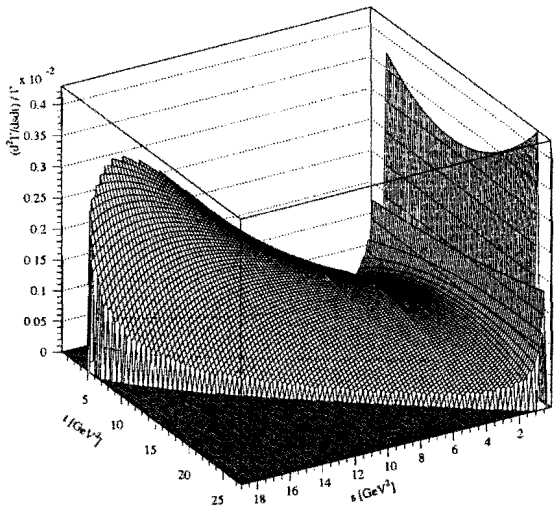

Figure A.1: *The double-differential decay width* $\frac{d^2\Gamma}{d\hat{s}\,d\hat{t}}$ *of the short distance processes using the CQM form factors in the allowed phase space.*

A.2.1. The $B_s^0 \rightarrow J/\psi\,\phi$ decay model

The analytical expression of the double-differential partial width $\frac{d^2\Gamma}{d\hat{s}\,d\hat{t}}$[1], based on the calculation of the effective weak Hamiltonian describing the $b \rightarrow s$ transition, is presented in Reference [75][2]. This reference also presents the analytical expression of $\frac{d\Gamma}{d\hat{s}}$, obtained after integrating $\frac{d^2\Gamma}{d\hat{s}\,d\hat{t}}$ over $\hat{t}$.

Two calculations of $B_s^0 \rightarrow \phi$ form factors have been published, one using the LCSR model [81] and the other using the CQM model [83] (c.f. Section 4.4.2). The more recent CQM form factors are used for the Monte Carlo studies, and the LCSR form factors are used to estimate the uncertainty associated with the choice of a particular model.

The expressions of the Wilson coefficients are presented in Reference [66]. These have to be estimated at the same renormalization scale μ as the form factors, to cancel the scale dependence. The CQM form factors have been calculated at $\mu = 4.85\ \mathrm{GeV}/c^2$ and the LCSR form factors at $\mu = 4.80\ \mathrm{GeV}/c^2$. [3]

Figure A.1 shows the double-differential decay width of the short distance processes

[1] $\hat{s} = s/M_{B_s^0}^2 = q^2/M_{B_s^0}^2$ $(q^2 = M^2(\mu^+\mu^-))$, $\hat{t} = t/M_{B_s^0}^2 = (p_B - p_{l+})^2/M_{B_s^0}^2$.

[2] It should be noted that the expression of one of the terms in $\frac{d^2\Gamma}{d\hat{s}\,d\hat{t}}$ presented in Reference [75] contains an error. The third term of the expression of $\beta_V^{(1)}$ (page 6821) should be read as $\frac{\lambda(1,\hat{s},\hat{r})}{2\hat{r}}\hat{\Pi}|H_+(q^2)|^2$, instead of $\frac{\lambda^2(1,\hat{s},\hat{r})}{2\hat{r}}\hat{\Pi}|H_+(q^2)|^2$ [192].

[3] Further parameters are the masses of the *strange*, *charm* and *top* quarks. These are set to $m_s = 0.35\ \mathrm{GeV}/c^2$ and $m_c = 1.45\ \mathrm{GeV}/c^2$ for the CQM form factors and $m_s = 0.15\ \mathrm{GeV}/c^2$ and $m_c = 1.40\ \mathrm{GeV}/c^2$ for the LCSR form factors. The *top* quark mass is set to $m_t = 174.3\ \mathrm{GeV}/c^2$.

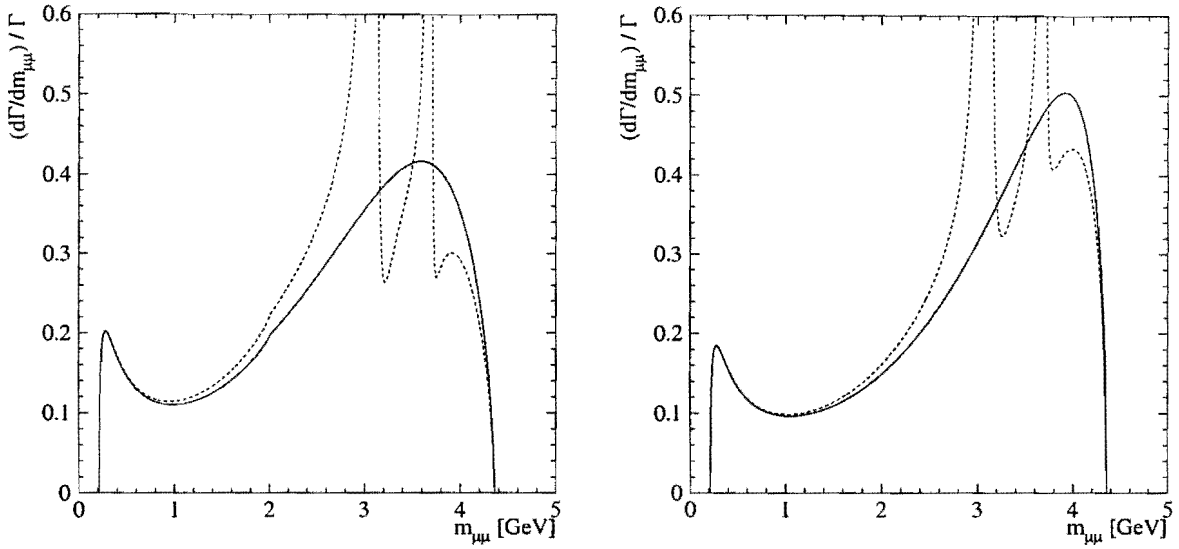

Figure A.2: *The differential decay width $\frac{d\Gamma}{d\hat{s}}$ using the CQM (left) and the LCSR (right) form factors. The solid line includes only short distance processes and the dotted line includes both short and long distance processes. The two peaks correspond to the J/ψ and $\psi(2S)$ resonances.*

using the CQM form factors in the allowed phase space, and Figure A.2 shows the invariant mass distribution of the muon pair with and without the long distance contributions for the two models. The lower limit of the invariant mass of the muon pair is $s = 2m_\mu$ and the upper limit $s = (m_{B_s^0} - m_\phi)$.

Including the differential matrix element [192] into the CLEOMC 'user' function permits to simulate the $B_s^0 \to \mu^+\mu^-\phi$ decay with and without the long-distance contributions, for either of the two form factor calculations.

A.3. The detector simulation

The final state particles are then passed to a detector simulation [193], which will simulate their passage through the detector using a parameterization of the detector response. Rather then producing raw data, which would necessitate a complete reconstruction, high-level banks, similar to the ones produced by the reconstruction software, are produced. This permits subsequently to process the simulated events in the same manner as data events.

Instead of using the default wire efficiencies for each layer of wires in the CTC, these have been measured from J/ψ data. Using the measured wire efficiencies permits to reproduce the mass resolutions observed in the data by the Monte Carlo simulations, as shown in Table 9.7 and Figure 9.9

A.4. The Level 1 and Level 2 dimuon trigger simulation

As the detector simulation does not simulate the triggers, these will have to be simulated separately. The Level 1 and Level 2 dimuon trigger simulation [194] implements the measured efficiency curves of the Run 1A TWO_CMU_ONE_CFT trigger and the Run 1B TWO_CMU_TWO_CFT_2_2, CMX_CMU_TWO_CFT_2_2, TWO_CMU_CMX_ONE_CFT_3_4 and TWO_CMU_ONE_CFT_2_2_6TOW triggers.

Their efficiencies have been measured using an unbiased sample of $J/\psi \rightarrow \mu^+\mu^-$ and $Z^0 \rightarrow \mu^+\mu^-$ candidates [157, 195].

The Level 1 triggers (c.f. Section 6.7.1) were nearly identical between Run 1A and Run 1B, and their efficiencies are considered to be mainly dependent on the p_T of the muons.

The Level 2 triggers (c.f. Section 6.7.2) were substantially modified between Run 1A and Run 1B. The efficiencies of these triggers were found to be dependent on the charge, pseudorapidity and azimuth of the muons and on the integrated luminosity. The ϕ dependence is due to the beam offset from the CTC axis, which introduces a false curvature term in the measured CFT curvature, affecting the CFT track-finding efficiency. Due to the geometry of the CTC, positive tracks have a higher probability of being found by the CFT. Over time, loss of individual hit efficiency ageing effects of the CTC have been observed, which in turn degrade the CFT track-finding efficiency. This loss of efficiency appears to be more pronounced for tracks at small $|\eta|$.

The Run 1B Level 2 trigger efficiencies implemented in the trigger simulation were parametrized as functions of p_T, charge, η and ϕ of the muon. With modifications on the hardware and CFT pattern maps occurring in the course of Run 1B, different parameterizations were implemented, and trigger efficiencies were averaged over the run range for which the dimuons were simulated. The simulation accounts also for the prescale factors of the different triggers and for muon chambers inefficiencies. The trigger efficiencies could also be calculated separately for specific run ranges.

As the Level 3 dimuon trigger efficiency, was found to be independent on the transverse momentum of the muons, no Level 3 trigger was necessary. It has nevertheless been performed for some of the studies.

Appendix B

Limit calculations

B.1. Confidence intervals

Most often, measurements of a certain parameter are reported with a statistical uncertainty, also referred to as *standard error*, in the form $\hat{\theta} \pm \hat{\sigma}_{\hat{\theta}}$. This is often taken as the standard deviation of the estimator, which can be regarded as a measurement of how widely the estimates of the parameter would be distributed if the experiment were repeated many times with the same number of observations per experiment.

Instead of the estimated parameter and the standard error, a *confidence interval* can be reported. The formal construction of confidence intervals can be found in References [196, 1], and only a brief definition of confidence intervals will be given here.

For a measured value ($\hat{\theta}$), an interval $[a, b]$ can be constructed such that, if the experiment were repeated many times, this interval would include the (unknown) true value (θ) of the parameter attempted to be measured in a fraction $1 - \epsilon$ of the experiments:

$$P[a(\hat{\theta}) < \theta < b(\hat{\theta})] = 1 - \epsilon \,. \tag{B.1}$$

This interval is called the *confidence interval* at a *confidence level*, or *coverage probability*, of $1 - \epsilon$. The parameters a and b are determined from the measurements, and thus depend on the measured parameter $\hat{\theta}$. They are obtained from the probability density function $f(\hat{\theta}, \theta)$, which gives the probability of measuring $\hat{\theta}$ for a given θ.

Methods in which a probability density function exists that can yield (for all θ) confidence intervals that contain the true value θ with a probability $1 - \epsilon$ are said to have *coverage*.

For cases where the probability density function $f(\hat{\theta}, \theta)$ is a Gaussian with mean θ,the interval covered by $\hat{\theta} \pm \hat{\sigma}_{\hat{\theta}}$ corresponds to the confidence interval at a confidence level of 68.3%.

When measured values for which no clear signal can be found are close to a physical boundary, a one-sided confidence interval, or limit, can be reported. By setting a to the physical boundary (e.g. 0), b will be the upper limit on the true parameter such that $P(\theta < b) = 1 - \epsilon$.

For two sided confidence intervals, the probability $1-\epsilon$ is not enough to determine a and b uniquely. Two probabilities have to be specified, α and β, with $\epsilon = \alpha + \beta$, such that

$$\begin{aligned} P[a(\hat{\theta}) \geq \theta] &= \alpha \\ P[b(\hat{\theta}) \leq \theta] &= \beta \,. \end{aligned} \tag{B.2}$$

Central confidence intervals are usually chosen, where $\alpha = \beta = \epsilon/2$.

B.2. Confidence intervals for Poisson distributions

In the case of a counting experiment such as the one conducted here, the measurements are restricted to integer values, usually the numbers of events observed (n_{obs}). The distribution of n_{obs} ($\equiv \hat{\theta}$) will then be a binomial or, for small numbers, a Poisson distribution.

In a Poisson distribution with mean λ ($\equiv \theta$), the probability to observe n_{obs} events is

$$P(n_{obs}, \lambda) = \frac{\lambda^{n_{obs}}}{n_{obs}!} e^{-\lambda} \,. \tag{B.3}$$

The probability defined in Equation B.1 will be the sum of finite terms, and will not be equal to the confidence level $1-\epsilon$ for on all values of λ. The intervals are then constructed in such a way that for some values of λ, the intervals have exact coverage ($P[a < \lambda < b] = 1-\epsilon$), while for the other values, the intervals have over-coverage ($P[a < \lambda < b] > 1-\epsilon$).

The limits of a two-sided interval will so be given by solving the equations

$$\begin{aligned} \alpha &= \sum_{n=n_{obs}}^{\infty} \frac{a^n}{n!} e^{-a} \\ \beta &= \sum_{n=0}^{n_{obs}} \frac{b^n}{n!} e^{-b} \,, \end{aligned} \tag{B.4}$$

and the upper limit U of a one-sided interval will be given by solving

$$1-\epsilon = \sum_{n=n_{obs}+1}^{\infty} \frac{U^n}{n!} e^{-U} \,. \tag{B.5}$$

Alas, this represents an ideal situation, as usually the number of observed events will be the sum of signal and background events, with the latter usually not known accurately. Furthermore, the final measurement will be composed of other factors beside the number of observed events, and the systematic uncertainties on these factors will also have to be included. In these cases, no universally accepted method of calculating the result exists, and reporting such a result is still controversial.

The methods which are used to calculate the confidence intervals for the measurements performed in this study will be presented briefly in the following, including these complications one after the other.

B.2.1. Including a systematic uncertainty

The limits obtained above take only into account the Poisson fluctuation, ignoring all systematic uncertainties. In the case where a significant number of events are observed, the result will not be presented as an interval, but as the estimator with the statistical and systematic uncertainties, the latter two terms usually added in quadrature. For a Poisson distribution, the estimator is simply n_{obs}, and the statistical uncertainty is then taken as the standard deviation of the Poisson distribution, $\sqrt{n_{obs}}$.

In the case where the number of observed events is small, the method presented above do not permit to include readily the systematic uncertainties into the confidence intervals.

In the method presented in Reference [197], the Poisson probability (Equation B.3) is expanded about the standard upper limit point which would be obtained without error (Equation B.5). The modified upper limit of candidates would then be given by the expression:

$$U = U_0 \left[1 + \frac{E\sigma_r^2}{2} \left\{ 1 + \left(\frac{E\sigma_r}{2} \right)^2 \right\} \right] , \tag{B.6}$$

where U_0 is the Poisson upper limit for n_{obs} events as found in Equation B.5, $E = U_0 - n_{obs}$, and σ_r is the relative systematic error.

This is the method used in this study to calculate the upper limits on the branching fractions, since, in each search, the number of background events is estimated to be small.

B.2.2. Including a background known without error

More often, the observed events will be the sum of the sought signal and of an irreducible background. Both the numbers of signal (n_s) and background events (n_b) will follow a Poisson distribution, with means λ_s and λ_b respectively. Being the sum of two Poisson variables ($n_{obs} = n_s + n_b$), the number of observed events will be distributed according to a Poisson distribution as well:

$$P(n_{obs}, \lambda_s + \lambda_b) = \frac{(\lambda_s + \lambda_b)^{n_{obs}}}{n_{obs}!} e^{-(\lambda_s + \lambda_b)} . \tag{B.7}$$

In this section, the mean of the background λ_b will first be supposed to be known without uncertainty. The uncertainties will be included in the next section.

If the number of observed events is large compared to the expected number of background events, the excess can be considered to come from the signal, and a two-sided interval can be constructed as previously by solving

$$\begin{aligned} \alpha &= \sum_{n=n_{obs}}^{\infty} \frac{(a + \lambda_b)^n}{n!} e^{-(a+\lambda_b)} \\ \beta &= \sum_{n=0}^{n_{obs}} \frac{(b + \lambda_b)^n}{n!} e^{-(b+\lambda_b)} . \end{aligned} \tag{B.8}$$

As expected, in the case where the background can be eliminated completely ($\lambda_b = 0$), Equations B.4 are found.

This method breaks down when the number of observed events is *not* large compared to the expected number of background events. In this case, if n_{obs} actually becomes smaller than λ_b, the upper limit derived from Equations B.5 may be a negative number, which is physically impossible.

The solution proposed in References [198, 199] is to renormalize the Poisson distribution describing the background, requiring that the number of background events present in the data n_b be smaller or equal to the total number of observed events n_{obs}. The renormalized distribution is then given by

$$P'(n_b, \lambda_b) = \frac{P(n_b, \lambda_b)}{\sum_{n=0}^{n_{obs}} P(n, \lambda_b)} = \frac{\frac{\lambda_b^{n_b}}{n_b!} e^{-\lambda_b}}{\sum_{n=0}^{n_{obs}} \frac{\lambda^n}{n!} e^{-\lambda_b}} . \tag{B.9}$$

With the signal still described by a Poisson distribution (Equation B.3), the probability to observe n_{obs} events will be given by

$$W(n_{obs}, \lambda_s, \lambda_b) = \frac{\frac{(\lambda_s + \lambda_b)^{n_{obs}}}{n_{obs}!} e^{-(\lambda_s + \lambda_b)}}{\sum_{n=0}^{n_{obs}} \frac{\lambda^n}{n!} e^{-\lambda_b}} , \tag{B.10}$$

and the upper limit U of the one-sided interval will be given by solving

$$1 - \epsilon = \frac{\sum_{n=0}^{n_{obs}} \frac{(\mu_B + U)^n}{n!} e^{-(\mu_B + U)}}{\sum_{n=0}^{n_{obs}} \frac{\mu_B^n}{n!} e^{-\mu_B}} . \tag{B.11}$$

B.2.3. Including a background and all systematic uncertainties

The expected background can usually not be estimated without an uncertainty. The method described in Reference [200] permits to incorporate both the uncertainty on the background and the overall systematic uncertainty in the upper limit[1].

In this method, the *true* value of the mean of the background contribution λ_b (which is unknown) is assumed to be distributed according to a Gaussian whose mean is the *estimated* background contribution $\hat{\lambda}_b$ and standard deviation is the uncertainty of the estimation σ_b:

$$G(\lambda_b; \hat{\lambda}_b, \sigma_b) = \frac{1}{\sqrt{2\pi}\sigma_b} e^{-\frac{(\lambda_b - \hat{\lambda}_b)^2}{2\sigma_b^2}} . \tag{B.12}$$

The distribution of the number of background events is the convolution of the Poisson distribution with the Gaussian, renormalized as before to constrain the number of background

[1] In the case where the background contribution is known without uncertainty, and only the overall systematic uncertainty is to be accounted, Reference [197] provides a formula similar to Equation B.6 to calculate the upper limit.

events present in the data n_b to be smaller than the observed number of events:

$$P'(n_b, \hat{\lambda}_b) = \frac{\int P(n_b, \hat{\lambda}_b)\, G(\lambda_b; \hat{\lambda}_b, \sigma_b)\, d\hat{\lambda}_b}{\sum_{n=0}^{n_{obs}} \int P(n, \hat{\lambda}_b)\, G(\lambda_b; \hat{\lambda}_b, \sigma_b)\, d\hat{\lambda}_b} = \frac{\int \frac{\hat{\lambda}_b^{n_b}}{n_b!} e^{-\hat{\lambda}_b} e^{-\frac{(\lambda_b - \hat{\lambda}_b)^2}{2\sigma_b^2}}\, d\hat{\lambda}_b}{\sum_{n=0}^{n_{obs}} \int \frac{\hat{\lambda}_b^{n}}{n!} e^{-\hat{\lambda}_b} e^{-\frac{(\lambda_b - \hat{\lambda}_b)^2}{2\sigma_b^2}}\, d\hat{\lambda}_b} \,. \tag{B.13}$$

To include the overall systematic uncertainty, the *true* mean of the signal λ_s is similarly assumed to be distributed according to a Gaussian whose mean is the 'observed' signal $\hat{\lambda}_s$. Here, the standard deviation of the Gaussian is given by $\sigma_r \cdot \hat{\lambda}_s$, where σ_r is the relative systematic uncertainty:

$$G(\lambda_s; \hat{\lambda}_s, \sigma_r \hat{\lambda}_s) = \frac{1}{\sqrt{2\pi}(\sigma_r \hat{\lambda}_s)} e^{-\frac{(\lambda_s - \hat{\lambda}_s)^2}{2(\sigma_r \hat{\lambda}_s)^2}} \,. \tag{B.14}$$

The distribution of the number of signal events is then convoluted to this Gaussian, and the upper limit U of the one-sided interval will be given by solving

$$1 - \epsilon = \frac{\sum_{n=0}^{n_{obs}} \int\int P(n, \lambda_s + \lambda_b)\, G(\lambda_b; \hat{\lambda}_b, \sigma_b)\, G(\lambda_s; U, \sigma_r U)\, d\lambda_s\, d\lambda_b}{\sum_{n=0}^{n_{obs}} \int P(n, \lambda_b)\, G(\lambda_b; \hat{\lambda}_b, \sigma_b)\, d\lambda_b} \tag{B.15}$$

$$= \frac{\sum_{n=0}^{n_{obs}} \frac{1}{\sqrt{2\pi}\sigma_r U} \int\int \frac{(\lambda_s + \lambda_b)^n}{n!} e^{-(\lambda_s + \lambda_b)} e^{-\frac{(\lambda_b - \hat{\lambda}_b)^2}{2\sigma_b^2}} e^{-\frac{(\lambda_s - U)^2}{2(\sigma_r U)^2}}\, d\lambda_s\, d\lambda_b}{\sum_{n=0}^{n_{obs}} \int \frac{\lambda_b^n}{n!} e^{-\lambda_b} e^{-\frac{(\lambda_b - \hat{\lambda}_b)^2}{2\sigma_b^2}}\, d\lambda_b} \,. \tag{B.16}$$

Appendix C

The signal optimization tables

In this Annex are presented the two tables (Tables C.1 and C.1) showing the values of the signal-to-background significance obtained for the various sets of requirements tested to optimize the selection requirements for the decays $B^0 \to \mu^+\mu^-$.

Also shown is the table (Table C.3) showing the values of the sensitivity obtained for the various sets of requirements tested to optimize the selection requirements for the decay $B_s^0 \to \mu^+\mu^-\phi$.

$c\tau$ [μm]	Isolation	Φ [radians]	like sign [events]	Rejection	Efficiency ϵ_S [%]	*sig*
no cut	no cut	no cut	2221	1.0	100.0	1.0 ± .0
no cut	> 0.7	no cut	387	5.7	76.2	3.3 ± .2
no cut	> 0.75	no cut	252	8.8	68.9	4.2 ± .3
no cut	> 0.8	no cut	160	13.9	54.4	4.1 ± .5
> 100	no cut	no cut	395	5.6	81.0	3.7 ± .2
> 100	> 0.7	no cut	47	47.3	61.7	18.0 ± 2.8
> 100	> 0.7	< 0.1	10	222.1	49.6	54.6 ± 17.5
> 100	> 0.7	< 0.2	16	138.8	58.3	47.2 ± 12.0
> 100	> 0.75	no cut	28	79.3	55.8	24.7 ± 4.9
> 100	**> 0.75**	**< 0.1**	5	444.2	44.8	89.2 ± 40.2
> 100	> 0.75	< 0.2	9	246.8	52.7	68.6 ± 23.2
> 100	> 0.8	no cut	19	116.9	44.1	22.7 ± 5.5
> 100	> 0.8	< 0.1	3	740.3	35.4	92.7 ± 54.1
> 100	> 0.8	< 0.2	6	370.2	41.6	64.2 ± 26.7
> 150	no cut	no cut	309	7.2	72.7	3.8 ± .2
> 150	> 0.7	no cut	34	65.3	55.4	20.0 ± 3.6
> 150	> 0.7	< 0.1	8	277.6	44.5	54.9 ± 19.6
> 150	> 0.7	< 0.2	12	185.1	52.4	50.7 ± 14.8
> 150	> 0.75	no cut	21	105.8	50.1	26.5 ± 6.0
> 150	> 0.75	< 0.1	5	444.2	40.2	71.9 ± 32.4
> 150	> 0.75	< 0.2	8	277.6	47.3	62.2 ± 22.3
> 150	> 0.8	no cut	13	170.8	39.5	26.7 ± 7.7
> 150	> 0.8	< 0.1	3	740.3	31.8	74.7 ± 43.6
> 150	> 0.8	< 0.2	5	444.2	37.4	62.0 ± 28.2
> 200	no cut	no cut	253	8.8	65.1	3.7 ± .2
> 200	> 0.7	no cut	30	74.0	49.6	18.2 ± 3.4
> 200	> 0.7	< 0.1	7	317.3	39.8	50.3 ± 19.2
> 200	> 0.7	< 0.2	11	201.9	46.9	44.4 ± 13.5
> 200	> 0.75	no cut	20	111.1	44.9	22.3 ± 5.1
> 200	> 0.75	< 0.1	4	555.3	36.0	72.0 ± 36.3
> 200	> 0.75	< 0.2	7	317.3	42.4	57.0 ± 21.8
> 200	> 0.8	no cut	13	170.8	35.4	21.4 ± 6.2
> 200	> 0.8	< 0.1	3	740.3	28.4	59.9 ± 34.9
> 200	> 0.8	< 0.2	5	444.2	33.5	49.8 ± 22.6
no cut	no cut	< 0.1	107	20.8	80.3	13.4 ± 1.3
no cut	no cut	< 0.2	219	10.1	94.5	9.1 ± .6
> 100	no cut	< 0.1	47	47.3	65.0	20.0 ± 2.9
> 100	no cut	< 0.2	99	22.4	76.5	13.1 ± 1.3
> 150	no cut	< 0.1	38	58.4	58.4	19.9 ± 3.2
> 150	no cut	< 0.2	77	28.8	68.7	13.6 ± 1.5
> 200	no cut	< 0.1	31	71.6	52.3	19.6 ± 3.5
> 200	no cut	< 0.2	63	35.3	61.5	13.3 ± 1.7

Table C.1: *Number of events remaining and rejection factor of same-signed muon pairs in the* $5 - 6\ \mathrm{GeV}/c^2$ *mass range with the signal efficiency and the signal-to-background significance. The requirements selected are highlighted.*

$c\tau$ [μm]	Isolation	$\Delta\varphi(\vec{p}_T^{\mu\mu}, \vec{P}_{vtx})$ [radians]	sideband [events]	Rejection	Efficiency ϵ_S [%]	*sig*
no cut	no cut	no cut	2229	1.0	100.0	1.0 ± .0
no cut	> 0.7	no cut	565	3.9	76.2	2.3 ± .1
no cut	> 0.75	no cut	413	5.4	68.9	2.6 ± .2
no cut	> 0.8	no cut	300	7.4	54.4	2.2 ± .2
> 100	no cut	no cut	434	5.1	81.0	3.4 ± .1
> 100	> 0.7	no cut	72	31.0	61.7	11.8 ± 1.5
> 100	> 0.7	< 0.1	2	1114.5	49.6	273.8 ± 194.1
> 100	> 0.7	< 0.2	13	171.5	58.3	58.3 ± 16.4
> 100	> 0.75	no cut	46	48.5	55.8	15.1 ± 2.4
> 100	**> 0.75**	**< 0.1**	1	2229.0	44.8	447.7 ± 448.4
> 100	> 0.75	< 0.2	8	278.6	52.7	77.5 ± 27.7
> 100	> 0.8	no cut	24	92.9	44.1	18.0 ± 4.0
> 100	> 0.8	< 0.1	0	∞	35.4	∞
> 100	> 0.8	< 0.2	4	557.3	41.6	96.6 ± 49.0
> 150	no cut	no cut	343	6.5	72.7	3.4 ± .2
> 150	> 0.7	no cut	50	44.6	55.4	13.7 ± 2.0
> 150	> 0.7	< 0.1	1	2229.0	44.5	441.1 ± 441.6
> 150	> 0.7	< 0.2	9	247.7	52.4	67.9 ± 22.9
> 150	> 0.75	no cut	33	67.5	50.1	16.9 ± 3.1
> 150	> 0.75	< 0.1	0	∞	40.2	∞
> 150	> 0.75	< 0.2	5	445.8	47.3	99.9 ± 45.0
> 150	> 0.8	no cut	17	131.1	39.5	20.5 ± 5.3
> 150	> 0.8	< 0.1	0	∞	31.8	∞
> 150	> 0.8	< 0.2	4	557.3	37.4	77.8 ± 39.5
> 200	no cut	no cut	280	8.0	65.1	3.4 ± .2
> 200	> 0.7	no cut	44	50.7	49.6	12.5 ± 2.0
> 200	> 0.7	< 0.1	1	2229.0	39.8	353.7 ± 354.1
> 200	> 0.7	< 0.2	9	247.7	46.9	54.4 ± 18.3
> 200	> 0.75	no cut	28	79.6	44.9	16.0 ± 3.2
> 200	> 0.75	< 0.1	0	∞	36.0	∞
> 200	> 0.75	< 0.2	5	445.8	42.4	80.1 ± 36.1
> 200	> 0.8	no cut	17	131.1	35.4	16.4 ± 4.2
> 200	> 0.8	< 0.1	0	∞	28.4	∞
> 200	> 0.8	< 0.2	4	557.3	33.5	62.4 ± 31.6
no cut	no cut	< 0.1	102	21.9	80.3	14.1 ± 1.4
no cut	no cut	< 0.2	221	10.1	94.5	9.0 ± .6
> 100	no cut	< 0.1	35	63.7	65.0	26.9 ± 4.5
> 100	no cut	< 0.2	100	22.3	76.5	13.1 ± 1.3
> 150	no cut	< 0.1	27	82.6	58.4	28.1 ± 5.4
> 150	no cut	< 0.2	76	29.3	68.7	13.8 ± 1.6
> 200	no cut	< 0.1	23	96.9	52.3	26.5 ± 5.5
> 200	no cut	< 0.2	63	35.4	61.5	13.4 ± 1.7

Table C.2: *Number of events remaining and rejection factor of opposite-signed sideband muon pairs with the signal efficiency and the signal-to-background significance. The requirements selected are highlighted.*

bin	$c\tau$	Isolation	Background	$N_{obs}(J/\psi\phi)$	$\bar{N}$	$\mathcal{S}$
1	0.	.00	39.3	21.53 ± 7.60	15.79	0.733
2	0.	.65	14.0	12.85 ± 4.39	10.60	0.825
3	0.	.70	10.0	10.86 ± 3.89	9.43	0.869
4	0.	.75	7.0	10.92 ± 3.72	8.38	0.768
5	0.	.80	4.0	8.21 ± 3.20	7.04	0.858
6	0.	.85	2.0	7.47 ± 0.05	5.55	0.743
7	50.	.00	16.7	16.67 ± 4.09	11.30	0.678
8	50.	.65	4.0	10.95 ± 3.19	7.04	0.643
9	50.	.70	3.0	10.69 ± 2.94	6.42	0.601
10	50.	.75	1.7	9.83 ± 2.82	5.16	0.524
11	50.	.80	0.7	8.66 ± 2.52	3.33	0.384
12	50.	.85	0.7	8.46 ± 1.88	3.33	0.393
13	100.	.00	7.0	17.52 ± 3.48	8.38	0.478
14	100.	.65	1.7	12.26 ± 2.74	5.16	0.420
15	100.	.70	1.3	11.85 ± 2.39	4.68	0.395
16	100.	.75	0.7	11.03 ± 2.23	3.33	0.302
17	100.	.80	0.0	9.50 ± 1.91	0.00	0.000
18	100.	.85	0.0	8.77 ± 0.04	0.00	0.000
19	150.	.00	3.0	15.30 ± 2.85	6.42	0.420
20	150.	.65	1.3	10.96 ± 2.25	4.68	0.427
21	150.	.70	1.0	10.15 ± 0.06	4.08	0.402
22	150.	.75	0.7	9.40 ± 0.08	3.33	0.354
23	150.	.80	0.0	7.83 ± 1.44	0.00	0.000
24	150.	.85	0.0	6.85 ± 0.04	0.00	0.000
25	200.	.00	2.7	13.77 ± 2.62	6.17	0.448
26	200.	.65	1.3	9.25 ± 2.10	4.68	0.506
27	200.	.70	1.0	8.45 ± 0.06	4.08	0.483
28	200.	.75	0.7	7.68 ± 0.08	3.33	0.434
29	200.	.80	0.0	6.80 ± 1.42	0.00	0.000
30	200.	.85	0.0	6.85 ± 0.04	0.00	0.000
31	250.	.00	2.0	10.38 ± 1.99	5.55	0.535
32	250.	.65	0.7	6.51 ± 0.07	3.33	0.512
33	250.	.70	0.7	5.61 ± 0.06	3.33	0.593
34	250.	.75	0.3	4.73 ± 1.37	2.34	0.495
35	250.	.80	0.0	4.73 ± 1.37	0.00	0.000
36	250.	.85	0.0	4.81 ± 0.04	0.00	0.000
37	300.	.00	2.0	9.35 ± 1.97	5.55	0.594
38	300.	.65	0.7	5.36 ± 0.06	3.33	0.621
39	300.	.70	0.7	4.58 ± 0.06	3.33	0.727
40	300.	.75	0.3	3.69 ± 1.33	2.34	0.635
41	300.	.80	0.0	3.69 ± 1.33	0.00	0.000

Table C.3: *The sensitivity of different selection requirements for the Run 1B sample.*

bin	$c\tau$	Isolation	Background	$N_{obs}(J/\psi\phi)$	$\bar{N}$	$\mathcal{S}$
42	300.	.85	0.0	3.80 ± 0.03	0.00	0.000
43	350.	.00	1.3	7.51 ± 1.72	4.68	0.623
44	350.	.65	0.3	3.67 ± 1.34	2.34	0.637
45	350.	.70	0.3	3.67 ± 1.34	2.34	0.637
46	350.	.75	0.0	2.62 ± 1.28	0.00	0.000
47	350.	.80	0.0	2.62 ± 1.28	0.00	0.000
48	350.	.85	0.0	2.79 ± 0.03	0.00	0.000
49	400.	.00	1.0	5.64 ± 1.40	4.08	0.724
50	400.	.65	0.3	3.79 ± 0.03	2.34	0.618
51	400.	.70	0.3	3.79 ± 0.03	2.34	0.618
52	400.	.75	0.0	2.79 ± 0.03	0.00	0.000
53	400.	.80	0.0	2.79 ± 0.03	0.00	0.000
54	400.	.85	0.0	2.79 ± 0.03	0.00	0.000

Table C.3(**continued**): *The sensitivity of different selection requirements for the Run 1B sample.*

Appendix D

B_s^0 yield check

The $B_s^0 \to J/\psi\,\phi$ sample observed in this analysis can be compared to the samples observed in other B_s^0 analyses, such as the $B \to VV$ polarization study [201]. The number of B_s^0 candidates observed in this study is 40.3 ± 9.7 (Figure 2.5 in Reference [201]), while 21.53 ± 7.60 candidates are observed in this search after applying the basic selection requirements.

The first difference between the two samples is that the polarization study uses the whole Stream A J/ψ dataset, with an integrated luminosity of 87 pb^{-1}. For this search, only runs present in all the four data streams (BHMB, PSAB, PSPB and Stream C) are kept, which reduces the integrated luminosity of the used sample to 72 pb^{-1}.

The selection requirements of the two studies show some significant differences as well. The selection requirements applied in this search are in many cases much tighter already at the preselection stage. This is dictated by the need to reduce the huge Stream C data sample to a manageable size. The main differences in the selection requirements applied are listed in Table D.1.

Requirement	Preselection	Basic req.	'Polarization' req.
1) $p_T(\mu)$	$> (2.0, 2.0)/(2.8, 1.8)$ GeV/c	same	> 1.43 GeV/c
2) $p_T(\phi)$	> 1.4 GeV/c	> 2.0 GeV/c	> 1.5 GeV/c
3) $p_T(B)$	> 5.4 GeV/c	> 6.0 GeV/c	> 4.5 GeV/c
4) $c\tau$	-	> 0 μm	> 50 μm
5) Isolation	-	-	< 0.54
6) SVX	$\lvert z_0(\mu)\rvert < 50$ cm	$2\ \mu + \geq 1\ K$ in SVX	≥ 2 tracks in SVX
7) CMP	-	$\geq 1\ \mu$ in CMP	no CMP requirement

Table D.1: *List of the main differences in the selection requirements between the polarization study and this search.*

To ascertain that the reduction in yield is due to the reasons outlined above, the selection requirements have been loosened to the values of the polarization study. It is not possible to reproduce the polarization B_s^0 yield from the preselected J/ψ sample available (from the PSAB dataset), as the preselection requirements have already been applied to it. The Stream A J/ψ dataset has therefore to be used.

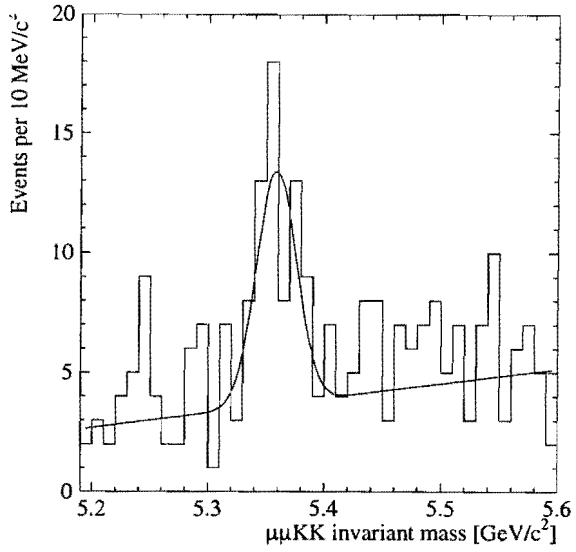

Figure D.1: *Invariant mass distribution of resonant candidates with the modified selection requirements (Run 1B Stream A J/ψ sample only).*

Most selection requirements in Table D.1 have been changed to be the same as the requirements imposed in the polarization study. A slight difference persists in the SVX quality requirements, as the SVX-χ^2/hit requirement (SVX-$\chi^2/hit < 6$) is not imposed in the polarization study. This requirement is maintained for the cross-check.

The main difference between the two samples still remaining is the isolation requirement, as a different definition of the isolation variable is used. In the polarization study, the isolation is defined as

$$I_{pol} = \frac{1}{|\vec{p}(B)|} \sum \vec{p}_i \cdot \hat{p}(B) \tag{D.1}$$

which can be compared to the definition of the isolation used in the present study (Equation 8.3). For both variables, the tracks added in the sum are the same, i.e. all tracks (excluding the four tracks composing the candidate) within a cone of $\Delta R < 1$ which pass within 5 cm of the B candidate z-vertex.

Maintaining the isolation variable used throughout this work, a requirement of $I > 0.5$ is judged to be equivalent.

The resulting invariant mass distribution is shown in Fig. D.1 and a fit of a Gaussian and a linear background on this distribution yields 40.5 ± 13.3 B_s^0 candidates. The results of this fit, compared with the results found in the polarization study, are given in Table D.2.

	'Loose' selection	'Polarization' study
Yield	41.8 ± 13.5	40.3 ± 9.7
Mass	5358.7 ± 4.3 MeV/c^2	5359.2 ± 3.6 MeV/c^2
Width	17.0 ± 3.5 MeV/c^2	14.3 ± 3.8 MeV/c^2

Table D.2: *Results of the fit on the B_s^0 candidate mass distribution for the selection with the loose set of requirements ('Loose' selection) and the results found in the Polarization study.*

List of Tables

Bibliography

[1] Particle Data Group, *Review of Particle Properties*, C. Caso *et al.*, *E. Phys. J.* C **3**, 1 (1998) and 1999 off-year partial update for the 2000 edition available on the PDG WWW pages (URL: http://pdg.lbl.gov/)

[2] J.-P. Derendinger, *Théorie Quantique des Champs*, ed. Troisième cycle de la Physique en Suisse Romande, 1995

[3] F. Halzen and A.D. Martin, *Quarks and Leptons*, J. Wiley & Sons, New York, 1984

[4] P. Renton, *Electroweak Interactions*, Cambridge University Press, Cambridge, 1990

[5] C. Quigg, *Gauge Theories of the Strong, Weak and Electromagnetic Interactions*, Frontiers of Physics, Volume 56, Addison-Wesly Publishing Company, Reading, MA, 1983

[6] G. Sternman, *Quantum Field Theory*, Cambridge University Press, Cambridge, 1993

[7] E. Leader and E. Predazzi, *An introduction to gauge theories and modern particle physics*, Cambridge monographs on particle physic-, nuclear physics and cosmology, Volumes 3 and 4, Cambridge University Press, Cambridge, 1993

[8] S.L. Glashow, Nucl. Phys. **22**, 579 (1961)

[9] S. Weinberg, *Phys. Rev. Lett.* **19**, 1264 (1967)

[10] A. Salam, p.367 of *Elementary Particle Theory*, ed. N.Svartholm, Almquist and Wiksells, Stockholm, 1969

[11] G. 't Hooft and M. Veltman, *Diagrammer*, in *Particle Interactions at Very High Energies*, ed. F. Halzen, D.Speiser and J. Weyers, Plenum Press, New York, 1974

[12] R.P. Feynman anf M. Gell-Mann, *Phys. Rev.* **109**, 193 (1958)

[13] N. Cabibbo, *Phys. Rev. Lett.* **10**, 531 (1963)

[14] S.L. Glashow, J. Iliopoulos and L. Maiani, *Phys. Rev.* D **2**, 1285 (1970)

[15] M.K. Gaillard and B.W. Lee, *Phys. Rev.* **10**, 897 (1974)

[16] J.H. Christenson *et al.*, *Phys. Rev. Lett.* **13**, 138 (1964)

[17] M. Kobayashi and T. Maskawa, *Prog. Theor. Phys.* **49**, 652 (1973)

[18] C. Jarlskog, *Phys. Rev. Lett.* **55**, 1039 (1985),
C. Jarlskog, *Z. Phys.* C **29**, 491 (1985)

[19] J.V. Narlikar, *Introduction to Cosmology*, Cambridge University Press, Cambridge, 1983

[20] M. Gell-Mann, *Phys. Rev. Lett.* **8**, 214 (1964)

[21] J.J. Aubert *et al.*, *Phys. Rev. Lett.* **33**, 1404 (1974)

[22] J.E. Augustin *et al.*, *Phys. Rev. Lett.* **33**, 1406 (1974)

[23] S. Okubo, *Phys. Lett.* **5**, 163 (1963)
G. Zweig, CERN Preprints (Unpublished), Th 401, 412 (1964)
J. Iizuka, *Suppl. Progr. Theor. Phys.* **35**, 37-38 (1966)

[24] M.L. Perl *et al.*, *Phys. Rev. Lett.* **35**, 1489 (1975)

[25] S.W. Herb *et al.*, *Phys. Rev. Lett.* **39**, 252 (1977)

[26] E. Eichten and K. Gottfried, *Phys. Lett.* B **66**, 286 (1976)

[27] F. Abe *et al.*, *Phys. Rev.* D **50**, 2966 (1994)

[28] F. Abe *et al.*, *Phys. Rev. Lett.* **74**, 2626 (1995)

[29] S. Abachi *et al.*, *Phys. Rev. Lett.* **74**, 2632 (1995)

[30] J.H. Kühn and P.M. Zerwas, *Heavy Flavors in High Energy Electron-Positron Collisions*, in *Heavy Flavours II*, edited by A.J. Buras and M. Lindner, Advanced series on Directions in High Energy Physics, World Scientific, Singapore, 1998.

[31] P. Nason, *Heavy Quark production*, in *Heavy Flavours*, edited by A.J. Buras and M. Lindner, Advanced series on Directions in High Energy Physics, World Scientific, Singapore, 1992.

[32] S. Frixione, M.L. Mangano, P. Nason and G. Ridolfi, *Heavy Quark production*, in *Heavy Flavours II*, edited by A.J. Buras and M. Lindner, Advanced series on Directions in High Energy Physics, World Scientific, Singapore, 1998.

[33] A. Acciarri *et al.*, *Z. Phys.* C **62**, 551 (1994)

[34] G. Altarelli and G. Parisi, *Nucl. Phys.* B **126**, 298 (1977)

[35] M. Gluck, J.F. Ovens and E. Reya, *Phys. Rev.* D **17**, 2324 (1978)

[36] B.L. Combridge, *Nucl. Phys.* B **1517**, 429 (1979)

[37] J. Babcock, D. Sivers and S. Wolfram, *Phys. Rev.* D **18**, 162 (1978)

[38] P. Nason, S. Dawson and R.K. Ellis, *Nucl. Phys.* B **303**, 607 (1988), *Nucl. Phys.* B **327**, 49 (1988) and Erratum in *Nucl. Phys.* B **335**, 260 (1990)

[39] M.L. Mangano, P. Nason and G. Ridolfi, *Nucl. Phys.* B **373**, 160 (1992)

[40] The CDF Collaboration, *Measurement of the Ratio of b-Quark Production Cross Sections at* $\sqrt{s}$ = 630 GeV *and* $\sqrt{s}$ = 1800 GeV, FEMILAB-CONF-96/176-E, PA04-059,*28th International Conference on High-Energy Physics (ICHEP '96), Warsaw, Poland*, Publ. in: Proceedings, Edited by Z. Ajduk and A.K. Wróblewski, World Scientific, Singapore, 1997

[41] B.T. Huffmann, for the CDF collaboration. FERMILAB-CONF-92-337-E, Nov 1992, published in DPF Conf.1992, 771 (1992)

[42] F. Abe *et al.*, *Phys. Rev. Lett.* **79**, 572 (1997)

[43] F. Abe *et al.*, Fermilab-Pub-94/131-E

[44] F. Abe *et al.*, *Phys. Rev.* D **53**, 1051 (1996)

[45] M. Artuso, *Experimental Facilities for b-Quark Physics*, in B *Decays*, edited by S. Stone, World Scientific, Singapore, 1992.

[46] The ATLAS Collaboration, *ATLAS Detector and Physics Performance, Volume II, Technical Design Report*, CERN/LHCC/99-15 (1999)

[47] C. Peterson, D. Schlatter, I. Schmitt and P. Zerwas, *Phys. Rev.* D **27**, 105 (1983)

[48] G. Alexander *et al.*, *Phys. Lett.* B **364**, 93 (1995)

[49] F. Abe *et al.*, Fermilab-Pub-96/198-E

[50] A.J. Buras and R. Fleischer, *Quark Mixing, CP Violation and Rare Decays After the Top Quark discovery*, in *Heavy Flavours II*, edited by A.J. Buras and M. Lindner, Advanced series on Directions in High Energy Physics, World Scientific, Singapore, 1998.

[51] G. Buchalla, AJ. Buras and M.E. Lautenbacher, Rev. Mod. Phys **68**, 1125 (96)

[52] R. Ammar *et al.*, *Phys. Rev. Lett.* **71**, 674 (1993)

[53] D. Cronin-Hennessy *et al.*, hep-ex/0001010, Submitted to Phys. Rev. Lett.
R. Godang *et al.*, *Phys. Rev. Lett.* **80**, 3456 (1998)

[54] K.G. Wilson, *Phys. Rev.* **179**, 1499 (1969)

[55] G. 't Hooft and M. Veltman, *Nucl. Phys.* B **44**, 189 (1972)

[56] T.E. Coan *et al.*, The CLEO collaboration, hep-ph/9912057, Submitted to Phys. Rev. Lett.

[57] The CLEO collaboration, *Improved Measurement of* $\mathcal{B}(b \to s\gamma)$, CLEO/CONF 98-17, ICHEP98 1011, *29th International Conference on High-Energy Physics (ICHEP '98), Vancouver, Canada*, Publ. in: Proceedings, Edited by: A. Astbury, D. Axen and J. Robinson, World Scientific, Singapore, 1999

[58] R. Barate *et al.*, *Phys. Lett.* B **429**, 169 (1998)

[59] A.J. Buras, A. Kwiatkowski and N. Pott, *Phys. Lett.* B **414**, 157 (1997)

[60] K. Lingel, T. Skwarnicki and J.G. Smith, Ann. Rev. Nucl. Part. Sci. **48**, 253 (1998)

[61] J.L Hewett, *B Physics Beyond the Standard Model*, Publ. in: *Proceedings of the 7th. International Symposium on Heavy Flavor Physics*, Santa Barbara, CA, World Scientific, Singapore, 1998. (hep-ph/9803370)

[62] A. Ali and C. Greub, *Phys. Lett.* B **287**, 191 (1992)

[63] L. Del Debbio, J.M. Flynn, L. Lellouch and J.Nieves, *Phys. Lett.* B **416**, 392 (1998)

[64] B. Grinstein, M.J. Savage and M.B. Wise, *Nucl. Phys.* B **319**, 271 (1989)

[65] W.S. Hou, R.I. Willey and A. Soni, *Phys. Rev. Lett.* **58**, 1608 (1987)

[66] A.J.Buras and M. Münz, *Phys. Rev.* D **52**, 186 (1995)

[67] M. Misiak, *Nucl. Phys.* B **393**, 23 (1993) and Erratum in M. Misiak, *Nucl. Phys.* B **439**, 461(E) (1995)

[68] C.S. Lim, T. Morozumi and A.I. Sanda, *Phys. Lett.* B **218**, 343 (1989)

[69] M.R. Ahmadi, *Phys. Rev.* D **53**, 2843 (1996)

[70] A. Ali, G. Hiller, L.T. Handoko and T. Morozumi, *Phys. Rev.* D **55**, 4105 (1997)

[71] A. Ali, T. Mannel and T. Morozumi, *Phys. Lett.* B **273**, 505 (1991)

[72] Z. Ligeti and M.B. Wise, *Phys. Rev.* D **53**, 4937 (1996)

[73] M. Neubert, *Phys. Lett.* B **397**, 279 (1997)

[74] J.L. Hewett, *Phys. Rev.* D **58**, 4964 (1996)

[75] D. Melikhov, N. Nikitin and S. Simula, *Phys. Rev.* D **57**, 6814 (1998)

[76] M. Neubert, *Phys. Rev.* **245**, 259 (1994)

[77] S. Glenn *et al.*, *Phys. Rev. Lett.* **80**, 2289 (1998)

[78] N. Isgur and M.B. Wises, *Phys. Rev.* D **42**, 2388 (1990)

[79] P. Colangelo, F. De Fazio, P. Santorelli and E. Scrimieri, *Phys. Rev.* D **53**, 3672 (1996)

[80] T.M. Aliev, M. Savci and A. Özpineci, *Phys. Rev.* D **56**, 4260 (1997)
T.M. Aliev, M. Savci and A. Özpineci, *Phys. Lett.* B **400**, 194 (1997)

[81] P. Ball and V.M. Braun, *Phys. Rev.* D **58**, 094016-1 (1998)

[82] A. Ali, P. Ball, L.T. Handoko and G. Hiller, *Phys. Rev.* D **61**, 074024 (2000)

[83] D. Melikhov, B. Stech, *Phys. Rev.* D **62**, 014006 (2000)

[84] C.Q. Geng and C.P. Kao, *Phys. Rev.* D **54**, 5636 (1996)
W. Jaus and D. Wyler, *Phys. Rev.* D **41**, 3405 (1990)
W. Jaus, *Phys. Rev.* D **41**, 3394 (1990)

[85] P. Colangelo, F. De Fazio, M. Ladisa, G. Nardulli, P. Santorelli and E. Scrimieri, A. Tricarico, hep-ph/9809372

[86] A. Ali and D. London, *Z. Phys.* C **65**, 431 (1995),
A. Ali, hep-ph/9606324,
A. Ali, *Nucl. Instrum. Methods* A **384**, 8 (1996)

[87] The CLEO collaboration, *Search for Electroweak Penguin Decays* $B^+ \to l^+l^-K^+$ *and* $B^0 \to l^+l^-K^{*0}$ *at CLEO*, CLEO/CONF 98-22, ICHEP98 1012, *29th International Conference on High-Energy Physics (ICHEP '98), Vancouver, Canada*, Publ. in: Proceedings, Edited by: A. Astbury, D. Axen and J. Robinson, World Scientific, Singapore, 1999

[88] T. Affolder *et al.*, *Phys. Rev. Lett.* **83**, 3378 (1999)

[89] A.J. Buras, pp243-270 in *28th International Conference on High-Energy Physics (ICHEP '96), Warsaw, Poland*, Publ. in: Proceedings, Edited by Z. Ajduk and A.K. Wróblewski, World Scientific, Singapore, 1997

[90] D. Buskulic *et al.*, *Phys. Lett.* B **343**, 444 (1995)

[91] The ALEPH collaboration, *Measurement of* $\mathcal{B}(b \to \tau\nu X)$ *and upper limits on* $\mathcal{B}(B \to \tau\nu)$ *and* $\mathcal{B}(b \to s\nu\bar{\nu})$, PA10-019, *28th International Conference on High-Energy Physics (ICHEP '96), Warsaw, Poland*, Publ. in: Proceedings, Edited by Z. Ajduk and A.K. Wróblewski, World Scientific, Singapore, 1997

[92] W. Adam *et al.*, *Z. Phys.* C **72**, 207 (1996)

[93] G. Buchalla and A. J. Buras, *Nucl. Phys.* B **400**, 225 (1993)

[94] A. Ali, *Rare B Decays in the Standard Model*, in 4^{th} *International Workshop on B Physics at Hadron Machines*, Beauty '96 Rome, Italy, Publ. in: Proceedings, Edited by F. Ferroni and P. Schlein, Nucl. Instrum. Methods Phys. Res., A384 (1996).

[95] R. Ammar *et al.*, *Phys. Rev.* D **49**, 5701 (1994)

[96] M. Acciarri *et al.*, *Phys. Lett.* B **391**, 474 (1997)

[97] F. Abe *et al.*, *Phys. Rev.* D **57**, R3811 (1998)

[98] Y. Grossman, Z. Ligeti and E. Nardi, *Phys. Rev.* D **55**, 2847 (1997)

[99] F. Abe *et al.*, *Phys. Rev. Lett.* **81**, 5742 (1998)

[100] Y. Nir and H.R. Quinn, Ann. Rev. Nucl. Part. Sci. **42**, 211 (1992)

[101] Particle Data Group, *Review of Particle Properties*, D.E. Groom et al, *E. Phys. J.* C **15**, 1 (2000)

[102] C. Greub, A. Ionissian and D. Wyler, *Phys. Lett.* B **346**, 145 (1995)

[103] J.L. Hewett and J.D. Wells, *Phys. Rev.* D **55**, 5549 (1997)

[104] M. Gronau and D. London, *Phys. Rev.* D **55**, 2845 (1997)

[105] Y. Grossman, Z. Ligeti and E. Nardi, *Nucl. Phys.* B **465**, 369 (1996) and Erratum in *Nucl. Phys.* B **480**, 753 (1996)

[106] C. Albajar *et al.*, *Phys. Lett.* B **262**, 163 (1991)

[107] M.S. Alam *et al.*, *Phys. Rev. Lett.* **74**, 2885 (1995)

[108] Y. Okada, Y.Shimizu and M. Tanaka, *Phys. Lett.* B **405**, 297 (1997)

[109] T.M. Aliev and E.O. Iltan, *Phys. Lett.* B **451**, 175 (1999)

[110] G. Burdman, *Phys. Rev.* D **59**, 035001 (1999)

[111] M. Misiak, S. Pokorski and J. Rosiek, *Supersymmetry and FCNC Effects*, in *Heavy Flavours*, edited by A.J. Buras and M. Lindner, Advanced series on Directions in High Energy Physics, World Scientific, Singapore, 1998.

[112] S.R. Choudhury and N. Gaur, *Phys. Lett.* B **451**, 86 (1999)

[113] Particle Data Group, *Review of Particle Properties*, *Phys. Rev.* D **45**, (1992)

[114] J. Thompson, *Introduction to Colliding Beams at Fermilab*, FERMILAB-TM-1909 (1994)

[115] J. Marriner *et al.*,*The Run II Handbook*, WWW document: `http://www-bd.fnal.gov/lug/runII_handbook/RunII_index.html`

[116] G.P. Jackson, *Fermilab Recycler Ring: Technical Design Report*, FERMILAB-TM-1991 (1996)

[117] F. Abe *et al.*, *Nucl. Instrum. Methods* A **271**, 387 (1988)

[118] H. Minemura *et al.*, *Nucl. Instrum. Methods* A **238**, 18 (1985)

[119] D. Amidei *et al.*, *Nucl. Instrum. Methods* A **350**, 73 (1994)

[120] S. Cihangir *et al.*, *Nucl. Instrum. Methods* A **360**, 137 (1995)

[121] S.A. Kleinfelder, *IEEE Trans. Nucl Sci.* **NS-35**, 171 (1988)
C. Haber *et al.*, *IEEE Trans. Nucl Sci.* **NS-37**, 1200 (1990)

[122] M. Laakso *et al.*, *Nucl. Instrum. Methods* A **327**, 517 (1993)

[123] F. Bedeschi *et al.*, *Nucl. Instrum. Methods* A **268**, 50 (1988)

[124] L. Balka *et al.*, *Nucl. Instrum. Methods* A **267**, 272 (1988)

[125] Y. Fukui *et al.*, *Nucl. Instrum. Methods* A **267**, 280 (1988)

[126] G. Brandenburg *et al.*, *Nucl. Instrum. Methods* A **267**, 257 (1988)

[127] L. Nodulman *et al.*, *Nucl. Instrum. Methods* A **204**, 351 (1983)

[128] S. Bertolucci *et al.*, *Nucl. Instrum. Methods* A **267**, 301 (1988)

[129] S. Cihangir*et al.*, *Nucl. Instrum. Methods* A **267**, 249 (1988)

[130] G. Ascoli *et al.*, *Nucl. Instrum. Methods* A **268**, 33 (1988)

[131] J.D. Lewis *et al.*, *The 1992 CDF Muon Upgrade System*, CDF internal note 2858 (1995), to be submitted to *Nucl. Instrum. Methods* A

[132] J.D. Lewis *et al.*, *The Central Muon Extension Scintillators (CSX)*, CDF internal note 3989, unpublished

[133] K. Byrum *et al.*, *Nucl. Instrum. Methods* A **268**, 46 (1988)

[134] D. Cronin-Hennessy and A. Beretvas, *Luminosity at CDF*, CDF internal note 4721 (1998), unpublished

[135] F. Abe *et al.*, *Phys. Rev.* D **50**, 5550 (1994)

[136] D. Amidei *et al.*, *Nucl. Instrum. Methods* A **269**, 51 (1988)

[137] G. Ascoli *et al.*, *Nucl. Instrum. Methods* A **269**, 63 (1988)

[138] G.W. Foster, J. Freeman, C. Newman-Holmes and J. Patrick, *Nucl. Instrum. Methods* A **269**, 93 (1988)
J.D. Lewis and K.T. Pitts, *A Summary of CFT Operation in Run 1*, CDF internal note 3999, unpublished

[139] J. Kroll, P. Sphicas, and D. Vučinić, *Search for the Decay* $B^0 \to \mu^+\mu^-$, CDF internal note 2766 (1994), unpublished
F. Abe *et al.*, *Phys. Rev. Lett.* **76**, 2015 (1996)

[140] F. Abe *et al.*, *Phys. Rev. Lett.* **75**, 1451 (1996)

[141] F. Abe *et al.*, *Phys. Rev.* D **54**, 6596 (1996)

[142] T. Affolder *et al.*,*Phys. Rev. Lett.* **84**, 1663 (2000)

[143] J. Lee-Franzini *et al.*, *Phys. Rev. Lett.* **65**, 2947 (1990)

[144] D. Buskulic *et al.*, *Phys. Lett.* B **294**, 145 (1992)

[145] F. Abe *et al.*, *Phys. Rev. Lett.* (, 7 (1))16851993BUSKULIC D

[146] The ALPEH Collaboration, *A Study of the width difference in the $B_s - \bar{B}_s$ system*, ALEPH 98-064, ICHEP98 1054, *29th International Conference on High-Energy Physics (ICHEP '98), Vancouver, Canada*, Publ. in: Proceedings, Edited by: A. Astbury, D. Axen and J. Robinson, World Scientific, Singapore, 1999

[147] F. Abe *et al.*, *Phys. Rev.* D **53**, 3496 (1996)

[148] R. Akers *et al.*, *Phys. Lett.* B **337**, 196 (1994)

[149] D. Buskulic *et al.*, *Phys. Lett.* B **311**, 425 (1993)

[150] P. Abreu *et al.*, *Phys. Lett.* B **324**, 500 (1994)

[151] R. Fleischer and I. Dunietz, *Phys. Rev.* D **55**, 259 (1997)

[152] I. Dunietz, *CP Violation with Additional B Decays*, in B *Decays*, edited by S. Stone, World Scientific, Singapore, 1992.

[153] M. Benecke, G. Buchalla and I. Dunietz, *Phys. Rev.* D **54**, 4419 (1996)

[154] A.S. Dighe, I.Dunietz, H.L. Lipkin and J.L. Rosner, *Phys. Lett.* B **369**, 144 (1996)

[155] J. Lewis and S. Tkaczyk, CDFNEWS 12954.

[156] H. Wenzel, *Tracking in the SVX*, CDF internal note 1790 (1992), unpublished

[157] S. P. Pappas, J. D. Lewis, G. Michail, *Run IB Low pT Central Dimuon Trigger Efficiencies*, CDF internal note 4076 (1997), unpublished
S. P. Pappas, J. D. Lewis, *Run IB Low pT Central Dimuon Trigger Efficiencies*, CDF internal note 3070 (1995), unpublished

[158] K. Kelley, B. Mattingly, and P. Sphicas, *A Study of the Isolation of B mesons*, CDF internal note 2765 (1994), unpublished

[159] G.Bauer, J. Friedman, K. Kelley, T. Shah, and P. Sphicas, *A Study of the Isolation of B mesons Part II*, CDF internal note 3684 (1996), unpublished

[160] H. Wenzel, K. Maeshima, D. Benjamin and E. Hayashi, *A Study of the CTC Tracking Performance during Run 1B*, CDF internal note 3421 (1995), unpublished

[161] M.W. Bailey, A.F. Garfinkel, S.M. Tkaczyk, *CTC Tracking Efficiency for the B Cross-Section Analysis*, CDF internal note 2815 (1994), unpublished

[162] A. Warburton, *Run 1A and Run 1B Low-p_T Single- and Double-Track CTC Pattern Recognition Efficiencies*, CDF internal note 4139 (1997), unpublished

[163] G. Field, J.D. Lewis, V. Papadimitriou and M. Schmidt, *Upsilon Cross Section Measurements in Run 1B*, CDF internal note 5027 (1999), unpublished

[164] G. Field, J.D. Lewis, M. Schmidt and W. Trischuk, *Study of Run 1B Data Sets*, CDF internal note 4312 (1997), unpublished

[165] P. Ngan, P. Sphicas and J.D. Lewis, *Luminosity Dependence of 1B J/ψ yield*, CDF internal note 4313 (1997), unpublished

[166] A. Warburton, private communication.

[167] T. Lecompte and J.D. Lewis, *Update on the B cross-section measurement via $D^0 + \mu$ and $D^* + \mu$*, CDF internal note 2588 (1994), unpublished

[168] D. Kestenbaum and P. Schlabach, *A Measurement of the CMX Stub Finding Efficiency*, CDF internal note 3115 (1995), unpublished

[169] Tom Lecompte, *A Study of Muon Stub-Track Misassociation Probabilities*, CDF internal note 2700 (1994), unpublished

[170] C.E. Anway-Wiese, *Offline Muon Matching Cuts*, CDF internal note 1996 (1993), unpublished

[171] F. DeJongh, *Level 3 Dimuon Efficiency for Run 1A*, CDF internal note 1984 (1993), unpublished

[172] Particle Data Group, *Review of Particle Properties*, *Phys. Rev.* D **54**, (July 1996)

[173] H. Wenzel and D. Benjamin, *Optimizing SVX/CTC track quality cuts*, CDF internal note 3181 (1995), unpublished

[174] G.J. Feldman and R.D. Cousins, *Phys. Rev.* D **57**, 3873 (1998)

[175] J. D. Lewis, *CLEOMC: The CDF Interface to the CLEO Monte Carlo (QQ)*, CDF internal note 2724 (1994), unpublished

[176] G. Feild, J.D. Lewis and M. Schmidt, *J/psi Cross Sections and Instantaneous Luminosity*, CDF internal note 4769 (1999), unpublished

[177] D. Boutigny *et al.*, *BABAR Technical Design Report*, SLAC-R-0457, Mar. 1995.

[178] The BELLE Collaboration *BELLE Technical Design Report*, KEK-Report 95-1, April 1995.

[179] The CLEO Collaboration, *The CLEO III detector : design and physics goals*, CLNS 94-1277, 1994

[180] The HERA-B Collaboration, *HERA-B Technical Design Report*, DESY-PRC 95/01, 1995.

[181] W.W. Armstrong *et al.*, *ATLAS: Technical Proposal for a general-purpose p p experiment at the Large Hadron Collider at CERN*, CERN-LHCC-94-43, Dec 1994.

[182] The CMS collaboration, *CMS, the Compact Muon Solenoid: Technical Proposal*, CERN-LHCC-94-38, 1994

[183] LHCb Collaboration. A Large Hadron Collider Beauty experiment for precision measurements of CP–violation and rare decays, CERN/LHCC/98-4, February 1998.

[184] ALICE Collaboration. Technical Proposal for a Large Ion Collider Experiment at the CERN LHC, CERN/LHCC/95–71, December 1995.

[185] B. Abbot *et al.*, "The D0 Upgrade: The Detector and its Physics", FERMILAB-Pub-96/357-E, October 1996

[186] The CDF II Collaboration, *The CDF II Detector: Technical Design Report*, FERMILAB-Pub-96/390-E 1996

[187] M. Kirk, J. D. Lewis and M. Tanaka, *Rareb Decays at Run II at CDF*, CDF internal note 5279 (2000), unpublished

[188] D. Melikhov, N. Nikitin, F. Rizatdinova and L. Smirnova, *Studying the physics beyond the Standard Model in rare semileptonic B-decays $B \to K^*\mu^+\mu^-$ with the ATLAS detector*, ATLAS internal note, PHYS-NO-123, 1998. and S. Simula, *Phys. Rev.* D **57**, 6814 (1998)

[189] P. Sphicas, *A B-BBAR Monte Carlo Generator*, CDF internal note 2655, unpublished

[190] A.D. Martin, W.J. Stirling and R.G. Roberts, *Phys. Rev.* D **47**, 867 (1993)

[191] J. Chrin, *Z. Phys.* C **36**, 163 (1987)

[192] N. Nikitin, private communication.

[193] M. Shapiro *et al.*, *A User's Guide to QFL*, CDF internal note 1810, unpublished

[194] S. P. Pappas, *DIMUTG: Dimuon Trigger Simulation for Run IB*, CDF internal note 3537, unpublished

[195] F. DeJongh and R. Hans, *Level 1 and Level 2 Low p_T Central Muon Trigger Efficiencies for Run 1A*, CDF internal note 1999, unpublished

[196] G. Cowan, *Statistical Data Analysis*, Oxford University Press, Oxford, 1998.

[197] R.D. Cousins and V.L. Highland, *Nucl. Instrum. Methods* A **320**, 331-335 (1992)

[198] G. Zech, *Nucl. Instrum. Methods* A **277**, 608 (1989)

[199] O. Helene, *Nucl. Instrum. Methods* A **212**, 319 (1983)

[200] J. Conway and K. Maeshima, *Upper Limits on Poisson Processes Incorporating Uncertainties in Acceptance and Background*, CDF internal note 4476 (1998), unpublished

[201] S. P. Pappas and M.P. Schmidt, *Measurement of the Polarization in $B \to VV$*, CDF internal note 4672 (1998), unpublished